UNIVERSITÀ DEGLI STUDI DI TRIESTE

XXXVIII CICLO DEL DOTTORATO DI RICERCA IN FISICA

Measurement of the ^{30}Si(n, γ) and ^{64}Ni(n, γ) cross sections at CERN n_TOF

Settore scientifico-disciplinare: **FIS/01**

DOTTORANDO
MICHELE SPELTA
Michele Spelta

COORDINATORE
PROF. FRANCESCO LONGO
Francesco Longo

SUPERVISORE DI TESI
DOTT. PAOLO MARIA MILAZZO
DOTT. STEFANO PIANO
Paolo Maria Milazzo
Stefano Piano

ANNO ACCADEMICO 2024/2025

A special thanks to Riccardo, Fran, Alice, Alberto, Paolo and Roberto for their valuable help in this work.

Abstract

Neutron capture reactions play a crucial role in nuclear astrophysics as they are at the base of the stellar nucleosynthesis processes that synthesize the elements heavier than iron. The cross sections of these reactions represent therefore important inputs for stellar nucleosynthesis models and their accurate knowledge is essential to predict reliable stellar yields and isotopic abundances. In particular, the neutron capture cross section of ^{30}Si plays a pivotal role in explaining the silicon isotopic abundances observed in presolar components of meteorites (SiC grains), while the capture cross section of ^{64}Ni has been found to significantly affect the predicted abundance of many isotopes produced by neutron-capture nucleosynthesis in massive and Asymptotic Giant Branch (AGB) stars.

The small cross sections of these isotopes make their measurement particularly challenging and therefore, despite their importance, data available in the literature are scarce and discrepant. For this reason, new time-of-flight measurements have been performed at the n_TOF facility, a pulsed white neutron source at CERN characterized by a wide neutron energy range, high instantaneous neutron flux and excellent energy resolution. Highly isotopically enriched samples have been employed in the measurements, together with a setup of deuterated benzene liquid scintillators optimized to minimize the background induced by scattered neutrons. The measured reaction yields have been fitted with the R-Matrix code SAMMY to extract resonance parameters and the Maxwellian Averaged Cross Sections (MACS) of astrophysical interest at different stellar temperatures have been finally computed.

The results obtained from both measurements show important discrepancies with respect to the cross sections recommended in most of the evaluated nuclear data libraries: huge resonances expected in the energy range of astrophysical interest are not observed and the measured resonance kernels are significantly different from the recommended values. As a consequence, our MACS at 25 keV for ^{30}Si(n,γ) lies in between the values recommended by different evaluations and between the values reported by the two latest measurements, while our MACS for ^{64}Ni(n,γ) at 8 keV is significantly lower than all the current evaluations, but similar to the results of previous measurements.

Contents

Appendix

Introduction

Most of the elements that we currently observe in the Universe have been forged in stars or during stellar explosions. Nuclear astrophysics, the topic of Chapter 1, studies exactly the nuclear reactions in stellar environments that are responsible both for the stellar nucleosynthesis and for the generation of energy in stars.

In this context, neutron capture reactions play a crucial role, as they are responsible for the nucleosynthesis of all elements heavier than iron. In fact, charged-particle-induced reactions require increasingly high stellar temperatures to overcome the Coulomb barrier of heavier nuclei, eventually leading to an equilibrium between fusion and disintegration reactions that halts the nucleosynthesis in correspondence of the most stable nuclei, located around iron. In contrast, neutrons do not carry an electrical charge and can be captured at any temperature, enabling the nucleosynthesis to proceed beyond iron and up to the heaviest elements. The probabilities of neutron capture reactions, expressed by their cross sections, represent therefore important input parameters for stellar nucleosynthesis models, especially concerning the s-process, one of the neutron-based nucleosynthesis mechanisms that occurs in Asymptotic Giant Branch (AGB) stars and in helium- or carbon-burning massive star and that builds nuclei up to lead along the valley of stability over timescales of several tens of thousands of years.

Only accurate neutron capture cross section data allow models to provide reliable stellar yields and isotopic abundances, that can be compared to stellar observations and to the measured composition of pre-solar components of meteorites to assess the validity of the models themselves or constrain stellar properties not directly accessible.

The accurate characterization of neutron capture reaction cross sections requires a basic knowledge of the reaction mechanisms and respective parametrizations, that will be the topic of Chapter 2. Neutron capture reactions typically proceed via the formation of a compound nucleus in an excited state, which later decays to its ground state emitting a cascade of γ rays. This mechanism explains the occurrence of resonances, peaks observed in neutron-induced cross sections when the energy of the incoming neutron matches one of the discrete quasi-bound excited states of the compound nucleus. The accurate experimental characterization of resonances is crucial, as they typically dominate neutron capture cross sections in the energy range of astrophysical interest (especially for light nuclei), but they cannot be theoretically predicted with precision. The R-Matrix theory is used to parametrize resonances with a set of parameters, such as peak energy and widths, that can be fitted from experimental data.

Neutron capture reactions can also proceed via a direct mechanism, without the formation of a compound nucleus. This mechanism can be important especially for light nuclei in the valleys between resonances and at thermal energy, where measurements are particularly important to estimate its contribution.

This work is focused on the study of two particular reactions: the neutron capture on ^{30}Si and on ^{64}Ni. The former is important to understand the silicon isotopic abundances measured in some pre-solar components of meteorites, the SiC grains. Despite silicon is the most abundant element found in these grains, its isotopic ratios represent a long-standing problem that current astrophysical models have not yet been able to explain definitively. An accurate knowledge of the neutron capture cross sections of the silicon isotopes (including ^{30}Si) is a fundamental prerequisite to address this problem. On the other hand, ^{64}Ni is important because it is among the seeds of the s-process. Therefore, the value of its capture cross section has a significant effect on the predicted abundances of many heavier isotopes synthesized in the process.

The capture cross sections of these isotopes in the energy range of astrophysical interest are very small, therefore they are challenging and difficult to measure. This is one of the reasons why, despite their importance, data available in the literature for their capture cross sections are scarce and discrepant. For example, the two most recent measurements of the Maxwellian Average capture Cross Section (MACS) of ^{30}Si at the stellar temperature of 25 keV, performed respectively in 2002 and 2003, are discrepant of more than 60%. Concerning ^{64}Ni, the two latest time-of-flight measurements (performed in 1975 and 1984) report resonance parameters differing by almost a factor 2, and a similar discrepancy is observed in the energy extrapolation of the MACS at 8 keV recommended in different dedicated databases. As a consequence, the recommended cross sections in different evaluated nuclear data libraries also show discrepancies in the positions and the widths of resonances.

For these reasons, new measurements of these cross sections have been performed at the n_TOF facility, a white neutron source at CERN based on the spallation of high energy protons. The description of the facility and the experimental setups will be the topic of Chapter 3. Highly isotopically enriched samples (> 99.5% enrichment) have been irradiated in the neutron beams of the facility, characterized by excellent energy resolution (between 10^{-4} and 10^{-2} in the energy region of resonances), high instantaneous flux (up to more than 10^7 neutrons per bunch) and wide neutron energy range (from meV to GeV). The measurements have been performed at both the Experimental ARea of the facility. EAR1, characterized by better energy resolution, has been employed for the characterization of the resonances of ^{30}Si. EAR2, characterized by a higher neutron flux, has been employed for the measurement of ^{64}Ni, which was available only in a smaller quantity. Setups of liquid deuterated benzene scintillators (C_6D_6) have been used to detect γ rays produced by neutron capture reactions. The setups are optimized differently to minimize the background induced by scattered neutron (in EAR1) and maximize the signal-to-background ratio (in EAR2). The time-of-flight technique has been adopted to measure the neutron capture cross sections as a function of the neutron energy.

The analysis of the data will be described in detail in Chapters 4 and 5 for the two experimental areas. The procedure is similar and includes the calibration of the detectors, the determination of the efficiency of the setups, the characterization of the dead time and the estimation and subtraction of the background. Monte Carlo simulations in GEANT4 have been additionally performed to complement the data analysis for the characterization of the detectors and for the study of the background induced by scattered neutrons. The capture yield, i.e. the probability for neutrons to undergo a capture reaction, has been finally computed, normalized and fitted with the R-Matrix code SAMMY in order to extract the resonance parameters that describe the cross sections in the region of astrophysical interest. The direct neutron capture component has been additionally assessed for ^{30}Si, while the thermal capture cross section has been fitted for ^{64}Ni. The cross sections have been finally integrated to provide the MACS at different stellar temperatures within the range of astrophysical interest. The preliminary results will be presented in Chapter 6 and they will be compared with previous measurements and recommended values from different databases and evaluated nuclear data libraries.

Part of this work has been finally devoted to perform Monte Carlo simulations of the previous n_TOF spallation target, aimed at studying the possible effects on the neutron fluxes from a cavity discovered after the autopsy of the target. Simulations have been performed in FLUKA and will be described in Appendix A.

Chapter 1

Nuclear Astrophysics

Astronomy has been subject of human enquiry for millennia, dating back to the ancient civilizations that first looked at celestial bodies while trying to understand their nature and their motion. However, only in the second half of the 19^{th} century the formalization of thermodynamics, stating that energy cannot be produced or destroyed, brought attention to the necessity of a continuous energy source within stars to compensate for their radiative energy losses. Early theories attempted to explain this energy source through mechanisms such as the periodic impact of meteorites on the stellar surface (R. J. Von Meyer, 1847) or the stellar gravitational contraction, converting gravitational potential energy to heat and radiation. However, this last model, known as the Kelvin-Helmholtz mechanism [1], was not a sufficient as source of the solar energy, as it predicted a solar lifetime of "only" some tens of millions years, conflicting with Darwin's geological and biological evidences indicating that Earth was far older (hundreds millions years at least).

The beginning of XX century also marked the birth of nuclear physics: natural radioactivity was discovered and studied by scientists such as H. Becquerel, the Curie spouses and E. Rutherford and later used to probe the inner structure of matter. In this way, the atomic nucleus was discovered (Geiger-Marsden experiment, 1909) and protons, first observed by Rutherford himself in 1919 [2], were assumed to be the elementary constituents of nuclei together with neutrons, discovered later in 1932.

Thanks to the development of mass spectrography, in 1920 F. W. Aston discovered that the mass of the helium nucleus is smaller than the sum of the masses of its constituents [3], meaning that energy must be released in the reactions converting hydrogen to helium. Since these two elements were known to be present in stars since the second half of the 20^{th} century thanks to atomic spectroscopy, in his presidential address to the British Association for the Advancement of Science [4] Sir Arthur Eddington suggested that Aston's discovery would have explained the energy generation in stars, via the conversion of hydrogen to helium. This idea bridged for the first time astrophysics with the nascent field of nuclear physics, paving the way for the future development of nuclear astrophysics.

The field advanced significantly in the following decades with the formalization of the pp chain and CNO cycle (Bethe, 1939 [5]), finally explaining the energy generation in the Sun, up to the publication of the review article by Burbidge, Burbidge, Fowler and Hoyle (commonly referred to as B^2FH) in 1957 [6]. This paper provided a comprehensive explanation of how elements are synthesized in stars through nuclear fusion and neutron capture processes, establishing the ground for modern nuclear astrophysics. The following two sections will give an introductory overview of the topic, mainly concerning stellar evolution (Section 1.1) and related nucleosynthesis (Section 1.2) based on reference [7]. In Section 1.3 a more detailed explanation of the s-process, one of the processes responsible for nucleosynthesis beyond iron, will be presented, followed by particular insights on the importance of the ^{30}Si(n,γ) and ^{64}Ni(n,γ) reactions in the process (Sections 1.4 and 1.5, respectively).

1.1 Stellar Evolution

Stars are massive, self-gravitating objects originated from the gravitational collapse of gas clouds in the interstellar medium, mainly composed of hydrogen, helium and smaller fractions of heavier elements (generically defined as *metals* in astrophysics). The metal content of a star is defined as *metallicity*, while the total energy irradiated per unit area is called *luminosity*.

According to the current models of stellar formation, gravity drives the contraction of the gas clouds in the early stages of stellar evolution. During the contraction, gravitational potential energy is converted into heat that partially increases the temperature of the inner layers of the star and partially is irradiated away, explaining the source of the luminosity of the star at this stage.

When the temperature inside the stars reaches some millions kelvin, the nuclear fusion of hydrogen to helium is finally ignited and it becomes gradually the main source of energy that is irradiated by the star (see Section 1.2.1). The star is now in hydrostatic and thermal equilibrium and it will spend the majority of its lifetime in this evolutionary stage, called *Main Sequence*. The further evolution of the star is basically based on the repetition of the same mechanism: when a main-sequence star exhausts the fuel in its core, nuclear processes can no longer compensate for the gravitational contraction and the stellar core starts to contract again. The contraction produces heat that raises the temperature until the fusion of the heavier products of the previous burning stage can be ignited in the core. Equilibrium is established again, until the nuclear fuel is exhausted, and so on.

During this cycle, a star experiences strong variations in both its luminosity and surface temperature. The correlation between these two quantities defines indeed some groups of stars that correspond to different stages of stellar evolution. These groups can be associated with the stellar clusters observed in the *Hertzsprung-Russel diagram*, a scatter plot displaying luminosity against surface temperature of stars. The evolution of stars is indeed usually depicted as a trajectory in this diagram. Examples of the evolution of stars of different mass are shown in Figure 1.1.

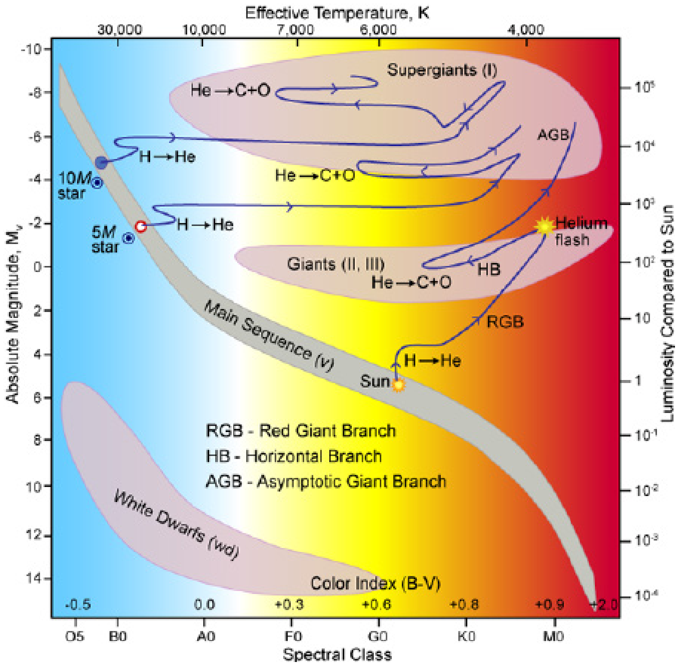

Figure 1.1: Hertzsprung-Russell diagram showing surface temperature versus luminosity of stars. Different stellar clusters corresponding to different stellar evolutionary stages are highlighted, together with typical evolution trajectories for stars of different masses. Image from [8].

For example, low and intermediate-mass stars with masses ranging between 0.5 and 8 solar masses ($M_\odot$) spend several tens of millions of years in the main sequence. After hydrogen is exhausted in the core, gravitational contraction enables first the fusion of hydrogen in the stellar shell, causing an increase in the stellar luminosity and an expansion (cool-down) of its surface leading to a *Red Giant Branch* (*RGB*) star, and, afterwards, the fusion of helium in the core (*Horizontal Branch* (*HB*) stars, see Section 1.2.1). In low-mass stars, helium burning is ignited explosively with a so-called *He-flash*, as the core is in a degenerate state. Once helium is exhausted in the core, a low or intermediate-mass star alternatively burns hydrogen and helium in its outer shells, moving to the so-called *Asymptotic Giant Branch* (AGB). AGB stars will be described in details in Section 1.3.1, as they are one of the main sites of neutron-induced stellar nucleosynthesis. This kind of stars does not reach temperatures high enough to trigger more advanced fusion processes to generate energy.

The situation is different for massive stars, characterized by masses larger than 8 $M_\odot$. These stars are hotter and more luminous. They can reach higher temperatures in their core, so that more advanced burning stages can be ignited once helium in the core is exhausted, up to the production of iron. See Section 1.2.1 for more details.

When fusion reactions can no longer be ignited (as in low-mass stars after the AGB stage) or do no longer release energy (as fusion reactions beyond Iron in massive stars), the gravitational contraction eventually takes over and leads stars to their death.

In low-mass stars (typically below the so-called *Chandrasekhar limit* [9]), the core contracts until it reaches a degenerate state that provides a degeneracy pressure counteracting the gravitational collapse. Therefore, the star just fades away in a sort of equilibrium first in a *White Dwarf*, still irradiating the residual heat of the core, and finally in a *Black Dwarf*.

On the other hand, in massive stars the degeneracy pressure is not enough to balance the gravitational contraction and the stellar core quickly collapses. In these stage, electrons and protons in the core are converted to neutrons with a consequent emission of neutrinos. According to the current theories, the bounce of the external layers of the star on the dense collapsed stellar core together with the released neutrinos produce a wavefront that triggers a stellar explosion referred to as *Core Collapse Supernova* (*CCSN*) or *Type II Supernova*. Several nucleosynthesis processes (n-process, p-process, r-process,...) are believed to take place in this explosive scenario, that also releases the elements synthesized by the star before and during the explosion in the interstellar medium. The remnant of the explosion is the dense degenerate stellar core, that can be either a *Black Hole* or a *Neutron Star*, depending on the mass of the exploded star.

Neutron stars can enter binary systems and collide with another neutron star in a phenomenon called *Neutron Star Merger*, that is currently recognised as one of the most promising astrophysical sites for the rapid neutron-induced nucleosynthesis (Section 1.2.2).

1.1.1 Galactic Chemical Evolution

The chemical composition of the early galaxies reflected the result of the *Big Bang Nucleosynthesis*. It consisted of only hydrogen, ^{4}He (75% and 25% in mass, respectively) and trace amounts of deuterium, ^{3}He and ^{7}Li. The first stars formed in this environment and therefore were characterized by an extremely poor (if not null) initial metal content. They are referred to as *Population III* stars.

During their life, stars convert part of their initial chemical content to heavier elements through different nucleosynthesis mechanisms, that will be explained in the next section. These elements are later released in the InterStellar Medium (ISM) either through stellar winds (in the case of low and intermediate mass stars) or through supernova explosions (in the case of massive stars).

As a consequence, the ISM gets progressively enriched in metals and the new stars that condense in this environment are characterized by an increasing initial metallicity. Older and still relatively metal-poor stars make up the so-called *Population II* stars, while metal-rich younger stars (like the Sun) constitute the *Population I* stars. In turn, these stars reprocess the metals in their interiors and release them back to the ISM and so on.

Eventually, thanks to the action of stars, this cycle has allowed the evolution of our galaxy from a primordial chemical composition to the current chemical composition, characterized by elements ranging from hydrogen to uranium with different abundances, as shown in Figure 1.2. This process is called *Galactic Chemical Evolution* [10, 11].

This field is rather complex to study, as it needs to combine together several ingredi-

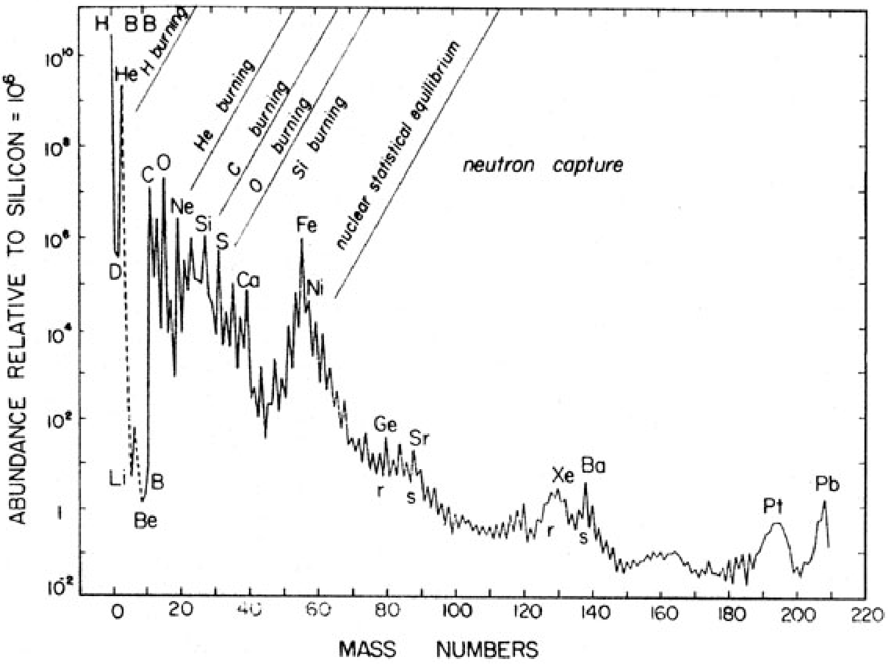

Figure 1.2: Abundance of isobars in the Solar System, from reference [12]. The simplest elements (H, ^{4}He) are the most abundant, followed by the products of stellar burning up to the iron group, where the most stable isotopes are located. Beyond the iron peak, elements are mainly synthesized via neutron-capture processes and they are less abundant, with peaks corresponding to the neutron magic numbers of 50, 82, 126.

ents related to stellar and galactic evolution, like stellar lifetimes, stellar formation rates and stellar yields. Stellar yields, defined as the mass of a chemical element ejected by a star during its evolution, are particularly important and ultimately depend on stellar evolution and stellar nucleosynthesis. The former, describing how materials are ejected, has been already discussed in this section, while the latter, describing how elements are processed and produced in the stellar interior, will be the topic of the next section.

1.2 Stellar Nucleosynthesis

Nuclear reactions represent the main source of energy in stars at different stages of their evolution, as presented in the previous section. However, at the same time nuclear reactions in stars also transform the products of the Big Bang in all the heavier elements that exist in nature, up to uranium. This process is named stellar nucleosynthesis.

The first evidence of nucleosynthesis in stars dates back to 1952, when P. W. Merril observed spectroscopic lines of technetium in the spectrum of a Red Giant star. Since the longest lived isotope of technetium has a half-life (4×10^6 years) much shorter than the age of this kind of star, this element must have been produced in the star itself during its evolution, proving the concept of stellar nucleosynthesis. Detection of γ rays from the radioactive ^{26}Al [13] and ^{60}Fe isotopes are additional proofs of nucleosynthesis in massive stars and supernovae.

Light elements up to iron are mainly synthesized through charged-particle-induced reactions in nuclear burning processes, while beyond iron nucleosynthesis mainly proceeds through neutron capture processes.

1.2.1 Nuclear burning processes

Nuclear burning processes roughly fuse light elements into heavier and heavier elements via a complex network of fusion reactions, charged-particle-induced reactions and photo-disintegrations. Even if these processes are overall characterized by a net release of energy (overall positive Q-values) until the iron group elements are synthesized, their ignition is strongly suppressed by the electric repulsion between charged particles, that increases with the charge (and the mass) of the nuclei. For this reason, high temperatures in the stellar core are needed to ensure a sufficiently large probability of quantum tunnelling through the Coulomb potential barrier to enable fusion reactions. The higher the mass of the star, the higher the temperature in its core and the more advanced the burning stages that can be ignited.

Hydrogen Burning

Hydrogen burning is the first and probably most important burning process in stars. It is activated in stars with masses larger than $0.08M_\odot$ when their core reaches temperatures of some MK and takes place in the core of main sequence stars and in the hydrogen shells of subsequent evolutionary stages.

Overall, the process consumes four hydrogen nuclei to produce a Helium nucleus, two positrons and two electron neutrinos and releases 26.7 MeV of energy:
$4\text{p} \rightarrow {}^4\text{He} + 2\text{e}^+ + 2\nu_e + 26.7$ MeV.
This process is realized via different possible reaction networks.

The simplest one is called *proton-proton (pp) chain* and it is initiated by the fusion of two protons to a deuteron: $\text{p} + \text{p} \rightarrow \text{d} + \text{e}^+ + \nu_e + 1.44$ MeV. Being mediated by the weak interaction, this reaction has an extremely small cross section ($\approx 10^{-24}$ barn at 0.5 MeV) that makes it the bottleneck of the whole burning process and explains its long duration. Proton capture on deuterium ($\text{d} + \text{p} \rightarrow {}^3\text{He} + \gamma + 5.49$ MeV) and ^{3}He fusion ($^3\text{He} + {}^3\text{He} \rightarrow {}^4\text{He} + 2\text{p} + 12.9$ MeV) eventually complete the conversion to ^{4}He in the simplest case. Different reactions involving ^{4}He, Li, B, Be can become more probable to complete the chain (*pp2 and pp3 chains*) once the temperature of the star and the ^{4}He abundance increase.

Another process involved in Hydrogen burning is the *CNO cycle*. This process achieves the fusion of Hydrogen to Helium via series of β decays, (p,α) and (p,γ) reactions on Carbon, Nitrogen, Oxygen and Fluorine nuclei. These nuclei can be found in stars as a result of the chemical evolution of galaxies and simply act as catalysts, while only Hydrogen is consumed. Because of the higher Coulomb barriers to overcome, the process only takes place at higher temperatures and in more massive stars (larger than 1.2-1.3$M_\odot$) than the pp-chain, but in these conditions it is much more efficient. In conclusion, it is worth mentioning that, if on the one side the total abundance of the catalysts does not change during the cycle, the abundances of the single catalysts do. In particular, ^{14}N is built up in the CNO cycle as the ^{14}N(p,γ) reaction represents the bottleneck of the process. This will be important to understand the source of neutrons in massive stars.

Helium Burning

Helium burning is the process that follows hydrogen burning when the core of a star reaches temperatures around 200 MK. It converts ^{4}He nuclei to ^{12}C and ^{16}O nuclei via the so-called *triple alpha process*, that bypasses the unstable isobar with mass number 8. In fact, the fusion of only two α particles produces the unstable ^{8}Be, that decays with a half-life of only 8.2×10^{-17} s. Only the existence of an excited state in ^{12}C with an energy close to the Q-value of the ^{8}Be(α,γ)^{12}C reaction (7.7 MeV) enables the efficient capture of a third alpha particle and the synthesis of ^{12}C. This excited state is called *Hoyle state* because it was first theoretically proposed by F. Hoyle in 1953 to explain the high abundance of ^{12}C in the universe [14].

Once ^{12}C is produced, subsequent alpha capture reactions lead to the production of ^{16}O and, to lower extent, ^{20}Ne, with an efficiency proportional to the mass of the star.

Advanced Burning Stages

As already mentioned, only stars with masses larger than approximately 8$M_\odot$ can ignite advanced burning processes that convert the products of the helium burning to heavier nuclei.

Carbon burning is the first of these processes and it is based on the fusion of two ^{12}C nuclei that produces mainly ^{20}Ne, ^{24}Mg and ^{23}Na. Because of the high excitation energies available and because of the increasing complexity of heavier nuclei, several output channels for fusion reactions become possible. Most of them release secondary particles (p, n and α particles) that can in turn induce other reactions, leading to increasingly complex reaction networks.

Moreover, when the temperature increases above some GK, photo-disintegrations reactions also gain importance. ^{20}Ne(γ, α)^{16}O is the first reaction of this kind to be ignited. It releases α particles that are captured mainly by ^{20}Ne and ^{24}Mg, building up ^{24}Mg and Silicon (^{28}Si mainly, but also ^{29,30}Si). The process is referred to as *neon burning*.

Increasing again the stellar temperature, once ^{20}Ne is exhausted in the core, *oxygen burning* occurs, with a mechanism similar to carbon burning. It mainly produces ^{28}Si and ^{32}S.

Eventually, at core temperatures around 3.5 GK, *silicon burning* takes place via the disintegration of the heavy nuclei produced in the previous steps and the subsequent capture of the released secondary particles. The process build up the elements up to the calcium and the iron peaks. Because of the high temperatures during these processes, photo-disintegration reactions become increasingly more important, reaching an equilibrium with the capture and fusion reactions: this stage is called *Nuclear Statistical Equilibrium*. In this equilibrium condition, single reaction rates do not play significant roles, because the abundance of the different isotopes ultimately depends on their nuclear binding energies and on the stellar conditions (like the electron fraction). For this reason, the process favours the production of the nuclei in the Iron region, characterized by the highest nuclear binding energy per nucleon.

These advanced burning stages are repeated in an explosive environment when massive stars explode after the core collapse, as described in the previous section. In fact, the shock propagating outwards after the core collapse compresses and heats the inner layers of the stars, where the products of the previous hydrostatic nucleosynthesis are located. Therefore, the chemical composition of these layers is completely reprocessed: heavy nuclei previously synthesized are disintegrated to light particles that are later captured in the explosive burning stages and other nucleosynthesis processes. For example, iron from hydrostatic silicon burning is completely disintegrated in the core, but it is produced again in the explosive silicon and oxygen burning shells, where ^{56}Ni is built up and decays to ^{56}Fe. ^{26}Al, mentioned among the direct observations of stellar nucleosynthesis, is also believed to be produced in the explosive carbon-neon burning shell. As the shock wave moves outwards, it gets attenuated and affects only to a lower extent the composition of the outer layers of the star.

1.2.2 Nucleosynthesis beyond iron

The nucleosynthesis beyond iron cannot proceed via charged-particle fusion reactions for several reasons.

First of all, as ^{56}Fe is the most tightly bound nucleus in nature, fusion reactions involving heavier nuclei consume energy rather than releasing energy and they are therefore not sustainable for the star.

Secondly, the transmission through the Coulomb barrier decreases with drastically increasing the nuclear charge. For this reason, charged-particle-induced reactions involving elements heavier than iron are strongly suppressed at the typical stellar temperatures and therefore cannot justify the observed solar system abundances.

Moreover, at very high temperatures charged-particle capture and fusion reactions compete with their inverse disintegration reactions in a situation of nuclear statistical equilibrium. As already seen in the previous section, this equilibrium favours the most stable nuclides in the Iron peak and blocks the synthesis of less stable heavier nuclei.

For these reasons, nucleosynthesis beyond the iron region mainly proceeds through a series of neutron capture reactions and β decays. Being neutral particles, neutrons are indeed not affected by electric repulsion and can react at whatever temperature. Depending on the neutron density, three different neutron-capture processes can be distinguished: the *s-process* (described in detail in section 1.3), the *r-process* and the *i-process*. Their typical paths can be observed in figure 1.3.

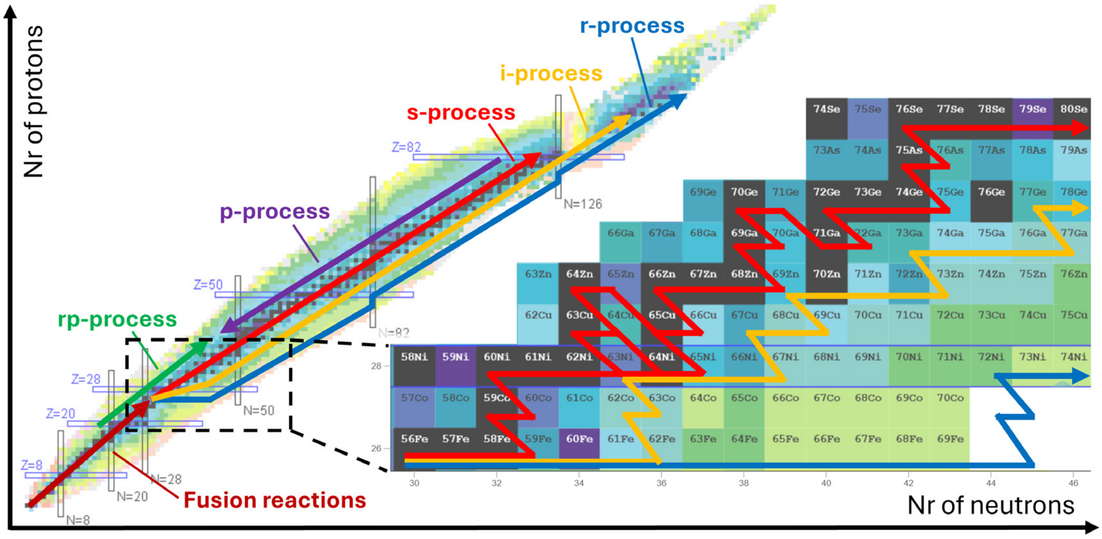

Figure 1.3: Sketch of the paths of the main processes responsible for stellar nucleosynthesis beyond the iron peak. On the right, the paths for the neutron-capture processes (s-process, i-process and r-process) are compared for isotopes just after iron.

The r-process

The *r-process* [15](standing for *rapid neutron capture process*) is characterized by high neutron densities ($N_n > 10^{20}$ cm^{-3}) that make neutron capture reactions faster than β decays, with a rate on the order of one capture event each μs-ms. As a result, the process pushes nuclei far away from stability towards the neutron-drip line before they can decay. The r-process competes with the other neutron-capture processes in the synthesis of the stable elements heavier than iron and it is the main responsible for the synthesis of the unstable elements heavier than lead, that cannot be reached by the s-process.

More in details, the r-process consists in two different moments that take place on a timescale shorter than a second: an initial neutron irradiation and a subsequent decay.

In the first stage, because of the high temperature (some GK) and neutron density, an equilibrium is reached between neutron capture reactions (n,γ) and photo-disintegration reactions (γ,n), while β decays are ignored because of their longer timescale. As already discussed in previous sections, in these conditions the abundance of each isotope mainly depends on the neutron separation energy, on the temperature and on the neutron density. For each isotopic chain, abundance maxima at equilibrium are indeed located in correspondence of nuclei with a specific neutron separation energy, determined by the stellar conditions. These nuclei are referred to as *waiting points* of the process.

Since these nuclei are the most abundant during the r-process, they represent the main source of β decays that, on a longer timescale, transfer material from one isotopic chain to another. The isotopic chain populated by β decay quickly reaches the equilibrium, building up the isotope that corresponds to the waiting point. This isotope β

decays to a new isotopic chains and so on, defining the r-process path that is shown in Figure 1.3. In first approximation, β decays also reach a steady flow that makes the elemental abundance inversely proportional to the average β decay rate of the element during the r-process.

A special condition occurs when the r-process path encounters a neutron shell closure. In this situation, the waiting points for different elements are all located in correspondence of the neutron magic number (N = 50, 82, 126, 184), where isotopes are more stable against neutron capture and disintegration. The r-process path therefore moves up vertically towards the valley of stability, where nuclei are more stable against β decay and therefore built up to relatively large abundances. When nuclei are close enough to stability that their neutron separation energy is high enough, the r-process path can proceed again towards the neutron-drip line.

When the process reaches very heavy nuclei, fission can become faster than β decays and break the heavy nuclei into lighter fission fragments. These fragments can be reconverted by the r-process to heavy nuclei creating the so-called *fission cycling*, that can eventually increase the abundance of heavy nuclei.

After the end of the neutron irradiation, the unstable neutron-rich isotopes decay towards stability via β decay or neutron emission. In particular, the decay of the most abundant nuclei in correspondence of the neutron shell closures produces the peaks of abundance at the corresponding mass number in the valley of stability (the so-called *r-process peaks* observed in Figure 1.2).

However, the classic r-process model described above can only qualitatively reproduce the observed r-process abundances. A quantitative agreement can be reached only by considering more advanced models that go beyond the equilibrium approximation and including components from different astrophysical sites or from single sites varying their conditions. Because of the high neutron densities required, explosive environments are assumed as the astrophysical sites for the r-process, in particular core-collapse supernovae and neutron star mergers. Supernovae represent a possible site for a "weak" r-process, thanks to neutrino winds that can produce neutron-rich environments. Neutron star mergers create multiple neutron-rich environments with different neutron densities throughout their evolution, each potentially contributing to a different "component" of the r-process.

The i-process

The *i-process* (standing for *intermediate neutron capture process*) is characterized by neutron densities of approximately 10^{12} - 10^{16} cm^{-3}, intermediate between the r and the s-process. It was first introduced in the ’70s [16], but it gained attention mainly in the last 10 years after the observation of some carbon-enhanced metal-poor stars whose isotopic abundances cannot be reproduced by a combination of solely s-process and r-process [17].

Current i-process models are based on the ingestion of protons into a convective helium-burning region [18]. This condition can occur for example in low-metallicity AGB stars, one of the most promising candidate as astrophysical site of the i-process. In this event, protons are entrained by the convective flow to regions of higher temperature (T > 100 MK) where they can produce ^{13}C, that eventually releases neutrons via the ^{13}C(α,n) reaction. The mechanism is somehow similar to what will be described for the s-process (section 1.3). The important difference is that the i-process models require the proton ingestion during the convective thermal pulse. In this way, ^{13}C can be accumulated in the bottom layer of the Helium intershell, where the higher temperature can explain the higher neutron density. Moreover, the i-process takes place on a shorter timescale on the order of days to a year.

Similarly to the r-process, the i-process drives nuclei far from stability towards the neutron drip line, though to a lesser extent. When nuclei decay back to stability after the neutron irradiation, stable heavy elements are produced with an abundance pattern that fits reasonably well the observations from several carbon-enhanced metal-poor stars. The i-process is also a valuable candidate for the synthesis of the actinides, in competition with the r-process.

The p-process

Although dominant, neutron-capture processes cannot be the only mechanisms for nucleosynthesis beyond iron. Indeed, these processes cannot explain the synthesis of stable proton-rich nuclides (*p-nuclides*), even if they are typically a factor 100 less abundant than the adjacent s- and r-nuclides.

The synthesis of these nuclei is based on photon-induced (γ,n), (γ,p), (γ, α) reactions depleting the more abundant s-process and r-process nuclides. This process is referred to as *γ-process* (or *p-process*) and requires high temperatures (T $\approx$ 2 - 3 GK) that can be found in explosive scenarios like core-collapse supernovae.

Lighter p-nuclides can be additionally synthesized by charged-particle-induced (p, γ) reactions occurring in proton-rich explosive environments, like the regions characterized by neutrino winds in core-collapse supernovae (*νp-process*) or the X-Rays Bursts (*rp-process*).

1.3 The s-process

The *s-process* [19, 20] deserves a full detailed section as it is the most sensitive process to neutron capture cross sections that can be measured in laboratory.

The s-process (standing for *slow neutron capture process*) is characterized by neutron densities between 10^7 and 10^{11} cm^{-3}, that imply a neutron capture reaction rate of the order of one neutron capture every 10 years. In these conditions, β decays are generally faster. For this reason, when an unstable isotope is produced by capture reactions, it generally decays to its stable isobar before another neutron capture reaction can occur. In this way, the resulting s-process path closely follows the valley of nuclear stability (Figure 1.3) and synthesizes about half of the abundances of the stable isotopes between

^{56}Fe, the most abundant seed of the s-process, and ^{209}Bi. The isotopes immediately after ^{209}Bi are generally short-lived α-decaying nuclei that decay back to Bismuth and Lead before they can capture another neutron, eventually terminating the s-process reaction flow.

To have a more quantitative picture of the s-process, it is possible to write the abundance evolution of any stable nuclide with mass number A as the difference between its production and destruction rates:

$$\frac{dn_A}{dt} = n_n v_T \Big(n_{A-1}\langle\sigma\rangle_{A-1} - n_A\langle\sigma\rangle_A \Big) \tag{1.1}$$

where n_n is the neutron density, v_T is the thermal mean velocity of neutrons, $n_A\langle\sigma\rangle_A$ and $n_{A-1}\langle\sigma\rangle_{A-1}$ are the product of the number density and the Maxwellian Averaged capture cross section (MACS, see section 2.1.2) for the nucleus itself and the $A - 1$ nucleus in the s-process path. In first approximation, β decay rates can be neglected because faster than neutron captures, while neutron density and temperature (that determines in turn the MACS and the thermal neutron velocity) can be assumed constant for the moment.

Instead of using the time variable, the *neutron exposure* τ can be defined as the integrated neutron flux over time per unit area: $\tau = v_T \int n_n dt$. In this case, Equation (1.1) reduces to:

$$\frac{dn_A}{d\tau} = n_{A-1}\langle\sigma\rangle_{A-1} - n_A\langle\sigma\rangle_A. \tag{1.2}$$

Classical s-process models assume that a fraction f of the observed abundance of ^{56}Fe seed nuclei $n_{56,0}$ is irradiated by an exponential distribution of neutron exposures

$$p(\tau) = \frac{f\, n_{56,0}}{\tau_0} e^{-\tau/\tau_0} \tag{1.3}$$

where τ_0 is the mean neutron exposure. This distribution reflects the reasonable assumption that higher neutron exposures are less probable, as neutron exposure is related to the number of times materials are reprocessed in successive generations of stars or successive burning episodes in a star [21, 22].

Assuming this distribution, the system of differential Equations (1.2) can be solved analytically, providing a general result for the abundance of a stable isotope with mass number A:

$$n_A\langle\sigma\rangle_A = \frac{f\, n_{56,0}}{\tau_0} \prod_{i=56}^{A} \frac{1}{1 + \frac{1}{\tau_0\langle\sigma\rangle_i}} \tag{1.4}$$

f and τ_0 can be regarded as free parameters, that can be estimated comparing the analytical abundances with the observed abundances of the *s-only nuclei*, specific nuclei that are shielded by stable isobars towards the neutron-drip line and therefore cannot be synthesized by the r-process, but only by the s-process. Figure 1.4 shows the comparison.

A single set of parameters cannot reproduce the full observed abundance pattern (thick line in the Figure), but assuming the combination of two different exponential

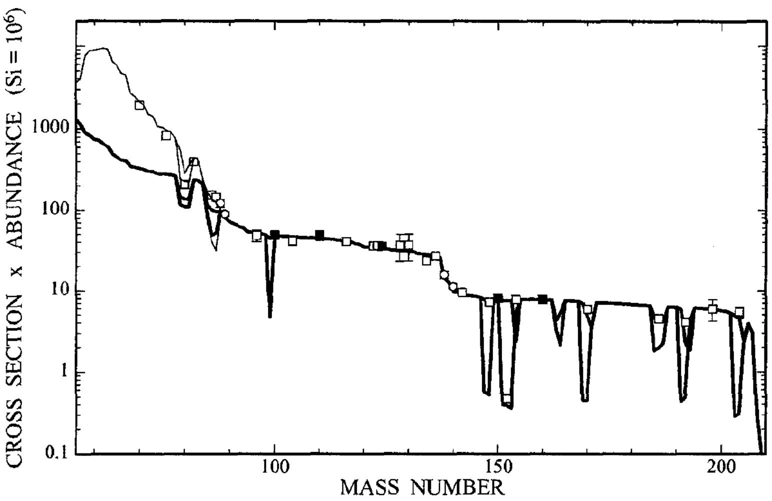

Figure 1.4: The product of the Maxwellian averaged neutron capture cross section times s-process abundances as a function of the mass number [19]. The squares represents empirical products for the s-only nuclei, while the thick and the thin solid lines represent the analytical predictions for the main and the weak components of the s-process, respectively. Some branching points are also represented, where lines bifurcate (see text).

distributions of neutron exposures (thin line) a remarkable agreement is reached. These two contributions correspond to the so-called *main s-process component* and *weak s-process component*, that will be described in the following subsections. An additional *strong s-process component* could explain the discrepancies observed in the region of lead and bismuth.

Before going on, it is important to mention that, contrary to one of the initial approximations, the s-process path can actually encounter unstable nuclei whose decay rate λ_β is comparable in magnitude to the competing neutron capture rate $\lambda_{n\gamma}$. These nuclei are referred to as *branching points* of the s-process, as they split the s-process path in two branches: one corresponds to the case in which a neutron capture occurs before the branching point decays, the other corresponds to the opposite case. This is also the explanation of the sharp, double structures observed in Figure 1.4. The fraction of decaying nuclei f_B is defined as the *branching ratio* and, in equilibrium approximation, can be written as:

$$f_B = \frac{\lambda_\beta}{\lambda_\beta + \lambda_{n\gamma}} = \frac{\ln 2 \,/\, t_{1/2}}{\ln 2 \,/\, t_{1/2} + n_n v_T \langle \sigma_{n\gamma} \rangle} \tag{1.5}$$

where $t_{1/2}$ is the half-life of the branching point. This quantity is crucial because it can be compared with observed abundances and, if reliable nuclear data are available, can be used to constrain stellar quantities like the neutron density n_n and the temperature (related to v_T) in s-process environments (see also subsection 1.3.4).

When more precise neutron capture cross section measurements became available in the ’90s, it was exactly the inconsistency in the abundance predictions around some branching points that showed the limitation of the classical s-process model described above. Neutron density and temperature cannot indeed be considered constant during the process. Current s-process models indeed require complex numerical simulations that include time evolution models of the astrophysical sites where the s-process takes place.

1.3.1 Main s-process in AGB stars

Referring to Figure 1.4, the main s-process component is represented by the thick line. It is the main responsible for the synthesis of nuclei with mass number A > 90 and, according to the classical model fit, it is characterized by a relatively high mean neutron exposure of 0.3 mb^{-1} that irradiates a fraction $f = 0.06\%$ of the observed ^{56}Fe seed nucleus abundance [7].

Because of the relatively high neutron exposure, in the region between the closed neutron shells the product $\tau_0 \langle \sigma \rangle_i$ is relatively large and Equation (1.4) reduces to

$$n_A \langle \sigma \rangle_A \approx constant, \tag{1.6}$$

meaning that a local equilibrium condition is reached. This condition explains why the $n_A \langle \sigma \rangle_A$ curve is essentially flat in the region between magic neutron number nuclei, as clearly shown in Figure 1.4.

This condition no longer holds when nuclei characterized by closed neutron shells are reached (N = 50, 82, 126, corresponding to A ≈ 90, 140, 208). These nuclei are indeed characterized by so small neutron capture cross sections that the denominator in Equation (1.4) gets larger when the corresponding mass numbers are reached. This behaviour produces the steps in the $n_A \langle \sigma \rangle_A$ curve that identify the neutron magic number nuclides as bottlenecks of the s-process path.

The main s-process takes place in the helium intershell of thermally pulsing AGB stars with masses between $1.5 M_\odot$ and $3 M_\odot$ [20]. AGB stars consist of an inert carbon-oxygen core surrounded by a hydrogen and a helium burning shells alternately activated and a convective envelope [23]. The two burning shells are separated by a thin zone in radiative equilibrium called *helium intershell*, as sketched in Figure 1.5.

When the hydrogen-burning shell is activated, the helium intershell grows in mass and it gets progressively heated and compressed, until helium burning can be temporarily activated in an explosive way in the so-called *Thermal Pulse (TP)*. The extra-energy released by the TP drives convection in the helium intershell, that diffuses ^{12}C produced by the helium burning. Moreover, the hydrogen shell expands and cools down, stopping the hydrogen burning. In this moment, the convective envelope penetrates deep into the H-He discontinuity beyond the region where the hydrogen shell was active, leading to the so-called *Third Dredge-Up (TDU)*, that mixes the chemical composition of the two layers. Therefore, protons from the envelope are injected in the top of the helium intershell, already enriched in ^{12}C, leading to the formation of a ^{13}*C pocket* through the reactions ^{12}C(p,γ)^{13}N($\beta^+ \nu$)^{13}C when the hydrogen shell is reignited. ^{14}N also builds up via ^{13}C(p,γ)^{14}N.

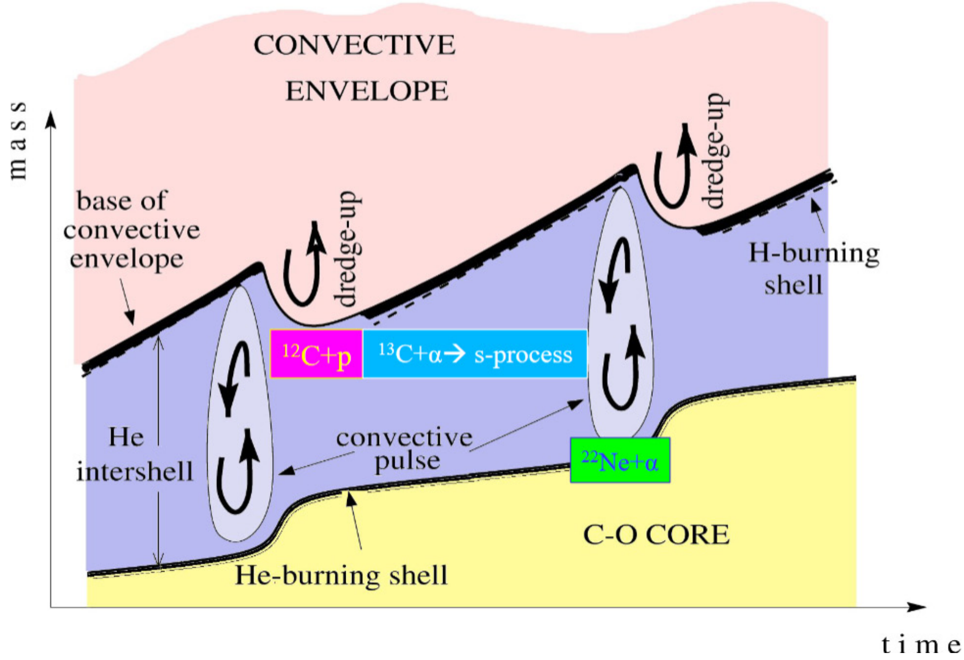

Figure 1.5: Structure of a thermally pulsing AGB star as a function of time, showing the alternation between thermal pulses establishing convection during the He burning and the interpulse periods when H burns in ordinary radiative conditions. The sites where the main component of the s-process takes place are highlighted in light blue and green and the corresponding neutron sources are reported. See text for details. Image from S. Cristallo [24].

The ^{13}C(α,n) reaction represents the source of neutrons that drives the main component of the s-process in the helium intershell throughout the entire interpulse period (approximately 10^4 years), when this region is in radiative equilibrium and its temperature is around 0.09 GK (corresponding to a neutron thermal kinetic energy $E_n \approx 8$ keV). The neutron density reached in this condition is relatively low ($n_n \approx 10^7$ cm^{-3}), but the long timescale of the process ensures the high neutron exposure required for the main s-process component to take place.

When the helium burning is activated again with a TP and convection is established, the TDU not only mixes protons in the Helium intershell, but also injects the isotopes freshly synthesized by the s-process from the He inteshell to the convective envelope, that brings them to the surface of the star. Stellar winds eventually release these isotopes in the interstellar medium. The process is repeated several times, until the complete erosion of the envelope by stellar winds.

However, ^{13}C(α,n) reaction is not the only source of neutrons in the main component of the s-process. In fact, thanks to the higher temperature reached during the TP (T≈ 0.27 GK), a series of α capture reactions on ^{14}N can be ignited, producing ^{22}Ne in the helium intershell:

$$^{14}N(\alpha,\gamma)^{18}F(\beta^+\nu)^{18}O(\alpha,\gamma)^{22}Ne. \tag{1.7}$$

As a consequence, only during the TP, the ^{22}Ne(α,n) reaction is also marginally activated as an additional neutron source. Under these conditions, the neutrons that are produced have a thermal energy $E_n \approx 23$ keV and reach a density of approximately 10^{10} cm^{-3}. However, because of the short timescale of the TP ($\approx$ 100 years), the resulting neutron exposure is low and does not significantly contribute to the overall s-process, but it can importantly influence the abundances around the branching points.

Metallicity also strongly influences the s-process in AGB stars. The lower the metallicity, the higher the neutron-to-seed ratio, that leads to an enhanced production of heavy elements in the Bi and Pb region. The strong s-process, characterized by a high neutron exposure of 7 mb^{-1} acting on a very small fraction $f = 10^{-4}\%$ of seed nuclei, is indeed thought to occur in low-metallicity AGB stars [7].

1.3.2 Weak s-process in massive stars

A weak s-process component is needed to reproduce the s-process abundances of the isotopes with mass number A < 90, as shown by the thin line in Figure 1.4. According to the classical model fit, it is characterized by a lower neutron exposure of 0.07 mb^{-1} irradiating a larger fraction $f = 1.6\%$ of the observed ^{56}Fe abundance with respect to the main s-process component [7]. Because of the lower exposure, a local equilibrium condition cannot be established in the weak component of the s-process, meaning that the neutron capture cross section of an isotope does not only influence the abundance of the isotope itself, but also affects the abundance of all the heavier isotopes along the s-process path.

The weak s-process components occurs during the core helium burning and in the carbon shell burning in massive stars (M > $8M_\odot$).

In core helium burning, ^{14}N built up by the CNO cycle in the previous hydrogen burning phase is rapidly converted to ^{22}Ne, via the reaction chain already described in Equation 1.7. Thanks to the high temperature reached in this phase ($\approx$ 250 MK), the ^{22}Ne(α,n) reaction is efficiently activated and represents the main source of neutrons for the process. In these conditions, the neutron density can reach 10^7 cm^{-3} and the neutron mean kinetic energy is $E_n \approx 23$ keV.

If the ^{22}Ne is not fully consumed, ^{22}Ne(α,n) is activated again during the carbon-burning stage. The contribution of the core carbon burning to the s-process is negligible, as heavy elements in the core are destroyed by more advanced burning stages. On the opposite, the carbon shell is ejected by supernova explosions with an almost unchanged chemical composition and therefore can contribute proficiently to the s-process nucleosynthesis. In this astrophysical site, temperatures are around 1 GK, resulting in neutrons with a mean kinetic energy of $E_n \approx 90$ keV and a density of approximately 10^{11} cm^{-3}.

In these burning stages, light neutron-rich isotopes can be also synthesized.

1.3.3 Presolar grains

Presolar grains are tiny particles of ancient interstellar stardust that can be found in meteorites [25, 26]. They were formed in stellar outflows of late-type stars and in the ejecta of stellar explosions and survived the formation of the solar system, preserving the isotopic composition of their pre-solar parent star.

For this reason, the isotopic compositions of presolar grains are powerful direct measurements that can constrain stellar nucleosynthesis models in single stars and at a level of detail much higher than astronomical observations. In fact, presolar grains can be isolated from meteorites and their isotopic composition can be measured in laboratory with advanced techniques and mass spectrometry with a precision of only a few percent.

The most studied grains are the *silicon carbide (SiC) grains*, mainly formed in the stellar envelope of AGB stars and therefore providing experimental tests of s-process nucleosynthesis models.

As already described, in thermally pulsing AGB stars the TDU episodes mix materials from the helium intershell to the convective stellar envelope. Therefore, the envelope gets particularly enriched of the heavy elements synthesized by the s-process and of carbon, produced by the helium burning. The star becomes a *carbon star* and in this condition carbon bonds chemically with silicon, creating silicon carbide crystals that include as impurities a small fraction of the heavier elements present in the stellar envelope. These grains are particularly hard and stable and, for this reason, they can survive further stellar processing until they are incorporated in meteorites and fall to the Earth, keeping the heavy element isotopic abundance pattern of their pre-solar parent star.

SiC grains are classified in different types based on the isotopic content of silicon, carbon and nitrogen, that are the most abundant elements typically found in the grains. Each type is typically associated to a particular origin. For example, the vast majority of SiC grains belong to the so-called *Mainstream grains*, characterized by a ^{12}C/^{13}C ratio between 13.5 and 100, a ^{14}N/^{15}N ratio above 200 and a correlation between ^{29}Si and ^{30}Si abundances (normalized to ^{28}Si) close to a defined correlation line (defined as *mainstream line*). These grains originated in the envelope of AGB stars. Type Y and type Z grains also originated in the envelope of AGB stars of lower metallicity, but they are characterized by different Carbon or Silicon isotopic ratios, respectively. Type X and type C SiC grains, that represent together only 1.3% of the identified SiC grains, originated instead from core collapse Supernovae (CCSN). More details on rarer SiC types and on the classification parameters can be found in [26].

1.3.4 Impact of nuclear cross sections

The s-process is extremely sensitive to the value of the neutron capture cross sections of the nuclei involved, that represent crucial nuclear physics inputs for numerical models. In the main s-process component this is clear from Equation 1.6, which shows that the s-process abundance of an isotope ultimately depends on its neutron capture cross section. In the weak s-process component, the situation is even more extreme since the neutron capture cross section of an isotope not only influences the abundance of the isotope itself, but also affects the abundances of all the heavier nuclei along the s-process path. Moreover, as shown in Equation 1.5, the study of s-process branching points also requires precise values of neutron capture cross sections (and β decay rates) to reliably constrain stellar properties like neutron exposure and stellar temperature. Eventually, since s-process abundances contribute to the stellar yields and are subtracted to solar abundances to determine the contribution of the r-process, neutron capture cross sections also indirectly affect the study of Galactic Chemical Evolution and of the r-process.

For all these reasons, an uncertainty of less than 5% is generally required for the Maxwellian averaged neutron capture cross sections used as inputs in stellar models, in order to get reliable results. Even more precise values may be necessary for magic nuclei, branching points and s-only isotopes (uncertainty ideally within 1%) [19]. Moreover, neutron capture cross sections vary with the neutron energy, i.e. the stellar temperature, and need to be known in a neutron energy range that covers all the possible s-process environments, spanning from approximately 8 keV (the temperature of the helium intershell in AGB stars between the TPs) to 90 keV (the temperature of the convective carbon burning shell of massive stars).

These needs represent the foundation of the strong connection between nuclear astrophysics and experimental neutron physics, which provides increasingly precise measurements of the required cross sections at different energies. This topic will be discussed in more detail in the next chapters. The following two subsections will examine the particular importance of the neutron capture cross section of the two isotopes measured in this work.

1.4 The importance of ^{30}Si(n,γ) reaction

Silicon is among the most abundant elements in nature. It occurs in three stable isotopes: ^{28}Si, ^{29}Si and ^{30}Si, with natural abundances of 92.2%, 4.7% and 3.1%, respectively [27].

^{28}Si is mainly produced by fusion and α-capture reactions in the explosive oxygen burning shell during core-collapse Supernovae. It is a *primary* isotope, meaning that it can be efficiently synthesized in early generation stars from a pure hydrogen and helium composition, independently on metallicity [28].

On the other hand, the bulk of ^{29}Si and ^{30}Si present in our galaxy is mainly produced by neutron-capture reactions on the stable silicon isotopes

$$^{28}\mathrm{Si}(\mathrm{n},\gamma)^{29}\mathrm{Si} \quad ^{29}\mathrm{Si}(\mathrm{n},\gamma)^{30}\mathrm{Si}$$

in the convective carbon burning shell of massive stars at temperatures around 1 GK [29, 30], and later ejected in the ISM by Supernovae explosions. Figure 1.6 shows the reaction flow. In these stellar conditions, nuclear reaction rates represent important inputs in stellar models and an accurate knowledge of the neutron capture cross sections of the Si isotopes, including ^{30}Si(n,γ) that destroys ^{30}Si, is therefore crucial to shape the final stellar yields and the relative abundances of ^{29}Si and ^{30}Si in galaxies [31].

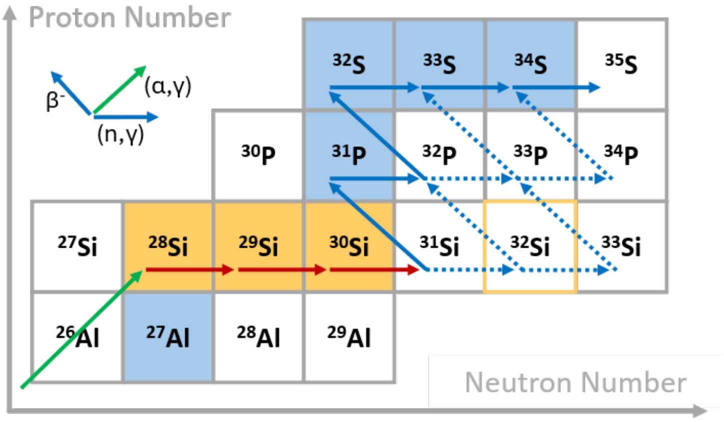

Figure 1.6: Reaction flow in the mass region of interest for the measurement of ^{30}Si(n,γ) cross section. Reactions indicated with a dashed line are likely to occur only in high neutron density environment, like CCSNe. Stable isotopes are highlighted in light blue, while Silicon stable isotopes in orange. ^{32}Si is outlined in orange because of its relatively long half-life (172 years).

The stellar yield and galactic abundance of phosphorus (naturally occurring only as ^{31}P) are also affected by the neutron capture cross section of ^{30}Si. In fact, as shown in Figure 1.6, the main source of ^{31}P is thought to be exactly the ^{30}Si(n,γ)^{31}Si reaction, followed by the β decay of the unstable ^{31}Si to ^{31}P. This process also takes place in the convective carbon burning shell of massive stars, where nuclear reaction rates play a crucial role [29, 32]. Moreover, as stellar models are still uncertain in reproducing the observed phosphorus abundance, some of them even suggesting different stellar sites for ^{31}P production [33], an accurate and updated value of the neutron capture cross section of ^{30}Si as an input to these stellar models is particularly important to address and solve the issue [32].

However, the great relevance of the neutron capture cross sections of silicon isotopes (including ^{30}Si) is related to the understanding of the silicon isotopic abundances measured in SiC presolar grains. Silicon represents about the 50% of the total number of atoms in these grains, but, unlike what happens for heavy elements, its isotopic abundances cannot be solely explained in terms of nucleosynthesis in their AGB parent stars.

Silicon isotopic abundances measured in SiC grains are shown in Figure 1.7 in a so-called three-isotope plot. Mainstream SiC grains are generally more enriched in ^{29}Si and ^{30}Si than the Sun (up to 200‰more) and the line that best fits their isotopic abundances has a slope of 1.34 [26].

As anticipated, neutron-capture nucleosynthesis in the AGB parent stars can reproduce neither the absolute values of the isotopic ratios nor the slope of the correlation line in the three-isotope plot, which is predicted only between 0.17 and 0.8 depending on the value of the neutron capture cross sections used [28, 34]. Therefore, an important contribution to the Si isotopic ratio of SiC grains must be given by the Galactic Chemical Evolution, that models the composition of the pristine stellar gas to which stellar

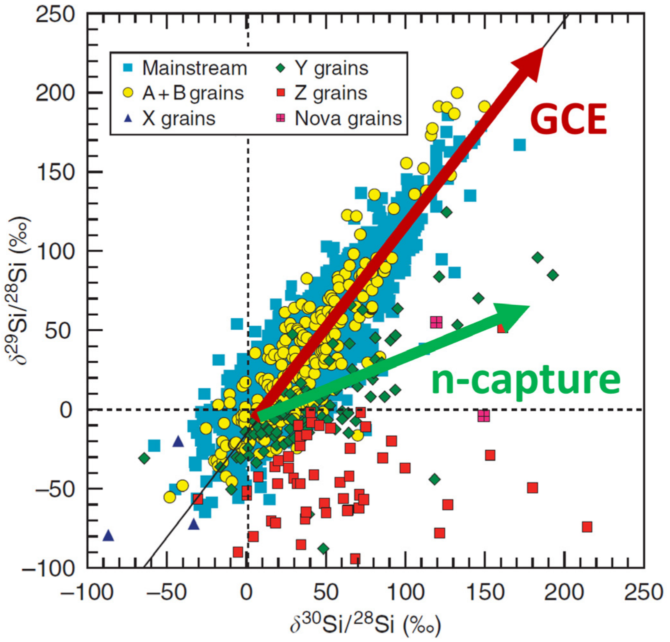

Figure 1.7: Three-isotope plots for the Silicon isotopic abundances measured in presolar SiC grains. The axes represent the ‰deviation from the solar isotopic ratios of ^{29}Si/^{28}Si and ^{30}Si/^{28}Si. Unlike heavy isotopes, Si isotopic abundances in SiC grains cannot be explained solely by stellar neutron-capture nucleosynthesis in the grains' parent stars, but a contribution from the Galactic Chemical Evolution modelling the pre-stellar gas is needed. The two contributions are represented by the arrows. Image adapted from [34].

neutron-capture nucleosynthesis is superimposed.

Accurate values of the neutron capture cross sections of silicon isotopes are crucial first of all to disentangle these two contributions, exactly quantifying the Si abundances produced by the neutron-capture processes in the grains' parent AGB stars [31]. This is only a minor negligible contribution in mainstream SiC grains, but it plays an important role to study the silicon isotopic composition of type Y and Z SiC grains, characterized by an enhanced abundance of ^{30}Si [35].

Moreover, accurate neutron capture cross sections of the silicon isotopes are also important for GCE models. At present, even classic GCE models are able to reproduce neither the values of the silicon isotopic ratios in SiC grains nor their correlation line. The main reason is that, as ^{29}Si and ^{30}Si are secondary isotopes, their isotopic ratios with respect to ^{28}Si are expected to continuously increase throughout the galactic history. According to classic GCE models, the fact that most of the mainstream SiC grains are more enriched in ^{29}Si and ^{30}Si than the Sun would therefore lead to the absurd conclusion that their parent stars were more evolved, i.e. younger, than the solar system.

Different solutions have been proposed to explain ^{29}Si and ^{30}Si enrichment. For example, Clayton suggested that the parent stars of mainstream SiC grains could have condensed in the metal-rich centre of the galaxy and later diffused outwards [36] or that they could have condensed after the merger between a dwarf galaxy and the Milky

Way disk before the solar system formation [37]. Lugaro suggested to consider local heterogeneities of the ISM, due to the admixture of material from a limited number of SN sources [28]. More recently, oxygen-carbon shell mergers in massive stars have been suggested to play a role in silicon nucleosynthesis, correctly reproducing the observed ^{29}Si/^{28}Si isotopic ratio [38, 39].

However, all these GCE models strongly rely on accurate predictions of the silicon stellar yields, that, as already pointed out, require accurate values of the neutron capture cross sections of silicon isotopes. Fok et al. have recently published a study of the effects of nuclear reaction rate uncertainties on the GCE of silicon [38]. In this study, some nuclear reaction rates particularly important for silicon nucleosynthesis (including the rates of neutron capture reactions on silicon isotopes) have been randomly varied within their reported uncertainty and used as inputs in CCSN and classic GCE models to produce a distribution of silicon isotopic ratios to be compared with the data from mainstream SiC grains.

On one side, there is no possibility to reproduce the observed silicon isotopic ratios. However, on the other side, the spread of the distribution of the predicted slope of the correlation line between ^{29}Si and ^{30}Si abundances is large enough to include the observed slope within the 95% confidence interval. In other words, this study demonstrates that the uncertainty in nuclear reaction rates can partially explain the discrepancy between GCE models and observations, showing the importance of more accurate data for neutron capture cross sections of $^{28,\ 29,\ 30}$Si.

Last but not least, neutron capture cross sections of Silicon isotopes are important concerning type C SiC grains, a rare type of carbon-rich SiC grains (approximately 0.1% of total) that condenses around CCSN. These grains are characterized by an enhanced abundance of ^{32}S that, according to Pignatari et al. [40], can be only explained by the presence of long-lived ^{32}Si ($t_{1/2}$ = 132 yr) condensing in the grains and later decaying to its stable isobar ^{32}S.

^{32}Si is produced by consecutive neutron capture reactions on the stable silicon isotopes, but only if the neutron density is high enough to overcome the short-lived ^{31}Si ($t_{1/2}$ = 2.6 h). Therefore, given the observed ^{32}S abundance, accurate neutron capture cross sections for Si isotopes (including ^{30}Si, but also ^{31}Si) are important to constrain the neutron density reached in CCSN explosions [31].

Despite the great astrophysical importance of the neutron capture cross sections of silicon isotopes, data available in the literature are scarce and discrepant, especially concerning the ^{30}Si(n,γ). Indeed, as will be discussed in Section 6.2, the most recent time-of-flight measurement [41] reports a MACS at 25 keV more than 3 times smaller than the previous reference cross section [42, 43] and 1.5 times smaller than a contemporary activation measurement [44].

For these reasons, a new time-of-flight measurement of the ^{30}Si(n,γ) cross section was strongly requested and it has been performed at the n_TOF facility, together with new measurements of ^{28}Si(n,γ) and ^{29}Si(n,γ) cross sections, whose analysis is ongoing.

1.5 The importance of ^{64}Ni(n,γ) reaction

Although it constitutes only 0.93% of natural nickel [27], ^{64}Ni is of great importance in nuclear astrophysics in modelling the s-process.

First of all, together with the other iron and nickel isotopes, ^{64}Ni represents one of the seeds of the s-process. Secondly, its particularly small neutron capture cross section (the smallest among nickel and iron isotopes [45]) makes it an effective bottleneck for the production of heavier nuclei along the s-process path, shown in the right image in Figure 1.3. For these reasons, the neutron capture cross section of ^{64}Ni does not only locally influence the s-process abundances predicted by stellar models, but it has a global impact on the predicted abundance of many isotopes synthesized both in the weak and in the main s-process components, as will be explained more in details in the following paragraphs.

Concerning the weak component of the s-process in massive stars, it has been already pointed out (Section 1.3.2) that the neutron capture cross section of an isotope affects the s-process abundances of all the heavier isotopes along the s-process path, up to strontium. Neutron capture cross sections of the s-process seed nuclei (including ^{64}Ni) are therefore particularly important, as they affect the abundance of all the isotopes synthesised in the process. For this reason, they need to be known with the highest possible precision in order to accurately and reliably model the s-process in massive stars.

The measurement of the neutron capture cross sections of the nickel and iron isotopes was indeed already proposed at the n_TOF facility in 2006 [46]. While most of them have been measured in the meantime (^{58}Ni [47], ^{62}Ni [48], ^{63}Ni [49], ^{54}Fe, ^{56}Fe [50], ^{57}Fe [51]), the measurement of ^{64}Ni has been postponed up to this work because of the high cost of a suitable enriched sample.

Concerning the main component of the s-process in AGB stars, a study of the impact of the neutron capture cross section of ^{64}Ni has been performed in this work, using the *Pizbuin* suite code [52]. This suite consists of a reaction network code that, given in input the nuclear reaction rates and a trajectory describing the time evolution of stellar thermodynamic quantities (like temperature or densities), provides the isotopic abundances resulting from nucleosynthesis in a star. In this case, the thermodynamic trajectory given as input describes the evolution of the Helium intershell of an AGB star of $3M_\odot$ and metallicity 0.014 in radiative equilibrium during the 6^{th} interpulse [53]. The input reaction rates are a combination of theoretical values by Rauscher & Thielemann [54] supplemented by experimental rates taken from KADoNiS 0.3 [45] and the JINA REACLIB database [55], while the decay rates are taken from a REACLIB database from references Freiburghaus & Rauscher [56].

In this framework, the input ^{64}Ni neutron capture rate, originally taken from KADoNiS 0.3, has been arbitrarily varied within the discrepancy observed in the literature in order to assess its impact on the main s-process predicted abundances. Figure 1.8 shows the effect of doubling the default neutron capture cross section of ^{64}Ni on the s-process

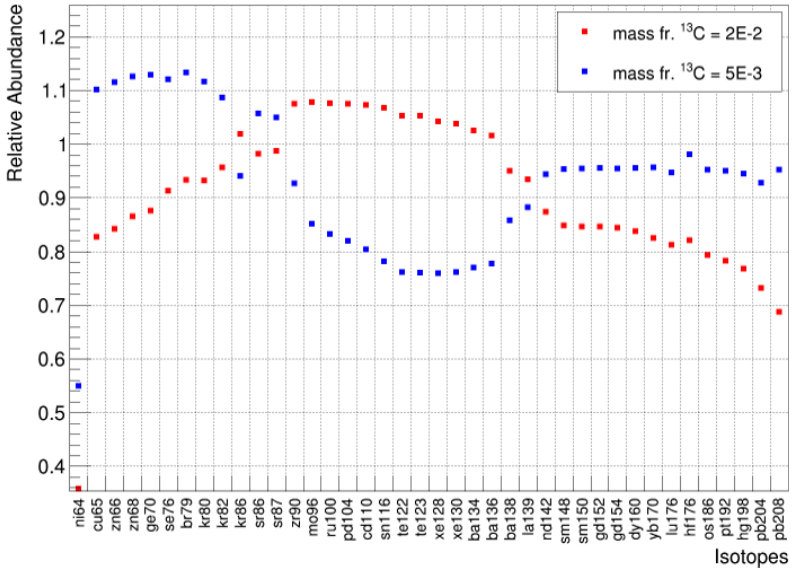

Figure 1.8: Relative variation of the predicted s-process abundances of some nuclei after doubling the neutron capture cross section of ^{64}Ni with respect to its default value taken from KADoNiS 0.3 [45]. The effect is studied considering two different initial abundances of ^{13}C (blue and red dots).

abundances of some nuclei spread along the s-process path, using two different initial concentration of ^{13}C that defines the neutron exposure in the process. From the picture it is clear that the neutron capture cross section of ^{64}Ni has a global impact in modelling the main s-process component, importantly affecting the predicted abundances of many isotopes, even far away from ^{64}Ni in the chart of nuclides. Moreover, this effect is strongly dependent on the stellar conditions, like the neutron exposure. The same conclusion has been drawn by other sensitivity studies recently performed by Koloczek et al. using a different simulation framework [57] and by Cescutti et al., also using Pizbuin [53].

In particular, the study by Cescutti et al. is a more comprehensive and larger scale Monte Carlo sensitivity study aimed at the determination of the uncertainty in the main s-process abundance predictions due to the uncertainty in nuclear reaction rates. In this case, not only the neutron capture rate of ^{64}Ni, but all the neutron capture and β decay rates involved in the s-process are randomly varied independently and simultaneously using a Monte Carlo driver, performing 10000 different nucleosynthesis simulations. The correlation between the variation of a reaction rate and the variation of predicted abundance has been studied for all the combinations of reactions and isotopes, in order to identify the key reactions dominating the uncertainty on the predicted abundance of each isotope. If most of the neutron capture reaction rates have been found to affect only the abundances of the nuclei they produce or destroy, as expected from the local equilibrium condition discussed in Section 1.3.1, the cross section of the ^{64}Ni(n,γ) (together with the ones of ^{56}Fe(n,γ) and ^{138}Ba(n,γ)) has been confirmed to influence a large number of predicted s-process abundances. For example, the rate of ^{64}Ni(n,γ) has been

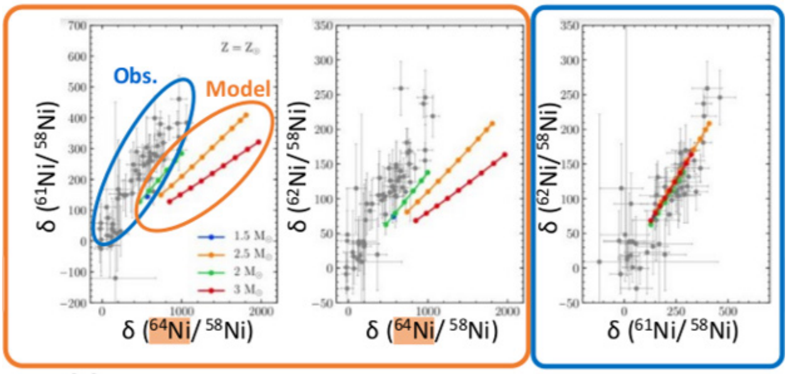

Figure 1.9: Three-isotope plots showing the comparison between isotopic ratios of Ni observed in mainstream SiC grains and predicted by a recent model of AGB stars [58]. The model seems to reproduce well the isotopic abundances of the nickel isotopes (blue box), except for that of ^{64}Ni (orange box). Image adapted from [59].

identified among the two reaction rates most correlated with the predicted abundance of ^{208}Pb.

In conclusion, a precise value of the neutron capture cross section of ^{64}Ni is not only important for accurate simulations of s-process isotopic abundances, but also for the validation of a recent stellar model for mixing in AGB stars.

The mixing between the convective envelope and the helium intershell in AGB stars is fundamental in creating the conditions for the s-process to occur, but its mechanism is still not completely understood. Different models have been suggested based on overshoot, rotation or gravity waves. However, only recently Vescovi et al. have introduced a model based on magnetic buoyancy that, for the first time, can simultaneously fit the majority of the isotopic abundances measured in mainstream SiC grains, assuming a single magnetic field configuration [58].

Among the few exceptions, the observed isotopic abundances of ^{64}Ni cannot be reproduced by the model, while a good agreement is reached for all the other Ni isotopes, as shown in Figure 1.9. This single discrepancy may suggest a possible incorrectness of the recommended value of the neutron capture cross section of ^{64}Ni used in calculations rather than a limitation of the model.

In fact, despite its great astrophysical importance, the literature on the ^{64}Ni(n,γ) cross section reports few and discrepant data, especially concerning time-of-flight data that are ultimately needed to extrapolate MACS at different energies. As an example, different extrapolations of the same MACS measured at 30 keV currently disagree by more than a factor of two at 8 keV [45, 60]. For these reasons, a new time-of-flight measurement of the neutron capture cross section of ^{64}Ni was requested.

Chapter 2

Neutron-Induced Reactions

Originally proposed by E. Rutherford in 1920 as a tightly bound state of a proton and a "nuclear electron" [61], the neutron was later discovered in 1932 by one of his students: J. Chadwick [62]. Neutrons were immediately assumed as elementary constituents of nuclei together with protons and were used to artificially synthesize new radioactive isotopes [63], eventually leading to the discovery of nuclear fission in 1938 [64]. Since then, the study of neutron-induced reactions has enormously grown and found applications not only in nuclear astrophysics (as described in the previous chapter), but also in the production of energy and in medicine.

An overview of the interaction of neutrons with matter and corresponding cross sections will be presented in Section 2.1, while the following Section 2.2 will describe in detail the theories and the parametrizations used to describe resonances. Direct reactions and direct capture specifically will be discussed in Section 2.3, while the last Section 2.4 will be dedicated to an introductory description of experimental techniques adopted for the measurement of neutron-induced cross sections and for the characterization of resonances.

2.1 Interaction of neutrons in matter

The distinctive feature of neutrons in the context of nuclear reactions is represented by their electrical neutrality. Charged particles are indeed repelled by the electric potential of atomic nuclei and therefore can efficiently trigger nuclear reactions starting from kinetic energies of a few MeV, while charged particles of lower energies are predominantly just scattered by nuclei or even lose their energy interacting with atomic electrons.

On the other hand, neutrons are insensitive to the Coulomb interaction and therefore can directly reach the atomic nucleus and induce nuclear reactions at whatever kinetic energy, even below the meV. Remarkably, some neutron-induced reactions (e.g. neutron capture) even become more probable as the neutron energy decreases.

This unique capability has led to the development of a broad and specialized field of neutron physics, dedicated to the study of neutron-induced reactions in the low energy region (meV - keV).

Neutron-induced reactions can be classified according to the reaction mechanism, such as compound-nucleus reactions (Section 2.2.1) or direct reactions (Section 2.3), or according to their output channel. In this case, one can distinguish:

- *Radiative neutron capture*, the reaction of interest in this thesis, that occurs when a neutron is captured by a nucleus and γ rays are released to de-excite the product nucleus to its ground state (see Section 2.2.2).
- *Elastic scattering*, that is the deflection of a neutron by a nucleus conserving the total kinetic energy. This reaction can proceed via different mechanisms (compound nucleus, potential scattering, ...) and can transfer a fraction of the kinetic energy of the neutron to kinetic energy of the target nucleus, depending on the scattering angle and on the mass of the target. This mechanism is typically used to slow down neutrons and it is called *neutron moderation*. It is particularly efficient with light target nuclei like hydrogen or carbon.
- *Neutron-induced fission*, that breaks heavy nuclei into two lighter fragments and some free neutrons, typically releasing an important amount of energy in the form of kinetic energy of the fission products.

Neutron capture and elastic scattering do not have threshold energies that need to be reached to initiate the reaction, therefore they are the most frequent reactions induced by low-energy neutrons (below a few hundreds of keV). Fission is also efficiently induced by low-energy neutrons, but only on some heavy nuclei, called *fissile* nuclei, such as ^{235}U or ^{239}Pu. The other heavy nuclei (such as ^{238}U, ^{232}Th), called *fissionable* nuclei, need neutrons of kinetic energy of at least a few MeV to undergo fission, to allow the fission fragments to overcome the nuclear electric potential barrier.

Increasing the kinetic energy of neutrons, other threshold reaction channels also open:

- *Inelastic neutron scattering*, that is the deflection of a neutron from a nucleus, where part of the kinetic energy of the neutron is transferred into internal excitation energy of the target nucleus, that is left in an unstable state. This reaction channel opens at the neutron energy that matches the energy of the first excited state of the target nucleus, that can vary from a few tenths of eV (as in ^{235}U) to a few MeV (as in light nuclei such as ^{12}C).
- *Light charged-particle reactions*, like (n,p) or (n,α) reactions. These reactions are usually characterized by neutron energy thresholds of some MeV due to energy conservation in the reaction or due to the need for the charged-particle products to overcome the nuclear Coulomb barrier. However, there are also important examples of charged-particle reactions on light nuclei that do not have an energy threshold, like the ^{10}B(n,α)^{7}Li or ^{6}Li(n,α)^{3}H.

Increasing the neutron energy even more, the de Broglie wavelength of neutrons decreases and neutrons start to interact with single nucleons, first elastically (in direct reactions for example) and then inelastically (starting at 290 MeV, where the pion production channel opens). Energetic particles are typically released by these reactions and they can initiate intra-nuclear reaction cascades that lead to the excitation of the whole nucleus and to the later emission of a large number of light particles and nuclear fragments. These complex reactions usually go under the name of *nuclear fragmentation reactions* or, at neutron energy higher than hundreds of MeV, *spallation* reactions. At even higher energies, these phenomena are at the basis of the development of *hadronic showers* in materials. However, this topic already enters the domain of particle physics and QCD, where neutron-induced reactions are not different from other particle-induced reactions and that are beyond the aim of this introduction.

On the opposite side, reducing the neutron energy below tens of meV (*thermal and cold neutrons*), the de Broglie wavelength of neutrons becomes comparable with interatomic distances in crystals and molecules. Hence, neutron scattering (or neutron diffraction) in this energy range can provide precious information on the atomic and magnetic structures of materials.

2.1.1 Neutron cross sections

Each reaction presented above is characterized by a different probability to occur, that depends on the target nucleus and on the neutron energy. The *reaction cross section* σ is the quantitative measurement of this probability and can be thought as the "effective" area exposed by a nucleus to an incoming projectile for the reaction to occur.

In terms of quantum mechanics, two interacting particles in a particular channel c and located at a distance larger than the nuclear interaction radius can be described by the wave function Ψ_c:

$$\Psi_c = I_c - \sum_{c'} U_{cc'} O_{c'} \,. \tag{2.1}$$

I_c is the incoming wave function for the entrance channel c, $O_{c'}$ are the outgoing wave functions for all the possible output reaction channels c' and $U_{cc'}$ are the elements of the collision matrix U, that defines the probability amplitudes for the transitions between channels. A channel is just defined as a specific pair of particles (projectile and target or ejecta and residual) in a particular excitation state and dynamic configuration, specified by the total intrinsic spin of the particles (S), their relative orbital angular momentum (l) and their total angular momentum (J), conserved in the interaction. More details can be found in references [65–68] on this topic.

The cross section for an interaction from channel c to c' can be derived as the solid angle integrated ratio of the probability fluxes j of the corresponding outgoing and incoming waves and it can be written as:

$$\sigma_{cc'} = \int \frac{j_{O_{c'}}}{j_{I_c}} r^2 d\Omega = \pi \bar{\lambda}_c^2 g(J) \mid \delta_{cc'} - U_{cc'} \mid^2 \tag{2.2}$$

$\lambdabar_c = \sqrt{2\mu_c E_c/\hbar^2}$ is the reduced wave length, that depends on the reduced mass of the particles in the entrance channel μ_c and on their total kinetic energy in the centre of mass frame E_c. It is just a kinematic factor relating probability to cross section. $g(J) = (2J+1)/\{(2s_1+1)(2s_2+1)\}$ is the statistical spin factor, that represents a weight associated to the total angular momentum relative to the number of channels that can be built from the intrinsic spin of the interacting particles (s_1 and s_2). $\delta_{cc'}$ is the Kronecker symbol.

Channel to channel cross sections are not useful in practice, as single channels cannot be experimentally distinguished. Equation 2.2 is therefore usually integrated over all the possible channels that correspond to a transition between a specific pair of particles α to another specific pair of particles α', resulting in the measurable cross section

$$\sigma_{\alpha\alpha'} = \sum_J \left[\pi \lambdabar_\alpha^2 g(J) \sum_{l,l',s,s'} \mid \delta_{ls,l's'} - U_{ls,l's'} \mid^2 \right]. \tag{2.3}$$

Additionally, summing on all the possible output particle pairs, one gets the total cross section σ_α, only dependent on the real part of the diagonal terms of the collision matrix:

$$\sigma_\alpha = \sum_J \left[2\pi \lambdabar_\alpha^2 g(J) \sum_{l,s} (1 - Re(U_{ls,ls}))\right]. \tag{2.4}$$

In this quantum description of reaction cross sections, the collision matrix **U** is the only term that ultimately represents the nuclear interaction. In principle, it can be theoretically predicted assuming a particular nuclear potential and/or a nuclear interaction model. However, because of the extreme complexity of nuclear systems, a "standard" model of the nucleus capable of describing nuclear interactions and accurately predicting measured cross sections does not yet exist [69].

For this reason, the current knowledge of neutron reaction cross sections is ultimately based on experimental measurements, that not only provide increasingly precise data, but can also be used indirectly to validate and improve theoretical nuclear reaction models.

Further details regarding neutron cross section measurements are provided in Section 2.4. For the moment it is enough to underline that experimental measurements also have limitations, for example when dealing with high neutron energies (a lot of reaction channels are open), particularly low cross sections and rare or unstable isotopes.

In the end, properly weighted information from both measurements and theoretical models is combined in the so-called *evaluated nuclear data* to provide recommended values and uncertainties of several reaction cross sections as a function of the energy. These evaluated data eventually represent the nuclear inputs used in the simulation of nuclear systems in different fields of application. Together with other important quantities, they are collected in the *Evaluated Nuclear Data Libraries*, that are regularly updated including new measurements and/or new theoretical models. Examples of the latest releases are ENDF/B-VIII.1 (USA, 2024 [70]), JEFF-4 (Europe, 2025 [71]), JENDL-5 (Japan, 2021 [72]), CENDL-3.2 (China, 2020 [73]), ENDF/B-VIII.0 (USA, 2018 [74]), JEFF-3.3 (Europe, 2017 [75]).

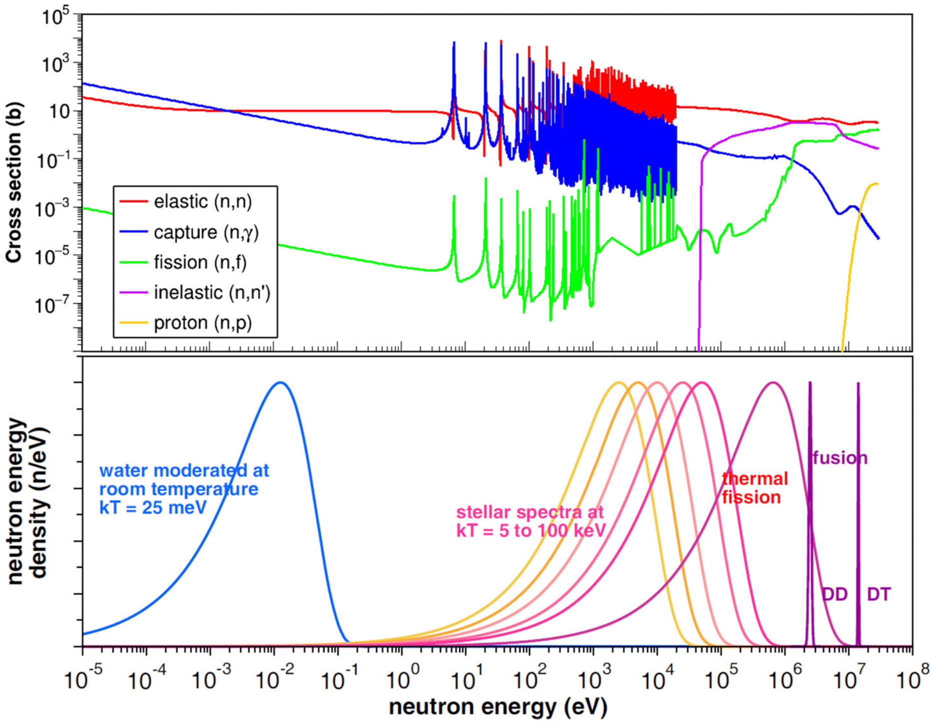

Figure 2.1: Top: evaluated cross sections of some neutron-induced reactions on ^{238}U, taken from ENDF/B-VIII.1. Bottom: typical neutron energy spectra in the different fields of application of neutron-induced reactions. Picture adapted from [67].

As an example, the upper part of Figure 2.1 shows the evaluated neutron cross sections of different reactions on ^{238}U. Despite neutron cross sections are different from one isotope to another, there are some similarities that can be commented starting from the figure. First of all, three different neutron energy regions can be distinguished: a thermal-epithermal region, a resonance region and a high-energy continuum region.

- The thermal-epithermal region goes from thermal neutron energy (25 meV) to the first resonance. In this energy range, elastic scattering and neutron capture reactions are always allowed, while fission and charged-particle reactions can occur only for some isotopes, as already discussed. The neutron cross section of these reactions exhibits a smooth behaviour: the elastic cross section is approximately constant with the neutron energy, while the capture cross section (as well as the other "absorption" reactions) is inversely proportional to the square root of the neutron energy ($1/\sqrt{E}$ or $1/v$ behaviour, where v is the neutron velocity).
- The resonance region is characterized by *resonances*, sharp structures that occur at well defined energies, corresponding to the excited states of the compound nucleus formed during the reaction. The energy limits of this region depend on the nucleus: heavy nuclei, that usually have low-energy excited states, present resonances in a range from a few eV to several keV, while the resonance region in

light or stable nuclei typically spans between some keV and several MeV. The resonance region can be additionally separated into two subregions. In the so-called *Resolved Resonance Region* (*RRR*), resonances are well separated and cross sections are parametrized using the *R-Matrix theory*, that can be used also for the thermal region. Increasing the neutron energy, the average spacing between resonances decreases to a point that it falls below the experimental resolution and resonances can no longer be experimentally resolved. In this region, called *Unresolved Resonance Region* (*URR*), cross sections are parametrized by average resonance parameters within the *Hauser-Feshbach theory*. As the resonance region is the most important one for this work, more details on resonances, compound nucleus theory and cross section parametrization will be given in the next section and in Appendix B.

- In the high energy region (hundreds or thousands keV), the average spacing between resonances decreases even below the average resonance width. Therefore, resonances are no longer intrinsically resolved and cross sections assume a continuum behaviour. In this energy range, the capture cross section typically decreases, while inelastic, threshold-reaction and direct reaction channels open and become increasingly important. Cross sections can be modelled and predicted using the *Optical Model Potential* (*OMP*) and the *Hauser-Feshback theory*, coupled with pre-equilibrium and statistical models of the nucleus. These models are included, for example, in the TALYS code [76], that can be used to analyse and simulate neutron cross sections up to 200 MeV. At higher energy, nucleon-nucleon elastic and inelastic cross sections are eventually used to parametrize nuclear cross sections, as described by the *Glauber Model* [77].

2.1.2 Maxwellian Averaged Cross Sections

In the previous paragraphs, pointwise neutron cross sections have been described over a wide range of neutron energies. However, in most practical situations, neutron energies are distributed according to specific energy distributions involving specific energy regions, as shown in the bottom part of Figure 2.1. For this reason, in many applications it is sometimes convenient to use integral cross sections mediated on the neutron energy spectrum, rather than pointwise cross sections.

In the particular context of nuclear astrophysics, neutron velocities v in a stellar plasma can be described by a Maxwell-Boltzmann distribution

$$\Phi(v) = 4\pi v^2 \left(\frac{m}{2\pi k_B T}\right)^{\frac{3}{2}} e^{-\frac{mv^2}{2k_B T}} \tag{2.5}$$

where $\Phi(v)$ is the probability of finding a neutron with a velocity within v and $v + dv$, k_B is the Boltzmann constant and T is the temperature of the stellar plasma. The corresponding integral cross section, averaged on this particular spectrum, is the so-called

Maxwellian Averaged Cross Section (*MACS*) $\langle\sigma\rangle$, that can be computed as

$$\langle\sigma\rangle \; = \; \frac{\langle\sigma v\rangle}{v_T} = \frac{2}{\sqrt{\pi}\,(k_B T)^2}\int_0^\infty \sigma(E)\; E\; e^{-\frac{E}{k_B T}} dE \qquad (2.6)$$

where the velocity has been transformed to the total energy in the centre-of-mass frame E.

As already mentioned, MACSs are particularly important in nuclear astrophysics as they represent the nuclear input needed to compute reaction rates in stars. However, experimental MACS only take into account reactions induced on nuclei in their ground state, while the high temperatures characterizing stellar plasmas can also maintain nuclei in excited states, characterized by different reaction cross sections. *Stellar Enhancement Factors* (*SEF*), based on statistical nuclear models and not directly measurable, are employed to correct the experimental MACS taking into account reactions with excited nuclei.

Updated MACS and SEF for several isotopes in the energy range of astrophysical interest (5 - 100 keV) are collected in databases such as KADoNiS [45, 60] (Karlsruhe Astrophysical Database of Nucleosynthesis in Stars), a specialized nuclear database for astrophysical applications.

2.2 The Resonance Region

Basic quantum mechanics shows that the possible energy levels of a nucleon moving in a potential well (first approximation of a nuclear average potential) form a spectrum that is discrete up to the nucleon separation energy and continuous for higher energies. However, in this continuum, there are some energy states whose wave functions match so well at the boundary of the potential well that they they are fully transmitted across the potential discontinuity. These energy states form a discrete spectrum of "quasi-bound" states above the nucleon separation energy that correspond to nuclear resonances [67].

2.2.1 Compound Nucleus Reactions

The *Compound Nucleus* model is among the first theories about nuclear reactions, suggested by N. Bohr in 1936 [78, 79] and still used, even if largely improved, to explain the resonant behaviour of neutron cross sections.

This model basically assumes that neutron-induced reactions proceed through two independent steps:

- the formation of an excited compound nucleus C^* from the fusion of the neutron and the target nucleus A
- the de-excitation of the compound nucleus C^* to a nucleus B through the emission of radiation or particles b, where B and b are the reaction products.

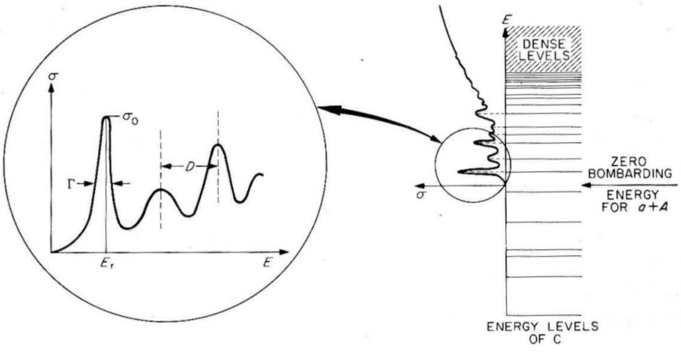

Figure 2.2: Resonances in neutron cross sections explained according to the compound nucleus model. On the right, a typical excitation spectrum for a compound nucleus is shown. The arrow represents the minimum energy of the neutron-target nucleus system before the formation of the compound nucleus. As the kinetic energy of the incoming neutron increases, excitation states of the compound nucleus are matched, producing the resonances shown in the figure on the left. Picture from [80].

The mechanism can be written as

$$n + A \rightarrow C^* \rightarrow B + b$$

and it is generally dominant for nuclear reactions up to approximately 10 MeV. In the following paragraphs the two steps of this process will be discussed more in detail.

Concerning the formation of the compound nucleus, the theory states that when the incoming neutron is captured, it shares its kinetic energy collectively among all the nucleons of the target nucleus. Therefore, the compound nucleus is formed in an excited state, with a well defined spin, parity and energy E_{CN}, that corresponds to the sum of the neutron binding energy (BE_n, usually some MeV) and the kinetic energy in the centre of mass frame

$$E_{CN} = BE_n + \frac{A}{A+1}E_n \tag{2.7}$$

where A is the mass number of the target nucleus and E_n the initial neutron kinetic energy.

A compound nucleus can assume whatever energy above the neutron separation energy, but if the excitation energy exactly matches one of the discrete "quasi-bound" states previously described, the probability for the compound nucleus to be created is maximized. This is the reason why, at the corresponding neutron kinetic energies, resonances appear in neutron cross sections, as explained in Figure 2.2. Increasing the excitation energy, quasi-bound states get closer up to the point they also form a dense continuum spectrum. At the corresponding neutron energy, resonances overlap until they cannot be distinguished anymore and neutron cross sections also assume a smooth behaviour.

From the theoretical point of view, the excited states of the compound nucleus are extremely complex nuclear states, as they involve the excitation of many nucleons and in several possible configurations, together with possible collective excitations. The situation gets increasingly complicated with increasing the excitation energy and the mass of the nucleus. The wave functions describing these states in a heavy nucleus may have as much as one million components, which therefore cannot be described separately [67]. The compound nucleus in this chaotic regime must be described by a statistical model based on average quantities like the level density and average matrix elements describing the transitions between nuclear states. This statistical model is usually referred to as *Gaussian Orthogonal Ensemble* (*GOE*) [81].

The second step of the reaction mechanism corresponds to the de-excitation of the compound nucleus. The lifetime of the quasi-bound excited states of compound nuclei spans typically from 10^{-18} to 10^{-15} s, that basically corresponds to the time duration of the reaction. This relatively long time duration is one of the distinguishing features of compound-nucleus reactions, since the characteristic nuclear time (i.e. time needed by a few MeV neutron to cross a medium-weight nucleus) that characterizes the duration of direct reactions is some order of magnitudes smaller (approximately 10^{-22} s). The Heisenberg's indeterminacy principle translates the lifetime of the quasi-bound nuclear states into an energy *total width* Γ of the corresponding resonances, that can be measured and typically is of the order of some eV.

The de-excitation of the compound nucleus can occur via several output channels b, each one with a different probability quantified by the *partial resonance widths* Γ_b. The sum of the partial widths of all the possible de-excitation channels returns the total width.

As already anticipated, the Bohr's compound nucleus model assumes that the de-excitation of the compound nucleus is completely independent by its formation, as the identity of the impinging neutron is lost during the process. For this reason, the cross section of compound-nucleus reactions can be factorized in the probability of the formation of the compound nucleus P_{CN} times the probability of its decay in the desired channel, that can be related to the corresponding partial widths as:

$$\sigma_{ab} \propto P_{CN} \cdot \frac{\Gamma_b}{\Gamma} \propto \frac{\Gamma_a \Gamma_b}{\Gamma^2}. \tag{2.8}$$

2.2.2 Electromagnetic de-excitation of the compound nucleus

As neutron radiative capture (n, γ) reactions are the topic of this thesis, they require a more detailed discussion.

Neutron radiative capture reactions occur when the compound nucleus formed by the neutron capture undergoes electromagnetic de-excitation to its ground state, through the emission of a cascade of γ rays.

The total energy of the γ rays emitted always corresponds to the excitation energy of the compound nucleus (equation 2.7). However, as an excited state can decay to different low-lying states before reaching the ground state, the de-excitation cascade of the compound nucleus is random, meaning that it can occur with different multiplicities

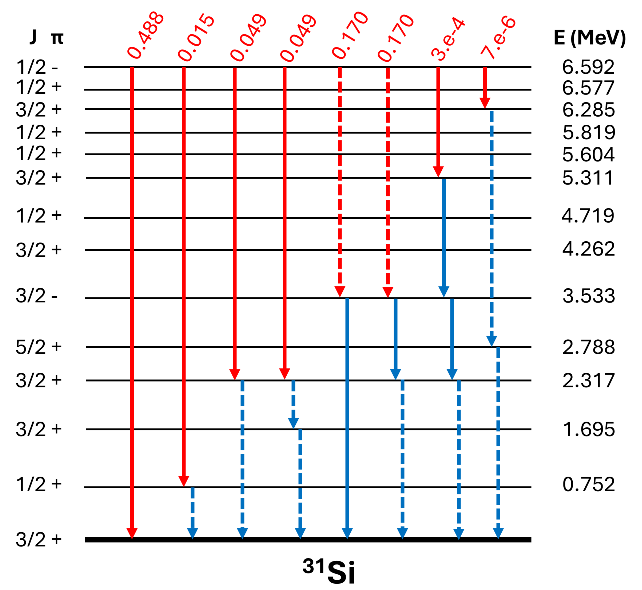

Figure 2.3: Some possible de-excitation cascades of the 6.592 MeV excited state of ^{31}Si, populated by the 4.98 keV resonance of the ^{30}Si(n,γ) reaction. Each arrow corresponds to a γ ray of the corresponding energy. E1 transitions are represented by continuum arrows, while M1 transitions by dashed arrow. Primary transitions, that only matter for the determination of the radiation width, are highlighted in red and their probabilities (fitted from experimental data, see Section 4.3.4) are reported on top. For clarity, the level scheme includes only some of the known levels of ^{31}Si taken from ENSDF [83].

following different paths, as shown in Figure 2.3. The resulting de-excitation γ energy spectra of nuclear resonances can be therefore quite complex and change from one resonance to another because of the different spin-parity. As they are typically required to determine corrections of the experimental yields (see Section 4.3.4), they can be either measured with high-resolution γ ray detectors like HPGe or LaBr$_3$, or simulated using specific toolkits like NuDEX [82].

The total radiative width Γ_γ of a resonance corresponds to the sum of the widths of all and only the possible *primary transitions*, which de-excite the quasi-bound state of the compound nucleus populated by the neutron capture to a whatever low-lying state.

Both the simulation of de-excitation cascades and the prediction of radiative neutron capture cross sections rely therefore on the determination of the partial widths quantifying the probabilities of single electromagnetic transitions between nuclear states. From a theoretical point of view, these widths can be computed using the Fermi's Golden Rule as:

$$\Gamma_{\gamma,if} \propto E_\gamma^{2L+1} \left| \langle f | E\hat{M} | i \rangle \right|^2, \tag{2.9}$$

where $|i\rangle$ and $\langle f|$ represent the wave functions of the initial and final states, characterized by defined energy E, spin J and parity π, E_γ is the energy of the γ ray and $\hat{EM}$ is the electromagnetic operator, that can be separated in an electric and in a magnetic part expanded in series of multipoles representing the angular momentum L of the photon. Selection rules are implicitly included in this last term and only enable $2L$-multipolarity transitions with $|J_i - J_f| \leq L \leq J_i + J_f$ between states with parities $\pi_i \pi_f = (-1)^L$ (Electric transitions) or $\pi_i \pi_f = (-1)^{L+1}$ (Magnetic transitions).

Assuming initial and final states as single-particle excited states, the expression 2.9 can be simplified in the so-called *Weisskopf estimates*, that can be found in nuclear physics books [84, 85]. These estimations show that the probability of transitions decreases with the multipolarity and that, at constant multipolarity, electric transitions are two order of magnitudes more probable than magnetic transitions. For these reasons, E1, E2 and M1 transitions mostly appear in the de-excitation cascades of resonances. Moreover, as the probability of a transition is proportional to its energy (Equation (2.9)), high energy photons are usually favoured, like for example direct E1 transitions from excited states to the ground state, when enabled by the selection rules.

Even if useful in first approximation, it must be pointed out that in general the Weisskopf estimates cannot exactly predict the probability of the electromagnetic transitions. Instead, experimental measurements are typically available at low excitation energies, where excited states are well separated and γ rays intensities can be measured via γ spectroscopy. These value can be found in nuclear databases like RIPL-3 [86]. However, beyond a certain excitation energy (often referred to as E_{cutoff}), excited levels get closer and it is not easy to disentangle them. A statistical treatment becomes therefore necessary. Energy level density is used instead of single excited states and *Photon Strength Functions* [85–87] are introduced to provide an average probability of electromagnetic transitions of energy E_γ and multipolarity XL between nuclear states. They are defined as:

$$f_{XL}(E_\gamma) = \langle \Gamma_{\gamma,if} \rangle \, E_\gamma^{-(2L+1)} \rho(E_i, J_i, \pi_i) \tag{2.10}$$

where $\rho(E_i, J_i, \pi_i)$ represents the density of states and $\langle \Gamma_{\gamma,if} \rangle$ is the average width for single transitions.

In conclusion, it is important to mention that excited compound nuclei can sometimes de-excite electromagnetically without releasing γ rays, but interacting and transferring their excitation energy to an atomic electron in the inner atomic shells. Electrons are therefore released together with a cascade of X-rays, due to the atomic electrons de-exciting to the vacancy left in the inner shell. This process is called *internal conversion* and mainly occurs in heavy (high Z) nuclei, where electrons are closer to the nucleus. This phenomenon is particularly relevant for low-energy transitions and in competition with high multipolarity γ transitions, while it is usually negligible for high-energy transitions. However, it becomes the dominant de-excitation process when γ emission is forbidden, like in the transition between 0 spin states.

2.2.3 The R-Matrix Theory

Cross sections in the resonance region are parametrized by the *R-Matrix Theory* [65–68]. The choice of parametrizing cross sections instead of directly reporting their value at different energies is advantageous under many aspects [66]:

- Resonance parameters enable the detailed representation of the cross section structures using relatively few numbers
- Experimental broadening effects related to Doppler effect, multiple scattering and energy resolution (see Section 2.4.1) can be introduced more easily
- Resonance parameters can be statistically studied to extrapolate and predict cross sections in the URR at higher energies.

The parameters describing a resonance in the R-Matrix theory are: the energy (E_r), the spin and the parity (J^π), the partial widths (e.g. neutron width Γ_n or the radiative width Γ_γ) and the total width Γ.

The basic idea of this theory consists in studying a nuclear reaction considering two different *regions*: an *external* region, where the interacting particles are separated by a distance larger than the nuclear interaction radius a_c, and an *internal* region, that corresponds to the compound nucleus formed by the fusion of the two particles during the reaction. As already described in a previous section, the wave function of the system in the external region can be described by the Equation 2.1, that includes an incoming wave for the entrance reaction channel c, an outgoing wave for the output reaction channel c' and the collision matrix element $U_{cc'}$, that accounts for the nuclear interaction. The R-Matrix theory basically provides an approximation of the wave function in the internal region, assuming that it can be expanded as a linear combination of the eigenstates of the compound nucleus, that correspond to the its excited levels λ observed through the resonances. Therefore, the R-Matrix theory is not a predictive theory, as it does not make any assumption on the nuclear potential.

Imposing the continuity and the differentiability of the total wave function of the system at the boundary between the internal and the external region eventually enables to relate the collision matrix $U_{cc'}$ to the so-called *R-Matrix* $R_{cc'}$

$$R_{cc'} = \sum_{\lambda} \frac{\gamma_{\lambda c}\gamma_{\lambda c'}}{E_\gamma - E}. \tag{2.11}$$

This matrix ultimately accounts for what happens inside the compound nucleus, defining the probability of transition between the reaction channels c and c' as a function of the properties of its eigenstates λ. In particular, E_λ can be identified with the energy of the resonances, while the $\gamma_{\lambda c}$ are called *level width amplitudes* and are related to the probability of transition between a level λ and a reaction channel c. These quantities are therefore related to the partial resonance widths for the different reaction channels ($\Gamma_{\lambda c}$), that can be written indeed as

$$\Gamma_{\lambda c} = 2P_c\gamma_{\lambda c}^2 \tag{2.12}$$

where P_c represents the penetrability of the channel in the nuclear potential through the centrifugal barrier and introduces a dependence on the energy and on the orbital angular momentum.

More theoretical details about the formulation of the R-Matrix theory can be found in Appendix B. However, as the general theory is quite convoluted, approximations are usually considered.

The *Single-Level Breit-Wigner* (*SLBW*) approximation is the easiest and most comprehensible approximation of the R-Matrix theory. It works well for isolated, well separated resonances as it assumes only one level λ of the compound nucleus. In this approximation, matrices reduce to numbers and therefore become very easy to handle.

Using this approximation and the Equation 2.2, the reaction cross section $\sigma_{cc'}$ can be written as:

$$\sigma_{cc'} = \pi\lambda\!\!\!^{-2} g_c(J) \frac{\Gamma_c \Gamma_{c'}}{(E - E_\lambda)^2 + \Gamma^2/4} \tag{2.13}$$

that is exactly the well-known Breit-Wigner formula, describing the shape of isolated resonances. This expression actually holds only when $c \neq c'$.

In the case of $c = c'$, two additional terms have to be taken into account: one is the shape elastic scattering (see Section 2.3), the second is the interference between the shape elastic scattering and the resonant scattering, that produces a characteristic dip in the shape of the resonances in neutron elastic scattering cross sections (see Figure 2.1).

The SLBW approximation can be extended considering more independent levels, neglecting all the non-diagonal terms of the matrices described. This is referred to as *Multi-level Breit-Wigner* (*MLBW*) approximation.

In conclusion, the *Reich-Moore Approximation* has to be mentioned, as it is the one employed in the R-Matrix computer code *SAMMY* [68], extensively used for fitting resonance parameters in this work. This approximation is superior, but significantly more complicated than the SLBW. It basically assumes that single radiative channels, corresponding to each possible de-excitation path of the compound nucleus, can be "eliminated" and treated in average way simply considering a total radiative width (Γ_γ). This approximation is particularly powerful at low neutron energy where, once that the photon channels are "eliminated", only the neutron scattering channel is usually open and the R-Matrix again reduces to a number. The radiative capture cross section can be eventually retrieved as the difference between the total cross section σ_c (equation 2.4) and the cross sections of the non-photonic channels:

$$\sigma_{c\gamma} = \sigma_c - \sum_{c' \notin \, photons} \sigma_{cc'}. \tag{2.14}$$

More details can be found in the Appendix B.

2.2.4 Thermal cross section

It has already been mentioned that, if allowed, thermal cross sections of neutron-induced reactions generally exhibit a smooth behaviour varying the neutron energy. In particular, the elastic scattering cross section is approximately constant with neutron energy, while the radiative capture cross section depends on the inverse square root of the neutron energy $1/\sqrt{E_n}$. These behaviours can be now explained using the theory of resonances, described in this section. The theory of the R-Matrix will be used in this case, but the Hauser-Feshback theory (Appendix B would lead to the same results, using transmission coefficients.

In the R-Matrix theory, the neutron energy dependence of the neutron partial widths is given by the penetrability term (Equation 2.12). At thermal energies s-wave neutrons dominate, whose penetrability is proportional to the square root of the neutron energy $\sqrt{E_n}$. On the other hand, radiative (and fission) partial widths are approximately independent on the neutron energy, as in the resonance region this energy is usually negligible compared to the energy released by the reaction (Q-value).

Let's now consider the SLBW approximated formula for the cross section 2.13. At thermal energy, $E \ll E_\lambda$, hence the denominator can be considered independent on the neutron energy to a first approximation, as dominated by the constant term E_λ. On the other hand, $\lambda\!\!\!^{-2}$ is inversely proportional to the neutron energy $\sim 1/E_n$.

If one considers now the elastic scattering cross section, the energy dependence of the Γ_n^2 ($\propto E_n$) exactly neutralizes the energy dependence of $\lambda\!\!\!^{-2}$ ($\propto 1/E_n$). Therefore, the thermal elastic scattering cross section does not depend on the neutron energy. Moreover, the shape elastic scattering term (not reported for clarity in Equation 2.13) is also independent on the neutron energy in the thermal region, as it only depends on the nuclear channel squared radius a_c^2.

On the other hand, if one considers the neutron radiative capture cross section, the product $\Gamma_n\Gamma_\gamma$ at the numerator of Equation 2.13 is only proportional to the square root of the neutron energy ($\propto \sqrt{E_n}$). Therefore a dependence on $1/\sqrt{E_n}$ is maintained and exhibited by the radiative capture cross section. In other words, the neutron capture cross section at thermal energy can be seen as the sum of low-energy tails of the s-wave resonances.

However, if this theory can accurately reproduce the energy dependence, it usually fails to reproduce the value of the thermal neutron capture cross sections. To reproduce this value, nuclear evaluations usually arbitrarily adopt negative-energy resonances, that can represent real low-lying resonances or that can symbolically represent the contribution of direct capture, the topic of the next section.

Moreover, the presence of resonances close to the thermal region can sometimes alter the $1/v$ dependence of the thermal cross section. This deviation can be quantified by the so-called *Westcott factors* [85].

2.3 Direct Reactions

At the opposite extreme of compound nucleus reactions, which have been discussed so far, there exists another reaction mechanism that identifies the so-called *direct reactions*.

If in the compound nucleus mechanism the energy of the incoming neutron is distributed among all the nucleons of the target nucleus, in direct reactions the projectile interacts directly only with a portion of the nucleus or even with a single nucleon. This reaction mechanism competes with the compound-nucleus mechanisms in most of the reactions described in Section 2.1 and it typically becomes dominant at neutron energies above tens of MeV, when the neutron wavelength is comparable to the dimension of the nucleons.

Characteristic features of direct reactions are the angular anisotropy of their products (mostly usually peaked in the forward direction) and the time interval in which the reaction takess place, compatible with the average time needed by a nucleon to cross a nucleus ($\approx 10^{-22}$ s) and much shorter than compound-nucleus reactions.

Stripping reactions, *pickup reactions*, *knockout reactions*, *charge-exchange reactions* are some notable examples of direct reactions. In addition to them, there are two other peculiar examples that can be dominant at low neutron energy.

The first is the *shape elastic scattering*, that has been already mentioned in the previous sections. This reaction can somehow be considered a direct reactions as it does not involve the formation of a compound nucleus. On the other hand, it is completely different from other direct reactions, as it does not involve any reaction with the single nucleons, but it implies the elastic scattering of a projectile from the potential of the nucleus seen as a whole, just as in the interaction with a hard sphere. Its corresponding cross section, at low energy, can be indeed written as

$$\sigma_{sh.el.} = 4\pi a^2 \tag{2.15}$$

where a is defined *neutron scattering length*.

The second example, relevant for this work, is the direct neutron radiative capture.

2.3.1 Direct Radiative Capture

Direct Radiative Capture occurs when a neutron (or whatever projectile) impinging on a target nucleus A undergoes an electromagnetic transition directly to a final bound state of the $A + 1$ nucleus, without forming a compound-nucleus state [76, 88, 89]. The electromagnetic transition produces a γ ray that carries away the released energy.

The compound-nucleus mechanism is usually the dominant mechanism behind neutron radiative capture reactions. However, when the level density of the compound nucleus is not so high, the direct capture can also play a significant role. This situation typically occurs at thermal energy (far from the resonance region) and in the valleys between resonances, especially for light and/or particularly stable nuclei.

Even if the reaction mechanisms are completely different, the direct radiative capture is experimentally indistinguishable from compound-nucleus capture reactions. Moreover, especially when the neutron capture cross section is particularly small as in silicon and nickel, only the resonances can be observed in time-of-flight measurements, while the valleys between them (where direct capture dominates) are often masked by the background. For this reason, it is often necessary to theoretically estimate the direct capture component, which is smooth and non-resonant and it can provide a significant contribution to the total capture cross section.

The cross section for direct neutron capture ultimately depends on the electromagnetic operator $\hat{EM}$, the same one encountered when discussing the gamma de-excitation of compound nuclei in Section 2.2.2. As already mentioned, the operator can be expanded in terms of electric and magnetic multipoles, and typically only E1 (electric dipole) transitions dominate, followed by E2 and M1 transitions. For example, the direct capture cross section for the dominant E1 transitions can be written as [88]:

$$\sigma_{DC} = \frac{16\pi}{9\hbar} k_\gamma^3 \bar{e}^2 \sum_f \left| \langle \Psi_i | \hat{EM}_{(E1)} | \Psi_f \rangle \right|^2 \tag{2.16}$$

where k_γ is the wave number for the emitted photon and $\bar{e}$ is the neutron effective E1 charge. The electromagnetic operator is sandwiched between the "external" wave function of the initial state (Ψ_i), describing free neutron and target nucleus, and the "internal" wave function of the final state (Ψ_f), that describes the final bound state produced by the reaction. The sum runs over all the possible final bound state reachable with the transition. In a first approximation, the matrix element for each transition can be decomposed in three factors: a term related to the projection one on the other of the radial internal and external wave functions (similarly to what was discussed for the R-Matrix theory), an angular coupling term (including the selection rules) and a term depending on the nuclear spectroscopic factors, quantities that quantify how "likely" a particular nuclear state can be described as a core nucleus plus a single nucleon in a specific configuration.

In the end, in the case of direct capture of s-wave neutrons, one obtains a smooth cross section depending on the inverse square root of the neutron energy that, as already discussed, can complement the compound-nucleus capture cross section in the thermal region. Given a measurement of the thermal capture cross section and the radiative widths of s-wave resonances of an isotope, the thermal region can be eventually used to constrain and evaluate the contribution of direct capture.

At higher neutron energy, direct capture of neutrons in partial waves of higher order (p or d wave) may dominate over direct capture in s-wave. These terms can originate broad bumps in the capture cross section, that are clearly observable in some elements like oxygen at neutron energies between several keV and several MeV.

2.4 Measurement of neutron cross sections

From a general point of view, the measurement of neutron-induced reaction cross sections of a particular isotope is performed irradiating a sample containing the isotope with a known neutron flux and counting the number of reactions of interest that occur. The ratio between the number of neutrons undergoing the reaction N_r and the total number of neutrons impinging on the sample N_n is defined as the *reaction yield* Y_r. If one introduces the detection efficiency ϵ to relate the real number of reactions in the sample and the number of experimentally detected reactions $N_{r,\ exp}$, this reaction yield can be written as:

$$Y_r = \frac{N_r}{N_n} = \frac{N_{r,\ exp}}{\epsilon\, N_n}. \tag{2.17}$$

The reaction cross section σ_r is eventually extracted from inverting the formula:

$$Y_r = (1 - e^{-n\sigma_t})\frac{\sigma_r}{\sigma_T} \; \approx \; n\,\sigma_r \tag{2.18}$$

where σ_T is the total neutron cross section of the isotope and n is the areal density of the isotope in the sample. The term $(1 - e^{-n\sigma_t})$ is the so-called *self-shielding* correction, that accounts for the variation of the neutron flux along the sample due to the absorption of neutrons in the first encountered layers of the sample. In the case of thin samples ($n\sigma_t \ll 1$), this effect can be neglected and the approximation reported in Equation 2.18 can be used.

Details on the experimental determination of the neutron flux impinging on a sample and on the determination of the efficiency will be treated in detail, in the specific case of this work, in chapters 4 and 5, dedicated to data analysis. For the moment, different experimental techniques to count the number of reactions occurring in a sample will be generally introduced in relation to the kind of reaction under study.

The first technique is *neutron transmission*. Transmission experiments measure the attenuation of a neutron beam after crossing a sample to quantify the number of neutrons that reacted in the sample. This technique is typically coupled with the time-of-flight technique to provide neutron total cross sections as a function of the neutron energy. However, as this technique is not sensitive to the kind of reaction that occur in the sample, it cannot be used to measure the partial cross sections of specific neutron-induced reactions.

In these cases, one has to rely on the detection of the specific products of the reaction under study. In general, two different techniques can be used for this purpose: the activation technique and the time-of-flight technique.

The *activation technique* is based on the fact that neutron-induced reactions can produce unstable nuclei, that can be counted by measuring their decay products in order to retrieve the number of reactions that occurred in a sample. Neutron activation measurements consist indeed of two steps. First, a sample is irradiated in a well-characterized neutron beam, where the reaction of interest produces a well defined unstable nucleus. Then, the sample is transferred to a decay station where the number of these unstable nuclei is measured, detecting the γ rays or the electrons from their decay. Using high energy resolution detectors, like HPGe detectors, it is possible to select only the specific γ rays from the decay of the nucleus of interest. For this reason, distinctive features of the activation technique are the high selectivity and the high sensitivity, meaning that it is possible to perform measurements even with non isotopically enriched and small-mass samples.

On the other hand, this technique suffers from some important drawbacks. First of all, it is only applicable to reactions that produce unstable nuclei with a lifetime neither too short, to allow the measurement of their activity after irradiation, nor too long, to have enough activity to be measured. Moreover, this technique does not allow one to scan the energy dependence of cross sections with high resolution and to resolve resonances, as mono-energetic neutron beams are usually not available at arbitrary and arbitrarily close energy.

However, if the energy spectrum of the neutron beam is Maxwellian, activation measurements can directly provide the MACS, that is advantageous especially for astrophysical applications. For instance, the ^{7}Li(p,n) reaction with protons accelerated just above the reaction threshold can produce a quasi-Maxwellian neutron spectrum with an average energy of about 25 keV, that has been extensively used in the measurement of MACS for astrophysics at the Karlsruhe Van de Graaph accelerator. Most of the activation measurements for silicon and nickel that will be quoted from the literature have been performed there. The ^{3}H(p,n) reaction can also be used to produce quasi-Maxwellian neutron spectra at 52 keV.

However, energy differential neutron-induced reaction cross sections are required to determine or extrapolate MACS at different energies and to correct for deviations of the real neutron spectrum from a perfect Maxwellian one.

The *time-of-flight technique* is the only technique capable of measuring neutron-induced reaction cross sections as a function of energy and resonance parameters. This technique employs pulsed neutron beams, so that the time-of-flight of neutrons can be correlated with their kinetic energy. This experimental method requires the prompt detection of the products of the reaction under study, during the irradiation. Example of common detected particles are fission fragments (to study fission reactions), light charged particles, neutrons (elastic scattering) or γ rays (radiative capture or inelastic scattering). This technique, employed in this work, will be treated in detail in Section 3.2.

2.4.1 Experimental characterization of resonances

The experimental characterization of a resonance requires the extraction of its parameters, expressed in the R-Matrix theory: energy (E_R), total width (Γ), partial widths (Γ_n, Γ_γ, ...), spin-parity (J^π).

An observable that is particularly useful for the characterization of a resonance is its area. The area of a resonance is related to the number of neutrons reacting and it is independent on experimental effects like the energy resolution. Moreover, the area of a resonance as observed in different neutron-induced reactions can provide information on the resonance parameters. In fact, considering only the resonant part of the SLBW approximation and neglecting the Doppler broadening (see later), the area of a resonance measured in the total, capture and elastic scattering yield can be written respectively as:

$$A_{(n,tot)}(thin) = 2n\pi^2\lambdabar_R^2 g\Gamma_n \tag{2.19a}$$

$$A_{(n,tot)}(thick) = 2\pi\lambdabar_R^2\sqrt{ng\Gamma_n\Gamma} \tag{2.19b}$$

$$A_{(n,\gamma)}(thin) = 2n\pi^2\lambdabar_R^2 g\frac{\Gamma_n\Gamma_\gamma}{\Gamma} \tag{2.19c}$$

$$A_{(n,n)}(thin) = 2n\pi^2\lambdabar_R^2 g\frac{\Gamma_n^2}{\Gamma} \tag{2.19d}$$

where n is the areal density of the sample, λ_R is the reduced wave function of the system at the energy of the resonance, g is the usual spin statistical factor. Thin and thick samples refer to the case where $n\sigma_{tot} \ll 1$ and $n\sigma_{tot} \gg 1$, respectively.

As can be observed in the formulae above, a single measurement is not sufficient to extract all the parameters of a resonance. Concerning the determination of the spin-parity, transmission measurements can sometimes provide some information based on the shape of the resonance [66]. Concerning the widths of resonances, combined transmission and capture measurements are typically needed to provide a complete characterization. In general, a single capture measurement, like this work, can provide only the capture kernel of a resonance k, defined as:

$$k = g\frac{\Gamma_n\Gamma_\gamma}{\Gamma} \tag{2.20}$$

This is the only parameter that can be extracted even in cases where the experimental energy resolution is worse than the natural width of a resonance, that therefore assumes the shape of the resolution function at the corresponding energy.

Nowadays, the most common technique to extract the resonance parameters is the *Resonance Shape Analysis*, based on the fit of the shape of resonances in reaction or transmission yields. The fit is typically performed with dedicated R-Matrix codes, like SAMMY [68] or REFIT [90]. This technique is more precise than the simple area analysis, especially because it enables to include different experimental effects that affect the shape of the resonances, usually different from the expected theoretical shape of Equation 2.13, as shown in Figure 2.4. These effects are:

- The *Doppler Broadening*, that is related to the thermal motion of the nuclei in the sample. In fact, depending on thermal energy of the target nucleus, the energy of the impinging neutrons needed to excite a particular state of the compound nucleus slightly varies, producing a broadening of the resonance. Different models can be used to implement this effect and an example is the *Fermi Gas Model* [91]. This model assumes that the target nuclei have the same velocity distribution of the atoms of an ideal gas. The Doppler-broadened cross section can be therefore expressed as:

$$\sigma_D(E) = \frac{1}{\Delta\sqrt{\pi}}\int_{-\infty}^{+\infty}\sigma(E')\sqrt{\frac{E'}{E}}e^{-\left(\frac{E'-E}{\Delta}\right)^2}dE' \tag{2.21}$$

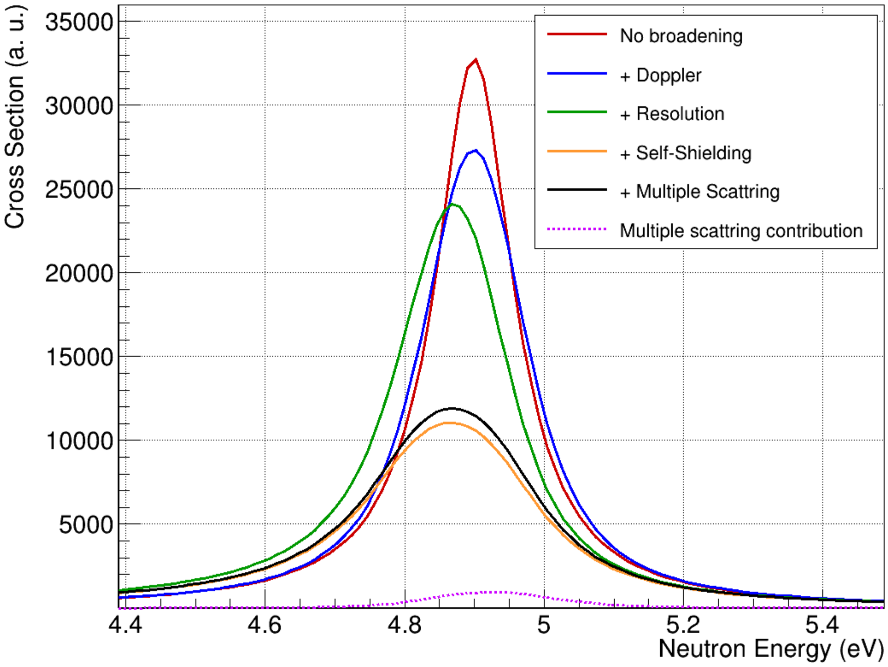

Figure 2.4: Experimental broadening and shifting effects on the shape of a resonance. The theoretical shape of the resonance is shown in red, while the other solid lines represent the effective shape after progressively adding experimental effects. See text for details. The dashed line represents the contribution of the multiple scattering, enhancing the high energy tail of resonances in capture cross section.

that is nothing but the Gaussian broadening of the cross section with a standard deviation Δ (called *Doppler Width*)

$$\Delta = \sqrt{\frac{4Ek_BT}{M}m_n} \tag{2.22}$$

where E is the resonance energy, T is the temperature, k is the Boltzmann constant, M and m_n are the mass of the target nucleus and the neutron, respectively.

- The *Energy Resolution*, that is related to the fact that, in the time-of-flight technique, neutrons of the same energy do not actually impact on a sample at the same moment, but they are spread in a time range due to the stochastic time interval spent in the spallation target and in the moderator assembly. For this reason, the resonances are broadened by the same time-of-flight range. Moreover, the effective flight-path in the target-moderator assembly can also produce a shift in the resonance energy. These issue will be described more in detail in the next chapter.

- The *Self Shielding* effect, that has been already mentioned, is related to the absorption of the neutrons in the first encountered layers of a sample. In the case of thick samples, neutron can be completely absorbed resulting in *saturated resonances*, characterized by an almost flat top.

- The *Multiple Scattering*, that typically only concerns neutron-capture data. In fact, neutrons can be scattered one or several times in a sample (especially a thick sample) before being captured. This effect enhances the capture yield in the high energy tail of resonances, where faster neutrons losing energy in the scattering process end up with an energy that matches the energy of the resonance and then are efficiently captured.

Chapter 3

The measurements at the n_TOF facility

The previous chapters introduced the astrophysical motivations behind the measurements of ^{30}Si(n,γ) and ^{64}Ni(n,γ) cross sections and the general characteristics of neutron-induced cross sections that one typically wants to measure, including the underlying theory, the parametrization and an introduction of some experimental techniques. The next chapters will instead focus on the detailed description of the measurements of the ^{30}Si(n,γ) and the ^{64}Ni(n,γ) cross sections as performed in this work. In particular, this chapter will describe the experimental setups and techniques used.

The measurements of the ^{30}Si(n,γ) and the ^{64}Ni(n,γ) cross sections have been performed at the n_TOF facility, that will be described in Section 3.1. The Time-of-Flight technique coupled with the Total Energy Detection technique has been used to extract the cross sections as a function of the neutron energy. They will be discussed in Sections 3.2 and 3.3, respectively. The last Section 3.4 will present in details the experimental setups, including the detectors and the samples employed in this work.

3.1 The n_TOF facility

The n_TOF facility (acronym of *neutron Time-Of-Flight*) is a pulsed white neutron spallation source, part of the fixed target experimental program at CERN [92]. The facility was conceived by C. Rubbia in 1998 [93] in order to provide accurate measurements of neutron-induced reaction cross sections in a wide energy range, useful for basic nuclear sciences, nuclear astrophysics and advanced nuclear technologies. It has been in operation since 2001.

A layout of the n_TOF facility is shown in Figure 3.1. Protons of 20 GeV/c momentum accelerated by the CERN Proton Synchrotron (PS) are fast-extracted and delivered to a lead target, where neutrons are produced by spallation. Neutrons are moderated and collimated towards two experimental areas designed for time-of-flight measurements: EAR1, at approximately 185 m from the target, and EAR2, at approximately 18 m from the target. An additional experimental area for activation measurements (NEAR) is available at only 3 m from the target. The high intensity and the small time length (down to

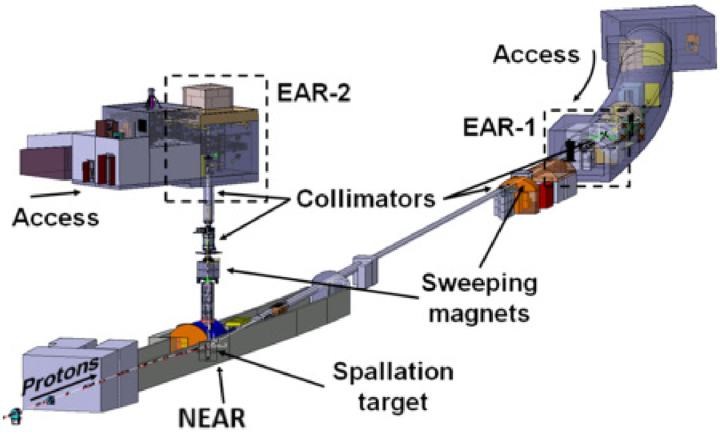

Figure 3.1: Layout of the n_TOF facility showing the spallation target, the three experimental areas (EAR1, EAR2, NEAR) and the main elements of the beam lines. Protons delivered to the target come from the CERN PS. Figure adapted from [94].

7 ns) of the proton bunches delivered on the target, their low repetition rate (1.2 s) and their high energy determine a unique combination of high instantaneous neutron flux, extremely wide neutron energy range and high energy resolution that has made n_TOF a cutting-edge facility for the measurement of neutron cross sections worldwide.

3.1.1 Spallation target

Spallation targets at the n_TOF facility are typically designed to guarantee 10 years of operations. Since 2021, the facility has been running with its third-generation spallation target [95, 96], characterized by a revolutionary design with respect to previous targets.

The target, shown in Figure 3.2, consists of six slices of pure lead (purity higher than 99.9%) hosted in an aluminium-alloy anti-creeping structure and cooled by a forced flow of gaseous nitrogen in between. The slices are 5 cm thick (except for the last slice that is 15 cm), 60 cm wide and are characterized by a flat-top geometry, optimized for EAR2. The choice of pure lead, unchanged since the first-generation target, is due to its superior physics performances in terms of number of neutrons released and reduced photon background (because of the low neutron capture cross section). However, lead is not a good structural material as it characterized by easy occurrence of creeping effects, a relatively low melting point and low corrosion resistance (see Appendix A). Hence, an anti-creeping structure and a powerful cooling system are needed. Nitrogen cooling has been employed starting from this third-generation target. It should limit the corrosion effects observed with water cooling, but it required slicing of the target because of its lower cooling efficiency.

High energy protons impinging on lead nuclei induce spallation reactions (already mentioned in the previous chapter) that release high energy particles, eventually triggering an inter-nuclear hadronic cascade in the target. This cascade releases several kinds of particles, including neutrons and γ rays.

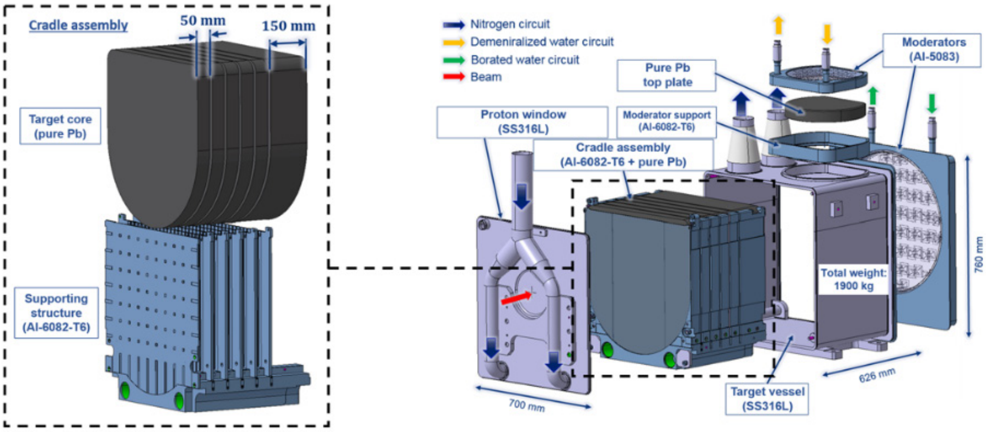

Figure 3.2: Exploded view of the n_TOF third generation spallation target. On the right the whole target assembly including the vessel and the moderators, on the left the cradle assembly enlarged [95].

γ rays immediately produced by the impact of the proton beam on the target (coming for example from pion decay or from prompt de-excitation of nuclei) make up the so-called γ-*flash*. The γ-*flash* is the prompt and intense burst of γ rays and ultra-relativistic charged particles produced in the hadronic cascade that, travelling at the speed of light, first reach the experimental areas after a spallation event. It is important for at least two reasons. On one side it is typically used to constrain the time-zero in the time-of-flight technique. On the other side, it is so intense that can saturate the detectors, limiting their performances at high neutron energy. Other γ rays are typically produced by neutron-induced reactions in the target-moderator assembly. Their production is delayed with respect to prompt flash described above, therefore they reach the experimental areas together with neutrons and they are referred to as *in-beam* γ *rays*.

Concerning neutrons, approximately 300 neutrons are ejected per each 20 GeV/c proton impinging on the target. High energy neutrons (above tens of MeV) are ejected, mainly in the forward direction, by direct reactions occurring in the first step of the spallation reactions. The majority of neutrons are ejected in the evaporation of the excited nuclei, isotropically and with an energy spectrum peaked in the MeV region.

In order to widen the energy spectrum of neutrons, two independent moderator circuits are installed on the target faces looking to the experimental areas. For EAR2, water is used as moderator. For EAR1, borated water (1.28 wt% ^{10}B) is employed to reduce the magnitude of the 2.2 MeV photon background caused by neutron capture in hydrogen, that can heavily affect capture measurements in the energy range of astrophysical interest.

3.1.2 Experimental areas

Dedicated beamlines drive neutrons exiting from the target-moderator assembly up to the two Experimental AReas (EAR1 and EAR2). Each beamline is equipped with:

- a SmCo permanent magnet, that deflects out of beam charged particles produced in spallation, preventing them from reaching the experimental areas
- a filter box, containing filters of different materials that can be remotely moved in beam to completely absorb γ-rays or neutrons of certain energy. They are typically used for background studies.
- two collimators to shape the neutron beam. Two downstream collimators with different apertures are available and they can be exchanged according to the experimental needs: fission measurements usually require the big-aperture collimator, while other measurements the small-aperture one. The small collimators, employed in this work, have an inner aperture of 18 mm and 21.8 mm in EAR1 and EAR2, respectively.

EAR1 [97, 98] is located underground at approximately 185 m from the spallation target in a direction that forms 10° with respect to the impinging proton beam. This angle was chosen to limit the forward background of prompt photons and relativistic charged particles reaching the area. Because of the extremely long distance from the target, EAR1 is characterized by an excellent energy resolution, down to 10^{-3} < ΔE/E < 10^{-4} in the energy region of resonances. For this reason, this area is particularly suitable for high resolution measurements of reaction cross sections on stable or long-lived ($t_{1/2}$ > 100 y) radioactive isotopes.

EAR2 [99] was built in 2014 at the ground level, in the direction perpendicular to the neutron beam at approximately 18.2 m from the spallation target. Because of this shorter distance, EAR2 has a slightly worse energy resolution, even if still remarkable, between $10^{-2} < \Delta E/E < 10^{-3}$. However, it is characterized by a neutron flux about 40 times larger than that in EAR1. This feature is particularly suitable for the measurement of small cross sections or measurements on small mass samples (sub-mg) and radioactive samples with half-lives as short as a few months, whose radioactivity would completely cover the signal in EAR1.

Both EAR1 and EAR2 are classified as *class A laboratories*, meaning that they are characterized by a series of enhanced safety and monitoring systems that allow the handling of unsealed radioactive samples.

Eventually, the last and most recent experimental area is *NEAR* [100, 101], that started its operations in 2021. It is located in the target area at only 3 meters from the spallation target, to which is connected just by a hole in the shielding wall. Due to the proximity of the target, NEAR is characterized by an extremely high neutron flux, of approximately 10^9 neutrons/bunch, which is suitable for low-mass sample irradiation and neutron activation measurements. Current activities in NEAR consist of benchmarking the feasibility of measuring MACS at different temperatures shaping the neutron spectrum to quasi-Maxwellian spectra using B_4C filters [102]. Irradiations of detectors and electronics for degradation studies are also performed.

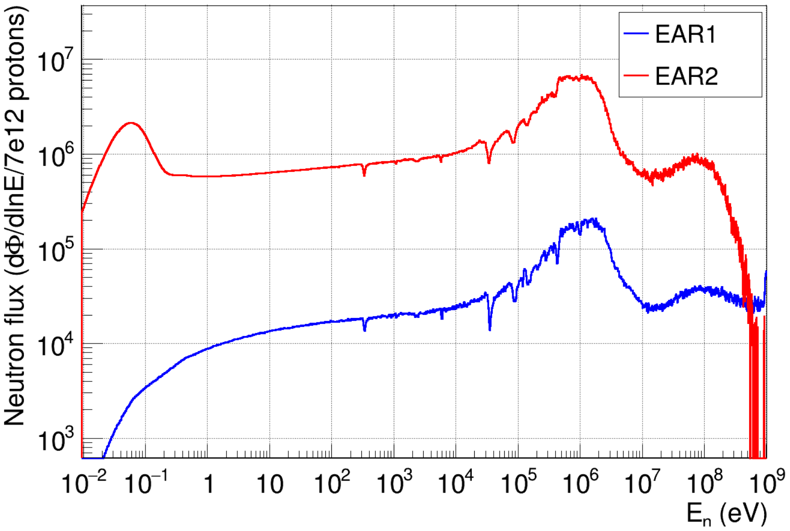

Figure 3.3: Evaluated neutron flux in EAR1 and EAR2 at 100 bins per decade, resulting from the average of the experimental data obtained with different detectors during the commissioning of the new target. The flux is reported in isolethargic units and normalized to 7×10^{12} protons on target.

3.1.3 Neutron beams

The accurate characterization of the neutron beams reaching the experimental areas is of paramount importance to measure reaction cross sections. For this reason, a beam monitor suitable for the energy range of interest is always installed during experiments. However, in order to fully characterize the neutron beams in terms of neutron flux, spatial profile and resolution function a commissioning of both the experimental areas (EAR1 and EAR2) was performed after the installation of the new target, in 2021 [103, 104].

During this commissioning, the neutron flux as a function of the neutron kinetic energy was measured over the full available energy range, using several detectors sensitive to neutrons of different energies. Activation measurements were also performed to complement and cross-check time-of-flight data. Experimental results were additionally compared with Monte Carlo simulations performed in FLUKA [105, 106].

Figure 3.3 shows the evaluated neutron flux, resulting from the average of the different measurements. The flux in EAR1 covers the full energy range from tens of meV to GeV, even if the thermal flux is strongly suppressed by boron in the moderation circuit. The neutron flux in EAR2 [104] is more than one order of magnitude larger and includes the peak of thermal neutrons, but high energy neutrons (above a few hundreds MeV) are suppressed by the forward-boosted kinematics of spallation in the target. The dips in the flux of both areas correspond to the resonances of materials in-beam that absorb neutrons (like aluminium). The integrated neutron fluxes are approximately 8.5×10^5 and 3.3×10^7 neutrons per 7×10^{12} protons on target in EAR1 and EAR2, respectively. At 100 bins per decade, the total uncertainty in the neutron flux is generally between 2% - 3% up to

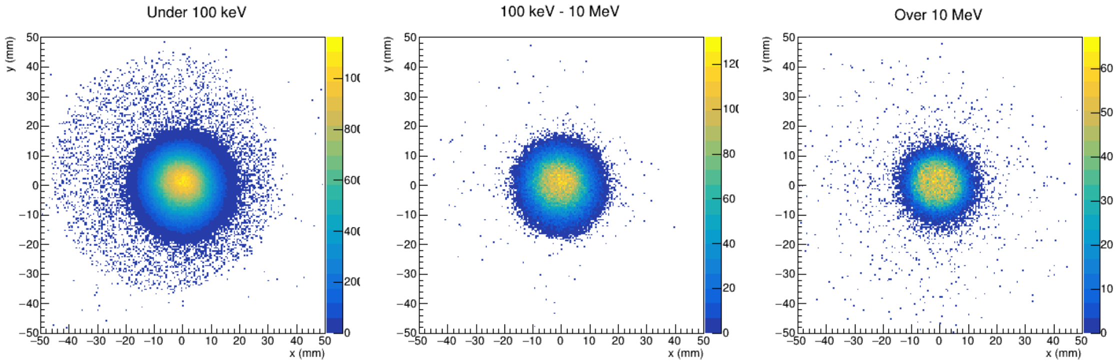

Figure 3.4: Neutron beam spatial profile of EAR1, measured with a fission chamber based on Parallel Plate Avalanche Counters (PPAC) in different neutron energy ranges.

a few hundreds keV, while increases gradually up to approximately 8% at hundreds MeV.

The spatial profile is another important characteristic of the neutron beam. Its knowledge is crucial in positioning samples with diameter smaller than the neutron beam, in order to ensure they intercept the maximum number of neutrons. Moreover, the variation of the neutron beam profile with the neutron energy requires corrections of the beam interception factor of small samples that can importantly affect the final extracted cross sections. The spatial beam profile in EAR1 and EAR2 was also measured as a function of the neutron energy during the commissioning of the new target. A fission chamber based on Parallel Plate Avalanche Counters and sensitive to the impact position of neutrons was employed.

Figure 3.4 shows the profile of the neutron beam in EAR1 at different neutron energies. Over the full energy range, the neutron beam has a FWHM of approximately 15 mm in the typical measuring position with the capture collimator. The beam becomes slightly more focused increasing the neutron energy above hundreds keV. As a consequence, the beam interception factor of a 20 mm diameter sample placed in the centre of the beam is pretty constant between the eV and a few hundreds keV, while it drastically increases (by approximately 20%) at higher energies. On the contrary, below the eV the beam interception factor decreases by several percent due to the effect of gravity on flying neutrons.

The beam profile in EAR2 is shown in the left images of Figure 3.5. Due to the shorter distance to the spallation target, the dimension of the beam in EAR2 is strongly dependent on the position. Around the typical measuring position the beam FWHM is approximately 25 mm, over the full energy range. Increasing the neutron energy above some MeV, the beam profile gets elongated towards the direction of the incoming proton beam due to a kinematic effect, as shown in the central image of Figure 3.5. Eventually, the right image of Figure 3.5 shows the beam interception factor of samples of different diameter placed at the centre of the neutron beam in the energy range of interest in this work. Corrections of up to 7% have to be applied to consider the variation of the beam

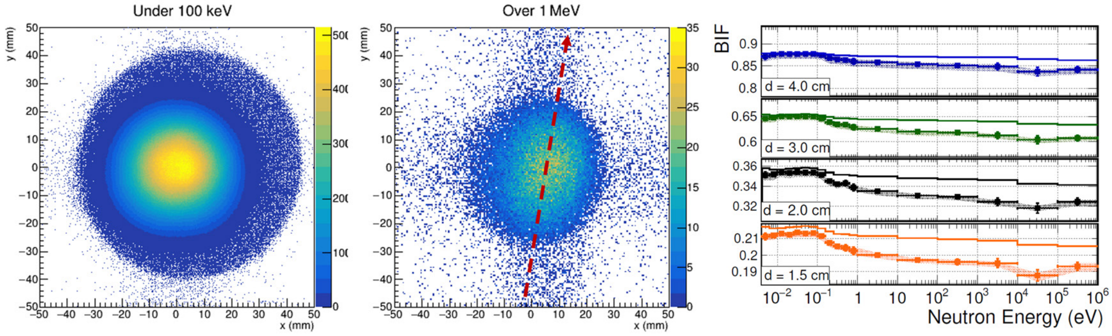

Figure 3.5: *Left and centre*: neutron beam spatial profile of EAR2, measured with a fission chamber based on Parallel Plate Avalanche Counters (PPAC) in two different energy ranges. At high neutron energy the beam profile gets elongated in the direction of the proton beam impinging on the spallation target. *Right*: beam interception factor as a function of the neutron energy for samples of different diameters placed at the centre of the beam. Experimental points are calculated from PPAC experimental data, while the solid line is obtained from FLUKA simulation. Figure from [104].

interception factor with respect to the value where capture cross section measurements are typically normalized (around the eV).

The neutron beam profile is usually checked using TimePix Silicon detectors after changes of the collimator, mainly to ensure the stability of the position of the centroid of the beam.

Even if not concerned in this work, just a few words about the NEAR station. The characterization of the neutron beam was performed in a completely different way. The neutron flux was indeed simulated with Monte Carlo simulations and experimentally validated using the Multi-Foil Activation technique, which consists in the simultaneous activation of different samples exploiting neutron-induced reactions sensitive to different energies [107]. A direct measurement of the neutron flux as a function of the neutron energy (only feasible at epithermal energy) and of the beam profile was also performed, using diamond detectors [108].

3.1.4 Proton beam monitors

Monitoring the proton beam impinging on the spallation target is another important point during experimental campaigns and it is required in order to check the stability of the beam, to determine the number of neutron actually arriving in the experimental areas and to guarantee the safe operation of the spallation target.

The CERN Proton Synchrotron typically delivers to n_TOF dedicated proton bunches and parasitic proton bunches (extracted from bunches dedicated to other CERN's experimental areas). The bunch intensity can currently vary from 50×10^{10} protons to 850×10^{10} protons, while in the past it was limited to 700×10^{10} protons. The beam configuration for the measurements in this work has consisted of dedicated bunches of 850×10^{10} protons and parasitic bunches of 350×10^{10} protons, required to check possible pile-up and dead time corrections. The minimum repetition rate, corresponding to the PS cycle, is 0.8 Hz. However, this repetition rate is usually limited by the maximum power that the target can safely sustain, without risking damages.

This is one reason why it is important to monitor the proton intensity. The other reason is to determine the total number of neutrons reaching the experimental areas, whose flux indeed scales with the proton bunch intensity. Two detectors are employed to monitor the proton intensity before the spallation target: a *Beam Current Transformer* (*BCT*) and a *Wall Current Monitor*.

The former consists of a toroidal magnetic core surrounding the beam. When a proton bunch passes through, it induces by electromagnetic induction a current in a secondary circuit connected to the magnetic core, whose intensity is proportional to the proton beam intensity.

The *Wall Current Monitor* is also based on the electromagnetic induction, but in this case the voltage induced on the walls of the pipe by the passage of the beam is measured. The area of the signal is also related to the beam intensity. Moreover, as this detector is placed just before the spallation target, the time of the signal from the Wall Current Monitor can be used to identify the moment when protons impinge on the target (the time-zero for the time-of-flight technique).

In addition to the proton intensity, the spatial profile of the proton beam is also monitored to guarantee the stability of the neutron beam and to avoid too peaked proton spatial distributions. In fact, protons should ideally impact always at the same position on the target to have the same neutron flux, while too peaked proton spatial distributions release more concentrated power that can damage the target at the impact point (see also Appendix A). A *Secondary Emission Monitor Grid* (*SEM Grid*) is used for this purpose. It consists of a system of thin wires that intercept the proton beam, giving information about its position and its spatial distribution.

3.1.5 Data Acquisition System

The n_TOF data acquisition system [109] is common to all the measurements performed at the facility. It digitalizes the analog signals from the detectors through flash analog-to-digital units and saves the digital data in the *CERN Tape Archive* (*CTA*) for their long-term archival storage.

Its architecture consists of several independent DAQ units equipped with a host controller, up to six Data Acquisition Cards (DAC) and a high writing speed local storage, able to potentially handle data rates of the order of GB/s and to guarantee a data buffer of approximately 20 TB.

The DACs are SP Devices ADQ412DC and ADQ14DC-4C modules. The former provides 4 acquisition channels with 12-bit resolution and a maximum sampling rate of 1.8 GHz, while the latter provides 4 acquisition channels with 14-bit resolution, but a maximum sampling frequency of only 1 GHz. A common clock is provided to all the cards by an external device, with a frequency of 10 MHz ± 10 ppm. A single common trigger is also provided to all the cards by an external time machine, that can either receive the trigger from the Proton Synchrotron when proton bunches are delivered to n_TOF or generate an internal trigger that can be used for detector calibration or beam-off data acquisition. The frequency of the triggers is up to 0.8 Hz when taking data with beam (it corresponds to PS cycle), while it can be set by the user up to 2 Hz in case of calibration triggers. The time acquisition window is typically set to 100 ms in EAR1 and 20 ms in EAR2, in order to include thermal neutrons.

After each acquisition, the digitalized data samples are written to the memory of the DAQ unit (providing a data buffer of approximately 20 TB) and collected by the Experimental Area Coordination System (EACS), a control machine available in each experimental area. This machine collects the digitalized raw signals from all the DAQ units available in the experimental area, applies the zero suppression and finally merges the zero-suppressed waveforms from all the channels into a single merged waveform per trigger, that is saved in the output file. The output raw data files contain waveforms from a maximum of 20 triggers and can be up to 4.2 GB in size. These files are finally transferred to the CERN EOS (EOS Open Storage) disk storage for immediate reading and processing (see Section 4.1) and to the CTA (CERN Tape Archive) for long-term data preservation. Only at this stage, the data are purged from the local machine.

In the measurements described in this work, raw data output files are typically between a few tens and a few hundreds of MB in size, depending on the sample, corresponding to a data rate up to a few MB/s.

3.2 The Time-Of-Flight technique

As anticipated in Section 2.4, the *Time-Of-Flight technique* is an experimental technique that allows the measurement of reaction cross sections as a function of the neutron kinetic energy. The energy of an interacting neutron can be indeed calculated from the time T the neutron takes to travel a known distance L at a constant speed as:

$$E = mc^2\left(\frac{1}{\sqrt{1-(L/(cT))^2}} - 1\right) \tag{3.1}$$

where m is the neutron mass and c is the speed of light. This technique requires a white pulsed neutron beam.

In this work (and at n_TOF in general), the flight-path L corresponds to the distance between the face of the target-moderator assembly and the sample where neutrons interact in the experimental areas. Along this distance, neutrons move at a constant speed. The corresponding time-of-flight T can be estimated as [110]:

$$T = t - t_0 - t_m \tag{3.2}$$

where:

- t is the time at which a neutron reaches and interacts with the sample in the experimental area. It corresponds to the time at which the neutron-induced reaction is detected.

- t_0 is the start-time that corresponds to the moment when neutrons are produced in the spallation target. It is given by the time of the Wall Current Monitor signal, corrected for the offset produced by the different lengths of signal cables. Alternatively, it can be calculated from the time when the γ-flash arrives in the experimental areas, since it travels the same flight-path at the speed of light.

- t_m is the time the neutron spends in the target-moderator assembly. During this time, the neutron stochastically undergo scattering reactions and moderation. As a consequence, its energy is not constant, it does not follow a linear measurable path and t_m is not a deterministic constant time, but it is distributed according to a probability distribution. This term can only be estimated with Monte Carlo simulations and it is the reason why a *resolution function* has to be introduced (see next subsection).

The energy resolution that can be reached with the time-of-flight technique can be expressed from Equation 3.1 as:

$$\frac{\Delta E}{E} = \gamma(\gamma + 1)\sqrt{\left(\frac{\Delta L}{L}\right)^2 + \left(\frac{\Delta T}{T}\right)^2} \tag{3.3}$$

where $\gamma = 1/\sqrt{1 - (L/(cT))^2}$ is the relativistic factor. From this equation it is clear that long flight-paths, like in EAR1, are useful to increase the energy resolution, as neutrons of different energies get more separated in time. Concerning the uncertainties, the main limitation to the energy resolution is the uncertainty on the time-of-flight ΔT. This term is generally dominated by the spread in the distribution of t_m, described by the resolution function. However, at high neutron energy the time length of the proton bunch also plays an important role and for this reason it should be kept as small as possible.

3.2.1 The resolution function

Neutrons of the same energy do not arrive in the experimental areas at the same time because of the different stochastic time t_m they spend in the target-moderator assembly. The *resolution function* describes indeed the probability distribution of this stochastic moderation time t_m at different neutron energies E_n [111]. Using the conservation of the probability, the resolution function is typically expressed in terms of an *effective moderation length* $\lambda = vt_m$, that be thought as the length travelled by the neutron at its final speed v in the time t_m. This effective moderation length can be added to the flight-path L, instead of subtracting the moderation time t_m in Equation 3.2. In this case,

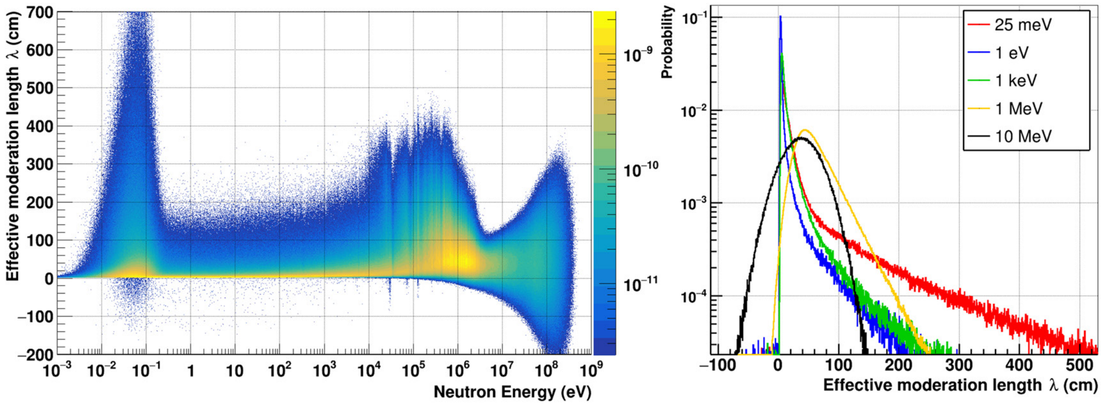

Figure 3.6: *Left*: Resolution function of EAR2 obtained from Monte Carlo simulation of the target. Distributions of the effective moderation length λ are represented in different neutron energy ranges in a full 2D plot. *Right*: Projection of the resolution function for some specific neutron energies.

Equation 3.1 can be rewritten as:

$$E = mc^2 \left(\frac{1}{\sqrt{1 - \left(\frac{L+\lambda(E)}{c(t-t_0)} \right)^2}} - 1 \right). \tag{3.4}$$

The resolution function is determined via dedicated Monte Carlo simulations of the target-moderator assembly, that are experimentally validated by comparing the measured and predicted shapes of some well-known resonances at different neutron energies. Figure 3.6 shows the resolution function expressed in terms of λ for EAR2. The Figure clearly shows that the resolution function has typically a strongly asymmetric shape, that cannot be easily parametrized. For this reason, the full simulated distribution is often used for data analysis. In particular, the central values of the distributions (mean or most probable value) are crucial to obtain a reliable time-to-energy conversion while the spread of the distribution is fundamental to determine the energy resolution and the broadening of resonances.

3.3 The Total Energy Detection technique

The time-of-flight measurement of radiative neutron capture cross sections requires the detection of the γ rays promptly released by the reaction. Two different experimental techniques are available: one is based on *Total Absorption Calorimeters* (*TAC*), the other is based on *Total Energy Detectors* (*TED*).

The TAC-based technique requires the detection of the full γ cascade produced by a neutron capture event, typically employing high-efficiency 4π segmented calorimeters. At n_TOF, an almost-4π calorimeter made of 40 crystals of BaF_2 is available in EAR1 for this purpose [112]. This technique is particularly advantageous as it ideally records the total energy released by the reaction, that can be used to discriminate neutron capture events from the background.

However, the amount of material placed close to the beam required for an efficient 4π system increases the sensitivity to scattered neutrons, limiting the application of this technique when dealing with samples characterized by a high scattering-to-capture cross section ratio. Moreover, these detectors are quite sensitive to the γ-flash and are typically characterized by slow signals (FWHM around the μs), that prevent the measurement of capture cross section above tens of keV in EAR1.

Since both ^{64}Ni and ^{30}Si show elastic cross sections much larger than the capture cross section and the energy range of astrophysical interest of their (n,γ) cross sections potentially extends to hundreds keV, the *Total Energy Detection* technique has been used in this work [113, 114]. This technique requires two conditions:

a) The efficiency to detect a γ-ray ϵ_γ is small, to safely assume that only one γ-ray per cascade is detected at maximum

$$\epsilon_\gamma \ll 1$$

b) The efficiency to detect a γ-ray ϵ_γ is proportional to the energy of the γ-ray E_γ

$$\epsilon_\gamma = \alpha E_\gamma$$

In general, the efficiency for detecting a capture event ϵ_c can be written as the complementary probability of not detecting any γ ray from the de-excitation cascade as:

$$\epsilon_c = 1 - \prod_{i=1}^{N}(1 - \epsilon_{\gamma,\,i}) \tag{3.5}$$

where N is the multiplicity of the cascade and i refers to the single γ rays. If the efficiency for detecting a γ-ray is not close to one (as in the TAC-based technique), the efficiency for detecting a capture event depends on the multiplicity and on the energy of the single γ rays of the cascade. In other words, it depends on the particular de-excitation path followed by the compound nucleus, that is random and cannot be experimentally reconstructed with a typical capture setup. This experimental condition is therefore prohibitive for measuring neutron capture cross sections.

However, assuming the conditions required by the Total Energy Detection technique, Equation (3.5) can be simplified to

$$\epsilon_c \approx \sum_{i=1}^{N} \epsilon_{\gamma,\,i} \tag{3.6}$$

using condition ***a*)** and finally to

$$\epsilon_c \approx \alpha \sum_{i=1}^{N} E_{\gamma,\, i} = \alpha E_c \tag{3.7}$$

using condition ***b*)**. In the end, the Total Energy Detection technique is based on the fact that the efficiency for detecting a capture event does not depend on the random de-excitation path of the compound nucleus, but only depends on the total energy released by the reaction, that is well-defined for each reaction at a particular neutron energy (Equation 2.7).

From a practical point of view, the low-efficiency condition (condition ***a***)) can be easily accomplished by using suitable geometries and/or detectors made of small volumes of low-Z materials. On the other side, the proportionality condition (condition ***a***)) is more tricky to achieve. The first attempts date back to the early sixties, when M. Moxon and E. Rae first applied the Total Energy Detection technique to a neutron capture measurement [113]. Their γ detector consisted in a thick slab of low-Z material (e.g. graphite) as γ-to-electron converter, backed with a thin plastic scintillator and a photomultiplier tube to detect electrons. However, a good proportionality between efficiency and energy could not be established below 500 keV.

An alternative method to achieve this proportionality condition was introduced by R. Macklin, J. Gibbons and H. Maier-Leibnitz [115] and it is the so-called *Pulse Height Weighting Technique* (*PHWT*). This is the technique employed in this work.

3.3.1 Pulse Height Weighting Technique

The *Pulse Height Weighting Technique* (*PHWT*) achieves the proportionality between the efficiency in detecting a γ ray and the energy of the γ ray by suitably weighting the counts of a detector according to the their deposited energy [114]. It consists therefore in a mathematical manipulation *a posteriori* of the detector output that can be applied in principle to any experimental setup and therefore it is particularly powerful.

In general, a γ-ray of energy E_j can deposit in a scintillator a different amount of energy E_i, that depends on the random interaction between photon and matter. The *response function* $R_{i,j}$ of the scintillator describes the probability distribution of the deposited energy, ranging from 0 to E_j. The integral of the response function over all the possible energy deposition E_i larger than the detection threshold represents the efficiency $\epsilon_{\gamma,\, j}$ of detecting a γ ray of energy E_j:

$$\epsilon_{\gamma,\, j} = \sum_{i=1}^{N} R_{i,j}. \tag{3.8}$$

The energy deposited has been realistically assumed as a binned variable (with index $i = 1, ..., N$), instead of a continuum variable, hence a sum has been used instead of an integral.

A *Weighting Function* W_i depending on the deposited energy (the only measurable quantity) can be applied to the response function in order to achieve the wanted proportionality, imposing:

$$\sum_{i=1}^{N} W_i R_{i,j} = \alpha E_j, \tag{3.9}$$

where α is just an arbitrary scaling factor that can fixed to 1 for convenience.

The Weighting Functions can be typically expressed, in the most simple case, as a polynomial function of degree l of the deposited energy, like:

$$W_i = \sum_{k=0}^{l} a_k E_i^k, \tag{3.10}$$

where a_k are just parameters. More details on the determination of the weighting functions will be presented in Sections 4.2.2 and 5.1.3.

3.4 The experimental setups

The experimental setups employed in this works aim at detecting the prompt γ rays produced by neutron radiative capture events in the sample, minimizing as much as possible the background induced by materials around the beam. In both the experimental areas, they consist of an array of liquid deuterated benzene (C_6D_6) scintillators looking at a sample of the material under study, placed in beam. In addition, a SIlicon MONitor (SiMon) placed upstream with respect to the sample is also employed to monitor the neutron beam in both the experimental areas.

3.4.1 C_6D_6 detectors in EAR1

The measurement of the capture cross section of ^{30}Si has been performed in EAR1, taking advantage of its superior energy resolution to accurately characterize the resonances in the energy range of astrophysical interest, between some keV and hundreds keV.

The experimental setup in EAR1 consists of four C_6D_6 liquid scintillators [116], placed at 9 cm from the in-beam sample and along a direction that forms an angle of 125° with respect to the neutron beam. This orientation minimizes the effects of the possible anisotropic distribution of γ rays. The setup is shown in Figure 3.7.

The detectors have been developed at the Legnaro INFN Laboratory with a custom design optimized to reduce as much as possible their neutron sensitivity, i.e. the sensitivity to scattered neutrons that can be captured in the detectors, generating a background signal that is indistinguishable from a capture event in the sample [116].

The detectors consist of 1 liter of C_6D_6 active volume, directly coupled with a 2-inch photomultiplier tube via a truncated conical volume of C_6D_6 (acting both as active volume and light guide) and a 2.8-mm-thick quartz window. An expansion volume connected with the active volume enables the thermal expansion of the liquid. The ensemble

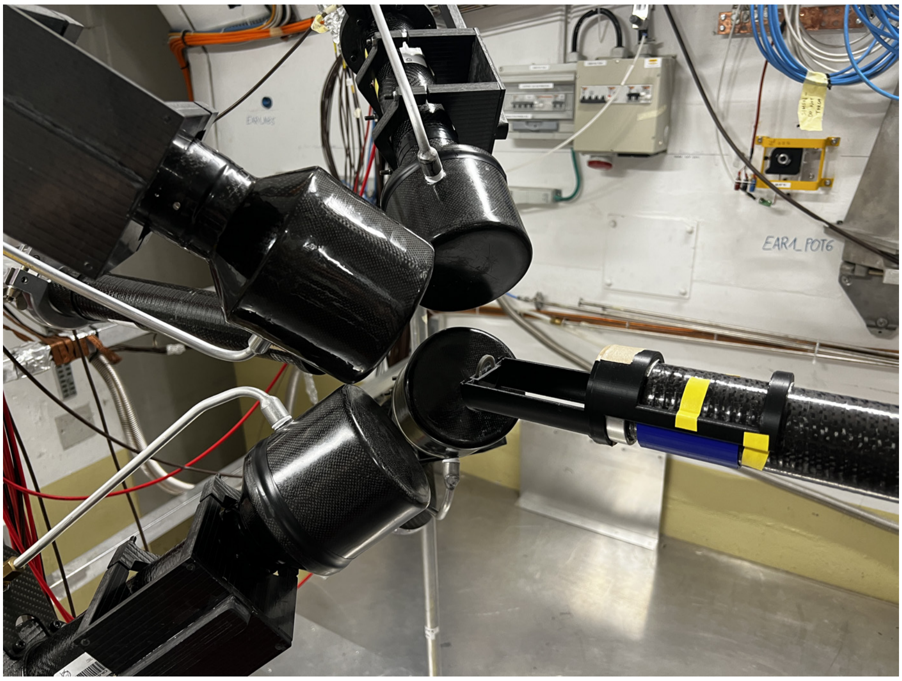

Figure 3.7: Experimental setup in EAR1, consisting of four C_6D_6 liquid scintillators, customized to reduce as much as possible the neutron sensitivity.

is hosted in a carbon fibre structure, that minimizes the neutron sensitivity thanks to the high scattering-to-capture cross section ratio of carbon. The detector supports have been also designed in order to minimize the amount of material around the sample, that can increase the neutron sensitivity. They consist of simple carbon fibre bars. The beam pipes close to the detectors are also in carbon fibre.

The choice of deuterated benzene is also driven by the need for a scintillating material (like benzene) with the lowest possible probability of capturing neutrons. Since deuterium has a neutron capture cross section three orders of magnitudes lower than hydrogen in the energy range of astrophysical interest, deuterated benzene (C_6D_6) in place of normal benzene (C_6H_6) is employed. The neutron sensitivity of the detector, intended as the ratio between the efficiency for detecting a neutron and the maximum efficiency for detecting a γ ray from a capture event in the sample, is lower than 10^{-3} in the typical neutron energy range of interest and generally lower than $5{\times}10^{-5}$ between 1 keV and 1 MeV neutron energy [117].

Moreover, liquid deuterated benzene together with the employed photomultiplier tubes guarantee a fast time response of the detector, whose signals are only a few tens ns wide. This is a crucial feature for time-of-flight measurements, in order to limit pile-up and reach high neutron energy.

The photomultiplier were powered with a high voltage between 1450 and 1590 V (negative polarity).

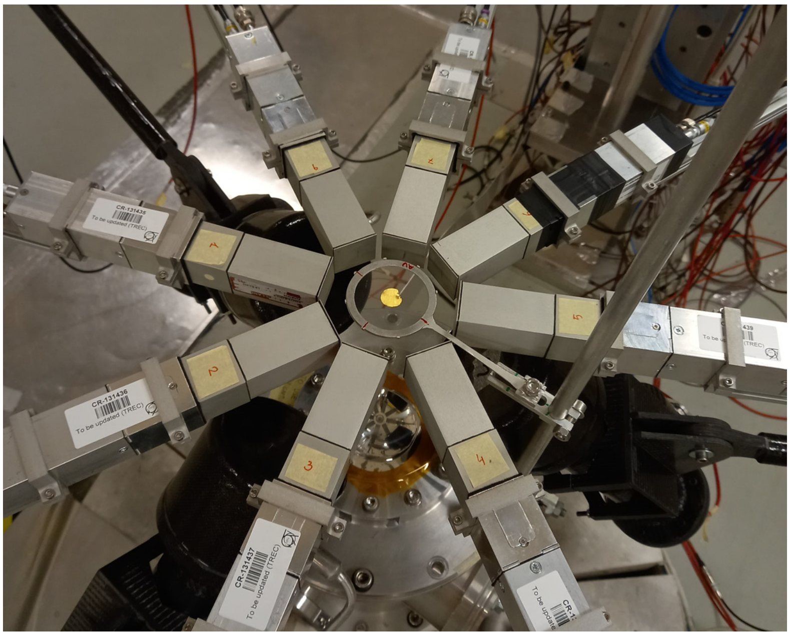

Figure 3.8: Experimental setup in EAR2, consisting of eight C_6D_6 segmented liquid scintillators (sTED), optimized for the high counting rate of EAR2 to reduce the signal-to-background ratio. The setup is complemented by three bigger C_6D_6 (as employed in EAR1).

3.4.2 sTED detectors in EAR2

As enriched ^{64}Ni is quite expensive, the measurement of its capture cross section has been performed only in EAR2, taking advantage of the larger neutron flux that enabled to employ a sample of smaller mass to reach a suitable statistics. Moreover, EAR2 has been also exploited for a complementary measurement of the capture cross section of ^{30}Si focused in the thermal energy region, as thermal neutrons are not available in EAR1. This measurement was intended to constrain the direct capture component.

The experimental setup in EAR2 also consisted of C_6D_6 liquid scintillators, but in this case eight smaller segmented detectors (sTED) were employed [118, 119]. The detectors were placed at 4.5 cm from the in-beam sample and oriented at an angle of 90° with respect to the neutron beam, in order to increase the efficiency of the setup. The setup was mounted at a lower position with respect to previous capture measurements in EAR2, at approximately 25 cm from the window of SiMon. This position was recommended from the results of a study of the background in EAR2 [120]. The setup is shown in Figure 3.8.

The sTED detectors have an active volume of only 0.044 litres of C_6D_6, directly coupled to a 1-inch photomultiplier tube via a 1.8-cm-thick quartz window. The ensemble is hosted in an aluminium case, whose walls are approximately 3 mm thick.

The sTED detectors have been recently developed by the Spanish CIEMAT (Centro de Investigaciones Energetica, MedioAmbientales y Tecnologicas) to cope with the higher neutron flux of EAR2. In fact, the C_6D_6 detectors used in EAR1 experience excessively high counting rates when employed in EAR2, leading to severe pile-up and significant gain shift of the detectors that limit neutron capture measurements far below neutron energies of 1 keV [121]. Moreover, these detectors have to be placed at large distances from the sample, decreasing the signal-to-background ratio. For these reasons, an array of smaller segmented detectors was developed. In fact, by decreasing the active volume of the detectors while increasing their number, a reasonable detection efficiency can be maintained, but decreasing the counting rate experienced by each single detector. In this way, detectors are more stable and the effects of pile-up and of the γ-flash are reduced. As a consequence, neutron capture measurements can be performed up to higher neutron energy and the detectors can be placed closer to the sample, significantly increasing the signal-to-background ratio. New photomultiplier tubes are also employed to increase the performance at high counting rates. These photomultipliers were powered with a high voltage ranging between 779 and 858 V (negative polarity) depending on the detector.

The performance of the sTED in terms of timing is slightly better than in the C_6D_6 employed in EAR1, with signals that are also few tens ns wide. However, the neutron sensitivity is significantly increased due to the aluminium casings, especially in the keV neutron energy region where the neutron capture cross section of aluminium exhibits resonances.

Despite the problems described above, the experimental setup of EAR2 is complemented with two (in case of ^{30}Si) or three (in case of ^{64}Ni) C_6D_6 scintillators of the same model used in EAR1, but equipped with different photomultiplier tubes optimized to handle higher counting rates. They are placed at 15 cm from the sample at 125° with respect to the direction of the neutron beam. The additional detector employed in the ^{64}Ni campaign is placed at 13 cm. They were powered with a high voltage between 854 and 871 V (negative polarity). These additional detectors would have been employed to cross check the sTED data and to possibly increase the statistics in the energy regions where they work properly. However, the data collected by these additional C_6D_6 detectors have exhibited a particularly low signal-to-background ratio, that has eventually prevented their use in the analysis.

3.4.3 SiMon

Two *SiMon* detectors [122, 123], one for each experimental area, have been used to monitor the neutron beam during the measurements performed in this work.

These detectors exploit the ^{6}Li(n,α)t reaction to convert neutrons into charged particles. The cross section of this reaction is a *standard cross section* [124] in the neutron energy range between 25.3 meV and 1 MeV, meaning that is known with very small uncertainty (generally lower than 1.2%). Therefore, it is particularly suited to measure the neutron flux in the energy range targeted by this work.

The α particles and tritons produced by the reaction (of 2.05 and 2.73 MeV, respectively) are detected by an array of four 300-μm-thick silicon detectors placed outside the beam, downstream of the converter foil and at 45° with respect to the direction of

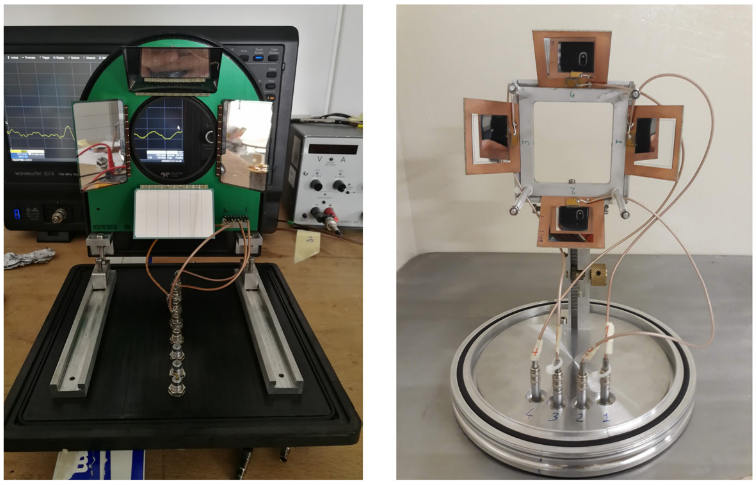

Figure 3.9: SiMon detectors employed in EAR1 (left) and in EAR2 (right), consisting of four silicon detectors placed outside the beam at 45° with respect to the direction of neutrons aimed at detecting α particles and tritons from neutron-converting ^{6}LiF foil.

neutrons. Figure 3.9 shows the setup for both the experimental areas. The detector is placed under vacuum, in order to prevent charged particles from being stopped by their interaction with air. Moreover, the in-beam lithium sample has to be sufficiently thin to enable charged particles to escape, but thick enough to guarantee sufficient statistics to monitor the beam. As lithium is a very reactive material, the more stable ^{6}LiF (95% ^{6}Li enrichment) is employed as neutron converter, deposited on 1.5-μm-thick Mylar backings.

In particular, the monitor used in EAR1 (SiMon) [122] was equipped with a 650 μg/cm^2 ^{6}LiF converter foil, looking at the incoming beam. In this case, α particles undergo quite severe energy degradation in the sample backing, therefore only tritium is selected to monitor the beam (see Figure 3.10). The detector is hosted in a carbon fibre vacuum chamber.

The monitor used in EAR2 (SiMon2) [123] was equipped with a thinner 82.66 μg/cm^2 ^{6}LiF sample, because of the higher neutron flux and consequent higher expected counting rate in EAR2. In this case, the converter foil looks towards the silicon detectors to avoid energy degradation in the backing, therefore both α and tritons can be potentially used to monitor the beam (see Figure 3.10).

In both detectors, the amount of material in beam and close to the beam is minimal, in order to avoid as much as possible the attenuation of the neutron beam and the induction of background in the experimental area. These features are indeed crucial for a good beam monitor.

3.4.4 Samples

The ^{30}Si and ^{64}Ni samples employed in this work are highly isotopically enriched samples, produced at the Goethe University of Frankfurt by the team including R. Reifarth,

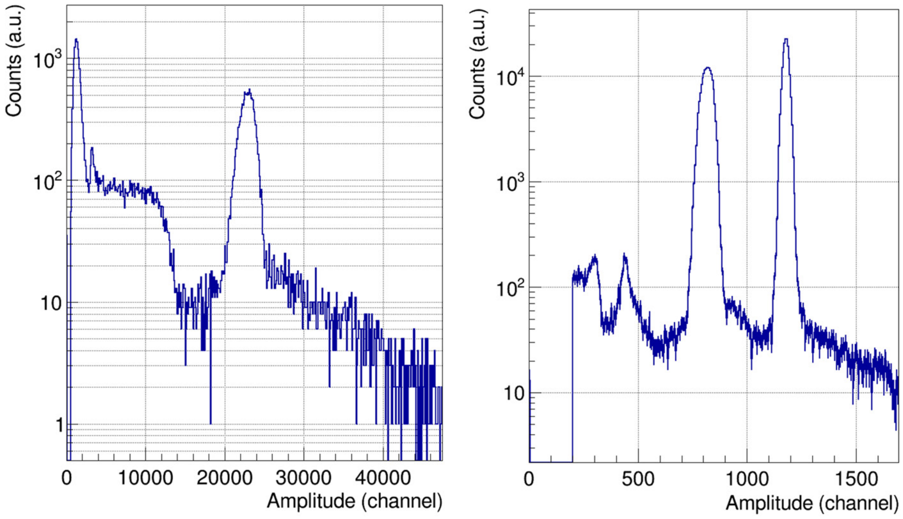

Figure 3.10: Amplitude spectra of the signals from the SiMon detectors in EAR1 (left) and EAR2 (right). In the first case, only the peak from tritons can be selected, while in the second case both α particles (around 800 channels) and tritons (around 1200 channels) can be distinguished.

T. Heftrich, D. Plonka and collaborators. Because of the low natural abundances of the isotopes studied in this work, isotopically enriched samples were necessary to obtain data not dominated by the other more abundant isotopes and to obtain good statistics in a reasonable time for a measurement campaign. In the case of ^{30}Si, this work is the first capture measurement performed with an isotopically enriched sample in the energy range of astrophysical interest.

The procedure followed for the preparation of the ^{30}Si and ^{64}Ni sample is similar. The samples were bought in the form of isotopically enriched small metal grains from ISOFLEX [125] and CortecNet [126], respectively. These grains were reduced in ultra fine powders (grains size $< 1\ \mu$m) in a nitrogen-cooled cryogenic mill, available at the University of Frankfurt. Finally, the powder was pressed in a hydraulic press (at 200 kN) to obtain self-sustained stable cylindrical samples. However, two different problems arose for the two samples during their preparation. They are described in the following lines.

^{30}Si sample

In order to increase its stability after pressing, the ^{30}Si sample was additionally sintered, i.e. heated (below its melting point) until the pressed powder bonded together to form a dense, solid and more stable sample. In particular, the sample was initially heated at 600°C for two hours to make it stable enough to be moved to another oven, where it was finally heated at the more suitable temperature of 1100°C for three hours.

However, after this process the mass of the sample increased by more than 30%. This increase was probably due to the oxidation of the sample during the sintering, that was performed at atmospheric pressure and atmospheric chemical conditions. Therefore, the

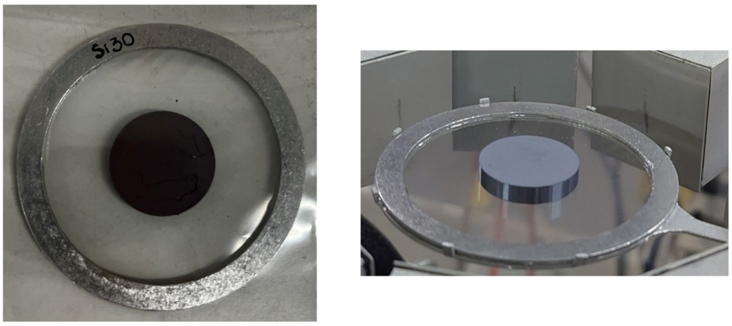

Figure 3.11: Silicon samples employed in this work: the ^{30}Si isotopically enriched sample, pressed and sintered, is shown on the left, while the natural silicon metallic sample used for normalization is shown on the right. Specifics of the samples are given in Table 3.1.

actual mass of ^{30}Si in the sample, that is a crucial quantity for cross section measurement, could not be directly measured, because of the unknown amount of oxygen absorbed. An indirect method had to be applied irradiating a natural silicon metallic sample, in which the mass of ^{30}Si is fixed by its natural abundance. More details will be discussed in Section 4.4.

The dimensions and the mass of the samples have been measured at the n_TOF facility and the specifics can be found in Table 3.1. The samples have been finally glued at the centre of a 6-μm-thick Mylar foil mounted on an aluminium ring of 6 cm external diameter, 5 cm internal diameter and 1 mm thickness. The ^{30}Si was covered with an additional Mylar foil, to avoid any potential loss of material in the experimental areas, as the sample was not particularly stable in the end. Pictures of the samples are shown in Figure 3.11.

^{64}Ni sample

The ^{64}Ni sample was stable enough after pressing, therefore the sintering has been avoided as not necessary. However, during the pressing procedure the sample partially stuck to the press due to magnetic effects, not observed with the natural nickel sample realized as a test. Therefore, the resulting shape of the ^{64}Ni sample is not symmetric, as shown in Figure 3.12. The area of the sample has been estimated with a software, using a picture of the sample taken on millimetre graph paper. However, the uncertainty in the area exceeds 10%.

Fortunately, as the sample is smaller than the transversal dimensions of the beam, what ultimately matters in the measurement of the neutron capture cross section is the mass of the sample, while possible inaccuracies in the value of the area are compensated in the normalization factor. However, it is crucial to perform the normalization with a sample that has exactly the same transversal dimensions, the same shape and the same orientation as the sample under study. More details will be discussed in sections 4.3.3 and 5.2.3. For this reason, great care was devoted to cut a gold sample with the same

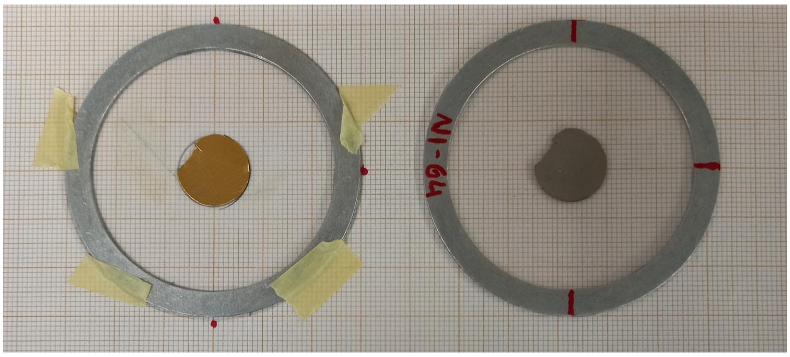

Figure 3.12: On the right the ^{64}Ni enriched sample, characterized by a non-symmetric shape because of magnetic issues during the pressing procedure. On the left, the gold sample cut to reproduce the same shape of the ^{64}Ni and used for normalization. Specifics of the samples are given in Table 3.1.

shape as the ^{64}Ni sample to use for normalization. The sample is also shown in Figure 3.12. Specifics of these samples are reported in Table 3.1.

Like the silicon samples, the ^{64}Ni has been enclosed between two Mylar foils attached to the aluminium ring frame. Only one layer of Mylar has been used for gold.

Ancillary samples

During the experimental campaign, not only the enriched samples of the isotopes under study were irradiated.

As already mentioned, gold samples of the same dimension and placed in the same position as the samples under study were irradiated for normalization purposes, as will be discussed in sections 4.3.3 and 5.2.3.

Moreover, some additional samples were irradiated to estimate and subtract the background, as will be shown in sections 4.3.1 and 5.2.1. In particular:

- Dummy sample, consisting of two layers of Mylar
- Empty sample, consisting of only one layer of Mylar
- A natural carbon sample, glued to one Mylar foil
- A natural lead sample, also glued to one Mylar foil

All the samples are mounted on aluminium ring frames with the same characteristics described above. Additional gold samples of the same dimension as the carbon and lead samples were irradiated for the respective normalizations. Specifics of these samples are found in Table 3.1.

All the samples employed in this work were placed in the beam on suitable sample holders, designed to guarantee the reproducibility of the same position of the samples with the minimum possible amount of material, that can induce background in the experimental areas. The sample holder in EAR1 consisted of a 3D-printed plastic low-mass structure, attached to the beam pipe just in front of the C_6D_6. The sample holder in EAR2 consisted of a very thin aluminium ring attached to a lateral bar coming from the flange of SiMon.

Sample	M (mg)	d (mm)	n (at/barn) °	t (mm)	Enrichment
^{30}Si*	*750.3(1)* [992.5(1)]	22.22(1)	*$3.888(4)\times10^{-3}$*	1.77(4)	99.64%
^{197}Au	753.0(1)	22.22(1)	$5.939(5)\times10^{-4}$	0.10(1)	–
^{64}Ni†	427.2(2)	*14(1)*	$2.5(4)\times10^{-3}$	*0.30(5)*	99.52%
^{197}Au	326.7(1)	*14(1)*	$6.3(9)\times10^{-4}$	0.10(1)	–
^{Nat}Si	2932.0(1)	20.00(2)	$2.001(4)\times10^{-2}$	3.98(1)	–
^{Nat}C	3933.45(1)	19.97(1)	$6.297(6)\times10^{-2}$	6.35(1)	–
^{197}Au	645.0(1)	20.00(1)	$6.277(6)\times10^{-4}$	0.10(1)	–
^{Nat}Pb	2064.0(1)	15.34(4)	$3.25(1)\times10^{-3}$	1.31(4)	–
^{197}Au	347.1(1)	15.04(3)	$5.98(3)\times10^{-4}$	0.10(1)	–

Table 3.1: Specifics of the samples irradiated in this work: mass (M), diameter (d), areal density (n), thickness (t) and isotopic enrichment. The samples are arranged according to their dimensions and, for each group, the information on the gold sample used for normalization is reported. Diameters, masses and thicknesses have been measured at n_TOF before gluing the samples on the frames.

* Only for ^{30}Si, the mass pre-sintering (before oxidation) is reported, as communicated by the team that prepared the sample. However, this value has been considered just as a starting point for the indirect evaluation of the ^{30}Si mass in the sample, that will be discussed in Section 4.4. The total mass of the sample, as measured at n_TOF after oxidation, is also reported in brackets.

† Concerning the ^{64}Ni sample, the reported area has been calculated via computerized reconstruction of the sample, while the reported diameter is intended as an average radius, as the sample was circular. The thickness has been only estimated theoretically due to the fragility of the sample.

° The reported uncertainties on the areal density include the uncertainty on the area, even if only the uncertainty on the mass will be important for determination of cross sections, as the samples are smaller than the beam. Possible inaccuracies in the area are indeed compensated in the normalization.

Chapter 4

Analysis of ^{30}Si(n,γ) data in EAR1

This section deals with the analysis of the data collected in EAR1, where, as described in the previous chapter, the experimental setup consists of four C_6D_6 liquid scintillators. The procedure followed for data analysis will be discussed in detail, starting from the identification of the signals (Section 4.1) and the characterization of the detectors (Section 4.2), up to the determination of the capture yield (Section 4.3). The analysis procedure will be discussed first in general and then focusing on the specificities of this work. The last section (Section 4.4) is specific about the estimation of the mass of ^{30}Si in the enriched sample. The fit of resonances in the capture yield and the results of the analysis will be reported in Chapter 6.

4.1 The Pulse Shape Analysis (PSA)

The first step of data analysis consists in the processing of raw data, in order to identify signals and extract their relevant information from the digitalized waveforms saved by the DAQ (Section 3.1.5). At n_TOF, this procedure is usually based on a *Pulse Shape Analysis* (*PSA*) routine [127, 128], characterized by a minimal number of explicit assumptions about the nature of signals and more than twenty adjustable input parameters, so that it can be tuned and applied to a large variety of detectors.

The routine works through different sequential steps:

1. *Pulse recognition*
   Pulses are recognized when the discrete derivative d_i of the digitalized waveform crosses four times some thresholds relative to the average noise fluctuation in a suitable time window. The discrete derivative is computed using a number of pre and post samples (referred to as step-size) defined as a compromise to smooth out electronic noise and to distinguish pile-up. Step size, derivative thresholds and signal width limits are some of the adjustable input parameters set by the user to select real signals and discard transients or noise.

2. *γ-flash recognition*

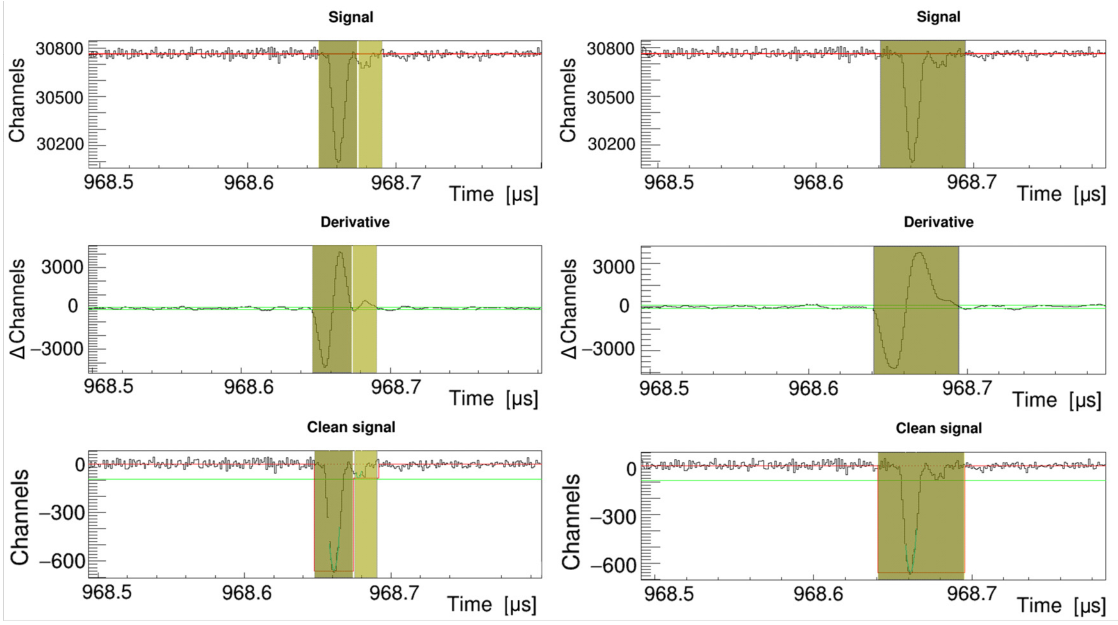

Figure 4.1: Graphical User Interface of the Pulse Shape Analysis routine used in this work. The first line represents the digitalized waveform acquired by the DAQ from the output of a C_6D_6 detector, the central line shows the discrete derivative of the waveform (with the thresholds defining a signal in green) and the last line depicts the final cleaned signal referred to the baseline. Parabolic fit to the signal peak is shown in blue, while yellow areas represent the recognized signals. On the left, a preliminary set of input parameters from past experiments is used, while on the right the final set of parameters adjusted for this measurement is employed to include the electronic rebound in the signal (see text for details).

The signal from the γ-flash is important to fix the time zero in the time-of-flight technique and it can be recognized using different methods, chosen in input by the user. In this case, it is recognized as the first saturated signal of an event.

3. *Baseline reconstruction*
The portions of the waveform that are not recognized as signal and γ-flash in the previous steps are averaged to determine the signal baseline. In the proximity of the γ-flash a moving average is typically used to reproduce possibly non-flat baselines.

4. *Signal information*
Eventually, the relevant information of each signal is extracted with respect to the computed baseline. In particular, the amplitude of the signal can be extracted either by finding the maximum height of the pulse, by a parabolic fitting at the top of the pulse or by fitting the entire pulse with a customized shape (Pulse Shape Fitting). In this analysis, since pile-up is negligible in EAR1 for this measurement, the second method was employed. The area of the signals is extracted as well. The time of the signal is finally extracted when the signal reaches the 30% of its

Source	Energy of γ ray (MeV)	Energy of Compton Edge (MeV)
^{137}Cs	0.662	0.478
^{88}Y	0.898	0.700
^{88}Y	1.836	1.612
AmBe	4.438	4.196
CmC	6.13	5.89

Table 4.1: Radioactive sources used for detector calibration, providing mono-energetic γ rays that cover the full energy range expected for γ rays produced by ^{30}Si(n,γ) and ^{64}Ni(n,γ).

maximum amplitude. The information for each pulse is saved in a ROOT file for further analysis.

Figure 4.1 shows an example of signal from a C_6D_6 detector in the PSA graphical interface, using two different sets of input parameters. On the left a preliminary set of input parameters from past experiments is used, while on the right the final set of parameters for this measurement is employed. As this measurement was not affected by pile-up, the step-size for calculation of the derivative could be increased and a more stringent lower limit for the signal width could be employed in order to include the electronic rebound at approximately 20 ns after the signal in the signal itself. This procedure allows the reduction of the amplitude threshold set in the analysis, with a consequent increase in the collected statistics (see Section 4.2.3). Including this rebound affects the area of the signal, but not its amplitude, which is therefore used for calibrating the deposited energy.

4.2 Characterization of the detectors

4.2.1 Detector Calibration

The Pulse Height Weighting Technique requires to weight counts according to the energy deposited. Therefore, an accurate calibration of detectors for converting pulse height into deposited energy is needed. For this purpose, periodical beamoff measurements with different radioactive γ sources have been performed during the data-taking period and repeated approximately every week to check the gain stability of the detectors. The sources have been chosen to provide mono-energetic γ rays covering the entire energy range expected for γ rays in the de-excitation cascade following the ^{30}Si(n,γ) reaction, whose Q-value is 6.587 MeV. A list of the sources with their characteristic γ rays can be found in Table 4.1. Two compound sources (AmBe and CmC) have been also used to provide high energy γ rays. In these sources, ^{241}Am and ^{244}Cm decay emitting α particles that induce (α,n) reactions on ^{9}Be and ^{13}C, respectively. A part from neutrons, these reactions release the high-energy γ rays from the de-excitation of the light nuclei.

Since deuterated benzene is a light material, the dominant mechanism of interaction of γ rays is the Compton scattering, where γ rays scatter on atomic electrons transferring

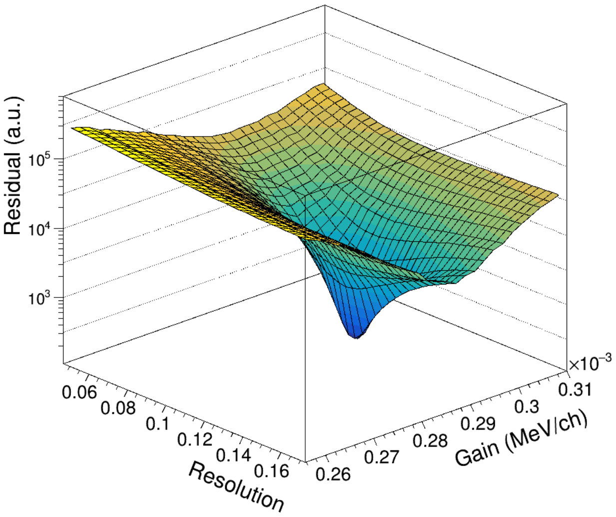

Figure 4.2: Residuals in the comparison between GEANT4 simulated and measured energy deposited spectra for ^{137}Cs, as a function of gain and resolution. The couple of value that minimizes the residual realizes the best agreement between data and simulations, shown in the first panel of Figure 4.3.

part of their energy. Moreover, since the detectors are relatively small, the efficiency is quite low and γ rays typically deposit only part of their energy in the detectors before they can escape. For this reason, no full energy photo-peak is observed in the detector response function. Therefore, the only structure that can be used for the detector calibration is the *Compton Edge*, that corresponds to the maximum energy that a γ ray can transfer to an electron in a single frontal Compton scattering event. The energy of the Compton Edge E_{CE} can be related to the energy of the interacting γ ray E_γ with the formula:

$$E_{CE} = \frac{2E_\gamma^2}{2E_\gamma + m_e c^2} \tag{4.1}$$

where m_e is the mass of the electron and c the speed of light. Values of the Compton Edge for the mono-energetic γ rays used in calibration can be also found in Table 4.1. However, the theoretically sharp structure of the Compton Edge (showed by simulations in Figures 4.3-4.5) is significantly blurred by the resolution of the detectors, making Monte Carlo simulations the only possible tool to perform accurate calibrations.

Before describing the procedure that has been adopted, it is interesting to point out that increasing the energy of the γ rays above some MeV, the pair-production mechanism also starts to play an important role in the interaction of γ rays. In this case, the interacting γ ray is converted into an electron-positron pair, which deposits its full kinetic energy in the scintillator. The positron eventually annihilates releasing two γ rays of 1.02 MeV total energy, that usually escape without interacting in small detectors made of light material. This is the reason why a sharp structure, the so-called *double escape peak*, appears in the simulated deposited energy spectra of the AmBe and CmC radioac-

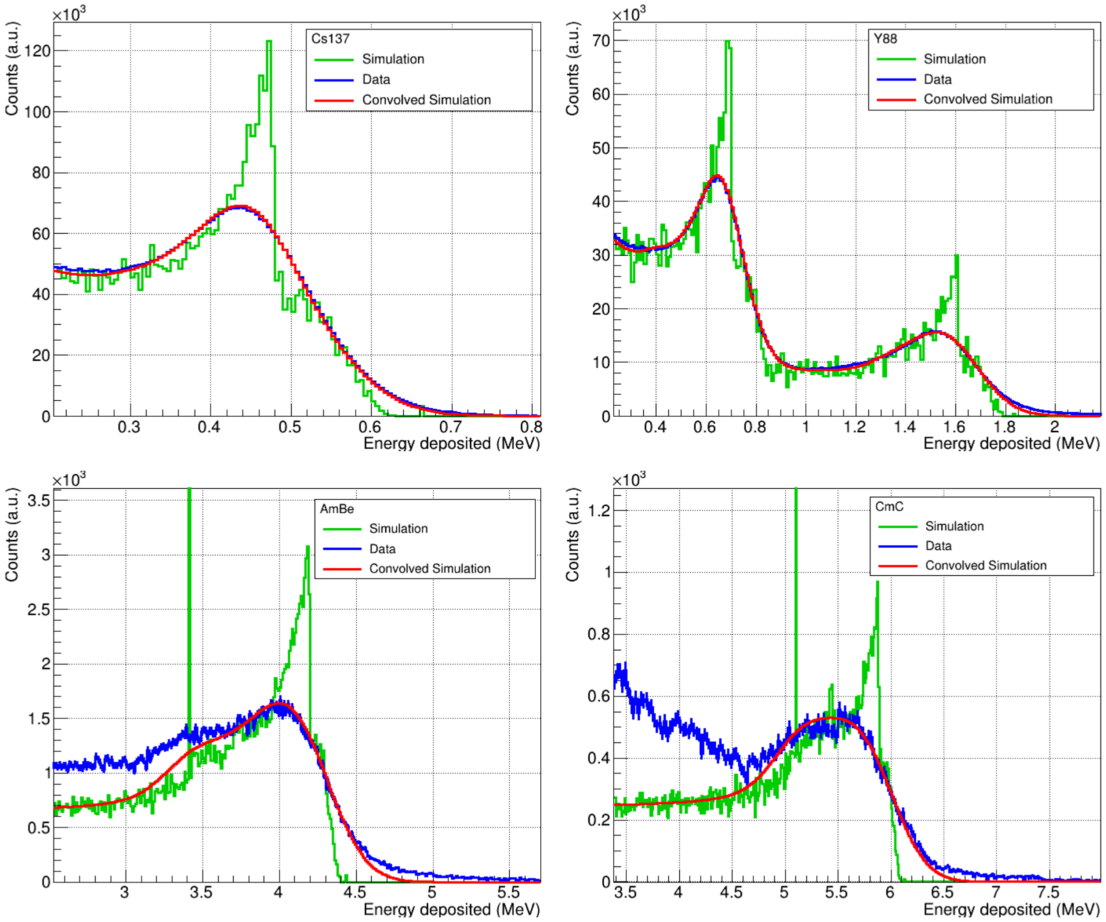

Figure 4.3: Comparison between simulated and measured energy deposited spectra in the C_6D_6-4 detector for the sources employed in this work. Final calibration and energy resolution curves are employed in the plots. Green lines represent GEANT4 simulated spectra, red lines represent the simulated spectra convolved with detector resolution and blue lines represent calibrated experimental data.

tive sources (Figure 4.4) at an energy exactly 1.02 MeV lower than the energy of their γ rays. However, this sharp structure is completely washed out by the energy resolution of the detectors and therefore cannot be exploited for energy calibration, even if it can be seen to clearly impact on the shape of the spectra.

The procedure followed to calibrate the detectors consists in the direct comparison between measured signal amplitude spectra and simulated energy deposited spectra for the different radioactive sources. In order to avoid confusion, it is now important to define some terms that will be used in the following lines: *energy resolution* will be intended as the ratio $\sigma_{E_{dep}}/E_{dep}$, while the *gain* will be addressed as the amplitude-to-energy conversion factor. Deposited energy spectra in the C_6D_6 detectors for all the radioactive sources employed have been simulated using GEANT4 [129], using its default

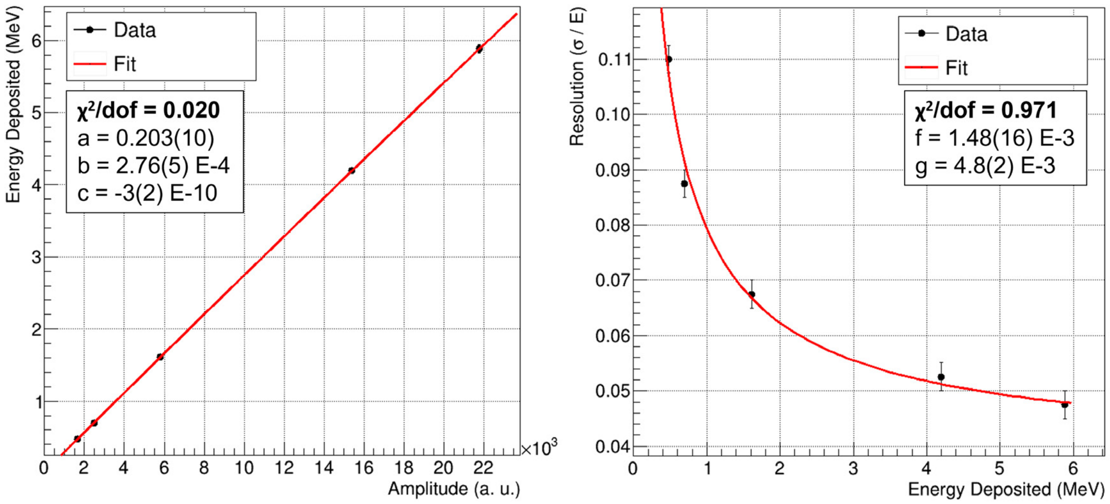

Figure 4.4: Fit of the calibration (left) and resolution (right) functions for the C_6D_6-4 detector, using the data obtained from direct comparison between measured and simulated amplitude spectra, as shown in Figure 4.3. The fitted parameters are referred to Equations 4.3 and 4.5, respectively.

electromagnetic physics package (good enough for the energy range of interest). Then, the simulated spectra have been convolved with Gaussian distributions of standard deviation $\sigma_{E_{dep}}$ to account for the energy resolution of the detectors. The convoluted simulated spectra have been eventually compared with the signal amplitude spectra, measured for every radioactive source and converted to deposited energy using a fixed gain. The gain and the resolution have been varied independently and simultaneously in order to find the couple of values realizing the best agreement between experimental data and Monte Carlo simulations around the Compton edge, i.e. minimizing the residual function shown in Figure 4.2. The agreements achieved with this procedure are shown in Figure 4.3 for all the sources employed.

The gain and the resolution found for the different sources have been finally fitted to get an energy calibration and an energy resolution curve for each detector, as shown in Figure 4.4 for the C_6D_6-4 detector. A linear calibration in the form

$$E_{dep} = a + bA, \tag{4.2}$$

where A is the signal amplitude, worked well for the C_6D_6-1 and C_6D_6-2 detectors, while a quadratic calibration

$$E_{dep} = a + bA + cA^2 \tag{4.3}$$

has been preferred for the C_6D_6-4 detector. The calibration of C_6D_6-3 detector turned out to be more tricky, as simple functions were not able to reproduce the data at high energy. After several attempts, the fit was eventually performed with a piecewise function of the form

$$E_{dep} = \begin{cases} a + bA & \text{if } A < A_0 \\ c + dA + eA^2 & \text{if } A \geq A_0 \end{cases} \tag{4.4}$$

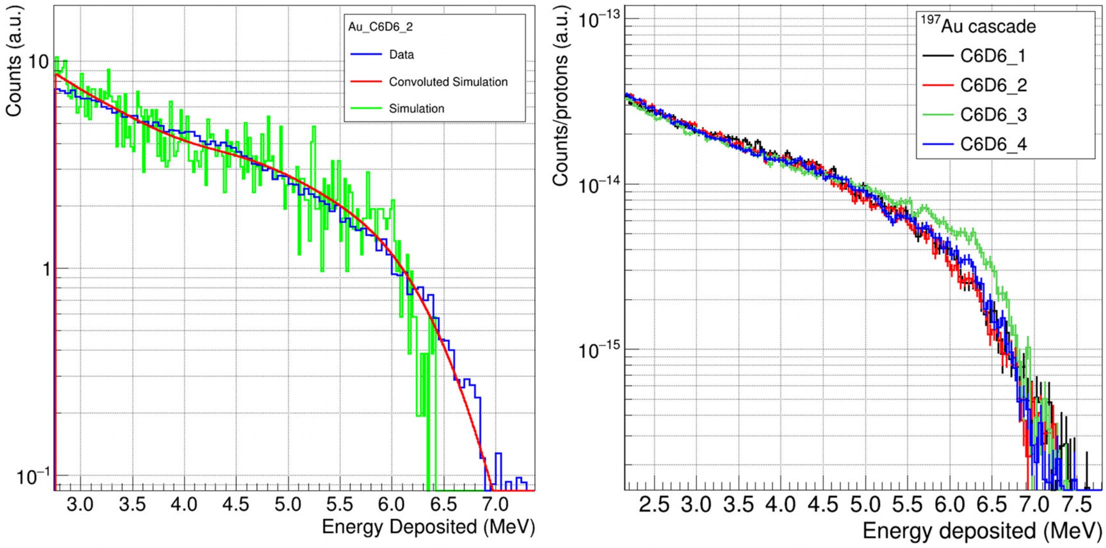

Figure 4.5: Check of the extracted calibration and resolution curves using the deposited energy spectra of the cascade of the 4.9 eV resonance in ^{197}Au. On the left, the comparison between the measured and the GEANT4 simulated spectra is shown for the C_6D_6-2 detector. On the right, the comparison between the cascades from all the detectors is shown.

where a, b, e, A_0 have been treated as free adjustable parameters, while c and d have been fixed as a function of the others in order to guarantee continuity and differentiability of the function in the junction point.
The energy resolution curve was well reproduced for all the detectors by a function as

$$\sigma_{E_{dep}}/E_{dep} = \sqrt{f + \frac{g}{E_{dep}}}. \tag{4.5}$$

In conclusion, the calibration and resolution curves have been tested employing the de-excitation cascade spectra of the 4.9 eV resonance of gold. As described in Section 2.2.2 and later in Section 4.3.4, neutron capture reactions create compound nuclei that de-excite to their ground state emitting a different number of γ rays of different energy, according to a random de-excitation path. All the possible γ rays emitted, convolved with their emission probability, constitute a de-excitation spectrum (cascade), typical of each resonance in general, whose end-point can be also used for energy calibration. First, the calibrated amplitude spectra have been compared with the resolution-convolved simulations for all the detectors. Secondly, the spectra of the different detectors have been compared, to ensure that they share the same end-point of the spectrum at approximately 6.51 MeV (Q-value of the ^{197}Au(n,γ) reaction), even if the shapes can be slightly different because of the different energy resolution of the detectors. The comparison is shown in Figure 4.5.

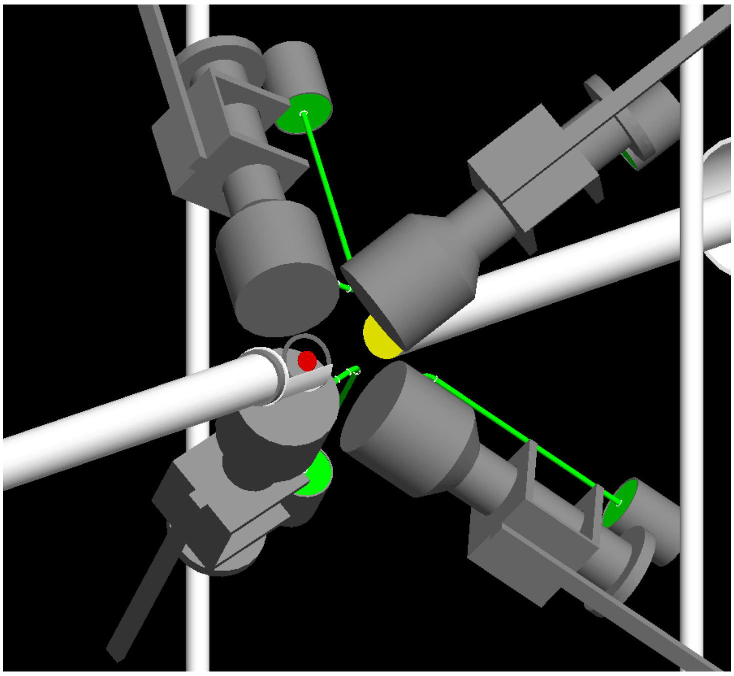

Figure 4.6: Experimental setup in EAR1 reproduced in GEANT4 for the determination of the weighting functions. The real setup is shown in Figure 3.7.

4.2.2 Weighting Functions

The Total Energy Detection technique coupled with the Pulse Height Weighting Technique has been already discussed in detail in Section 3.3. Basically, in order to account for the detector efficiencies for capture events, these techniques require to weight *a posteriori* each signal according to its deposited energy using suitable weighting functions, to achieve a linear proportionality between the efficiency of detecting a γ ray and its energy. This section deals with the procedure used to determine these weighting functions, which is based again on Monte Carlo simulations.

The experimental setup has been indeed accurately simulated in GEANT4, including the C_6D_6 detectors, but also the sample holder, the beam pipes and the walls of the experimental area, adapting the geometries already implemented in previous works [117, 130, 131]. Figure 4.6 shows the implemented geometry. The response functions $R_{i,j}$ of the C_6D_6 detectors for γ rays of different energy have been determined, simulating the energy deposited by mono-energetic γ rays in the detectors.

In particular, 10^7 γ rays have been simulated for each energy E_j, chosen between 100 keV and 1 MeV with an increment of 100 keV and between 1 MeV and 8.5 MeV with an increment of 250 keV, in order to cover the full γ ray energy range expected in the experiment. γ rays have been assumed isotropically emitted from the sample, while their origin has been determined using suitable distributions to account for the self-shielding effect for neutrons and the spatial distribution of the neutron beam. These simulations

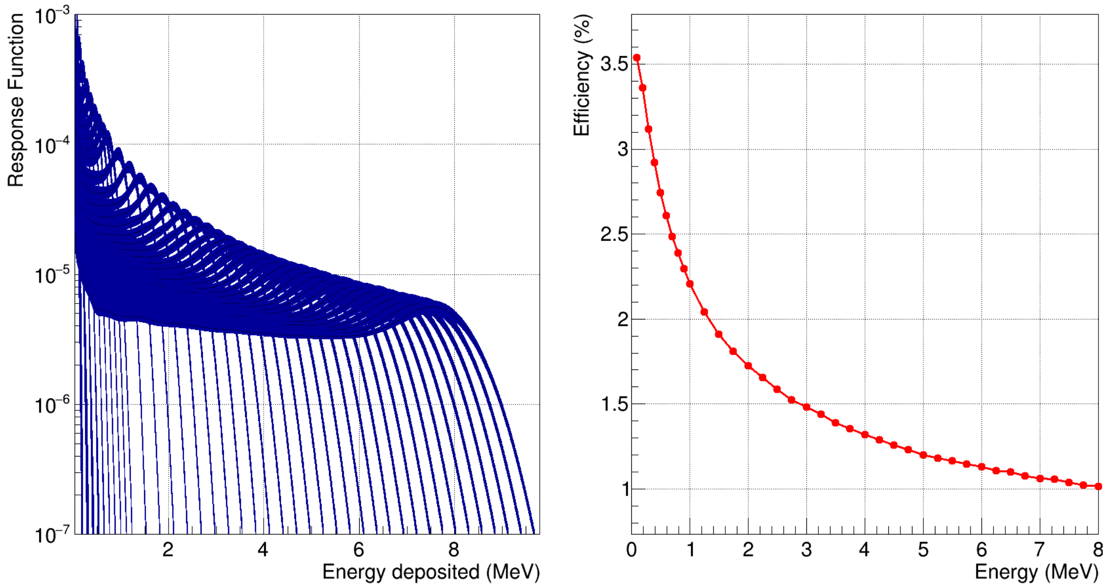

Figure 4.7: On the left: simulated response functions of the C_6D_6-2 detector for γ rays of different energies (from 100 keV to 8.5 MeV), convoluted with the energy resolution of the detector. On the right: the simulated efficiency of the C_6D_6-2 scintillator for detecting γ rays of different energies, obtained as the integral of the response functions.

have been repeated for the different samples irradiated during the campaign (^{30}Si, ^{Nat}Si and Au), to account for different thicknesses of the samples and relative attenuation of γ rays.

The simulated response functions have been finally convolved with the energy resolution of each detector, determined in Section 4.2.1, as shown in the left panel of Figure 4.7. The integral of the response functions for the different γ ray energies represents the detector efficiency for detecting γ ray of different energies, that is shown in the right panel of Figure 4.7. As requested by the Total Energy Detection technique, the efficiency of the detectors is low, always below 3.5%.

At this point, the weighting functions W_i for each detector and each sample have been determined imposing the condition 3.9, hence performing a least-square minimization of the expression:

$$\sum_j \left(\sum_{i=1}^{N} \left(\sum_{k=0}^{l} a_k E_i^k R_{i,j} \right) - E_j \right)^2 \tag{4.6}$$

where i is the index that runs over the bins corresponding to different deposited energies E_i and j runs over the different simulated energies of the γ rays. k runs over the monomials composing the weighting function, that is assumed as a polynomial function as expressed in Equation 3.10. In particular, polynomials of different degree l have been tested and, in the end, polynomials of degree 4 have been used for the weighting

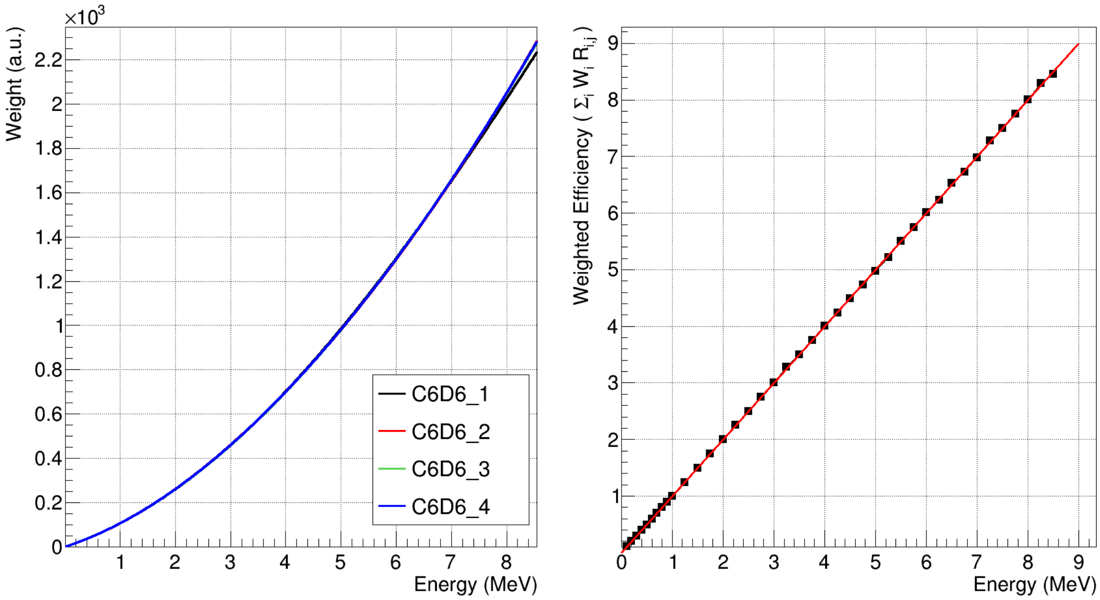

Figure 4.8: On the left: the weighting functions as a function of the deposited energy, determined for the ^{30}Si sample for all the detectors. On the right: final weighted efficiency simulated for the C_6D_6-2 detector using the weighting function on the left.

functions related to the silicon samples (Figure 4.8), while polynomials of degree 5 have been used for gold samples, since performing better.
The accuracy of the weighting function can be assessed considering the ratio

$$\frac{\sum_{i=0}^{N} W_i R_{i,j}}{E_j} \tag{4.7}$$

that, according to Equation 3.9, should be ideally one for all the simulated γ ray energies E_j. As shown in Figure 4.9, in this work the deviations of this ratio from unity are generally enclosed within ± 1%, indicating that the evaluation of the weighting functions is accurate. Larger deviations are only present at low deposited energies (below 200 keV), where they are not expected to produce relevant effects as counts are only weakly weighted or even below threshold.
Applying these weighting functions to the simulated response functions of the detectors for the different γ ray energies eventually results in a *weighted efficiency* that is proportional to the energy of the γ rays, as requested by the Total Energy Detection technique and as shown in Figure 4.8.

It is important also to point out that in this measurement the weighting functions have been estimated without imposing any threshold on the deposited energy. Therefore, corrections for the counts lost below the actual experimental threshold have to be applied and will be discussed in Section 4.3.4.

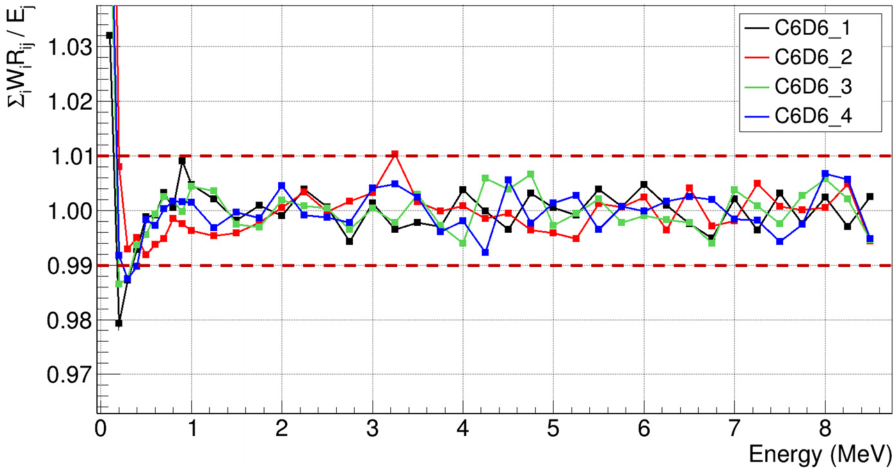

Figure 4.9: Evaluation of the accuracy of the weighting functions obtained for ^{30}Si sample for all the detectors. On the y-axis the weighted efficiency divided by the energy of the γ ray is shown, as a function of the energy of the γ ray on the x-axis. Deviations from unity are generally within ± 1%.

4.2.3 Deposited energy threshold

Signals recorded by the DAQ and identified by the PSA routine usually include low-amplitude noise and oscillations due to the electronics. Moreover, signals from the detectors are typically accompanied by low-amplitude electronic rebounds and after-pulses. The former are usually due to mismatches of the impedance of the cables used to connect the detectors with the DAQ and their time delay depends on the length of the cables (they typically appear from a few tens to a few hundreds ns after the signal). The latter are due to the ionizations of gaseous impurities in the photomultiplier tubes, like hydrogen, helium or nitrogen [132, 133]. These gases can be ionized during the electron multiplication process in the PMT and drift back toward the photocathode or previous dynodes, where upon impact they can liberate secondary electrons that produce the after-pulse. Since ions drift slower than electrons, these after-pulses are typically recorded hundreds of ns after the main signal.

In order to discard most of these fake signals, a threshold in the deposited energy is required. This threshold has been determined by studying the amplitude of the signal rebounds. In particular, high amplitude signals (deposited energy larger than 500 keV) have been selected and the energy deposited by subsequent signals identified within a time delay 1000 ns has been plotted as a function of the time delay, as shown in Figure 4.10. Peaks corresponding to electronic rebounds can be clearly distinguished between 20 and 50 ns, at 90 ns and at approximately 200 ns, together with the after-pulses due to the ionization of hydrogen and helium at approximately 280 and 600 ns, respectively. The deposited energy threshold has been chosen for every detector as the maximum amplitude of the rebounds. As shown in the left panel of Figure 4.10, prompt electronic rebounds at 20 ns would have required a very high threshold between 300 and

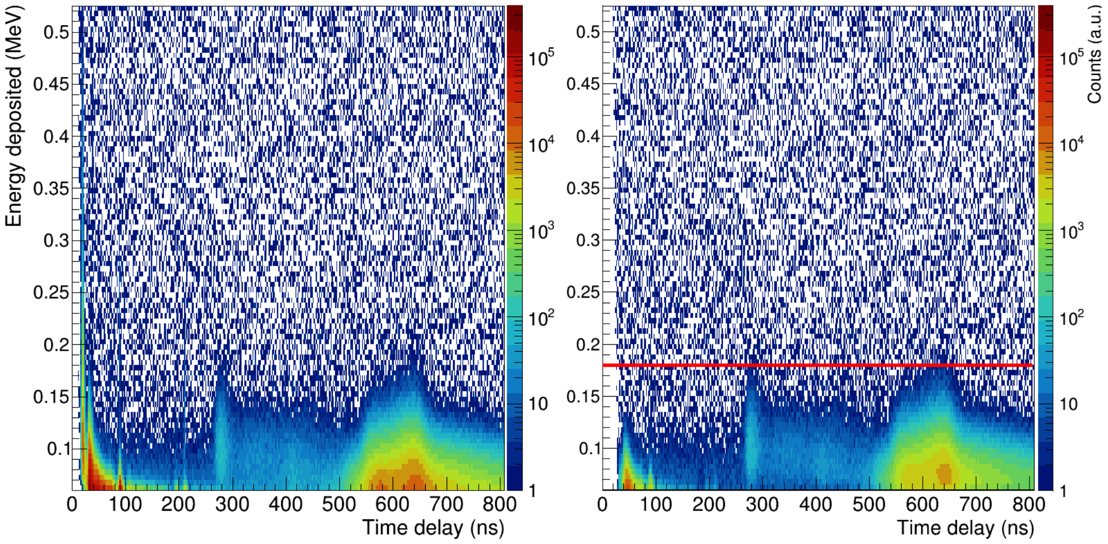

Figure 4.10: Amplitude of the signals following selected signals with amplitudes higher than 500 keV as a function of their time delay for the C_6D_6-1 detector. Electronic rebounds can be distinguished between 20 and 200 ns, together with after-pulses at 280 and 600 ns. The plot on the left refers to preliminary PSA parameters for pulse recognition, while the plot on the right refers to the final parameters (see text for details). The red line represents the final amplitude threshold set.

Detector	C_6D_6-1	C_6D_6-2	C_6D_6-3	C_6D_6-4
Energy threshold	180 keV	200 keV	170 keV	220 keV

Table 4.2: Final thresholds in the deposited energy set for the different C_6D_6 detectors.

400 keV, that would have rejected even a significant number of real signals, reducing the statistics. For this reason, as anticipated in Section 4.1, the PSA parameters have been slightly modified in order to eliminate the prompt rebounds, that have been included in the signals. As a consequence, the deposited energy thresholds could be significantly lowered between 170 keV and 220 keV depending on the detector, as shown in the right panel of Figure 4.10 and reported in Table 4.2. The few fake signals possibly remaining above the threshold are weakly weighted due to their relatively low amplitude and therefore contribute only to a negligible factor to the final yield.

4.2.4 Dead time corrections

Signals that come too close in time may not be separately recognized by the DAQ system or by the PSA routine, that may recognize a single merged signal (*pile-up*) or simply do not record one of the two signals. In case high counting rates are experienced by the detectors, this effect leads to a relevant loss of signals that has to be suitably corrected in order to obtain an accurate reaction yield.

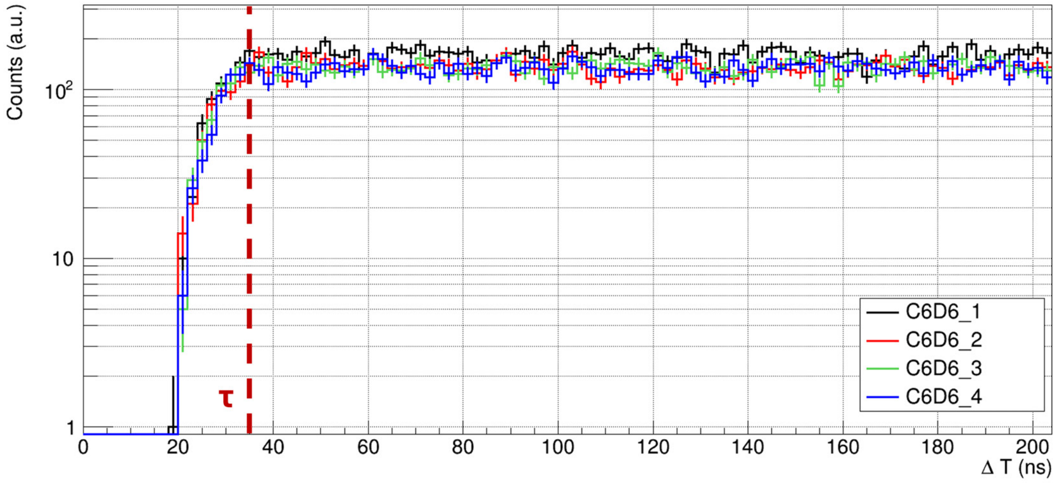

Figure 4.11: Distribution of the time interval between consecutive signals for all the detectors. The dead time has been estimated in correspondence of the red dashed line, where the distribution starts to deviate toward zero.

Several models can be applied to perform this correction [134]. In this work, the simplest one (the so-called *non-paralyzable model*) has been applied as it turned out sufficiently accurate. This model assumes that all the signals arriving within a time window τ (the *dead time*) after a given event are not recorded, without introducing any additional effect on the detector. The dead time depends on the detector, but also on the PSA parameters employed to recognize the signals. In this work, it has been evaluated by looking at the distribution of time intervals between consecutive events, shown in Figure 4.11. In particular, the dead time has been estimated as the time at which the distribution starts to deviate toward zero, at approximately 35 ns. All the signals delayed less than τ from a previous signal in the same detector have been artificially removed *a posteriori*, in order to fulfil the assumption of the non-paralyzable dead time model.

Under these conditions, the dead time correction can be evaluated as

$$N = \frac{M}{1 - m\tau} \tag{4.8}$$

where N are the expected counts, M are the measured counts (artificially corrected), m is the measured counting rate and τ is the dead time. In EAR1 dead time corrections have generally been estimated to be below 1% for all the sample measured. The correction factors for ^{30}Si and gold are shown in Figure 4.12.

The dead time correction depends on the measured counting rate, that in turn depends on the proton bunch intensity. Therefore, the effect of dead time and the relative corrections can be checked by comparing time-of-flight spectra normalized to the same number of protons obtained from dedicated and parasitic pulses, characterized by 8.5×10^{12} and 3.5×10^{12} protons per pulse, respectively. The comparison for the uncorrected spectra of the 4.9 eV saturated resonance of gold is shown in Figure 4.12: the two spectra are

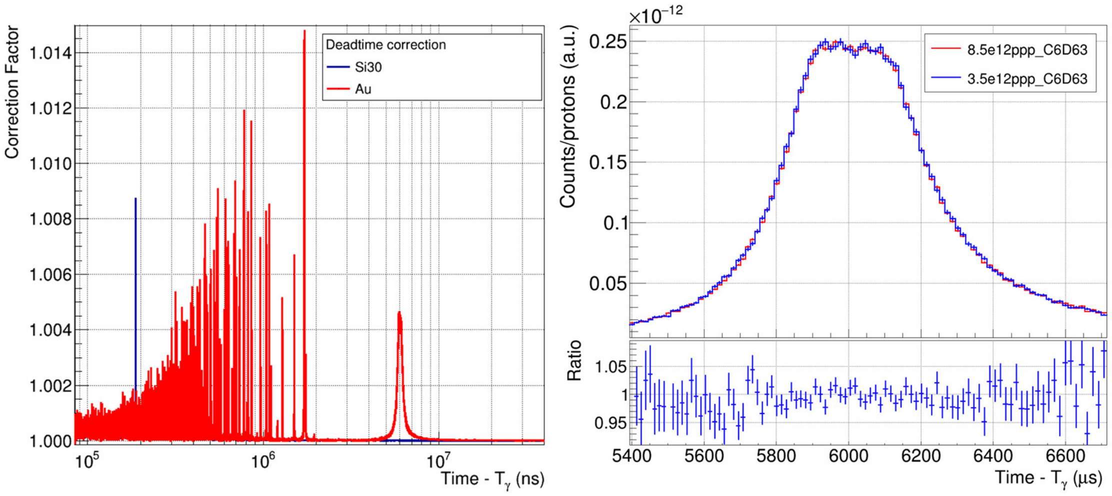

Figure 4.12: On the left: dead time corrections calculated for the ^{30}Si (blue) and 22-mm-diameter gold (red) spectra, as a function of the time of flight. On the right: comparison of the time-of-flight spectra of the 4.9 eV saturated resonance of gold obtained from dedicated and parasitic proton bunches. The spectra are compatible within the statistical uncertainty, confirming that dead time corrections are negligible for this resonance.

compatible within the uncertainty, confirming that dead time corrections are negligible for this resonance (the calculated correction factor is indeed below 0.5%).

4.3 Determination of the capture yield

Once the detectors have been characterized, beam-on data have been analysed to get the neutron capture yield, i.e. the fraction of neutrons intercepting the sample undergoing a capture reaction. This quantity was already introduced in Section 2.4, together with the simple formula used to compute it (Equation 2.17). In this work, some experimental correction factors have been added to this formula and the capture yield Y_γ as a function of the neutron energy has been finally extracted for both the enriched and natural silicon sample as

$$Y_\gamma(E_n) = \frac{f_{Corr}}{F_{Norm}} \frac{C_w(E_n) - B_w(E_n)}{\Phi(E_n)\left(Q_{(n,\gamma)} + \frac{A}{A+1}E_n\right)} \tag{4.9}$$

where:

- C_w are the counts measured by each detector, normalized by the number of protons on the spallation target, weighted and corrected for the dead time
- B_w are the estimated background counts for each detector, also normalized by the number of protons on the spallation target, weighted with the same weighting functions of the sample under study and corrected for dead time

- E_n stands for the energy of the neutron, obtained from the time of flight with the Time-Of-Flight Technique
- Φ is the evaluated neutron flux, discussed in Section 3.1.3 and normalized per the number of protons
- F_{Norm} is a normalization factor, obtained from the irradiation of a gold sample
- f_{Corr} is a correction factor to the normalization
- $Q_{(n,\gamma)}$ is Q-value of the reaction under study, while A is the atomic mass of the sample (normalized to the neutron mass). They are combined in the term in brackets at the denominator, that represents the total energy released in the capture reaction in the centre of mass system and that, according to the PHWT, corresponds to the efficiency of the detector for capture events.

The determination of each term of this formula will be discussed in detail in the following subsections.

The yield is computed separately for each C_6D_6 detector, considering each detector as an independent setup. The final yield is obtained performing a weighted average of the yields from all the detectors.

The number of protons on the target, that is used to normalize the measured counts and the evaluated neutron flux, is obtained from the BCT detector, presented in Section 3.1.4.

4.3.1 Background subtraction

The γ rays detected by the C_6D_6 detectors originate not only from neutron capture events in the sample under study, but also from other sources such as scattered neutrons captured in the experimental areas or natural radioactivity. These signals represent a background that, with the current setup, cannot be discriminated or distinguished from the signals of interest. However, their contribution can be estimated with ancillary measurements and subtracted *a posteriori* from the total measured counts. In this work three components of background have been considered: a beam-off component, a sample-independent beam-on component and a sample-dependent neutron-scattering component.

The beam-off background component is due to natural radioactivity and cosmic rays. It has been measured acquiring data without beam. Since these signals are not related to the beam operation, they are uniformly distributed in time and their time spectra can be easily fitted with a constant function, as shown in Figure 4.13. From the fitted counting rate, it is possible to reconstruct the number of beam-off counts per bin to be subtracted to the total time-of-flight spectra, normalizing to the number of triggers (i.e. to the acquisition time). This is typically the dominant source of background at neutron energies

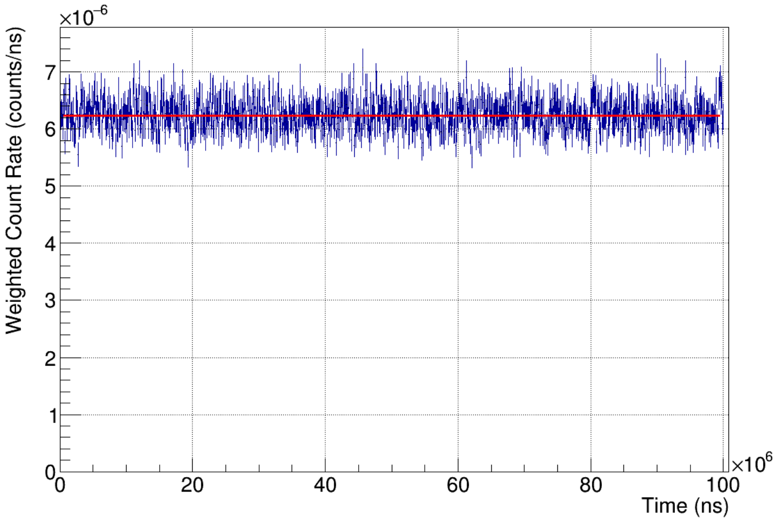

Figure 4.13: Weighted count rate for beam-off background measurement for the C_6D_6-4 detector as a function of time. The count rate is constant over time and it has been fitted with a constant function (red). The value of the fitted count rate is 6.239(9) counts/ms.

below the eV in EAR1.

The sample-independent beam-on background component is due to the interaction of the neutron beam with materials different from the sample. For example, neutrons can interact with the collimator just before the experimental area or with in-beam materials (pipe windows, Mylar supporting the samples) or they can be scattered and captured in the experimental area. This background component has been estimated irradiating a dummy sample for the ^{30}Si enriched sample or an empty sample for the ^{Nat}Si and the gold samples (refer to Section 3.4.4 for the description of the samples). The resulting count rates have been normalized to the corresponding number of protons on the spallation target. This contribution typically dominates the total background above the eV region.

The sample-dependent neutron-scattering background component is due to neutrons scattered by the sample under study and captured in the experimental areas. This is typically a smaller contribution, but it can become relevant for samples with huge scattering cross section. It has been estimated irradiating a natural carbon sample, that is characterized by a high neutron scattering cross section compared to neutron capture one. In this way, the measured signals can be safely attributed to the effect of scattered neutrons. Carbon spectra have been normalized to the corresponding number of protons on the spallation target, cleaned from the beam-off and sample-independent backgrounds and suitably scaled by a factor

$$f_{Carbon} = \frac{BIF_{sample}}{BIF_{Carbon}} \frac{n_{sample}}{n_{Carbon}} \frac{\overline{\sigma_{n,sample}}}{\overline{\sigma_{n,Carbon}}} \tag{4.10}$$

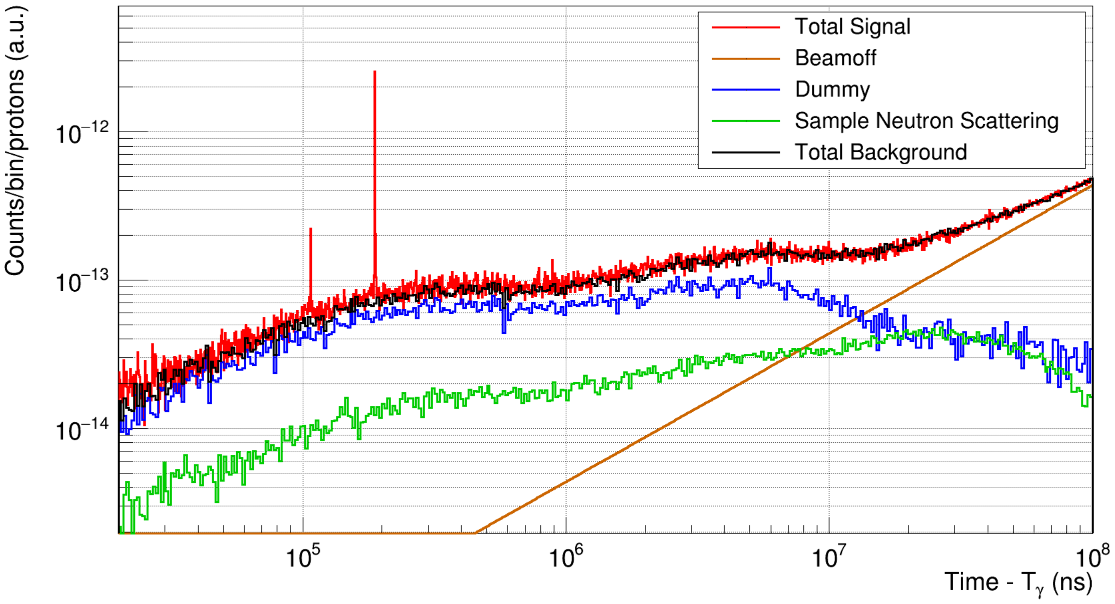

Figure 4.14: Weighted time-of-flight spectrum from ^{30}Si measurement in C_6D_6-2 at 400 bins per decade normalized to the number of protons on target (red), compared with the different estimated components of backgrounds at 100 bins per decade: beam-off (orange), sample-independent beam-on component (dummy, blue), sample-dependent neutron-scattering component (green). The total background is also shown in black.

to account for the different dimension and beam interception factor (BIF), the different thickness (n) and the different average neutron scattering cross section $\overline{\sigma_n}$ between carbon and the sample under study. In particular, the ratio between the BIF has been measured as the ratio between the top-level of the 4.9 eV saturated resonance in two gold samples, one with the same diameter of the carbon sample (20 mm) and the other with the same diameter of the sample under study (more details in Section 4.3.3). In the case of ^{30}Si (22 mm) this ratio is 1.125(12), while in the case of ^{Nat}Si it has been set at 1, as the samples have the same diameter. The ratio between the neutron scattering cross sections has been computed considering average spectral cross sections in the energy range of interest, removing possible resonances as recommended in Reference [130]. In fact, when neutrons are scattered, the correlation between neutron energy and reconstructed time of flight is lost, and scaling for pointwise scattering cross sections as a function of the neutron energy turned out therefore to be inappropriate.

Figure 4.14 shows the different estimated components of the background compared to the total counts for ^{30}Si. There are actually other background components that have not been considered in this work because expected to give a negligible contribution: the in-beam γ ray scattering and the neutron sensitivity. The former is negligible because silicon is a light nucleus and therefore quite transparent to γ rays. The latter, intended as the probability of directly detecting scattered neutrons in the detectors, is minimal

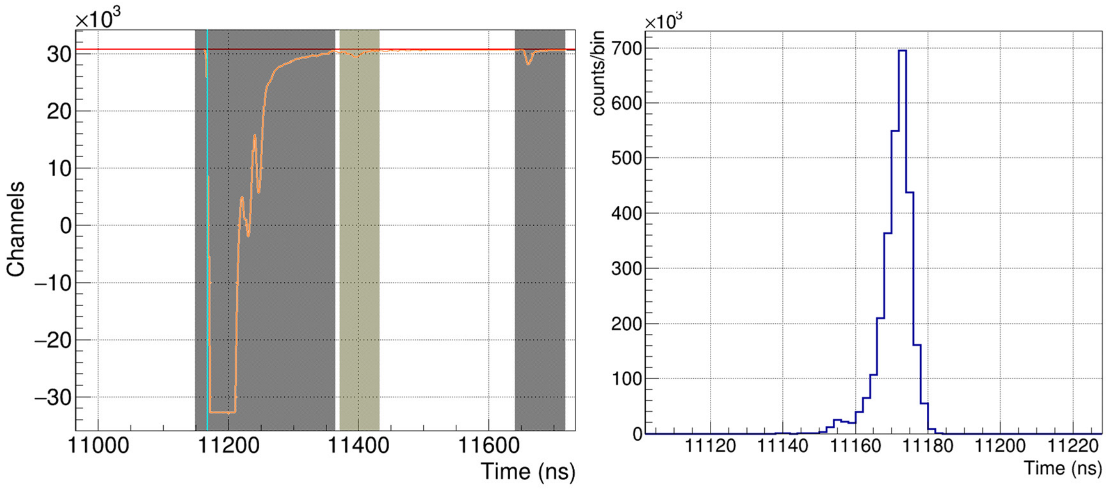

Figure 4.15: Left: typical raw signal of a γ flash seen by a C_6D_6 detector. The signal is recognized as the first saturated signal and its time t_γ is set at the 30% of the amplitude (light blue line). Right: distribution of the time of the γ flash t_γ for dedicated pulses in the C_6D_6-1 detector.

due to the optimized setup employed, as already explained in Section 3.4. In particular, considering the expected Γ_n and Γ_γ of ^{30}Si resonances and the neutron sensitivity of the setup estimated in Reference [117] in the energy range of interest (lower than 5×10^{-5}), the contribution of the neutron sensitivity has been estimated to be far below the experimental uncertainty (on the order of 0.05% for the first two resonances of ^{30}Si). However, these background components will be discussed more in detail in the analysis of data from EAR2, where they play a much more significant role.

In conclusion, it is important to consider that these procedures only provide an estimate of the background. Any possible residual background can be eventually fitted with SAMMY during the analysis of resonances (Section 6.2).

4.3.2 Time-to-Energy conversion

As already explained in Section 3.2, the Time-Of-Flight technique allows one to determine the energy of the interacting neutrons by measuring their time of flight and using the formula 3.4, that is reported also here below for convenience:

$$E_n = mc^2\left(\frac{1}{\sqrt{1-\left(\frac{L+\lambda(E_n)}{c(t-t_0)}\right)^2}}-1\right) \tag{4.11}$$

t is simply the time at which a neutron capture event is detected, while the start-time t_0, the flight-path L and the effective moderation length $\lambda(E_n)$ need to be determined, as discussed in the following lines.

The start time t_0, corresponding to the moment when neutrons are produced, has been determined using the time t_γ at which the γ-flash is observed in the C_6D_6 detectors. As the γ-flash travels at the speed of light c, t_0 can be expressed as:

$$t_0 = t_\gamma - \frac{L}{c}. \tag{4.12}$$

The time t_γ is identified by the PSA routine (Section 4.1) and its distribution has been checked to guarantee the correct identification and the elimination of possible outliers. Figure 4.15 shows a typical γ-flash signal and the t_γ distribution. Using the γ-flash to estimate t_0 is advantageous as it does not require the calibration of the time offset between detectors, which is needed if the PKUP signal is used instead. On the other hand, since the γ flash is saturated, its time identification can be less precise than using the PKUP: in fact, the t_γ distribution is approximately 20 ns wide. However, these effects become relevant at neutron energies far beyond the target of this work (higher than tens of MeV).

The neutron flight-path L, i.e. the distance between the limit of the target-moderator assembly and the sample under study, also needs to be estimated indirectly, as direct measurements are not available. A ^{197}Au sample in the same position of the sample under study is used and the neutron flight-path is fitted by SAMMY to best reproduce the energy of the well-known low-energy resonances of ^{197}Au, as shown in Figure 4.16. An iterative process is actually used: an initial flight-path is provided comparing the measured gold time-of-flight spectra with the outcome of FLUKA-based simulations and a preliminary time-to-energy conversion is performed to input the data in SAMMY, which is then used to adjust the flight-path. A second time-to-energy conversion is then performed with the adjusted flight-path and the data are again provided in input to SAMMY and so on, until reasonable convergence on the value of the flight-path is reached. In this work, this flight-path has been estimated to 183.794(1) m. The value has been additionally checked testing the alignment between measured and expected gold resonances in the keV energy region, as shown in Figure 4.16.

Eventually, the resolution function providing the effective moderation length λ has been determined from available FLUKA-based simulations of the target-moderator assembly. However, it is important to specify that the time-to-energy conversion has been performed ignoring the effective moderation length, as SAMMY includes *a posteriori* the full resolution function (shifting and broadening effects) when fitting resonances. The evaluated neutron flux is also reported following the same philosophy, for consistency.

4.3.3 Normalization

The evaluated neutron flux $\Phi(E_n)$ used in Equation 4.9 provides the energy dependence of the flux and its absolute value integrated over the full beam spatial profile. However, using a sample smaller than the beam, only a fraction of these neutrons impinges on

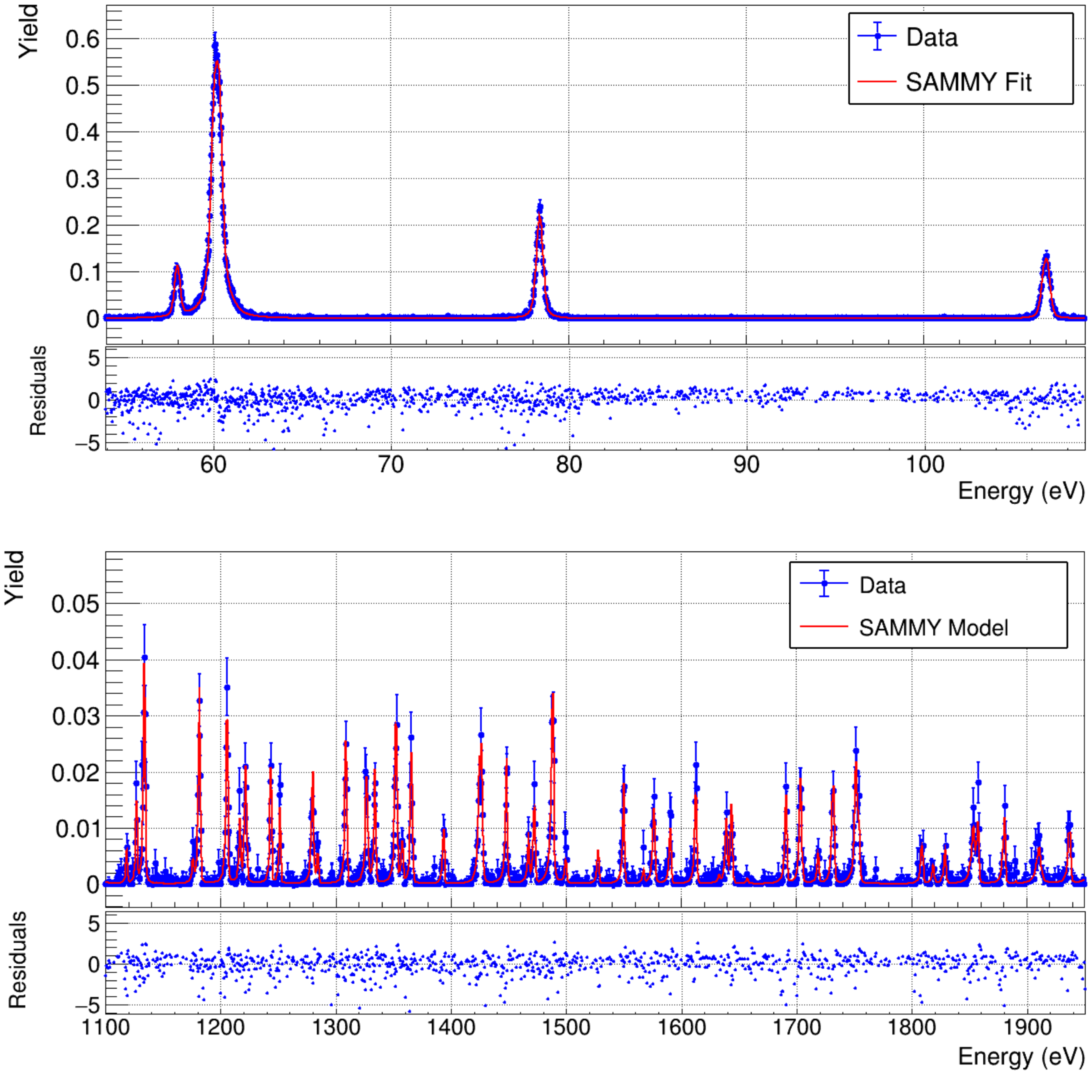

Figure 4.16: Top: fit of the low-energy resonances of gold performed with SAMMY to fit the flight-path. Bottom: comparison between the high-energy resonances of gold and the predictions from SAMMY, using the flight-path fitted at low energy. The agreement demonstrates that the flight-path is well defined.

the sample under study, referred to as *Beam Interception Factor* (*BIF*). A normalization factor F_{Norm} is therefore needed first of all to account for this BIF and determine the absolute neutron flux seen by the sample.

The normalization of the yield to a robust reference is also extremely useful to mitigate systematic uncertainties related, for example, to potentially inaccurate Monte Carlo simulations of the detector setup. In fact, small geometrical discrepancies between the simulated and the real experimental setup can exist, due to the difficulty of accurately measuring angles and positions of 3D complex objects. These discrepancies may eventually propagate to the yield through the weighting functions. Reproducing and nor-

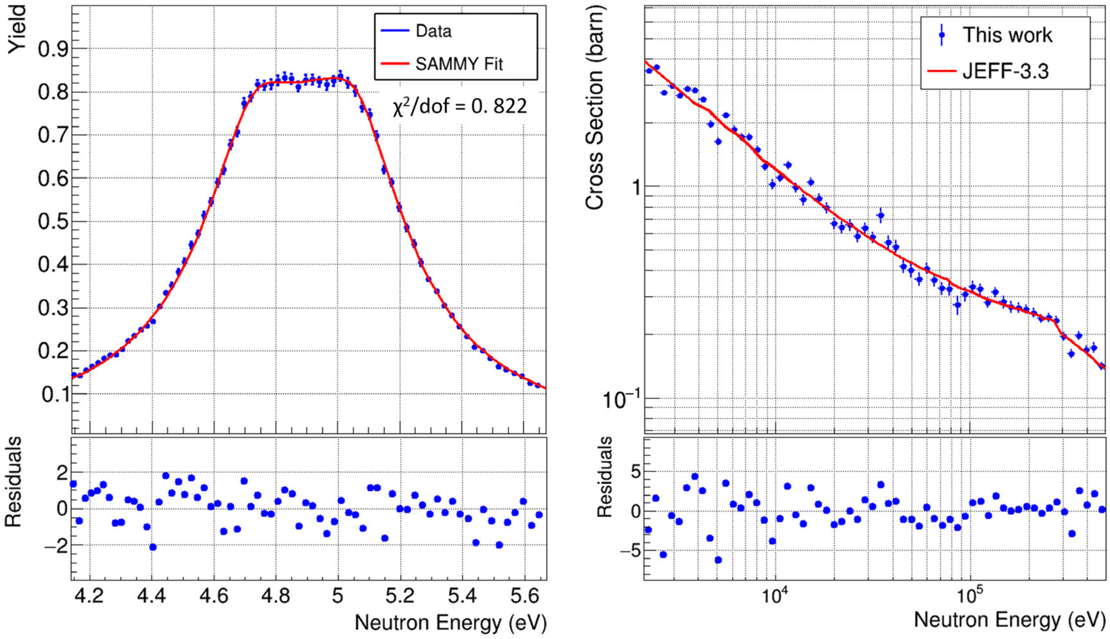

Figure 4.17: Left: fit of the 4.9 eV saturated resonance of gold performed in SAMMY to extract the normalization factor for the C_6D_6-4 detector (22-mm diameter gold sample). The double-peak structure at the top of the saturated resonance is due to multiple scattering, that is properly accounted in SAMMY. Right: comparison between measured capture cross section of gold, normalized with the value fitted in the 4.9 eV resonance, and the evaluated cross section from JEFF-3.3 in the 2 keV - 500 keV energy range. The agreement confirms the validity of the normalization factor even in the energy range of interest for this work.

malizing the capture yield to a robust standard reference allows one to include these potential discrepancies in the normalization factor, reducing the systematic uncertainty on the yield. The impact of possible inaccurate detector calibrations is also mitigated.

The normalization has been performed, for each sample, using a gold sample of the same diameter and in the same position as the sample under study, employing the *saturated resonance* technique. Details about the gold samples can be found in Table 3.1.

The method of the saturated resonance [135] is widely used in the normalization of neutron capture measurements and consists of exploiting resonances characterized by a radiative width much larger than the neutron width ($\Gamma_\gamma \gg \Gamma_n$) and by relatively large peak cross sections ($\sigma_{TOT} \approx \sigma_\gamma \geq 10^4 b$). In these resonances, even quite thin samples (which minimize the effects of self-shielding and multiple scattering) can capture almost all the impinging neutrons, leading to a capture yield that saturates to a value very close to one. Moreover, this value is nearly independent on slight variations of resonance parameters and on the sample thickness, therefore providing a robust normalization [114].

The 4.9 eV s-wave resonance of ^{179}Au meets these requirements and has been exploited in this work to estimate the normalization factor. In particular, the normalization

Sample	C_6D_6-1	C_6D_6-2	C_6D_6-3	C_6D_6-4
Au (20 mm)	0.734(4)	0.704(4)	0.783(4)	0.745(4)
Au (22 mm)	0.826(3)	0.785(3)	0.887(3)	0.842(3)

Table 4.3: Normalization factors F_{Norm} fitted for the 4.9 eV saturated resonance of gold for the 20-mm and 22-mm diameter samples using SAMMY. Differences between detectors demonstrate that the normalization factor does not only represent the BIF, but also includes corrections due to little discrepancies between real and simulated experimental setup.

factor has been fitted for each detector using SAMMY, comparing the measured and expected capture yield at the saturated top of the 4.9 eV resonance, as shown in Figure 4.17. Normalization factors fitted for the 20-mm and 22-mm diameter samples are reported in Table 4.3.

The normalization factors have been finally verified to work even in the energy range between the keV and a few hundreds of keV, that is of interest for this work and where ^{179}Au capture cross section is considered a standard (above 200 keV). In particular, the normalized measured neutron capture cross section of gold has been compared with the evaluated cross section of JEFF-3.3 [75], showing a good agreement within the uncertainty as shown in the right panel of Figure 4.17. The variation of the BIF as a function of the neutron energy is negligible in EAR1 in the energy range considered and indeed it does not affect the normalization factor.

4.3.4 Corrections to the normalization factor

The normalization factors obtained from the saturated resonance of gold require some second-order corrections before being applied to the capture yields of ^{30}Si and other samples.

First of all, the weighting functions accounting for the efficiency of the detectors have been calculated without considering any threshold on the deposited energy, which is instead actually applied in the data analysis and affects the efficiency of the setup. Therefore, for consistency, the yields need to be corrected for the counts that are lost below the threshold (*threshold correction*).

Moreover, the yields have to be corrected for the internal conversion, that occurs when a nucleus de-excites emitting an electron instead of a photon (Section 2.2.2). These events are typically not counted, as they do not deposit enough energy in the detectors: electrons can be indeed easily stopped in the sample itself and/or the accompanying X-rays are not enough energetic to be detectable. However, they need to be taken into account in a suitable correction factor (*internal conversion correction*) in order not to underestimate the capture yield .

These corrections are different and therefore have to be calculated for each sample, and potentially even for each resonance, as they depend on the de-excitation cascade and on the probability of internal conversion of the nuclear states involved in the de-excitation.

In the case of gold, these corrections are already included in the normalization fitted by SAMMY. However, if the same normalization has to be applied to other samples, a correction factor f_{Corr} has to be applied to account for the different threshold and internal conversion corrections on the sample under study. If f^{Au}_{Corr} and f^{S}_{Corr} are the total corrections to the yield of gold and of the sample under study, the correction to the normalization used in Equation 4.9 can be expressed as

$$f_{Corr} = \frac{f^{S}_{Corr}}{f^{Au}_{Corr}}. \tag{4.13}$$

As already mentioned, the estimation of these correction factors requires the simulation of the de-excitation cascade of the sample in the resonance under study. De-excitation cascades have been simulated using NuDEX [82], which provides a list of possible de-excitation paths that include γ rays and internal conversion electrons (if requested) and that are weighted by their probability. The outputs of NuDEX simulations have been coupled with GEANT4 simulations to obtain the simulated response functions of the C_6D_6 detectors to the cascades of the different samples. These functions have been finally convolved with the detector resolutions and compared with the measured energy deposited spectra of the resonances to check the accuracy of the simulations (Figure 4.18). If the gold cascade for the 4.9 eV resonance, widely employed in this kind of measurement, is well reproduced with the default parameters provided by NuDEX, the ^{31}Si cascade for the 4.98 keV resonance was not well reproduced, especially at low deposited energy where it is crucial to evaluate threshold corrections. Therefore, the NuDEX parameters had to be tuned in order to achieve a better agreement.

Simulation of the de-excitation cascade of ^{31}Si

NuDEX is based on the theory of electromagnetic de-excitation of nuclei discussed in Section 2.2.2. To model the de-excitation of a nucleus, NuDEX generates its full level scheme including all the possible electromagnetic transitions between levels with their relative probabilities. First, it assumes the known excitation levels and transition probabilities from a database based on RIPL-3 (Reference Input Parameter Library [86]) and ENSDF (Evaluated Nuclear Structure Data File [83]). Then, it fills the missing information with statistical models. In particular, the level scheme above E_{cutoff} (excitation energy below which the level scheme is assumed to be fully known) is generated randomly according to level density models. The unknown transition probabilities between levels are instead computed using the Photon Strength Functions multiplied by a random factor distributed as a Porter-Thomas distribution. In the de-excitation of the 4.98 keV resonance of ^{30}Si (i.e. 6.592 MeV excited state of ^{31}Si) the level scheme is known up to an energy well above the neutron separation energy, therefore only the probabilities of the different primary transitions have been tuned. In fact, none of these probabilities were included as known in the database, therefore they have been set to reproduce the experimental data instead of being set randomly, as NuDEX would have done by default.

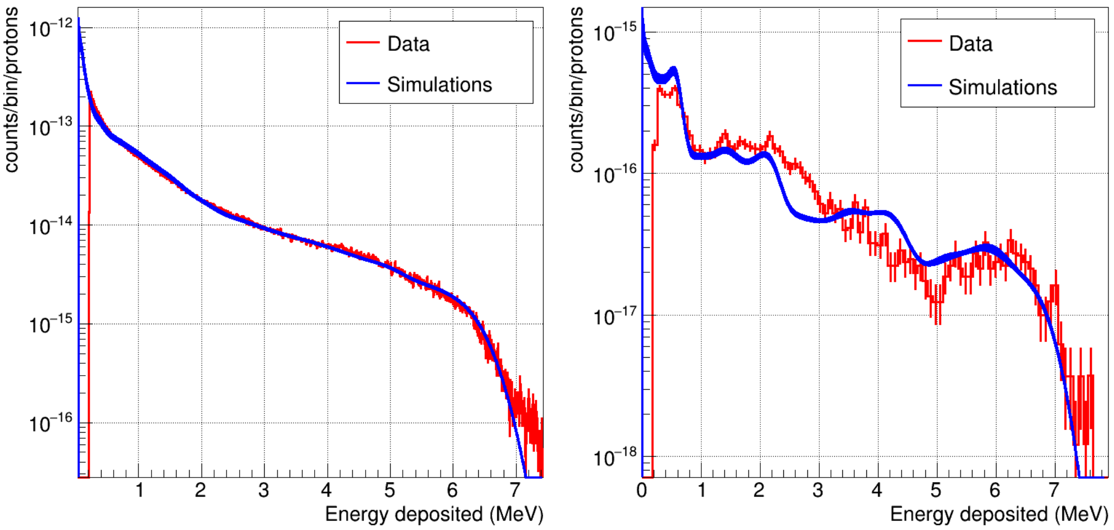

Figure 4.18: Comparison between measured and simulated response functions of C_6D_6-4 to the de-excitation cascade of the 4.9 eV resonance of gold (left) and the 4.98 keV resonance of ^{30}Si (right). Default cascades provided by NuDEX have been used in the simulations, that are in agreement with data for gold, but not for ^{30}Si.

In order to explain the procedure followed to tune these probabilities, the term "partial cascade" can be introduced referring to the de-excitation cascades initiated by a single, well defined primary transition. These partial cascades have been simulated separately in NuDEX, enabling only one primary transition at a time from the 6.592 MeV excited state of ^{31}Si. Each partial cascade has been then processed with GEANT4 and convolved with the experimental resolution to get the corresponding response functions of the C_6D_6 detectors. This procedure has been repeated only for the most energetic and therefore probable primary transitions.

The response function of the C_6D_6 detectors to the total de-excitation cascade R_C has been then built as a linear combination of the partial response functions R_{C_i}

$$R_C = a_1 R_{C_1} + a_2 R_{C_2} + a_3 R_{C_3} + a_4 R_{C_4} + ... + a_i R_{C_i} \tag{4.14}$$

and finally compared to the experimental deposited energy spectra. Since only the direct transition to the ground state (R_{C_1}) could explain the intense γ ray observed at approximately 6.5 MeV, the corresponding parameter a_1 could be easily fitted and fixed, providing a sort of normalization. All the other parameters a_i have been tuned in order to get the best agreement with the experimental data, as shown in Figure 4.19. The intensity of each primary transition has been finally determined by normalizing each coefficient a_i to the sum of all the coefficients $\sum_i a_i$. Some of the de-excitation path with the corresponding adjusted intensities have been already shown in Figure 2.3.

This tuning procedure could be performed only for the de-excitation cascade of the 4.98 keV resonance of ^{30}Si, while for other resonances the statistics was too poor to get an experimental cascade to compare simulations with. However, most of the resonances

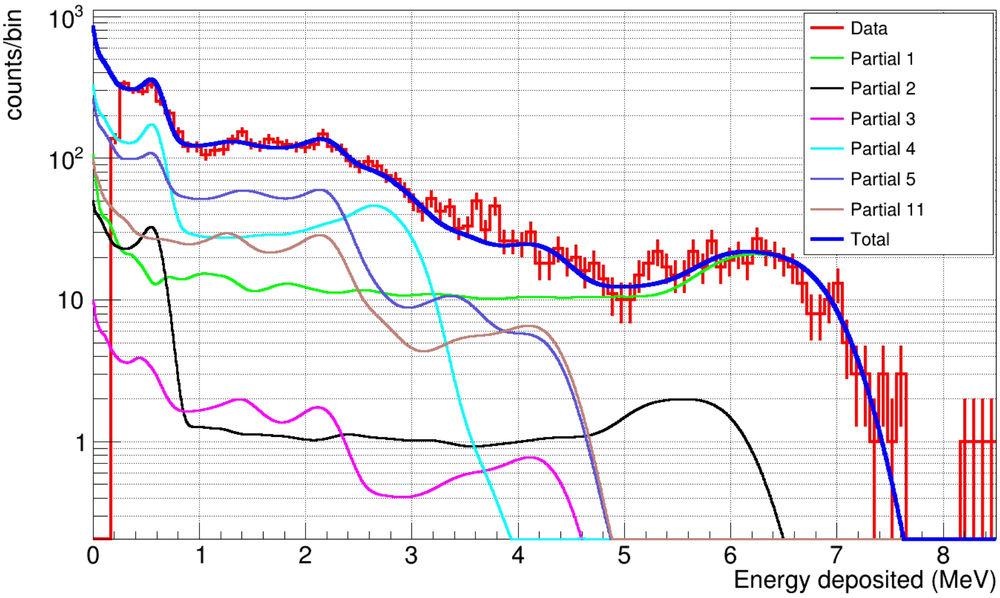

Figure 4.19: Comparison between measured (red) and simulated (blue) response functions of the C_6D_6-4 detector to the de-excitation cascade of the 4.98 keV resonance of ^{30}Si, using adjusted transition probabilities. The simulated response function has been built as a linear combination of the partial cascades shown in the plot, combined with coefficients tuned to get the best agreement with experimental data.

observed in ^{30}Si are characterized by the same spin-parity, therefore the corresponding cascades and relative corrections can be assumed to be quite similar. Moreover, for high energy resonances (above 100 keV) these corrections become less significant as the statistical uncertainty gets several factors higher.

Estimation of the correction factors

Once the de-excitation cascade and the corresponding response functions have been simulated, indications of the counts lost below threshold and because of internal conversion could be easily retrieved. The correction factor for each sample f^S_{Corr} can be indeed written as

$$f^S_{Corr} = \frac{\sum_{i=0}^{\infty} W_i R_{C,\, noIC,\, i}}{\sum_{i=thr}^{\infty} W_i R_{C,\, IC,\, i}} \tag{4.15}$$

where $R_{C,\, IC,\, i}$ and $R_{C,\, noIC,\, i}$ are the simulated response functions with and without internal conversion, respectively (this option can be set in NuDEX), W_i are the weighting functions computed in Section 4.2.2, i is an index running on the bins of energy deposited and thr is the threshold set on the deposited energy. The numerator of Equation 4.15 represents therefore the theoretical total expected counts, estimated as the integral of the simulated weighted response function over its full energy range without considering the internal conversion (that causes loss of counts). On the other side, the denominator

Factor	C_6D_6-1	C_6D_6-2	C_6D_6-3	C_6D_6-4
$f_{Corr}^{^{30}Si}$	1.0052(17)	1.0057(17)	1.004(2)	1.006(2)
f_{Corr}^{Au}	1.050(3)	1.058(3)	1.045(4)	1.052(3)
f_{Corr}	0.957(3)	0.950(3)	0.961(4)	0.957(4)

Table 4.4: Correction factors to the capture yields estimated from Monte Carlo simulations taking into account the effects of the threshold in energy deposited and the internal conversion. The factors refers in particular to the 4.98 keV resonance of ^{30}Si ($f_{Corr}^{^{30}Si}$) and to the 4.9 eV resonance of gold (f_{Corr}^{Au}). Their ratio (f_{Corr}, in the last line) represents the final correction to be applied to the normalization of the capture yield of ^{30}Si.

represents the experimentally expected counts, estimated as the integral of the simulated weighted response function only above the threshold and considering the impact of internal conversion, present in real experiments. The correction factors are reported in Table 4.4 together with their ratios, that represent the final corrections applied to the normalization factors. Corrections for the de-excitation cascade of the 4.9 eV resonance of gold are larger than for ^{30}Si because the excited levels of a heavier nucleus are typically closer, making internal conversion and low-energy transitions more probable than in a light nucleus. In fact, the internal conversion in the de-excitation of ^{31}Si turned out to be completely negligible.

Another potential correction to the yield that has to be mentioned is due to the *summing effect*, i.e. the possibility that two or more γ rays from the same cascade are detected simultaneously in the same detector. In this case, the individual signals are summed into a larger signal, that is weighted accordingly and, since the weighting functions are not linear with the deposited energy, leads to an overestimation of the capture yield. However, recent analyses of similar setups [133, 136] have shown that the corresponding corrections are typically negligible (on the order of or below 0.5%), therefore this effect has been ignored.

4.4 Estimation of ^{30}Si mass

It is not needed to know the mass of the sample (or its areal density) to extract the experimental yield, however it is a crucial parameter to fit and determine resonance parameters and cross sections, that is the final goal of this work.

As already mentioned in Section 3.4.4, the ^{30}Si enriched sample used in this work underwent oxidation during the preparation, increasing its mass. Therefore, the actual mass of ^{30}Si in the final sample could not be directly measured. This quantity had to be estimated indirectly irradiating a natural silicon metallic sample, whose ^{30}Si content could be determined from its known natural abundance of 3.092(11)% [27]. The procedure can be summarized as follows:

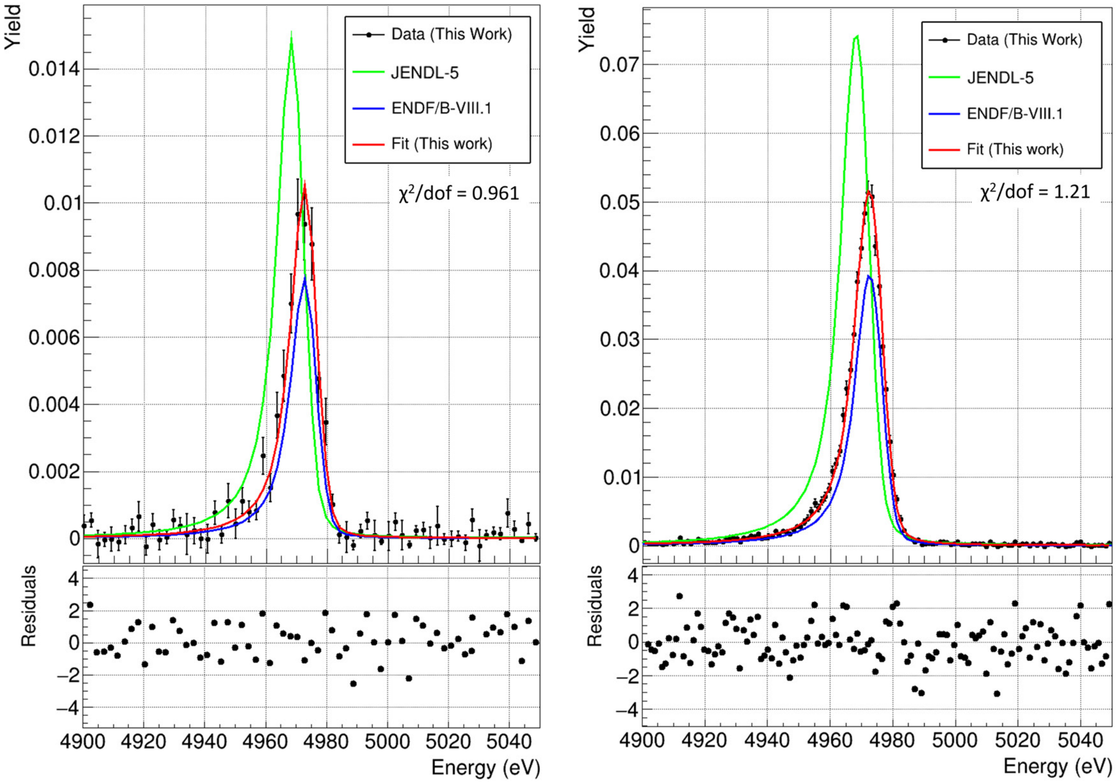

Figure 4.20: Fit of the 4.98 keV resonance of ^{30}Si in the measured capture yield from the ^{Nat}Si sample (left) and from the enriched ^{30}Si sample (right). The fit (red) has been performed with SAMMY and it is compared with the predictions of the evaluated nuclear data library JENDL-5 (green) [72] and the more recent ENDF/B-VIII.1 (blue) [70].

a) The capture yield from the natural metallic sample has been extracted and fitted with the R-Matrix code SAMMY (more details in Chapter 6) to determine the kernel of the 4.98 keV resonance of ^{30}Si, as shown in the left panel of Figure 4.20.

b) The same resonance has been fitted from the capture yield of the ^{30}Si enriched sample (right panel of Figure 4.20). The mass (and areal density) of the sample before the sintering has been used as an initial guess for the mass of ^{30}Si in the sample. This value is reported in Table 3.1.

c) The ratio between the kernels estimated in **a)** and **b)** eventually allowed the determination of the mass of ^{30}Si in the enriched sample. In fact, this ratio represents the correction factor that has to be applied to the initial guessed mass used in **b)** to determine the actual mass of ^{30}Si.

In addition, the mass of ^{30}Si has been also fitted directly from the capture yield of the enriched sample using SAMMY, fixing the 4.98 keV resonance parameters fitted in **a)**. The result is in agreement with the one obtained from the ratio of the kernels. Results are shown in Tables 4.5 and 4.6.

	^{30}Si sample	^{Nat}Si sample	Ratio
Kernel (meV)	242(3)	261(13)	0.93(5)

Table 4.5: Kernels of 4.98 keV ^{30}Si resonance, as fitted by SAMMY from the ^{Nat}Si capture yield and from the ^{30}Si capture yield using the pre-sintering sample mass as initial guess (Table 3.1). The ratio of the kernels represents the correction factor to get the actual mass of ^{30}Si.

	Total final	Total pre-sintering	^{30}Si Estimated (Ratio of kernels)	^{30}Si Estimated (SAMMY fit)
Mass (g)	0.9935(1)	0.7503(1)	0.69(3)	0.68(4)
Areal density (at/barn)	$6.5(4)\times10^{-3}$	$3.888(4)\times10^{-3}$	$3.59(18)\times10^{-3}$	$3.5(2)\times10^{-3}$

Table 4.6: Estimated ^{30}Si mass and areal density in the enriched sample, obtained from the ratio of the kernels reported in the previous table and directly from the fit of the ^{30}Si capture yield fixing the 4.98 keV resonance parameters. The results are compared with the final and the pre-sintering masses and areal densities. The final total areal density has been calculated assuming that the sample contains only oxygen apart from silicon.

The actual mass of ^{30}Si in the final sample has been found to be approximately 7% lower than the initial guess, which can be compatible with loss of material occurred in the manipulation of the sample. For example, during the preparation of the sample to place in beam, a quite significant amount of material was lost as powder that stuck on the sample container. In conclusion, only approximately 70% of the mass of the final sample has been estimated to actually be ^{30}Si, while the rest 30% is probably oxygen. In this case, the isotopic abundance of ^{30}Si in the sample would be only approximately 55%.

The mass (and consequent areal density) estimated in this section has been eventually fixed in SAMMY and used to fit resonance parameters from the capture yield of the enriched sample (Section 6.2). Only the kernel of the 4.98 keV resonance has been obtained from the yield of the natural sample.

However, it is important to underline an important drawback on this method: even if a highly enriched sample was available, the final accuracy of this work has been limited by the statistical uncertainty of the fit performed on the capture yield of the natural sample, whose ^{30}Si content is only approximately 3%. In fact, because of the low natural abundance of ^{30}Si and of the limited scheduled beam time, the statistical uncertainty on the fitted kernel of the 4.98 keV resonance of ^{30}Si is approximately 5%, four times larger than the 1.2% reached using the enriched sample. As it will be discussed in Section 6.2, this uncertainty eventually represents the systematic uncertainty associated to the ^{30}Si mass and it is the dominant contribution of the total systematic uncertainty. It is therefore propagated to all the resonance parameters, even if fitted from the yield of the ^{30}Si enriched sample.

Chapter 5

Analysis of ^{30}Si(n,γ) and ^{64}Ni(n,γ) data in EAR2

This section deals with the analysis of the data collected in EAR2, that has been exploited to measure the ^{64}Ni(n,γ) cross section and to try to measure the thermal cross section of ^{30}Si(n,γ) reaction. The analysis of the data from EAR2 is more complicated than in EAR1 because of several factors: higher counting rates due to the higher neutron flux, compressed kinematics due to the shorter flight path, worse energy resolution and a relatively recent experimental setup that still lacks thoroughly established experience. However, the procedure followed for the data analysis is the same as the one described in detail in the previous chapter, therefore it will not be repeated. Instead, this chapter will focus only on the specific results and on the additional work specifically performed for EAR2, in particular concerning dead-time corrections (Section 5.1.5), background evaluation (Section 5.2.1) and evaluation of thermal cross sections (Section 5.2.4). The fit of the capture yields and the preliminary results will be eventually reported in Chapter 6.

5.1 Pulse Shape Analysis and Characterization of the detectors

5.1.1 Pulse Shape Analysis (PSA)

Also in this case, the first step of the analysis has consisted in the processing of the raw data to identify signals and extract their relevant information. This procedure is based on the same Pulse Shape Analysis (PSA) routine described in the previous chapter (Section 4.1).

However, differently from EAR1, the amplitude, area and time of the signals have been retrieved by employing the pulse shape fitting option, which consists in fitting the full shape of the identified signal with a known shape provided as input. This option has been preferred due to the high counting rate and consequent pileup observed in EAR2, especially in gold samples. In fact, when a signal appears on the tail of another

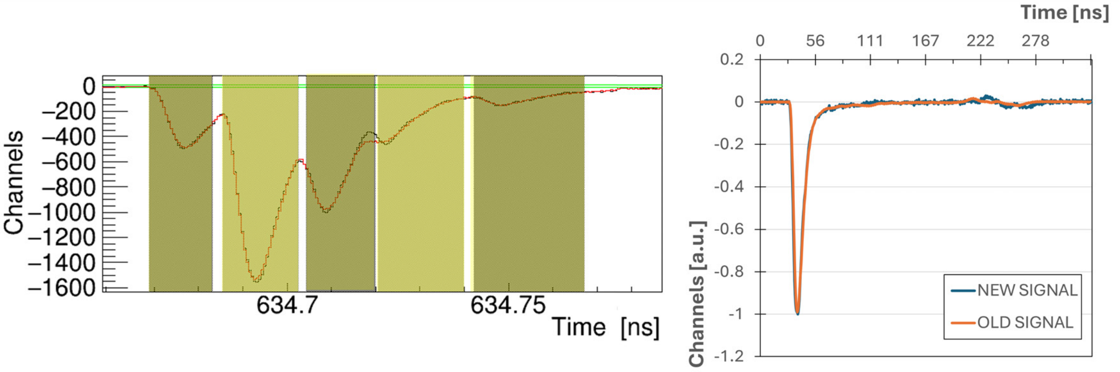

Figure 5.1: Left: pulse shape fit (red) of raw data waveform (black) in case of pileup in a gold spectrum. Right: input signal shape provided to PSA for pulse shape fitting. The original shape (orange) has been slightly adjusted (blue) to better reproduce signal rebounds.

signal, only the pulse shape fitting option allows one to properly disentangle and fit both signals, as shown in Figure 5.1. Simpler methods (such as the one applied in EAR1) would indeed fail in providing area and amplitude of the superimposed signals.

The input shapes of the signals are typically computed for each detector by averaging the shapes of many signals. In this work, the signal shapes have been taken from previous measurements, but they had to be slightly modified for some detectors (Figure 5.1) to better reproduce rebounds and decrease the threshold set on the deposited energy.

5.1.2 Detector calibration

The procedure followed for the calibration of the detectors is exactly the same as the one applied in EAR1, but employing the area of the signals instead of their amplitudes. In particular, measurements with the radioactive sources listed in Table 4.1 have been performed and repeated once per week to check the stability of the detectors. Then, the calibration has been performed by directly comparing measured signal area spectra with simulated energy deposited spectra for the different employed sources. Detector resolution and gain have been varied at the same time to achieve the best agreement between data and simulations and eventually fitted to get calibration and resolution curves for each detector. The agreement achieved with this procedure for sTED-6 detector is shown in Figure 5.2, while the final fitted curves are shown in Figure 5.3. Quadratic calibrations (Equation 4.3) have been used for all the detectors (even if they are pretty linear, especially the sTED), while the resolution has been fitted with the function 4.5 used in EAR1. The calibration curves have been finally checked by comparing the energy deposited spectra of the 4.9 eV resonance of ^{197}Au in the different detectors.

Concerning the C_6D_6 detectors, a gain shift was noticed when comparing the deposited energy spectra of the radioactive sources in different weeks. This is shown in Figure 5.4. In particular, the total gain shift during the whole campaign has been evaluated to be between 2.8% and 3.8%, depending on the detector. This effect has been

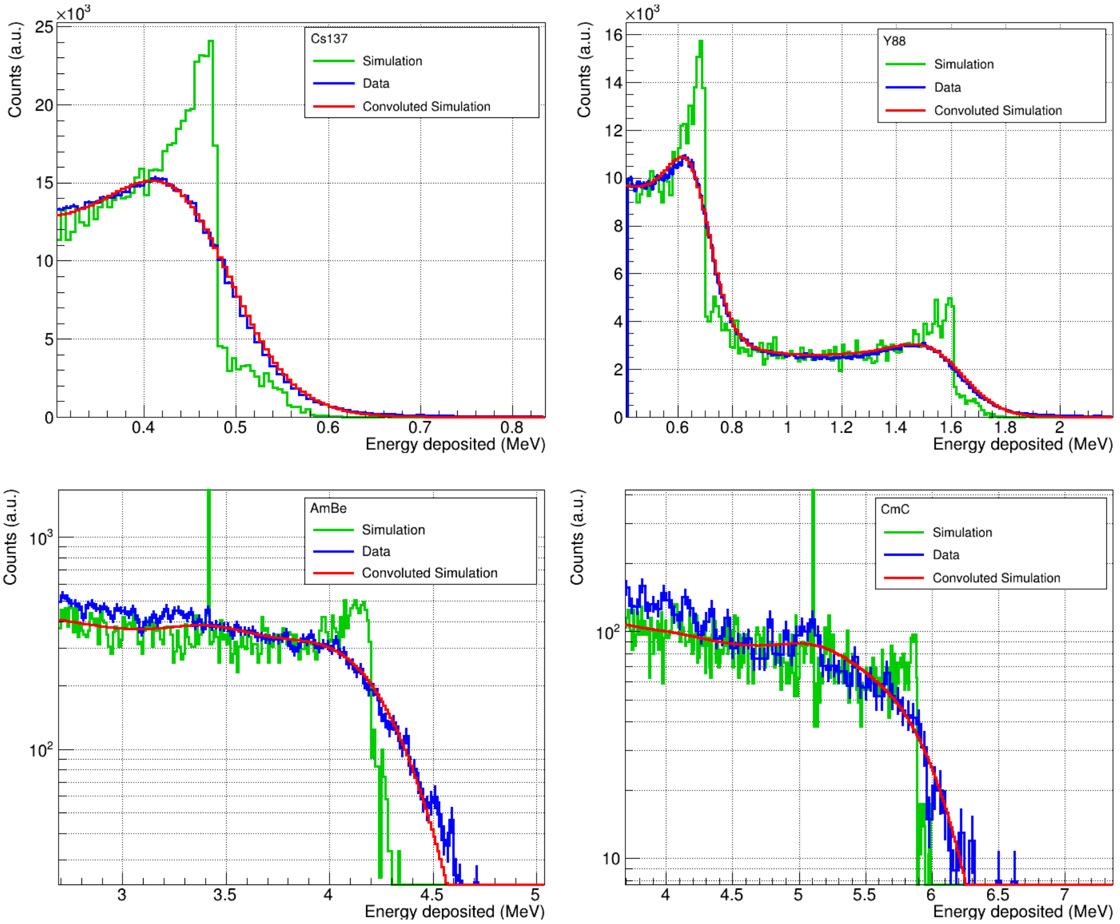

Figure 5.2: Comparison between simulated and measured deposited energy spectra in the sTED-6 detector for the sources employed in this work. The final calibration and energy resolution curves are employed in the plots. Green lines represent GEANT4 simulated spectra, red lines represent the simulated spectra convolved with the detector resolution and blue lines represent calibrated experimental data.

accounted for by fitting the gain shift as a function of time (using the weekly calibration runs, Figure 5.4) and applying a time-dependent correction to the area of the signals. In this way, the effect of gain shift has been eliminated and a single reference calibration function could be used for each detector.

5.1.3 Weighting functions

The weighting functions required by the Pulse Height Weighting Technique have been computed by performing Monte Carlo simulations, again using the same procedure described in the previous chapter.

The experimental setup of EAR2 has been accurately implemented in GEANT4, as shown in Figure 5.5, and the response functions of each detector for γ rays of different

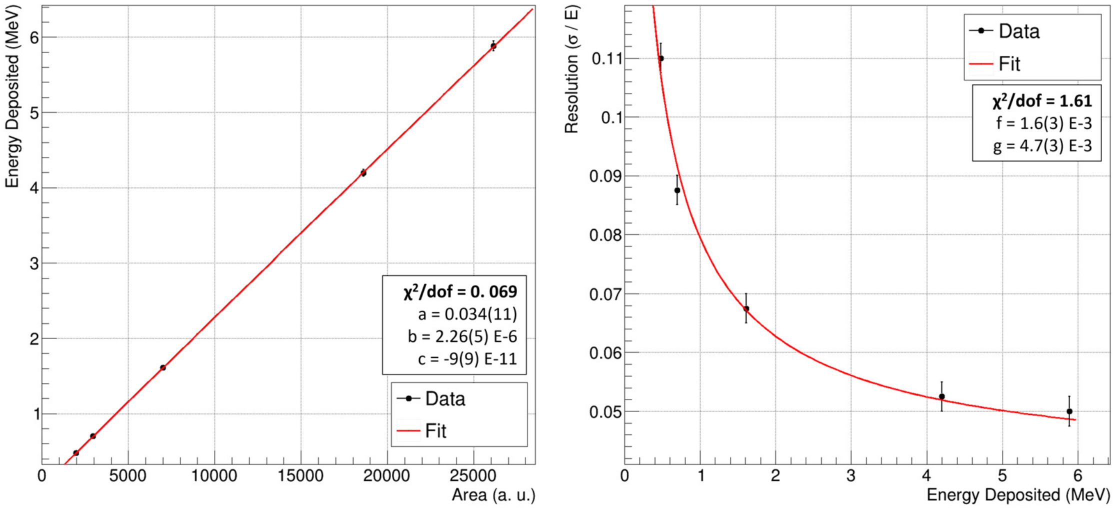

Figure 5.3: Fit of the calibration (left) and resolution (right) curves for the sTED-6 detector, using the data obtained from direct comparison between measured and simulated amplitude spectra, shown in the previous figure. The fitted parameters are referred to Equations 4.3 and 4.5, respectively.

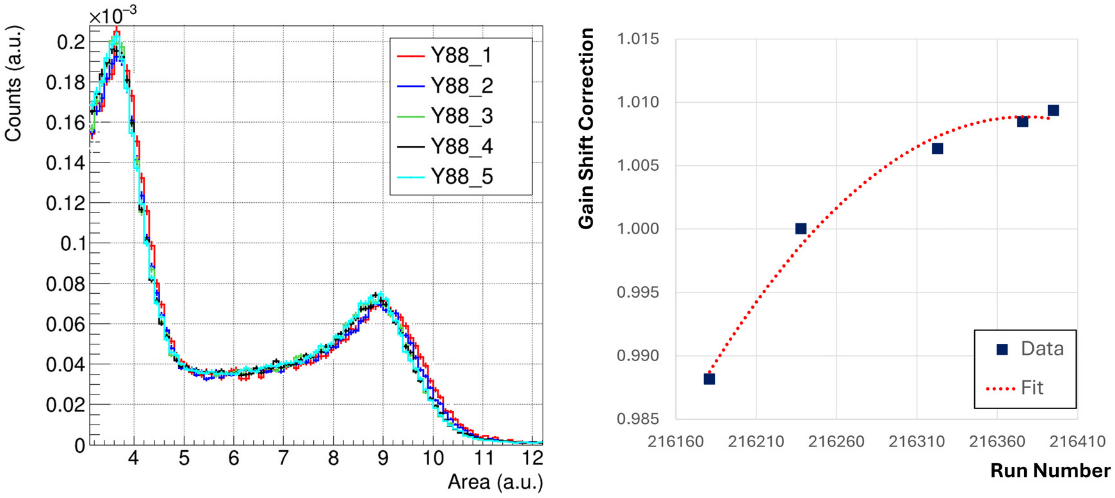

Figure 5.4: Left: ^{88}Y spectra of the C_6D_6-2 detector measured along the ^{64}Ni campaign and showing a detector gain shift. Right: fit of the gain shift (normalized to a reference run) as a function of the run number, used to correct for the gain shift run by run. A second-order polynomial has been used.

energies have been determined for the different samples irradiated (^{30}Si, ^{Nat}Si, ^{64}Ni and ^{197}Au of different diameters). In particular, $2{\times}10^7$ γ rays have been simulated for each energy, chosen between 100 keV and 1 MeV with an increment of 100 keV and between 1 MeV and 8.5 MeV with an increment of 500 keV. γ rays have been assumed to be isotropically emitted from the sample, while self-shielding effects and the transversal

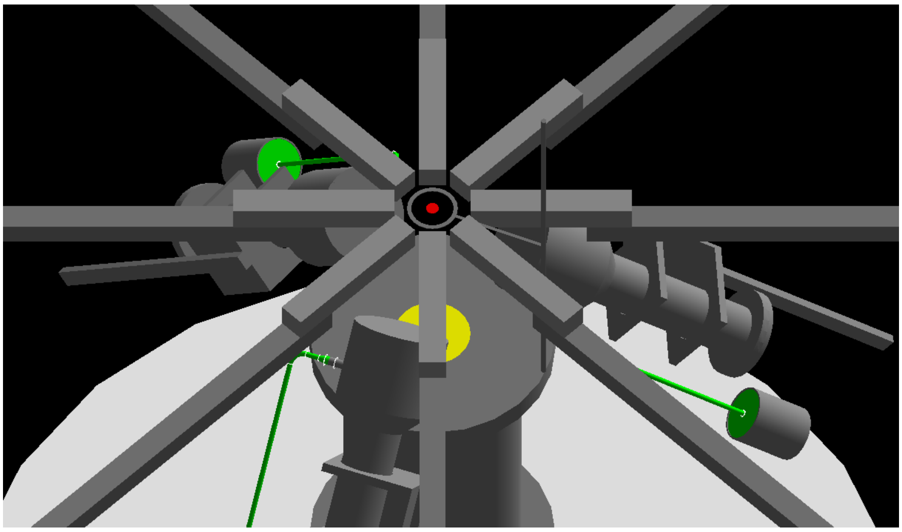

Figure 5.5: Experimental setup of EAR2 reproduced in GEANT4 for the determination of the weighting functions. A picture of the real setup can be found in Figure 3.8.

dimensions of the beam have been taken into account to simulate their origin position in the sample. No deposited energy threshold has been considered for the detectors.

The resulting efficiency of the sTED detectors as a function of the γ ray energy is shown in the left panel of Figure 5.6. As expected because of the smaller active volume, it is definitely smaller than the efficiency of the bigger C_6D_6 detectors: it is always below 1% and even below 0.3% for high energy γ rays.

The weighting functions have been finally computed by minimizing the expression 4.6 using polynomials of degree 4 for all the samples. The accuracy of the results has been assessed by considering the ratio 4.7, whose values are compatible with one generally within ± 1%, as shown in the right panel of Figure 5.6. As in EAR1, bigger deviations are observed at low deposited energy, but they are expected not to produce significant effects.

5.1.4 Deposited energy threshold

Signals from the sTED detectors also include low-amplitude noise and rebounds that require the application of a threshold on the deposited energy. The pulse shape fitting option in the PSA, employed for EAR2, enables the inclusion of prompt electronic rebounds in the shape of the signals, therefore decreasing their impact on the determination of the threshold.

The same procedure described in EAR1 has been employed to evaluate suitable deposited energy thresholds for each detector, by studying the energy deposited by rebounds. In conclusion, a threshold of 130 keV has been set for all the sTED detectors, while a threshold of 150 keV has been chosen for the bigger C_6D_6 detectors.

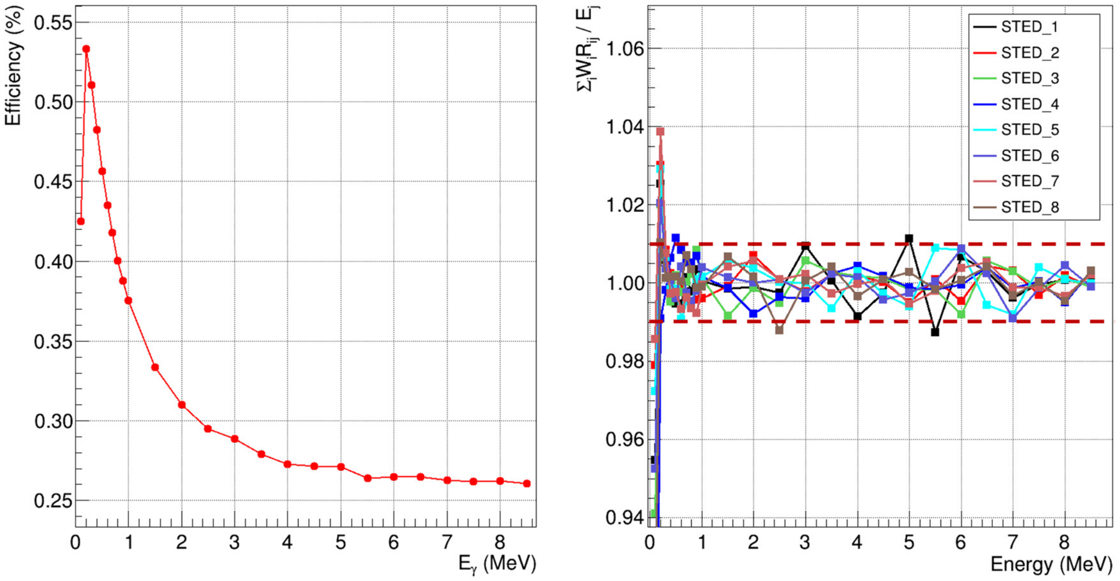

Figure 5.6: Left: simulated efficiency of one sTED detector for detecting γ rays of different energies. Because of the smaller active volume, the efficiency is smaller than in a C_6D_6 detector. Right: evaluation of the accuracy of the weighting functions obtained for ^{64}Ni sample for all the detectors. On the y-axis the weighted efficiency divided by the energy of the γ ray is reported, as a function of the energy of the γ ray on the x-axis. Deviations from unity are generally within ± 1%.

5.1.5 Dead time corrections

Dead time corrections require a more detailed discussion in EAR2, as they become significantly more important than in EAR1 because of the higher neutron flux and consequently higher counting rates.

The evaluation of the dead time has been performed in the same way as in EAR1: the distribution of the time interval between consecutive signals has been studied (Figure 5.7) and the value of the dead time has been fixed at 25 ns, corresponding to the time where this distribution starts to deviate toward zero. As expected, this distribution clearly resembles an exponential in EAR2, while in EAR1 it looked flatter because of the lower counting rate.

Once the dead time has been evaluated, the relative corrections have been computed using again the non-paralyzable model and the Equation 4.8. They are shown in Figure 5.8 for the different samples irradiated and considering dedicated bunches of 8.5×10^{12} protons, that require the biggest corrections. As anticipated, dead time corrections are definitely larger than in EAR1: in the saturated resonance of gold they range between 10% and 20% depending on the diameter of the sample, one order of magnitude higher than in EAR1.

As these huge effects were expected, a special beam configuration was adopted during the gold irradiation. Apart from the usual dedicated (8.5×10^{12} protons) and para-

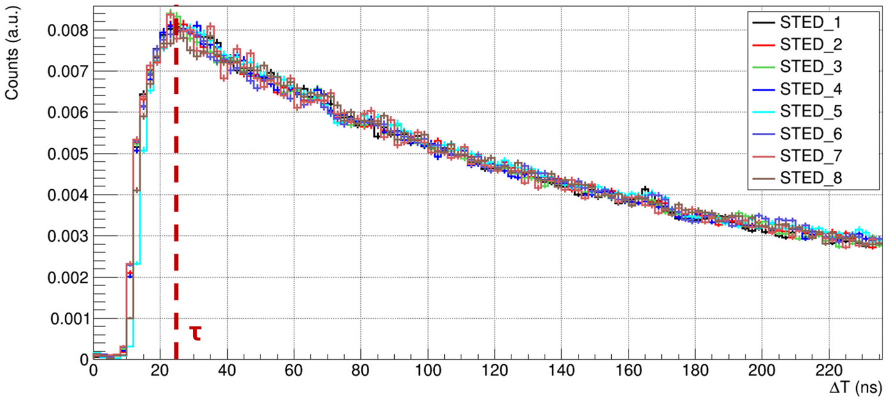

Figure 5.7: Distribution of the time interval between consecutive signals for all the detectors. The dead time has been estimated in correspondence of the red dashed line, where the distribution starts to deviate toward zero.

sitic (3.5×10^{12} protons) proton bunches, this configuration included bunches of 5×10^{11}, 1×10^{12} and 2×10^{12} protons on target, each of them characterized by different dead time corrections. The spectra from these different bunches have been compared before and after the application of the dead time corrections to experimentally assess the impact of the dead time and the validity of the model used to determine the corrections. The comparison is shown in Figure 5.9 for unweighted and weighted counts.

For unweighted counts, the dead time corrections obtained with the non-paralyzable model work properly, as a remarkable agreement is reached between spectra from bunches of different intensities after applying the corrections. However, the same corrections no longer work where considering weighted spectra.

This problem was already observed in previous measurements and explained in terms of pile-up [137]. In fact, if signals come too close in time, only one pulse may be recognized (dead time correction), but it may be characterized by a higher amplitude or area resulting from the superposition of more real signals (pile-up). This distortion of the amplitude spectrum does not affect dead time corrections themselves, but introduces a relevant effect opposite to the dead time when applying the weighting functions, that depend on the signal amplitude and assign greater weight to high-amplitude signals. In previous measurements this problem was solved with complex Monte Carlo simulations [137], whose results do not work if applied to the present case.

In this work a simpler strategy could be applied, at least in first approximation. The effects of dead time and pile-up seem to neutralize each other in the saturated resonance of the 15-mm-diameter ^{197}Au sample (the one used to normalize ^{64}Ni data). In fact, as shown in Figure 5.9, the weighted spectra from the bunches of different intensities are in agreement within 2% (within the statistical uncertainty in some cases) without applying any correction. Moreover, the normalizations fitted on the top of the saturated resonance can reproduce the thermal cross section of ^{197}Au, which is a standard, with a 3% accuracy (see Section 5.2.4). This uncertainty is well within the accuracy targeted by this measurement, therefore no dead time corrections have been applied to the spectra

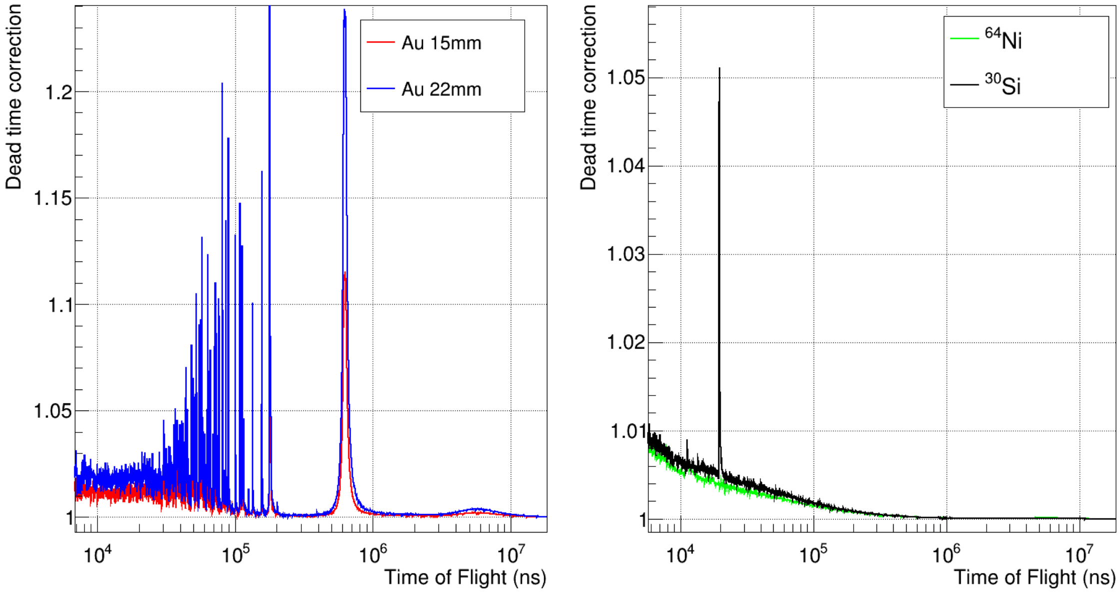

Figure 5.8: Dead time corrections calculated for the spectra of the the ^{197}Au (left panel), ^{30}Si and ^{64}Ni (right panel) samples. The corrections refer to dedicated bunches (8.5×10^{12} protons per pulse), that require the maximum correction, and have been computed using the non-paralyzable model.

of the 15-mm-diameter ^{197}Au sample.

Unfortunately, this approximation could not be applied to the 22-mm-diameter gold sample (used to normalize ^{30}Si data). In this case, as will be discussed in Section 5.2.3, the thermal cross section of ^{197}Au will be used for normalization, where dead time corrections are lower, at the level of EAR1 (within 0.5%).

Concerning the other samples (^{30}Si and ^{64}Ni), dead time corrections are almost negligible. In particular, they are completely negligible at thermal energies for both samples, while they are still below 1% for ^{64}Ni in the energy range of astrophysical interest. A correction of approximately 5% would be required for the 5 keV resonance of ^{30}Si, but it has already been measured in EAR1 and it is not the target of the measurement in EAR2.

The results described until now refer to the sTED detectors. Concerning the bigger C_6D_6 detectors, the dead time has been evaluated at 32 ns, but corrections in the saturated resonance of gold are always prohibitive (more than 20% in the 15 mm diameter sample). However, in the thermal region dead time corrections are within 1% also for the C_6D_6 detectors.

5.2 Determination of the capture yield

As discussed concerning EAR1 analysis, the capture yield has been calculated using the formula 4.9, performing background subtraction, time-to-energy conversion and normalization to gold that will be discussed in the next subsections.

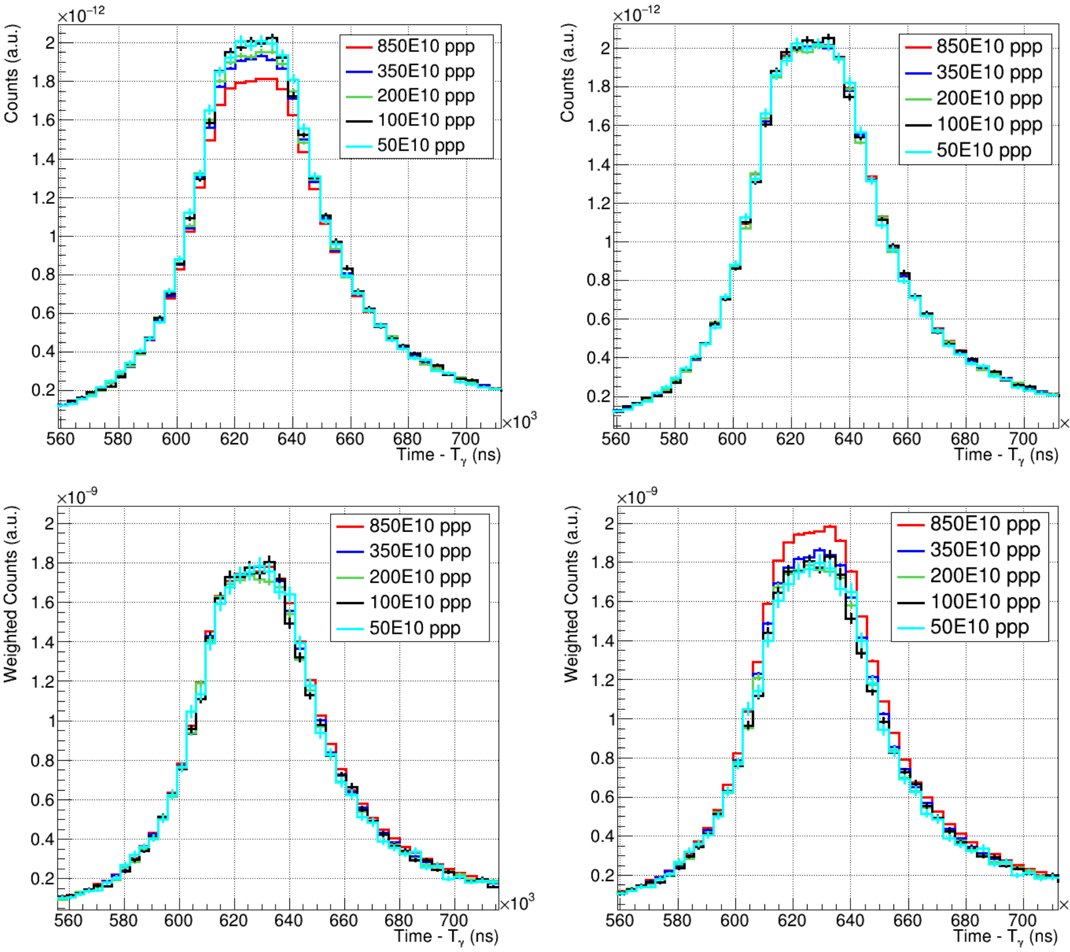

Figure 5.9: Spectra of the 4.9 eV saturated resonance of gold, detected by the sTED detectors using the 15-mm-diameter gold sample. Top plots are unweighted spectra, while bottom plots represent weighted spectra. Left plots do not have any dead time correction, while right plots have been corrected with a non-paralyzable dead time model. These plots show that this model works for unweighted counts, but it fails when applied to weighted counts.

However, unlike EAR1, the spectra of all the sTED detectors have been averaged before performing the following operations, in order to reduce the fluctuations due to the poor statistics collected by each single detector. The normalizations of the individual sTEDs have been checked separately and they agree within 10%.

For the moment, the larger C_6D_6 detectors have been ignored for the computation of the capture yield, because of their worse signal to background ratio in the region of interest. However, since their casings do not contain aluminium, they may be considered in the future to try to address the issue with the background (see next sections).

5.2.1 Background subtraction

The different components of background in a typical capture experiment have already been discussed in the previous chapter. The same methodology has been employed in EAR2 to evaluate and subtract these components, suitably scaling the spectra obtained from ancillary measurements (the description of the samples can be found in Section 3.4.4). In particular:

- The beam-off component has been estimated by acquiring data without beam, but it is negligible in EAR2, being three order of magnitude smaller than the signal in the thermal region (where it dominates in EAR1). Therefore it has been neglected.

- The sample-independent beam-on component has been estimated by irradiating a dummy sample and scaling its spectra by the corresponding number of protons on target. It is the dominant background component.

- The sample-dependent neutron-scattering background has been estimated by irradiating a carbon sample, scaling and shifting its spectrum and performing additional Monte Carlo simulations. The evaluation of this background component, entangled with the neutron sensitivity, is particularly tricky in EAR2 and required much more work than in EAR1. For this reason, this topic will be discussed more in detail in the next section.

An additional background component has been considered in EAR2 for the heavier ^{64}Ni: the sample-dependent scattering of in-beam γ rays. This component has been estimated by irradiating a natural lead sample, one of the heaviest stable elements and therefore expected to interact most strongly with photons. However, lead is also a good neutron scatterer. Therefore, the neutron scattering component estimated with the carbon sample had to be subtracted from the lead spectrum, normalizing the two spectra at thermal energy, where in-beam γ rays are not expected. The lead spectrum has been finally smoothed to remove capture resonances and scaled by a factor

$$f_{Lead} = \frac{BIF_{sample}}{BIF_{Lead}} \frac{n_{sample}}{n_{Lead}} \frac{Z_{sample}}{Z_{Carbon}} \tag{5.1}$$

to account for the different dimension and beam interception factor (BIF), the different thickness (n) and the different atomic number Z, that determines the interaction with γ rays, between the lead sample and the sample under study. This background component eventually reduces to a bump that affects the energy region of the keV (of astrophysical interest) and it is comparable in intensity with the neutron scattering component.

The scaling factors of these background components have been finally slightly adjusted to better reproduce the valley between resonances and background-related structures. The final estimation of the background for ^{64}Ni in the resonance region is shown in Figure 5.13.

5.2.2 Sample-dependent neutron-scattering background

The sample-dependent neutron-scattering component of the background has been one of the main issues in the analysis of EAR2 data, especially for ^{64}Ni(n,γ). As already mentioned, it is due to neutrons that are scattered by the sample and captured in the experimental area. Neutrons can be scattered far away and multiple times before undergoing a capture reaction, therefore the correlation between the neutron energy and the time-of-flight is lost. However, a fraction of the scattered neutrons can be immediately captured in the detectors (casings or active volume) or in the materials close to the detection setup. In this situation, the correlation between neutron energy and time-of-flight is maintained and structures like the capture resonances of the materials around the beam can be observed in the measured time-of-flight spectra. This background component will be referred to as *neutron sensitivity*, *prompt* or *direct neutron scattering background* in the following lines. This background component was negligible in EAR1 because of the optimized detection setup characterized by pipes, detector casings and detector supports made of carbon fibre, whose capture cross section is very small and does not present resonances in the neutron energy range of interest. On the contrary, the aluminium casings of the sTED detectors coupled with the high scattering cross sections of the samples under study (especially ^{64}Ni) make this prompt neutron scattering an important background component, affecting the neutron energy range of astrophysical interest (1 keV - hundreds of keV) in EAR2. In fact, the capture cross section of aluminium (^{27}Al) is characterized by huge resonances in this energy range, that are even superimposed to the resonances of ^{64}Ni in the region around 30 keV, as shown in Figure 5.10. For this reason, this background component requires an accurate evaluation.

In a first approximation, the sample-dependent neutron-scattering background has been evaluated by scaling the time-of-flight spectrum measured with a carbon sample, using the factor 4.10 as described for EAR1. However, differently from EAR1, the time-of-flight spectrum of carbon shows a resonant structure at corresponding neutron energy around 6 keV, due to neutrons scattered and promptly capture in the 5.9 keV resonance of aluminium. A similar structure is present around 35 keV. These structures are also present in the time-of-flight spectra of ^{64}Ni, but they appear shifted in time-of-flight by 1.2 μs with respect to the carbon spectra, as shown in Figure 5.11. The reason for this shift turned out to be purely kinematic. In fact, neutrons of 5.9 keV are captured by aluminium after being scattered at approximately 90° with respect to their initial direction of motion. The scattering implies a loss of energy by the neutrons, which depends on the mass of the scatterer nucleus M and on the scattering angle θ, according to the formula:

$$E_i = E_f \left[\frac{m\cos(\theta) - \sqrt{m^2[\cos^2(\theta) - 1] - M^2}}{m - M} \right]^2 \tag{5.2}$$

where m is the mass of the neutron, E_i and E_f are the energy of the neutron before and after the scattering. Since carbon and ^{64}Ni have different masses, scattered neutrons of 5.9 keV correspond to neutrons of different initial energy, namely 6.98 keV and 6.09

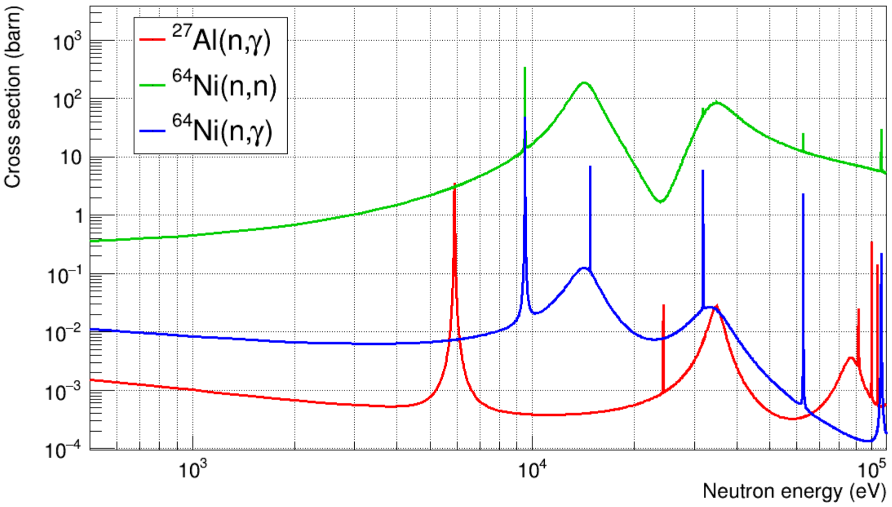

Figure 5.10: Relevant cross sections for the study of the background induced by scattered neutrons in the energy range of interest (corresponding to time-of-flights between 4.3 μs and 60 μs). ^{64}Ni neutron capture and scattering cross sections are shown in blue and green, respectively. ^{27}Al neutron capture cross section is plotted in red.

keV respectively for the two samples, if scattering at 90° is assumed. This difference in the initial neutron energy exactly corresponds to the 1.2 μs shift observed between carbon and ^{64}Ni spectra, confirming the hypothesis that the resonant structure observed is actually due to neutrons scattered at 90° in the sTED casings. Therefore, the carbon spectrum has not only to be scaled, but also shifted using Equation 5.2 to reproduce the effect of the neutron scattering from the sample under study. In this way, the resonant structure observed in carbon matches with the one observed in the sample under study, as shown in Figure 5.13 (at 17.7 μs for ^{64}Ni). An additional smaller and broader structure at around 16.5 μs is observed in the time-of-flight spectrum of the sample under study. In analogy with what has been described before, this structure is compatible with neutrons scattered by lighter materials (C, O, N) and captured in 5.9 keV resonance of aluminium. Since this structure is also observed in the dummy spectrum, it may be due to neutrons scattered by air and by the Mylar supporting the samples.

If the scaled and shifted carbon spectrum reproduces the sample-dependent neutron-scattering background (including the prompt neutron scattering component) at around 5.9 keV, it seems not to work in the region around 30 keV (700 - 800 ns), where resonances of aluminium and ^{64}Ni are superimposed. Here, a structure is observed in the spectrum of ^{64}Ni, that seems not compatible with its expected s-wave resonance at 33.8 keV (energy reported by several previous measurements, corresponding to ≈ 7.5 μs in this work). Similarly to what happens at 5.9 keV, this structure may be due to neutrons scattered by ^{64}Ni and captured by the 35 keV resonance of aluminium and it may be strongly enhanced by the huge scattering cross section of ^{64}Ni on the tail of its 33.8 keV resonance. This effect cannot be seen in the scaled carbon spectrum, because it

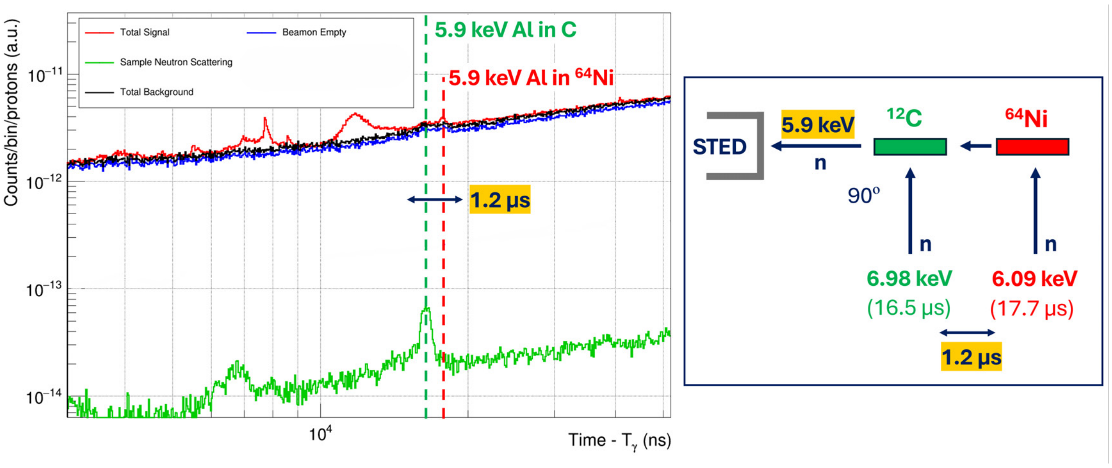

Figure 5.11: Weighted time-of-flight spectrum of ^{64}Ni in the energy range of interest preliminarily compared with some of the estimated background components. A shift of 1.2 μs is observed between ^{64}Ni (red) and carbon (green) spectra in correspondence of the 5.9 keV resonance of aluminium. This shift is due to kinematics of scattering, that implies a neutron energy loss depending on the mass of the scatterer, as shown in the sketch on the right (see text for more details).

has been scaled by using an average spectral scattering cross sections, that averages out the local effect of resonances. As already mentioned in the previous section, scaling the carbon spectrum by the pointwise scattering cross section would not be correct [117] and, in addition to that, it would result in an estimated background larger than the signal. Therefore, GEANT4 Monte Carlo simulations have been finally employed to study the background in this energy region more in detail. In this case, the High Precision (HP) physics packages of GEANT4 have been employed, in order to deal properly with low energy neutrons.

In order to reproduce the sample-induced neutron-scattering background in the energy range of interest, neutrons impinging on the sample under study have been simulated with energy above 1 keV, as all these neutrons can produce signals in the time interval of interest. The hits in the sTED detectors have been recorded, saving the time after the scattering of the primary neutron, the deposited energy and the energy of the primary neutron. Combining these information, a weighted time-of-flight spectrum has been reconstructed from the simulations and compared with data. First of all, the measured and simulated spectra of carbon have been compared in order to check the consistency between real data and simulations. Applying a scale factor, their agreement in the energy range of interest is good, as shown in Figure 5.12. However, this method turned out to be very inefficient in terms of computing time: in order to see resonances, a fine binning was required and therefore a large number of neutrons needed to be simulated to get suitable statistics to subtract from data. Moreover, neutrons up to thermal energy (in a range covering more than 10 orders of magnitude) should have been simulated to reproduce the background in the thermal region.

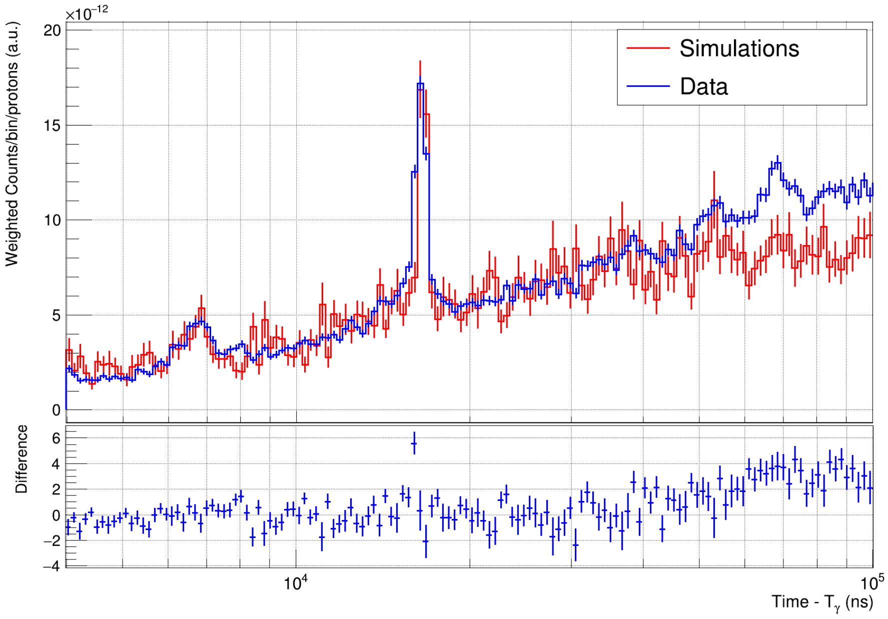

Figure 5.12: Weighted time-of-flight spectra of carbon in the energy range of interest resulting from measurement with sTED detectors (red) and GEANT4 simulations (blue). Neutrons in GEANT4 have been simulated with energy above 1 keV (≈ 40 μs), therefore the spectra cannot agree above the corresponding time-of-flight. The structure corresponding to the 5.9 keV resonance of aluminium is clearly reproduced by the simulations.

For this reason, a compromise has been finally adopted. The scaled and shifted carbon spectrum has been retained as the main reference for the evaluation of the sample-dependent neutron-scattering background, as it seems to provide a good general estimation. The scaling factor has been slightly adjusted to best match the 5.9 keV resonance of aluminium.

The evaluation of the background has been complemented with Monte Carlo simulations only to account for the enhanced neutron sensitivity due to ^{64}Ni resonances. Since the neutron sensitivity is due to the prompt effect of scattered neutrons, only neutrons in the energy range of interest could be simulated, namely between 4 and 100 keV. To further increase the statistics, neutrons have been simulated as being emitted isotropically from the sample. The energy of the neutrons before scattering has been reconstructed using Equation 5.2 and the resulting time-of-flight spectrum has been weighted by the scattering yield of the sample. The weighting functions depending on the deposited energy have been also applied. This procedure, suggested in previous studies [130], has been repeated for the ^{64}Ni and the carbon sample. The carbon simulated spectrum has been additionally scaled and shifted exactly in the same manner as the experimental data.

Since the contribution of these simulated neutrons in a restricted energy range is already included (on average) in the scaled carbon spectrum, only the difference between the simulated ^{64}Ni and carbon spectra has been considered as the estimation of the resid-

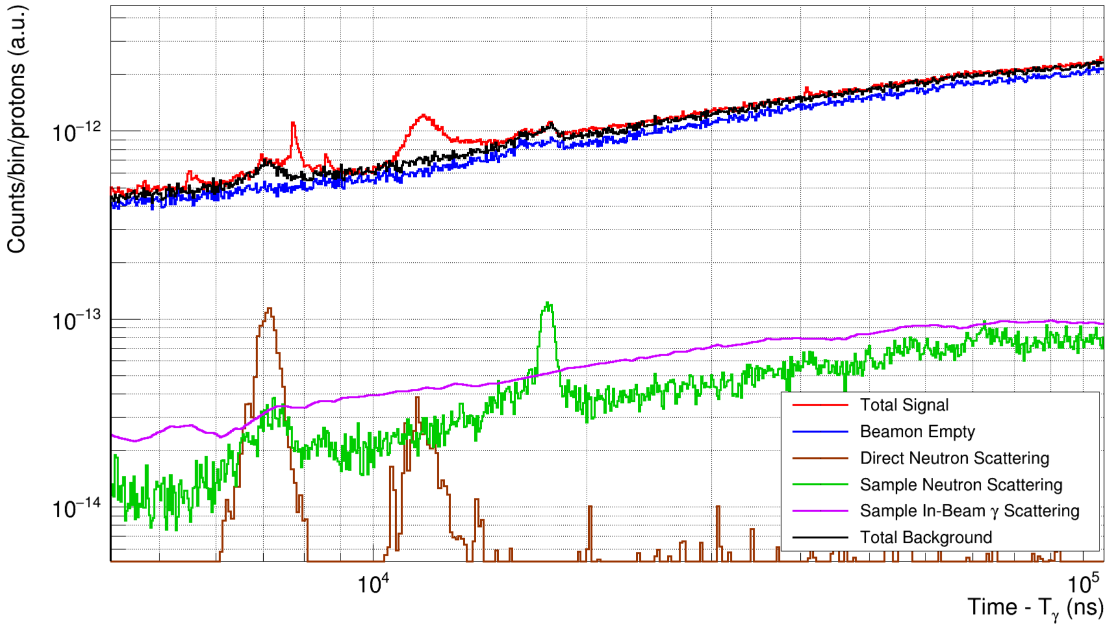

Figure 5.13: Weighted time-of-flight spectrum of ^{64}Ni in the energy range of interest compared with the estimated background components: sample-independent beam-on background (blue), sample-dependent scattering of in-beam γ rays (purple), sample-dependent neutron scattering background (green) and residual prompt neutron scattering background (brown). The total background is also shown in black.

ual neutron sensitivity background component, shown in brown in Figure 5.13.

As it is shown in the figure, this additional background component does not modify the shape of the background around the 5.9 keV resonance of aluminium, that was already well reproduced by the carbon spectrum. However, it accounts for neutron sensitivity in the nickel resonances. If the neutron sensitivity in the 13.8 keV resonance ($\approx$ 11.7 μs) is negligible, a significant increase of the background is observed in correspondence of the aforementioned structure at $\approx$ 7 μs, confirming that it is due to the effect of the neutrons scattered in the 33.8 s-wave resonance of ^{64}Ni and captured in the 35 keV resonance of aluminium. Finally, an additional residual background is also observed after the 13.8 keV resonance and it is probably originated by neutrons scattered in the resonance, but far away around the experimental area.

5.2.3 Time-to-Energy conversion and Normalization

Time-to-energy conversion and normalization have been performed exploiting ancillary measurements with gold samples of the same shape as the samples under study, as described in detail in EAR1.

The time-to-energy conversion has been carried out using Equation 3.4, where the flight-path L has been fixed at 19.098(1) m iteratively fitting the low energy resonances of ^{197}Au. The accuracy of the flight-path estimation has been assessed comparing the

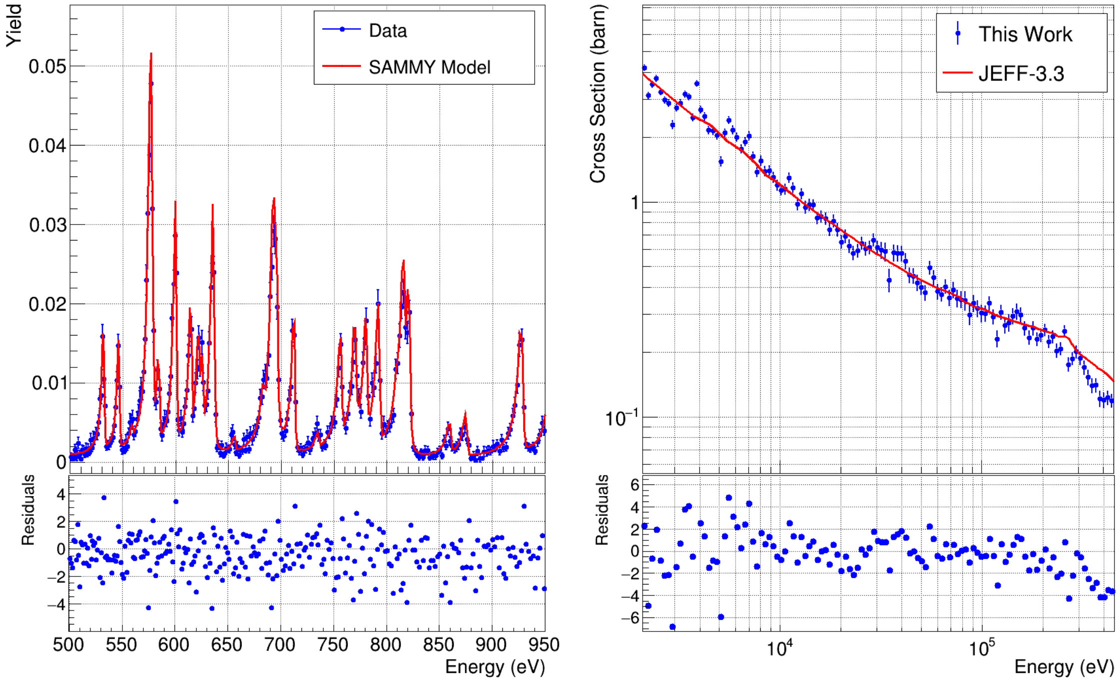

Figure 5.14: Comparison between the measured time-of-flight spectra of gold (normalized and converted to energy) and expectations from evaluated nuclear data at high energy region. The good agreement observed confirms that the flight-path and the normalization are well fitted.

measured and expected gold resonances at higher energy, as shown in Figure 5.14.

The normalization factor for the ^{64}Ni yield has been determined by fitting the saturated 4.9 eV resonance in the corresponding 15-mm-diameter gold sample, as described in Section 4.3.3 and shown in Figure 5.15. As demonstrated in Section 5.1.5, dead time corrections for the weighted spectra at the top of the saturated resonance in this gold sample could be neglected. Indeed the normalization factors obtained from the spectra of dedicated (8.5×10^{12}), parasitic (3.5×10^{12}) and low intensity (0.5×10^{12}) bunches agree within 1.4%, as shown in Table 5.1. The normalization factor fitted from parasitic bunches has been finally employed, as a compromise between statistics and goodness of the fit even in the tails of the resonance.

The normalization factor obtained at the saturated resonance has been checked in the energy range between 1 and a few hundreds keV comparing normalized data with the evaluated cross section of JEFF-3.3 [75]. A general good agreement has been obtained, as shown in Figure 5.14. Finally, the normalization factor has been also checked in the thermal energy region, where however additional corrections have been required. They will be discussed in the next section.

Concerning the other gold samples, the 20-mm-diameter gold sample has been also normalized using the 4.9 eV saturated resonance, but only using spectra from low intensity bunches, as dead time corrections for the others could no longer be neglected. For the 22-mm-diameter sample, needed to normalize the ^{30}Si(n,γ) yield, low intensity bunches were not available. Therefore, because of the important dead time corrections required in the saturated resonance, the normalization has been performed at the thermal region, after applying the corrections discussed in the next section. Normalization factors for these samples are also reported in Table 5.1.

Sample	Normalization for different bunch intensities		
	8.5×10^{12} ppp	3.5×10^{12} ppp	0.5×10^{12} ppp
Au (14 mm)	0.2830(5)	0.2800(5)	0.2790(14)
Au (20 mm)	-	-	0.4849(8)
Au (22 mm)	-	0.5655(5)	-

Table 5.1: Normalization factors F_{Norm} fitted using gold samples. The factors for the 15-mm and 20-mm-diameter samples have been fitted in the 4.9 eV saturated resonance, while for 22-mm-diameter the factor has been fitted in the thermal region. For the 15-mm-diameter sample, normalization fitted using different bunch intensities are reported, to demonstrate that dead time corrections are negligible.

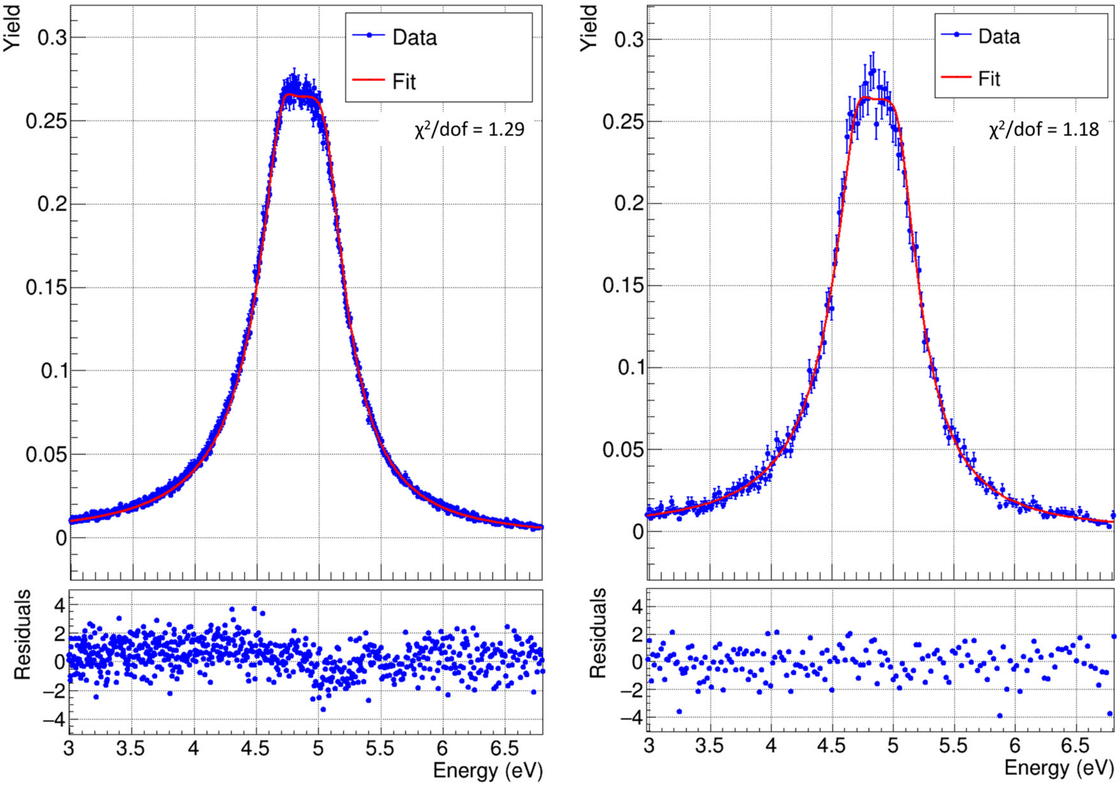

Figure 5.15: Fit of saturated 4.9 eV resonance of gold performed with SAMMY to extract the normalization for the 15-mm-diameter gold sample. The spectrum on the left refers to parasitic bunches (3.5×10^{12} protons per pulse), while the one on the right refers to low intensity bunches (0.5×10^{12} protons per pulse).

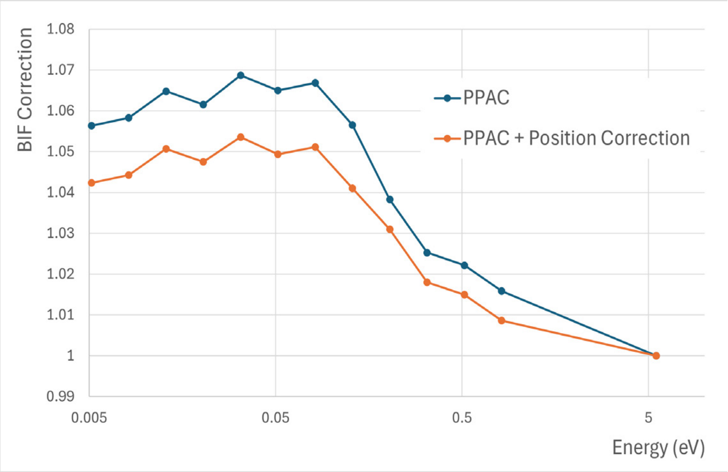

Figure 5.16: Variation of the Beam Interception Factor (BIF) as a function of the neutron energy for a 15-mm-diameter sample in the thermal and epithermal region. The value of the BIF is normalized at 5 eV. The blue line represents the data from the PPAC Monitor, while the orange line represents the final correction applied in this work, that considers the different positions where the measurements have been performed.

5.2.4 Thermal capture yield

As described in Section 3.1.3, the neutron flux at thermal energy is different between EAR1 and EAR2 due to the employment of two different moderators: simple water in EAR2, borated water in EAR1. As shown in Figure 3.3, thanks to the absence of boron the neutron flux of EAR2 include thermal neutrons and therefore allows the measurement of neutron cross sections in the thermal energy region. As demonstrated in Section 5.1.5, dead time corrections are almost negligible in this energy region, even for the 22-mm-diameter gold sample (corrections are below 0.5% for dedicated bunches). However, other corrections must be considered, such as the flux attenuation due to the SiMon detector and the variation of the beam interception factor (BIF) as a function of the neutron energy.

The SiMon monitor (Section 3.4.3) is placed upstream of the capture sample and contains a ^{6}LiF sample. ^{6}Li has a large total neutron cross section σ_T at thermal energy (more than 1000 barns) that can potentially attenuate the neutron beam before it reaches the capture sample. The transmission T through the SiMon sample has been calculated using the formula:

$$T = e^{-n\sigma_T} \tag{5.3}$$

where n is the areal density of the sample, 82.66 μg/cm^2. Because of the small thickness of the sample, the transmission coefficient at 25 meV has been evaluated to be 99.7%, therefore corrections are negligible.

A much more important effect is represented by the variation of the spatial distribution of the neutron beam as a function of the neutron energy, that leads to a variation of the beam interception factor of the samples under study [138, 139]. This effect is particularly relevant in the thermal region in EAR2, as already shown in Figure 3.5. The BIF variation was determined using data from a fission chamber based on Parallel Plate Avalanche Counters (PPACMon), capable of measuring the spatial distribution of the neutron beam as a function of the energy. These data have been collected during the commissioning of the experimental areas [104, 138]. However, since the PPACMon was installed in a different position with respect to the capture sample, further corrections for the position dependence of the BIF have been applied. In particular, the BIF in the PPACMon and in the capture sample position have been simulated at different neutron energies with a FLUKA-based tool simulating the transport of neutrons between the target and the experimental areas. Their ratio has been used to correct the data from the PPACMon. The BIF corrections, before and after position correction, are shown in Figure 5.16, normalized at the value at 5 eV. The same procedure has been repeated for all

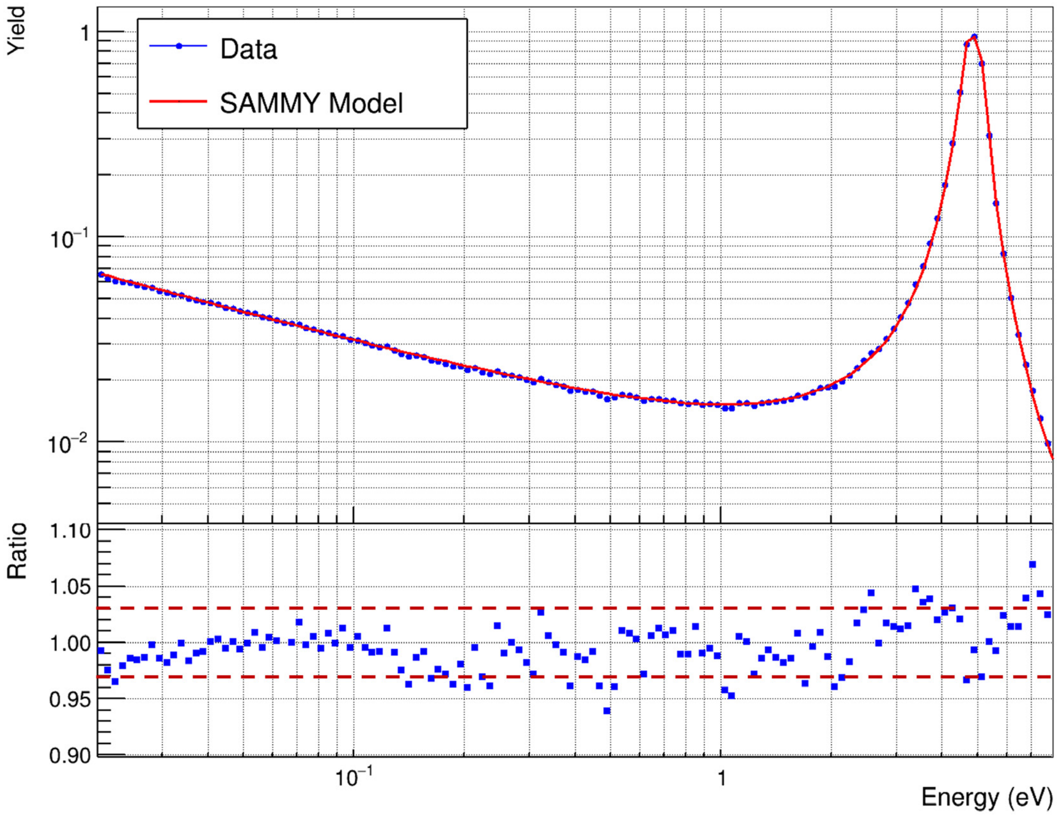

Figure 5.17: Comparison between the measured capture yield of the 15-mm-diameter gold sample and the prediction from evaluated nuclear data in the thermal-epithermal region. The normalization fitted at the top of the 4.9 eV saturated resonance has been applied to the data. In the bottom panel, the ratio between data and predictions is shown with dashed lines representing ± 3% discrepancy.

the samples of different diameters.

After applying these corrections and using the same normalization obtained at the 4.9 eV saturated resonance, the measured and expected capture yields for the 15-mm-diameter gold sample have been compared in the thermal energy region, as shown in Figure 5.17. In the range between 25 meV and 1 eV, the agreement between data and expectations is generally within 3%. Moreover, thanks to the large thermal capture cross section of ^{197}Au, the capture yield seems to be only weakly sensitive to adjustments of the evaluated background: scaling the background to better reproduce the valleys between resonances has produced an effect well below 1% at thermal energy.

In this way, the reproducibility of the thermal capture cross section of ^{197}Au within approximately 3% uncertainty has been demonstrated using the 15-mm and 20-mm-diameter gold samples. Therefore, the capture yield of the 22-mm-diameter gold sample could be finally normalized in the thermal region, considering the 3% uncertainty in the total budget of systematic uncertainties. The normalization is shown in Figure 5.18.

For other samples with lower capture cross sections, the contribution of the background in the thermal region becomes more relevant. For example, the adjustment of the neutron scattering background component in the resonance region produced a variation of approximately 3% in the thermal yield of ^{64}Ni. This uncertainty will be included

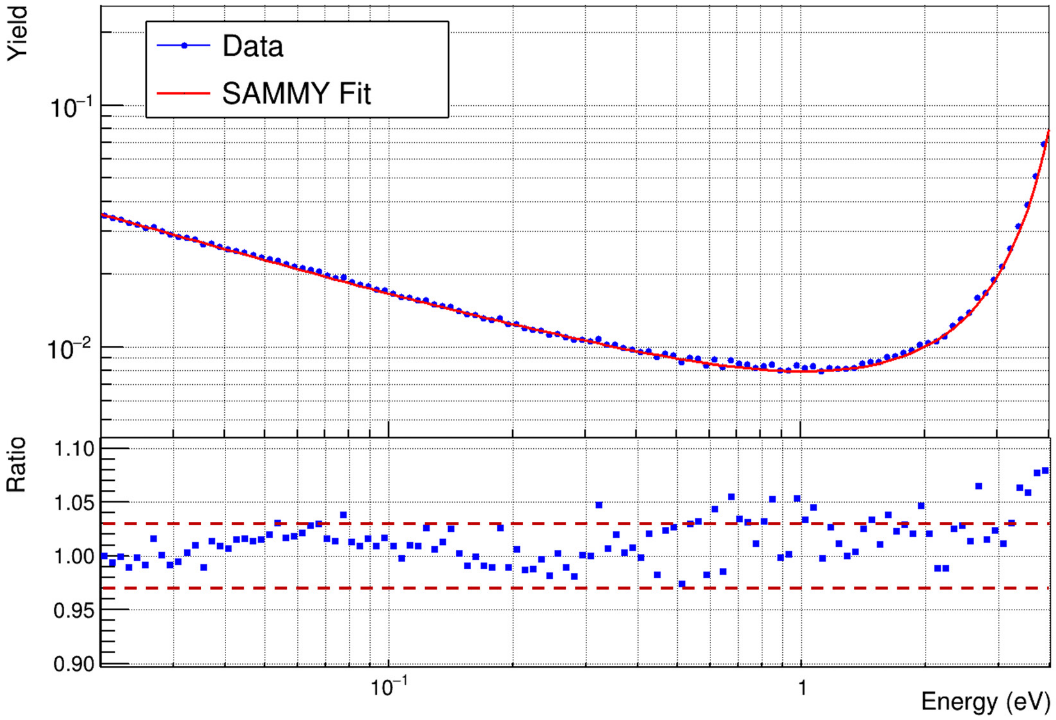

Figure 5.18: Fit of the capture yield of the 22-mm-diameter gold sample in the thermal - epithermal region. The fit has been performed with SAMMY. In the bottom panel, the ratio between data and fit is shown with dashed lines representing ± 3% discrepancy.

among the systematic uncertainties for the thermal cross section. This effect is drastically increased in ^{30}Si, that has a thermal capture cross section approximately 10 times smaller than ^{64}Ni (around 0.1 barn). For this reason, the analysis of the thermal region of ^{30}Si is still ongoing.

Another important effect to consider when measuring thermal cross sections is the possible presence of contaminants in the sample under study. These contaminants, even in small quantities, can significantly impact on the measured thermal capture yield if they are characterized by huge thermal capture cross sections. This is the case of europium, that has been identified in the ^{64}Ni sample thanks to the presence of its characteristic resonances in the measured capture yield in the epithermal region (0.3 - 10 eV). Fitting the yield in this energy region, the relative abundance of europium in the sample could be estimated at $2.4(5)\times10^{-4}\%$. However, its contribution to the measured thermal capture yield amounts to the $1.5(3)\%$. Contaminants will be therefore taken into account when fitting with SAMMY.

Chapter 6

Results

This last chapter deals with the results obtained by fitting and integrating the capture yields obtained in the two previous chapters. The procedure followed to extract these results is described in general in Section 6.1, while the following two Sections 6.2 and 6.3 deal with the results for the ^{30}Si(n,γ) and the ^{64}Ni(n,γ) cross sections, respectively. The cross sections, the resonance parameters and the Maxwellian Averaged Cross Section (MACS) from this work are finally compared with the values from previous measurements and from the current releases of different evaluated nuclear data libraries.

6.1 Resonance fitting

The two previous chapters have dealt with the extraction of the experimental capture yields. In the energy range of astrophysical interest (from hundreds of eV to hundreds of keV) the cross sections of light elements (such as ^{30}Si and ^{64}Ni) are still characterized by resolved resonances, as described in Section 2.1. Therefore, the R-Matrix theory has to be used to characterize these resonances through a set of parameters (energy, width, spin-parity,...), as reported in Section 2.2.3. In this work, the code SAMMY has been used to finally extract the resonance parameters from the measured capture yields. SAMMY [68], already mentioned in Section 2.4, is a nuclear data evaluation and analysis code developed at Oak Ridge National Laboratory (ORNL) in the 1980s that is primarily used for the R-Matrix parametrization and evaluation of neutron cross-section in the Resolved Resonance Region (RRR). In particular, SAMMY can reconstruct theoretical reaction yields starting from prior input resonance parameters. These theoretical yields can be additionally folded with the experimental effects discussed in Section 2.4, such as Doppler broadening, resolution broadening, self-shielding and multiple scattering. This procedure is more convenient than deconvoluting these effects from the experimental data and enables a direct comparison between predicted and measured yields. Exploiting this comparison, SAMMY can eventually perform an iterative Bayesian fit of the resonance parameters that consider both the new experimental data and the prior information. Normalization, time-to-energy conversion or background parameters can also be fitted, as already mentioned in the previous chapters.

At this stage of the work, the residual background has been fitted in the valley between the resonances and the energy, the radiative (Γ_γ) and the scattering widths (Γ_n) have been fitted for each resonance. The Reich-Moore approximation of the R-Matrix theory has been used and the prior resonance parameters have been taken from the recommended evaluated nuclear data. Since only the neutron capture yield has been measured, the partial widths cannot be reliably constrained separately, as anticipated in Section 2.4. Therefore, even if the partial widths have been fitted separately, the resonance kernel (Equation 2.20) is the only parameter that could be extracted, together with the resonance energy. In fact, the spin-parity (J^π) of the resonances could also not be determined, and it has been taken as a fixed parameter from evaluated nuclear data libraries. Possible inaccuracies in the assignment of the spin-parity should anyway affect the values of the resonance widths, but not the value of the measured kernel (related to the area of the resonance). It is also important to mention that the uncertainty on the resonance kernels resulting from the SAMMY fit only includes statistical uncertainties. Systematic uncertainties have been evaluated independently and finally added to the results.

In light isotopes like ^{30}Si and ^{64}Ni resonances are very well spaced in the range of astrophysical interest, therefore the valley between resonances can play an important role in the final determination of the Maxwellian Averaged capture Cross Section (MACS, Section 2.1.2). In these regions, the effects of the direct capture and/or negative resonances (details in Sections 2.2.4 and 2.3) can be dominant, but they cannot be directly observed as they typically fall below the experimental background. The only energy region where these effects can be potentially constrained corresponds to the thermal and epithermal region, where the capture cross section increases and it is characterized by a smooth 1/v behaviour. For this reason, after fitting the resonances, the thermal cross section has been additionally considered to fit negative resonances (for ^{64}Ni) or to constrain the calculated contribution of the direct capture (for ^{30}Si). The details will be explained in the next sections, separately for the two cases.

In conclusion, the capture cross section has been reconstructed using the fitted resonance parameters and adding the contribution of fitted negative resonances or calculated direct capture. It has been converted into the centre-of-mass reference system and it has been finally integrated according to Equation 2.6 to provide the MACS for astrophysical applications at different energies kT, corresponding to different stellar temperatures T.

6.2 Results for ^{30}Si(n,γ)

As anticipated in section 1.4, previous data on the ^{30}Si(n,γ) cross section and/or resonance parameters available in the literature are scarce and discrepant. The most recent measurements in the energy range of astrophysical interest that the data from this work will be compared to are:

- *Boldeman et al.* (1975) [42], a time-of-flight measurement performed at the 40-m station of the Oak Ridge Electron Linear Accelerator (ORELA, USA) using a natural silicon sample and C_6F_6 liquid scintillators
- *Beer et al.* (2002) [44], an activation measurement performed at the Karlsruhe and Tubingen 3.75 MV Van de Graaff accelerator measuring the β spectrum of a natural silicon sample
- *Guber et al.* (2003) [41], a time-of-flight measurement also performed at the 40-m station of ORELA using a natural silicon sample, but employing C_6D_6 liquid scintillators

The MACSs extracted from these measurements are taken as the recommended value at 30 keV in KADoNiS 0.0 [43] (Boldeman et al.) and in KADoNiS 0.3 [45] (Guber et al.). However, as will be shown in Figure 6.6, these values are strongly discrepant: there is almost a factor 2 between the first two measurements and between the second two measurements. The energy extrapolation of the MACS is typically based on the energy differential cross sections recommended in the evaluated nuclear data libraries, but also in this case large discrepancies are observed. For example, large discrepancies currently exist between JENDL-5 [72] on one side and ENDF/B-VIII.1 [70] or JEFF-4 [71] on the other. These discrepancies involve both the position of the resonances and their strength, as shown in Figure 6.1.

The following paragraphs will present the preliminary results from this work concerning the resonance parameters and the MACS.

6.2.1 Resonance fitting

As described in the previous section, the capture yields from Chapter 4 have been fitted with SAMMY to extract the resonance parameters.

As already discussed in Section 4.4, the 4.98 keV resonance (the largest one observed) has been fitted from the ^{Nat}Si capture yield (Figure 4.20), while the more accurate fit performed on the capture yield from the ^{30}Si enriched sample could only be used to estimate the mass of ^{30}Si. Using this mass, the other resonances could be fitted from the capture yield of the enriched ^{30}Si sample up to 303 keV, in particular at 15.1 keV (Figure 6.2), 235 keV (Figure 6.2) and 303 keV. The fitted resonance kernels are reported in Table 6.1 and compared with previous measurements and values recommended in the evaluated nuclear data libraries. A fit has been also performed concerning the broad s-wave resonance expected at 183.5 keV, observed in the transmission measurement on an enriched ^{30}Si sample by Harvey et al. [140]. The fit has been performed with both the energy and the scattering width of the resonance fixed. However, the profile of this resonance could not stand out from the background, therefore only an upper limit of 4 eV for its radiative width could be extracted (Figure 6.2). If the radiative width had been bigger, the resonance would have been clearly observed above the background.

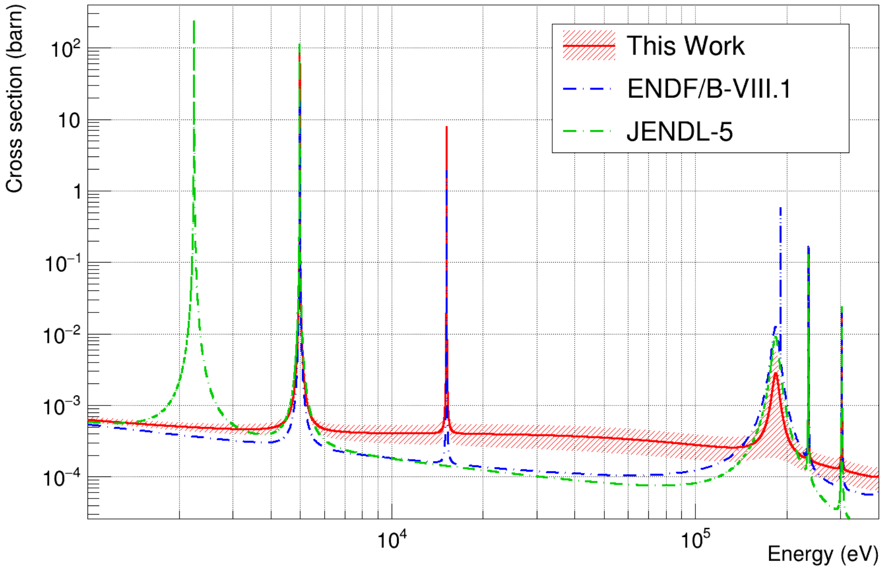

Figure 6.1: Comparison between the ^{30}Si(n,γ) cross sections obtained from this work and those recommended in the most recent releases of some major evaluated nuclear data libraries. The cross section recommended in ENDF/B-VIII.1 is the same as the one recommended in JEFF-4.

In conclusion, the main preliminary results concerning resonance fitting can be summarized as follows:

- the strong resonance at 2.35 keV reported in JENDL-5 has not been observed in this work, confirming the most recent ENDF/B-VIII.1 and JEFF-4 evaluations (Figure 6.1)

- the resonance at 15.1 keV, not reported in JENDL-5, has been observed, confirming the claim from previous measurements (Boldeman et al. and Guber et al.) and the most recent ENDF/B-VIII.1 and JEFF-4 evaluations

- the kernels of the two first resonances measured in this work (both measured with good statistics) are systematically higher than the values reported by Guber et al. and assumed in ENDF/B-VIII.1 (between 35% and 50% higher), but systematically lower than the values reported by Boldeman et al. and the values recommended in JENDL-5 (between 20% and 55% lower).

- the upper limit found for the radiative width of the 183.5 keV resonance (4 eV) is lower than the values currently recommended in the nuclear data evaluations (6 eV in JENDL-5 and 8.37 eV in ENDF/B-VIII.1). No previous measurements of this resonance in capture experiments exist to perform additional comparisons.

- no evidence of a 190.6 keV resonance could be observed in this work. This resonance was observed previously by Boldeman et al., Guber et al. and reported in

J	l	Energy (keV)	Resonance kernel (eV)				
			This work	Guber	Boldeman	ENDF/B-8.1	JENDL-5
-0.5	1	4.9815(3)	0.261(17)	0.194	0.60(6)	0.193	0.391
-0.5	1	15.1444(6)	0.141(12)	0.094	0.17(2)	0.094	–
0.5	0	180.49	1.8(4)			8.360	5.996
1.5	2	235.19(6)	1.16(19)	1.794	1.6(3)	1.794	1.589
-0.5	1	302.7(2)	0.5(2)			0.724	0.739

Table 6.1: Comparison between the kernels of the resonances fitted in this work and the values reported in the previous time-of-flight measurements by Guber et al. [41] and Boldeman et al. [42] as well as the values recommended in the JENDL-5 and ENDF/B-VIII.1 evaluations. *J* and *l* represent the spin of the resonances (the sign indicates the parity) and the orbital angular momentum, respectively. The 180.49 keV resonance represents a particular case, as only the radiative width has been fitted in this work (for this reason the uncertainty on the energy is missing). See text for more details. The reported uncertainties include both statistical and systematic contributions (Table 6.3). The values from Guber are actually quoted by Beer in [44], but without associated uncertainties.

ENDF/B-VIII.1 (Figure 6.2), but not observed in the transmission measurement by Harvey et al.

The statistics becomes drastically poorer with increasing the neutron energy, therefore no resonances could be fitted above 303 keV. In this energy range, the recommended capture cross section from evaluated nuclear data libraries has been assumed for the calculation of the MACS, even if the contribution of this energy range to the MACS at 100 keV is still negligible, as shown in Figure 6.5.

In conclusion, as anticipated in the previous section, it is important to point out that the uncertainty returned from the fits performed with SAMMY only includes the statistical uncertainties on the capture yield. Systematic uncertainties for the determination of the capture yields have been determined independently and added to the total uncertainty at the end.

Table 6.2 shows the different contributions to the systematic uncertainty, which include the uncertainties on:

- counting rate stability, due to possible problems in the detectors or in the beam alignment during the experimental campaign and evaluated as the standard deviation of the counting rate of the detectors (C_6D_6 and the SiMon monitor) per run, normalized to the number of protons

- PHWT, evaluated as the maximum deviation of the weighted efficiency from the γ ray energy, as described in Section 4.2.2 and Figure 4.9

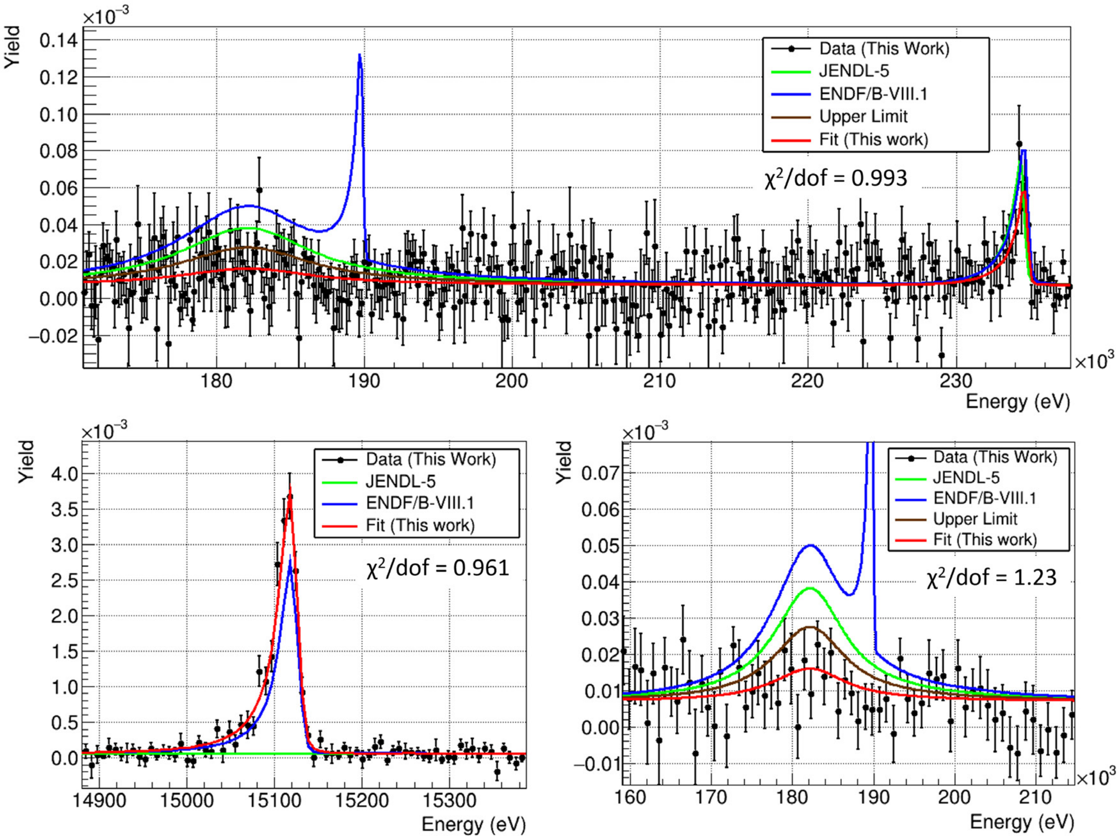

Figure 6.2: Fit of resonances in the ^{30}Si(n,γ) yield, compared with the predictions of evaluated nuclear data libraries. The figure on the top shows the fit in the high energy region at 2500 bins per decade, highlighting the 235 keV resonance and showing no evidence of the 190 keV resonance predicted by ENDF/B-VIII.1. The bottom-right figure is a zoom of the region around 180 keV with a coarser binning (500 bins per decade), that has been used to determine the upper limit of the 183.5 keV resonance. The bottom-left figure shows the fit of the 15.1 keV resonance.

- Normalization, evaluated as the uncertainty in the SAMMY fit of the saturated resonance of ^{197}Au (Section 4.3.3) summed to the uncertainty in the correction factors for the normalization (Section 4.3.4) and to the estimated uncertainty in the area of the samples (it has to be exactly the same area as the sample under study)
- Sample positioning, due to possible misalignments in the positioning of the samples that can lead to different beam interception factors. It has been evaluated by computing the variation of the BIF for a misalignment of 0.5 mm
- Energy dependence of the neutron flux, that has been taken from the preliminary results of the commissioning of EAR1
- Sample mass, that affects the capture yield of ^{30}Si and it has been evaluated in Section 4.4.

	Systematic Uncertainty (%)		
	^{30}Si yield		^{Nat}Si yield
	< 100 keV	> 100 keV	< 100 keV
Counting rate stability	3	3	3
PHWT	1	1	1
Normalization	1	1	1
Sample positioning	2	2	2
Neutron flux	2.2	3.1	2.2
Sample mass	5	5	0.003
Total	**6.7**	**7.0**	**4.5**

Table 6.2: Estimation of the systematic uncertainties affecting the measurements. The different contributions are reported separately and summed in the last row.

Table 6.1 already reports the total uncertainty for the fitted resonance kernels, while Table 6.3 reports separately the contribution of systematic and statistical uncertainty for each resonance, showing that the former dominates at low energy, while the latter prevails at high energy and in the ^{Nat}Si capture yield.

Energy (keV)	Resonance kernel (eV)	Uncertainty (eV)		
		Statistical	Systematic	Total
4.9815(3)	0.261	0.013	0.012	0.017
15.1444(6)	0.141	0.008	0.009	0.012
235.19(6)	1.16	0.18	0.08	0.19
302.7(2)	0.5	0.2	0.04	0.2

Table 6.3: Contribution of statistical and systematic uncertainties to the total uncertainties reported for the kernels of the resonances fitted in this work (Table 6.1). An upper limit is assumed for the 183.5 keV resonance, therefore its kernel is not considered here.

6.2.2 Direct Capture

As already explained in Section 2.3, direct capture may play a relevant role in the valley between resonances. This is the case of the capture cross section of ^{30}Si, that has only a few resonances in the energy range of astrophysical interest and no resonances at all between 15 keV and 180 keV, the most interesting region for studying nucleosynthesis in massive stars. Therefore, estimating the contribution of the direct capture to the total neutron capture cross section is of paramount importance for determining the MACS in

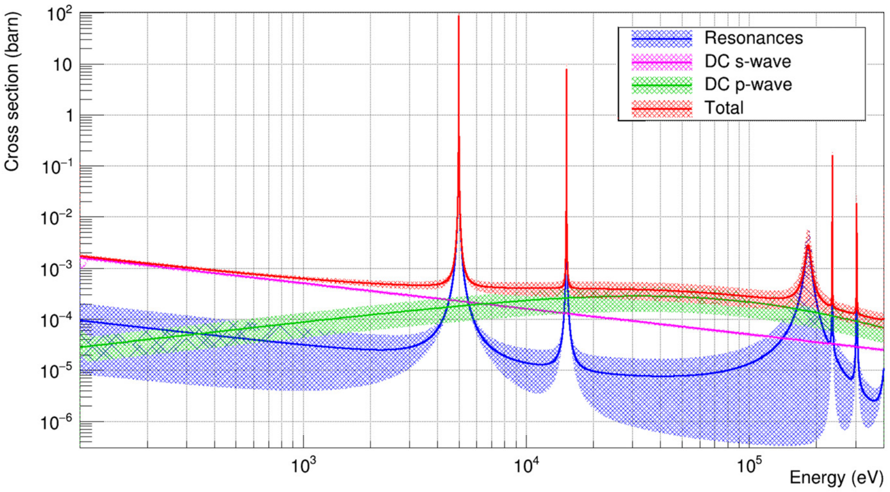

Figure 6.3: ^{30}Si(n,γ) cross section extracted in this work (red), plotted with the contributions of the resonances fitted in this work and of the direct capture (DC) in s-wave and p-wave, as provided by A. Mengoni (private communication).

this energy region. Details about the calculation of this contribution can be found in Section 2.3.

The preliminary estimation of the direct capture cross section used in this work has been provided by A. Mengoni (private communication), separately for the s-wave and the p-wave components. They are shown in Figure 6.3 together with the contribution of resonances.

The s-wave component exhibits a $1/v$ behaviour (v is the neutron velocity) and its value has been normalized at thermal energy. In fact, as discussed in Section 2.2.4, the neutron capture cross section of an isotope at thermal energy is due partially to the tails of the s-wave resonances observed at higher energy and partially due to the s-wave direct capture. The first contribution has been reconstructed with SAMMY, so that the direct capture contribution could be constrained using the thermal capture cross section recommended in the evaluated nuclear data libraries. This value is common in both ENDF/B-VIII.1 and JENDL-5 evaluations, it is reported with 3% uncertainty and it has been used as a preliminary input while awaiting the results of the analysis of ^{30}Si data from EAR2. However, since the radiative width of the 183.5 keV s-wave resonance in the ^{30}Si(n,γ) cross section is affected by a high uncertainty (only an upper limit could be given in this work), the resonance contribution to the thermal cross section is also uncertain and, in particular, it has been found to vary within ± 7%. This variation has been assumed as uncertainty on the s-wave direct capture contribution to the cross section. However, it is important to keep in mind, for later calculations, that this uncertainty is completely correlated to the uncertainty of the resonance contribution.

The p-wave component of the direct capture cross section is also particularly rele-

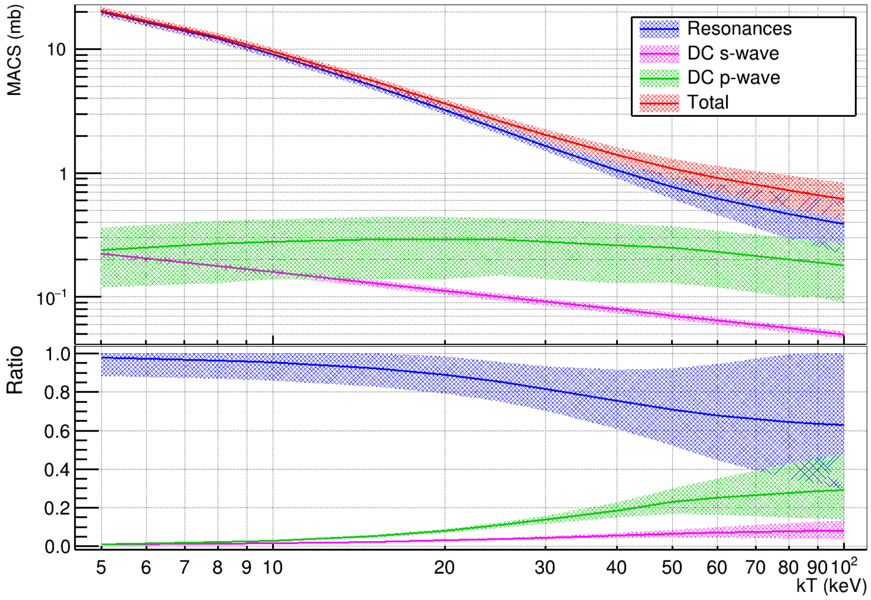

Figure 6.4: ^{30}Si(n,γ) Maxwellian Averaged Cross Section determined in this work, plotted with the contributions of the resonances fitted in this work and of the direct capture (DC) in s-wave and p-wave. The bottom pad shows the relative contribution of each component.

vant, as it affects exactly the energy range of astrophysical interest. However, its contribution cannot be experimentally constrained in this work, because it is completely covered by the background. An uncertainty of 50% has been preliminarily assigned to its theoretical estimation, compatible with the uncertainty reported by Guber et al. in its calculations [41]. The contribution of direct capture in higher partial waves is not important in the energy range of interest and therefore it has been neglected in this work.

6.2.3 Maxwellian Averaged Cross Section

As final result of this work, the MACS of the ^{30}Si(n,γ) has been computed at thermal energies kT ranging from 5 keV to 100 keV, integrating the cross section according to Equation 2.6. The contributions of resonances, s-wave and p-wave direct capture have been considered separately, as shown in Figure 6.4 and in Table 6.4, where the total MACS is also reported with its uncertainty.

The impact of this experimental work is mainly restricted to low energies. In fact, the MACSs at low energy are dominated by the contribution of resonances, in particular by the 4.98 keV and 15.1 keV resonances that could be characterized with good statistics in this work. This is also shown in Figure 6.5. However, increasing the energy, the contributions of the p-wave direct capture and of the 183.5 keV resonance increase. For example, at 90 keV only approximately 35% of the MACS is due to two aforementioned low-energy resonances, while 25% is due to the 183.5 keV resonance and more than 35% to the direct capture (Figure 6.5). Among these two last contributions, the former could

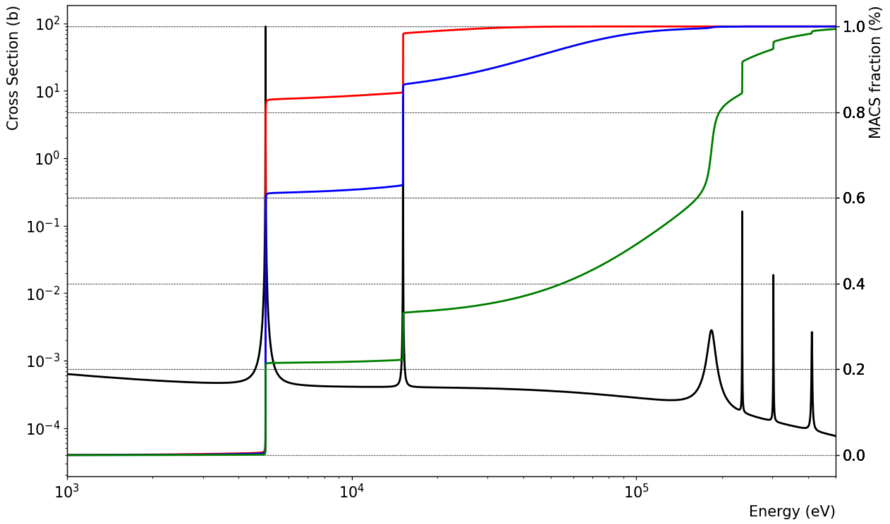

Figure 6.5: Contribution of the cross section extracted from this work (in black) to the MACS at 8 keV (red), 25 keV (blue) and 90 keV (green) as a function of the neutron energy.

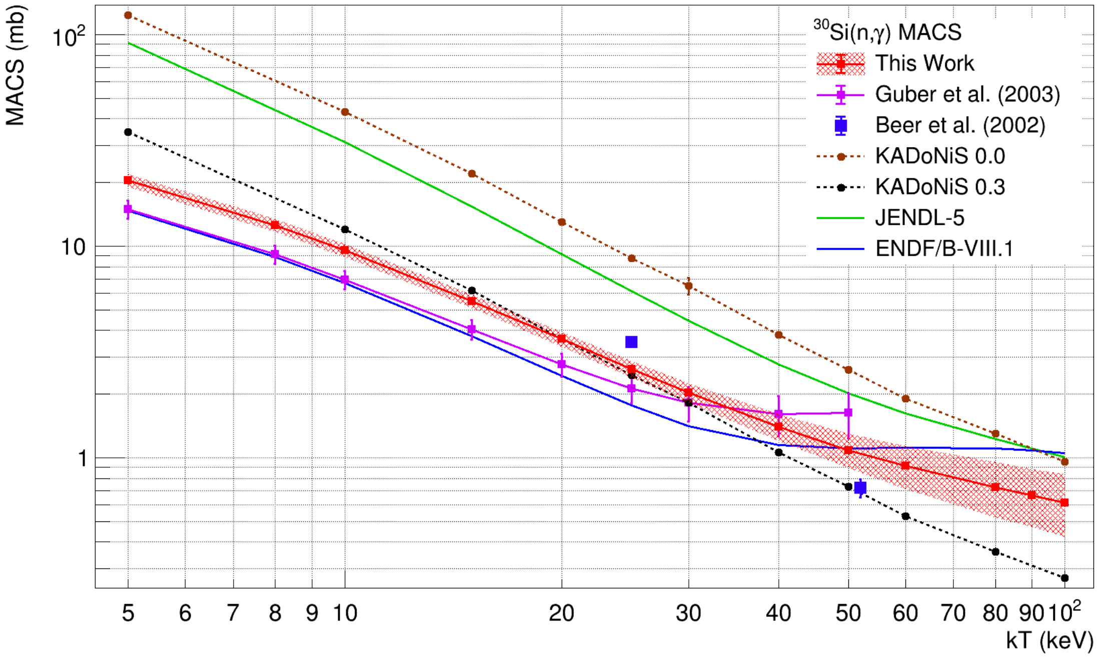

Figure 6.6: Comparison between the ^{30}Si(n,γ) MACS determined in this work and the values reported in previous measurements (Guber et al. [41], Beer et al. [44]), reported in the dedicated databases KADoNiS 0.0 [43] and KADoNiS 0.3 [45] and extracted from cross sections recommended in the most recent releases of some major evaluated nuclear data libraries (JENDL-5 [72] and ENDF/B-VIII.1 [70]).

only be partially constrained with an upper limit in this work, while the latter could only be theoretically estimated, resulting in very high uncertainties in the MACS, reaching more than 30%.

Figure 6.6 shows the MACS from this work compared with the values from previous measurements and extracted from dedicated databases and nuclear data evaluations. The values from this work are intermediate between the values from the two last measurements of Guber et al. and Beer et al. and, above 25 keV, they are compatible with Guber et al. within the uncertainty. Increasing the energy, the MACS from this work is intermediate between the values recommended in KADoNiS 0.0 [43] and KADoNiS 0.3 [45], but never compatible within the uncertainties, even if they increase up to more than 30%. Nevertheless, the uncertainties reported in this work are lower than what is reported in Guber et al. over all the energy range of interest.

kT	MACS (mb)			
(keV)	Resonances	DC s-wave	DC p-wave	Total
5	19.8 ± 1.4	$0.225 \pm^{0.015}_{0.012}$	0.24 ± 0.12	20.3 ± 1.4
8	12.0 ± 0.8	$0.178 \pm^{0.012}_{0.010}$	0.27 ± 0.14	12.4 ± 0.9
10	9.0 ± 0.6	$0.159 \pm^{0.011}_{0.008}$	0.28 ± 0.14	9.4 ± 0.7
15	5.0 ± 0.4	$0.130 \pm^{0.009}_{0.007}$	0.29 ± 0.15	5.4 ± 0.4
20	3.2 ± 0.2	$0.112 \pm^{0.008}_{0.006}$	0.29 ± 0.15	3.6 ± 0.3
25	2.19 ± 0.18	$0.100 \pm^{0.007}_{0.005}$	0.29 ± 0.14	2.6 ± 0.2
30	$1.62 \pm^{0.15}_{0.16}$	$0.092 \pm^{0.006}_{0.005}$	0.28 ± 0.14	2.0 ± 0.2
40	$1.03 \pm^{0.14}_{0.16}$	$0.079 \pm^{0.005}_{0.004}$	0.26 ± 0.13	1.4 ± 0.2
50	$0.76 \pm^{0.15}_{0.18}$	$0.071 \pm^{0.005}_{0.004}$	0.25 ± 0.12	1.1 ± 0.2
60	$0.61 \pm^{0.16}_{0.19}$	$0.065 \pm^{0.004}_{0.003}$	0.23 ± 0.11	0.9 ± 0.2
80	0.5 ± 0.2	$0.056 \pm^{0.004}_{0.003}$	0.20 ± 0.10	0.7 ± 0.2
90	0.4 ± 0.2	$0.053 \pm^{0.004}_{0.003}$	0.19 ± 0.09	0.7 ± 0.2
100	0.4 ± 0.2	0.050 ± 0.003	0.18 ± 0.09	0.6 ± 0.2

Table 6.4: MACS of ^{30}Si(n,γ) determined in this work at different energies kT, corresponding to different stellar temperatures T. The contributions of the resonances and of the direct capture in s-wave and p-wave are reported separately.

6.3 Results for ^{64}Ni(n,γ)

As anticipated in Section 1.5, previous data on the ^{64}Ni(n,γ) cross section in the range of astrophysical interest are scarce and discrepant, especially concerning time-of-flight measurements that are ultimately needed for the energy extrapolation of the MACS. The most recent time-of-flight capture measurements available in the literature in this energy range are:

- *Hockenbury et al.* (1969) [141], a capture measurement performed at the Rensselaer Electron Linear Accelerator (NY,USA) using an isotopically enriched sample (98.15% enrichment) at a neutron flight path of approximately 25 m. The total absorption technique was employed (see Section 3.3) using a massive xylene liquid scintillator.

- *Beer et al.* (1975) [142], combining both a transmission and a capture measurement performed at the 3 MV Van de Graaff accelerator of the Karlsruhe Institute of Technology (with a few meters of flight path) using an enriched ^{64}Ni sample (97.9% enrichment). The experiment could fully characterize the s-wave resonances below 100 keV and observe some p-wave resonances. However, a massive hydrogenated liquid scintillator was employed for the total absorption technique and no corrections for the neutron sensitivity were applied in the analysis (apart from a lower energy threshold of 3 MeV in the energy of γ rays).

- *Wisshak et al.* (1984) [44], a capture measurement also performed at the 3 MV Van de Graaff accelerator of the Karlsruhe Institute of Technology using an isotopically enriched sample (97.9% enrichment) at a few cm flight path, but employing a low neutron sensitivity setup exploiting the total energy detection technique (as in this work). This optimized setup resulted in a 50% reduction of the kernels measured for the two s-wave resonances below 100 keV. However, the characterization of p-wave resonances was not published, but only referenced as a private communication by Spencer and Macklin (1982), reporting resonances not observed in previous measurements.

The most recent releases of the major evaluated nuclear data libraries (ENDF/B-VIII.1 [70], JEFF-4 [71] and JENDL-5 [72]) agree on the capture cross section of ^{64}Ni up to hundreds keV, adopting the resonance parameters measured by Beer at al. [142]. However, these libraries additionally include a huge p-wave resonance at 9.52 keV (kernel of 1.75 eV) that has been observed by Hockenbury et al. [141], but not observed in any of the other mentioned measurements and neither in the transmission measurement performed by Farrell et al. (1966) [143]. This resonance is responsible for a huge increase in the ^{64}Ni(n,γ) cross section that heavily affects the calculation/extrapolation of the MACS at low energy (a few keV).

Two activation measurements of the MACS in the keV region are available in the literature:

- *Heil et al.* (2008) [144], performed again at the Karlsruhe Institute of Technology and obtaining a value of 9.0(3) at 25 keV

- *Domingo-Pardo et al.* (2009) [145], performed at the Physikalisch Technische Bundesaltstalt (PTB) in Brauschweig and obtaining a value of 7.1(3) at 52 keV.

The value measured by Heil et al. [144] has been recommended in the latest versions of the KADoNiS database, but the energy extrapolation of the MACS at lower energy presents large discrepancies between KADoNiS 0.3 [45] and KADoNiS 1.0 [60], mainly because of the 9.52 keV p-wave resonance. In fact, the energy extrapolation of KADoNiS 0.3 is based on the experimental data by Wisshak et al. not including the 9.52 keV resonance, while the energy extrapolation of KADoNiS 1.0 is based on the evaluated nuclear data libraries that include this resonance. The resulting discrepancy between the two extrapolations amounts to almost a factor 3 at 5 keV (see Table 6.9 and Figure 6.11). Finally, large discrepancies (almost a factor 3) currently exist between the MACSs from activation measurements and the values calculated from energy differential cross sections recommended in the evaluated libraries.

The following paragraphs will present the results from this work concerning the resonance parameters and the MACS.

6.3.1 Resonance fitting

Resonances in the ^{64}Ni capture yields could be fitted up to 63 keV, enough to provide a MACS based on experimental data up to 25-30 keV, where the contribution of resonances at higher energies is still lower than approximately 5% (Figure 6.10). This is the energy range important for most of the applications discussed in Section 1.5, related to AGB stars.

The fit of the resonances has been performed iteratively in the different energy regions, starting with a few bins per decade to fit the large s-wave resonances and gradually moving to a higher number of bins per decade to resolve the thinner p-wave resonances. Moreover, it is important to mention that, despite the efforts described in the previous chapter (Sections 5.2.1 and 5.2.2), the levels of the residual background between the resonances could not be reduced to a constant value. Therefore, the background had to be fitted locally for each energy region considered.

Figure 6.7 shows the fit of the capture yield in the energy range between 5 keV and 25 keV. In this region the residual background has been fitted using a function $a + b/\sqrt{E_n}$, where a, b are parameters and E_n is the neutron energy. A slight enhancement of the declared contamination from ^{62}Ni in our sample (0.3%) has also been fitted by SAMMY, in order to better reproduce the background in correspondence of its huge s-wave resonance of at 4.5 keV (see also Figure 6.9). The fits are shown at 100 bins per decade and at the finer binning of 500 bins per decade, to better investigate the possible presence of the predicted p-wave resonances. The results obtained from these fits can be summarized as follows:

- the huge p-wave resonance reported by evaluated nuclear data libraries at 9.52 keV is not present. This evidence already implies alone an important decrease of the MACS at a few keV compared with the values extracted from evaluated data libraries.

- the p-wave resonance expected at 14.8 keV is also not observed in the way it is

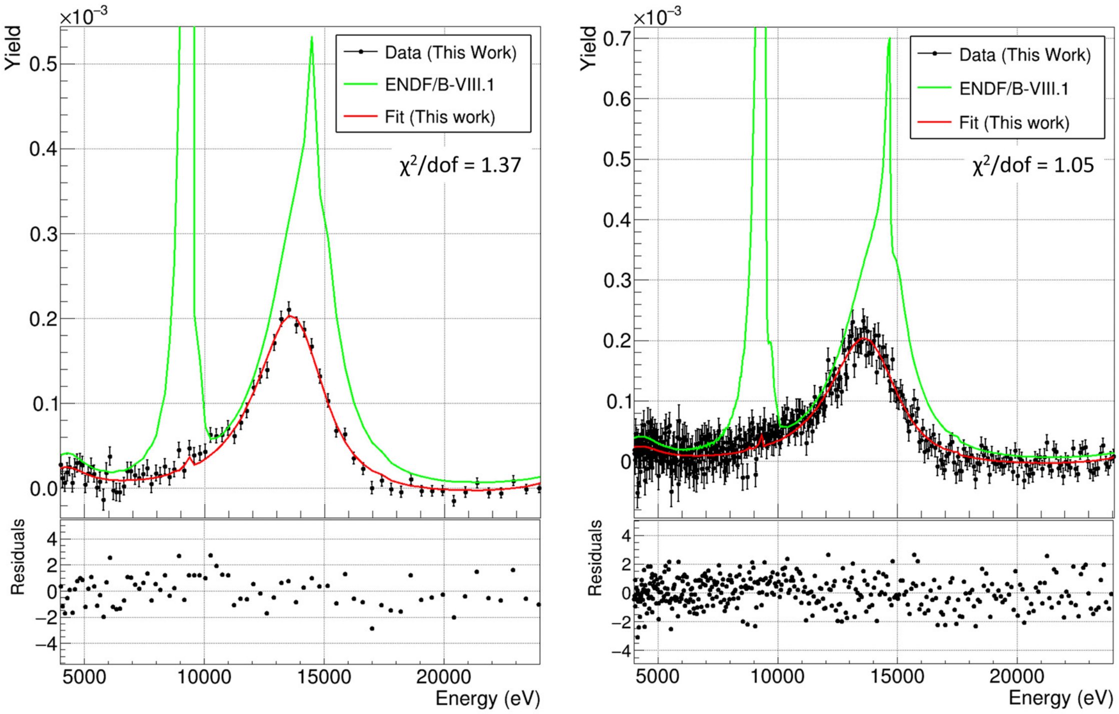

Figure 6.7: Fit of the ^{64}Ni(n,γ) yield in the energy range between 5 keV and 25 keV, compared with the yield expected from evaluated nuclear data libraries. In the left panel, the capture yield is plotted at 100 bins per decade, while in the right panel it is plotted at the finer binning of 500 bins per decade, to better resolve possible p-wave resonances.

reported by the evaluated data libraries. However, it is not possible to state whether this resonance does not exist or if it is just characterized by parameters slightly different from those reported, such that it cannot be resolved from the underlying s-wave resonance. The fit has been finally performed only considering the s-wave resonance, as its fitted kernel would also include the kernel of the possible p-wave resonance, without leading to a significant underestimation of the MACS.

- the kernel of the s-wave resonance at 13.8 keV is significantly reduced with respect to the value recommended in the libraries. Moreover, it is not compatible with any of the previous measurements, but it is closer to the value measured by Wisshak et al. (20% smaller) than to the value reported by Beer et al. (60% larger).

Figure 6.8 shows the fit in the region between 20 keV and 55 keV. In this energy region the residual background has been fitted with a function $a + c\sqrt{E_n}$, where a, c are parameters and E_n the neutron energy. Also in this case, the main results can be summarized in the following list:

- the huge p-wave resonance at 31.9 keV is observed and its fitted kernel is compatible with the values reported by Beer et al. and recommended in the evaluated data libraries

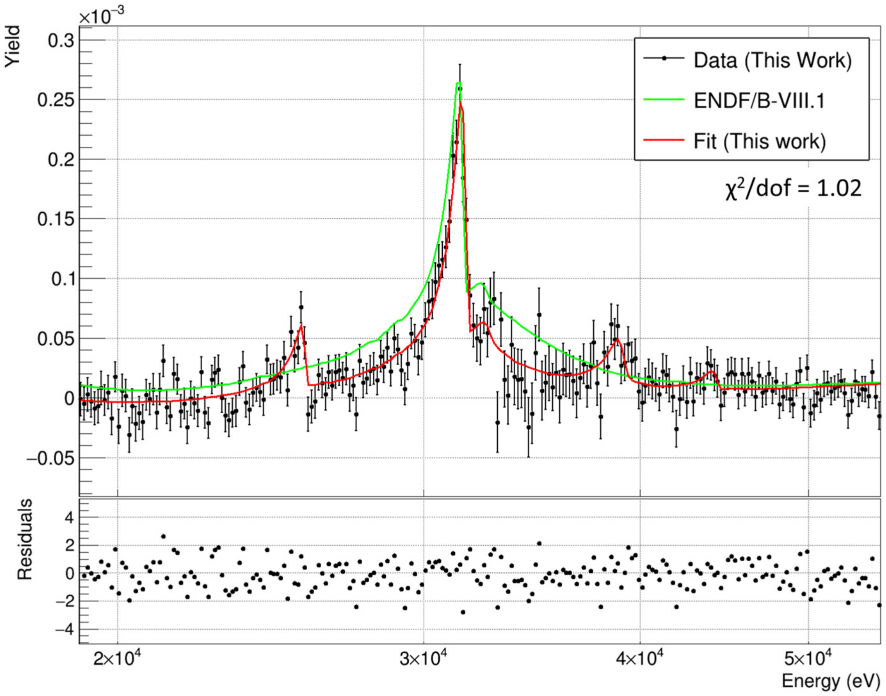

Figure 6.8: Fit of the ^{64}Ni(n,γ) yield in the energy range between 20 keV and 55 keV, compared with the prediction of evaluated nuclear data libraries.

- three resonances have been fitted at 25.8 keV, 39.5 keV and 44.7 keV. These resonances are reported neither in the evaluations, nor in any previous paper, but the first two of them were mentioned in a private communication of Spencer and Macklin to Wisshak [146]. The possibility that these resonances are due to scattered neutrons captured by the close 24.3-keV and 34.8-keV resonances of aluminium seems to be ruled out by the Monte Carlo simulations (where they do not appear) and by the fact that their energy does not correspond to the scattering scenario, as described in Section 5.2.2 for the structure at 5.9 keV. Therefore, they are proposed as new resonances for the ^{64}Ni(n,γ) cross section and they have been fitted as p-wave resonances.

- the broad s-wave resonance at 33.4 keV cannot be fitted with good accuracy because of the not completely resolved overlying p-wave resonance, but mainly because of the neutron sensitivity, due to the neutrons scattered by the sample and captured in the 34.8-keV resonance of aluminium (see Section 5.2.2). Even if this contribution has been studied with Monte Carlo simulations, a benchmarked scaling factor to compare simulations with data could not be fixed at the moment. Therefore, a systematic uncertainty related to the background has been evaluated as the difference between the fitted resonance kernels when considering a maximum neutron sensitivity (simulations normalized to the capture data) and when not considering the neutron sensitivity. It amounts to more than 40% and explains

J	l	Energy (keV)	Resonance kernel (eV)			
			This work	Wisshak	Beer	ENDF/B-8.1
0.5	0	13.76(2)	1.20 ± 0.09	1.01(7)	1.9(4)	1.9
-0.5	1	25.8327(4)	0.115 ± 0.017	0.134	-	-
-0.5	1	31.986(14)	$0.80 \pm ^{0.08}_{0.14}$	0.593	0.75(11)	0.75
0.5	0	33.4(5)	$1.2 \pm ^{0.5}_{0.4}$	1.16(8)	2.9(6)	2.9
-1.5	1	39.46(7)	$0.30 \pm ^{0.4}_{0.06}$	0.276	-	-
-0.5	1	44.6534(7)	0.11 ± 0.09	-	-	-
-0.5	1	62.813(17)	0.72 ± 0.09	0.820	0.85(18)	0.85

Table 6.5: Comparison between the kernels of the resonances fitted in this work, the values reported in the previous time-of-flight measurements by Wisshak et al. [147], Beer et al. [142] and the values recommended in the ENDF/B-VIII.1 evaluated nuclear data library (the same values are adopted in JEFF-4 and JENDL-5). J and l represent the spin of the resonances (the sign indicates the parity) and the orbital angular momentum, respectively. The kernels of the p-wave resonances (l=1) reported by Wisshak et al. are taken from a private communication by R. Spencer and R. Macklin (1982). The central values from this work are the ones adopted in Figures 6.7, 6.8 and 6.9. The reported uncertainties include both statistical and systematic contributions (Table 6.6).

the high systematic uncertainty associated to the kernels of the 33.4-keV and of the 39.5- keV resonances (Table 6.6). Despite the large uncertainty, the kernel of the 33.3 keV resonance obtained in this work is not compatible with the value reported by Beer et al. and recommended in the evaluated data libraries, but it is compatible with the smaller kernel measured by Wisshak et al.

Finally, a p-wave resonance has been fitted at 62.8 keV and its kernel is compatible with previous measurements. The fitted kernels of all the resonance observed in this work are resumed in Table 6.5 and compared with the values from previous measurements and recommended in the current releases of evaluated nuclear data libraries.

As for ^{30}Si, the final part of this section is devoted to the estimation of the systematic uncertainties affecting the measurement. Table 6.5 already reports the total uncertainty on the kernels, while Table 6.6 shows the separate contributions of statistical and systematic uncertainty for each resonance.

The detailed account of systematic uncertainties is shown in Table 6.7 and, similarly to what has been done for silicon, it includes the uncertainties due to:

- Counting rate stability, determined as the fluctuation of the counting rates of the sTED detectors and SiMon2, normalized to the number of protons

- PHWT, evaluated from Figure 5.6

Energy (keV)	Resonance kernel (eV)	Uncertainty (eV)		
		Statistical	Systematic	Total
13.76(2)	1.20	0.017	0.09	0.09
25.8327(4)	0.115	0.015	0.008	0.017
31.986(14)	0.80	0.04	$^{+0.07}_{-0.14}$	$^{+0.08}_{-0.14}$
33.4(5)	1.2	0.16	$^{+0.5}_{-0.4}$	$^{+0.5}_{-0.4}$
39.46(7)	0.30	0.05	$^{+0.4}_{-0.03}$	$^{+0.4}_{-0.06}$
44.6534(7)	0.11	0.09	0.008	0.09
62.813(17)	0.72	0.08	0.05	0.09

Table 6.6: Contribution of statistical and systematic uncertainties to the total uncertainties reported for the kernels of the resonances fitted in this work (Table 6.5). Systematic uncertainties dominate in the region of 30 keV because of the uncertainty in the neutron sensitivity background.

- Sample positioning, evaluated as the difference in the BIF for a possible sample misalignment of 0.5 mm. This contribution is smaller than in EAR1, probably because the sample is smaller, while the EAR2 beam plateau is larger.
- Energy dependence of the neutron flux, that is taken from the results of the commissioning of EAR2 [104]
- Dead time corrections, that have been evaluated in Section 5.1.5

Despite the evaluation of all these contributions, the systematic uncertainty affecting the measurement is in the end dominated by the uncertainties on the background and on the normalization. The former, mainly due to the neutron sensitivity affecting the region around 35 keV, has been already commented.

Concerning the uncertainty on the normalization, a detailed account is also shown in Table 6.7. It includes the uncertainty on the fit of the saturated resonance and the uncertainty in the reproducibility of the thermal capture cross section of ^{197}Au (which was checked to determine the accuracy of the normalization performed without dead time corrections, as explained in Sections 5.1.5 and 5.2.3). It also includes a contribution for the missing corrections due the counts lost below the threshold: since these corrections have been estimated at around 5% for ^{30}Si (Section 4.3.4), a 3% uncertainty is adopted for ^{64}Ni considering that the energy deposited threshold fixed in the sTED is lower and that nickel is heavier than silicon.

However, the biggest contribution to the systematic uncertainty in the normalization arises from the shape and area of the gold sample employed. As discussed in Section 5.2.3, the normalization has to be performed with a sample in the same position and with the exactly same shape as the sample under study. In order to reproduce the asymmetric shape of the ^{64}Ni sample (Figure 3.12), the gold sample used for normalization had to be cut by hand, with an accuracy that cannot be quoted below 0.3 mm in

	Systematic Uncertainty (%)	
	Resonance region	Thermal region
Normalization - corrections	3	3
Normalization - gold at thermal	3	3
Normalization - fit saturated resonance	0.5	0.5
Normalization - sample shape/area	5	5
Normalization	**6.6**	**6.6**
Counting rate stability	0.5	0.5
PHWT	1	1
Normalization	1	1
Sample positioning	0.5	0.5
Neutron flux	2.5	2.5
Dead time	1	1
Europium contamination	-	0.2
Fit extrapolation	-	2
Total (without background)	**7.2**	**7.5**
Background	1 - 44	3
Total	**7.3 - 45**	**8.1**

Table 6.7: Estimation of the systematic uncertainties affecting the measurement. The different contributions are reported separately and summed in the last lines. The first lines present a detailed estimation of all the contributions related to the normalization, that are summed in the fifth line. The uncertainty related to the background has been evaluated separately for each resonance, therefore only a range of values can be given here.

its dimensions. The corresponding variation of the area of the sample has been adopted as systematic uncertainty on the normalization. In fact, the normalization factor has been found to scale nearly linearly with the sample area, as shown by measurements on circular gold samples with slightly different radii around 7.5 mm.

6.3.2 Thermal cross section

Differently from the ^{30}Si(n,γ) cross section, the capture cross section of ^{64}Ni is characterized by broad resonances in the energy range of astrophysical interest, that dominate the MACS. Therefore, the direct capture component is believed to provide only a negligible contribution and it has not been considered.

However, as already discussed in Section 2.2.4, a relevant effect is expected in the thermal and epithermal region of the cross section, that can be only partially explained by the tails of the resonances fitted between 10 and 100 keV. In fact, after fitting the

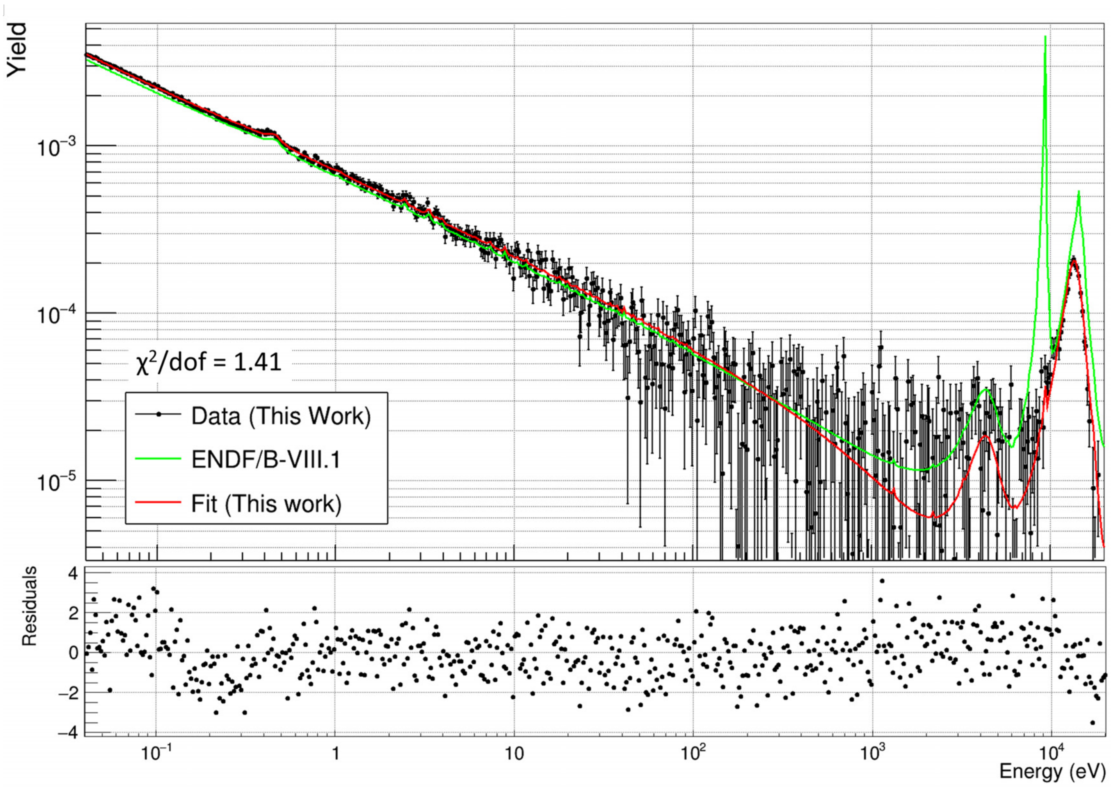

Figure 6.9: Fit of capture yield of ^{64}Ni in the 1/v region between 0.04 eV and 20 keV, compared with the evaluated nuclear data libraries. A negative resonance has been employed to properly fit the yield and extrapolate the thermal cross section.

s-wave resonances at 13.8 and 33.4 keV, the epithermal region of the measured capture yield of ^{64}Ni could not be reproduced. Therefore, a negative resonance has been assumed to properly fit the capture yield in the energy range between 0.04 eV and hundreds of eV, as shown in Figure 6.9.

The thermal capture yield could not be directly observed because of problems in the subtraction of the sample-dependent neutron scattering background, estimated with the yield of a carbon sample (Section 5.2.2). In fact, in the thermal energy region the carbon spectra exhibit peaked structures related to the internal structure of the sample, that prevent an accurate scaling to reproduce the neutron scattering background induced by a different sample. Therefore, the thermal capture cross section of ^{64}Ni (at 25.3 meV) has been extrapolated from the fit of the capture yield in the epithermal region. As a consequence, apart from the systematic uncertainties commented in the previous section, an additional contribution due to the extrapolation has been added, mainly based on the uncertainty associated to the fitted parameters of the negative resonance. The uncertainty on the fitted contamination of europium in the sample (see Section 5.2.4) has been finally taken into account, but its effects on the measured thermal capture yield turned out to be negligible. These additional uncertainties are shown in Table 6.7.

The thermal cross section of ^{64}Ni extrapolated in this work is finally shown in Ta-

Reference	Thermal Cross Section (b)
This Work	**1.68 ± 0.14**
ENDBF/B-VIII.1 [70]	1.48
Farina Arboccò et al. (2013) [148]	1.62 ± 0.01
Shivanshankar et al. (2012) [149]	1.59 ± 0.02
Venturini et al. (1997) [150]	1.6 ± 0.1
De Corte et al. (1989) [151]	1.67 ± 0.04
Gryntakis et al. (1978) [152]	1.58 ± 0.04
Heft at al. (1978) [153]	1.49 ± 0.02
Gleason et al. (1975) [154]	1.49 ± 0.07
Ryves et al. (1970) [155]	1.49 ± 0.02
Emery et al. (1968) [156]	1.4 ± 0.1
Lyon et al. (1960) [157]	1.45 ± 0.15
Seren et al. (1947) [158]	1.96 ± 0.39

Table 6.8: Thermal capture cross section of ^{64}Ni (at 0.0253 eV) extracted in this work and compared with the values recommended in the evaluated nuclear data libraries and reported by previous measurements available in EXFOR. The measurements are listed in chronological order, from the most recent to the most old one. The thermal cross section recommended in ENDF/B-VIII.1 (reported here) is adopted by all the current releases of the major evaluated data libraries such as JEFF-4 and JENDL-5.

ble 6.8 and compared to the values from previous measurements (mainly activation measurements in nuclear reactors) and recommended in the evaluations. Despite the relatively high uncertainty, the result from this work is not in agreement with the evaluated nuclear data libraries, but it is in agreement with the most recent measurements that suggest a thermal capture cross section slightly larger than the recommended value.

6.3.3 Maxwellian Averaged Cross Section

As a final result of this work, the MACS of the ^{64}Ni(n,γ) has been computed at thermal energies kT ranging from 5 keV to 50 keV, integrating the fitted capture cross section from the previous section. As shown in Figure 6.10, the MACS is almost fully based on the experimental data up to 25 keV, the energy range that is important for most of its astrophysical applications related to AGB stars. At higher energy, an increasing contribution of the higher energy resonances not accessible in this work is observed, reaching more than 25% for the MACS at 50 keV.

The MACS in shown with its total uncertainty in Table 6.9 and in Figure 6.11, where it is compared with previous activation measurements, values recommended in the KADoNiS database and values integrated from the capture cross section recommended in the evaluated data libraries.

First of all, it can be observed that, without any scaling factor, the values obtained from this work are significantly lower than the ones calculated using the evaluated data

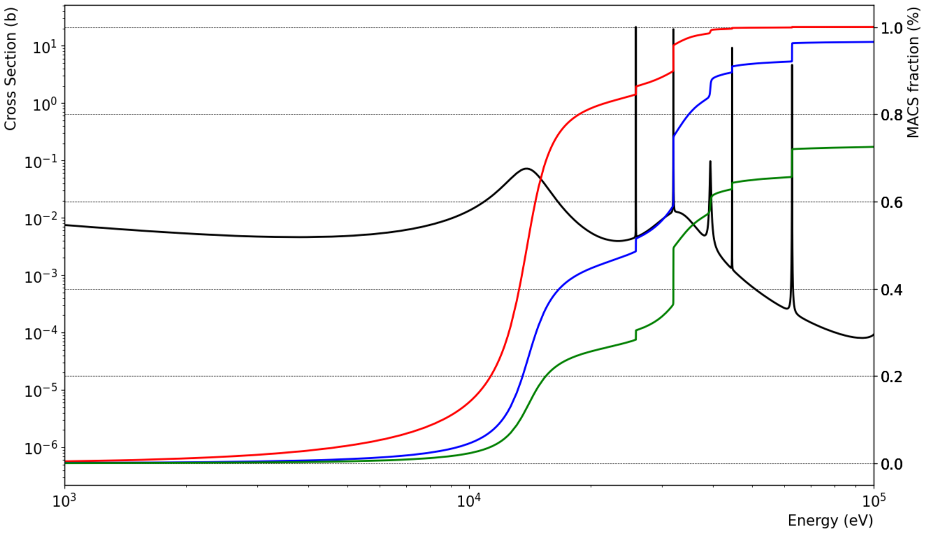

Figure 6.10: Contribution of the cross section extracted from this work (in black) to the MACS at 8 keV (red), 25 keV (blue) and 50 keV (green) as a function of the energy.

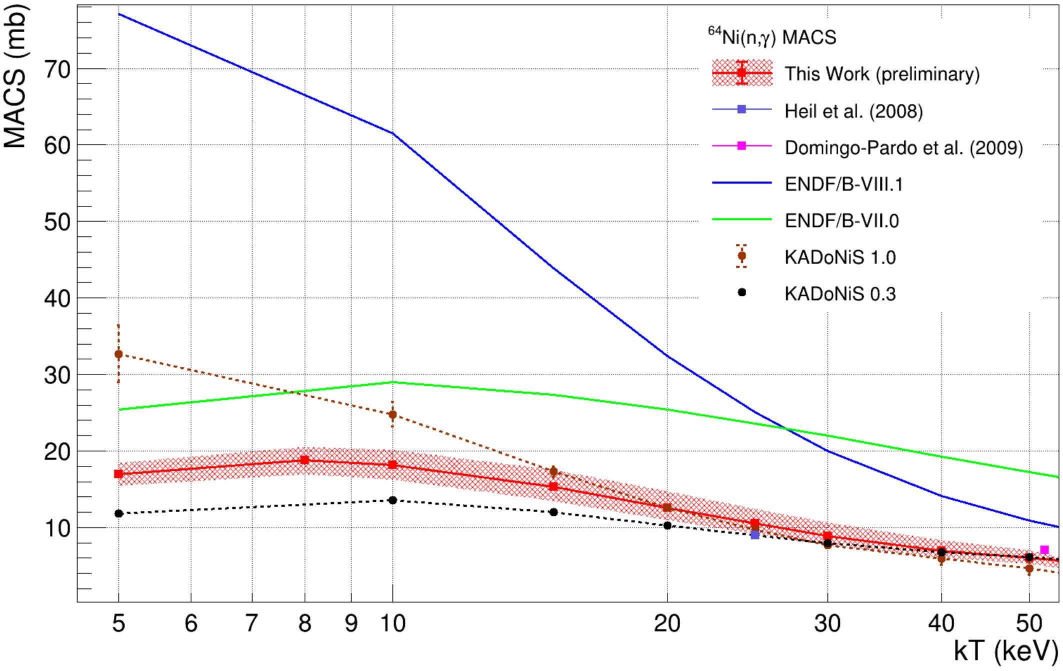

Figure 6.11: Comparison between the ^{64}Ni(n,γ) MACS determined in this work and the values reported in previous activation measurements (Heil et al. [144], Domingo-Pardo et al. [145]), reported in the dedicated databases KADoNiS 0.3 [45] and KADoNiS 1.0 [60] and extracted from the cross sections recommended in the current releases of the major data libraries (ENDF/B-VIII.1, the same as JEFF-4 and JENDL-5) and in the older ENDF/B-VII.0, which does not include p-wave resonances in the range of astrophysical interest.

libraries and they are compatible within the uncertainties with both the activation measurements available at 25 keV and 52 keV.

Comparing the results with the energy extrapolation of KADoNiS, at low energy the MACS from this work is discrepant with both the values reported in KADoNiS 0.3 and KADoNiS 1.0, but the shape is more similar to the former. Moving at higher energy, the uncertainty on the MACS increases because of the systematic effects related to the background in the region around 35 keV and the results of this work becomes compatible with both KADoNiS 0.3 and KADoNiS 1.0 within the uncertainty, even if again more similar to the former.

kT	MACS (mb)			
(keV)	This work	Prev. meas.	KADoNiS 0.3	KADoNiS 1.0
5	$17.0 \pm^{1.4}_{1.5}$		11.8	33(4)
8	$18.8 \pm^{1.7}_{1.8}$		-	-
10	$18.2 \pm^{1.9}_{1.9}$		13.6	24.8(1.6)
15	$15.3 \pm^{2.2}_{1.8}$		12.0	17.3(7)
20	$12.6 \pm^{2.1}_{1.6}$		10.3	12.6(4)
25	$10.5 \pm^{1.9}_{1.3}$	9.0(3)	9.0	9.7(3)
30	$8.9 \pm^{1.7}_{1.2}$		8.0(7)	7.7(3)
40	$7.0 \pm^{1.3}_{0.9}$		6.8	5.9(8)
50	$6.0 \pm^{1.0}_{0.7}$	7.1(3)	6.1	4.7(9)

Table 6.9: MACS of ^{64}Ni(n,γ) determined in this work at different energies kT, corresponding to different stellar temperatures T. These values are compared with the previous activation measurements performed by Heil et al. at 25 keV [144], Domingo-Pardo et al. at 52 keV [145] and with the extrapolated MACS recommended in KADoNiS 0.3 [45] and KADoNiS 1.0 [60].

Conclusions

The neutron capture cross sections of ^{30}Si and ^{64}Ni have been shown to represent key quantities for nuclear astrophysics. The former is relevant to understand the silicon isotopic abundances measured in some pre-solar components of meteorites (the SiC grains), that still cannot be reproduced by any astrophysical model of galactic chemical evolution. The latter is a key input parameter in nucleosynthesis models of the s-process in massive and Asymptotic Giant Branch stars that has been found to significantly affect the predicted abundances of a large number of isotopes, even up to lead.

Data available in the literature and in the evaluated nuclear data libraries for the capture cross sections of these isotopes are characterized by large discrepancies in terms of energy and strength of the resonances, that directly affect the energy extrapolations of the Maxwellian Averaged Cross Sections (MACS) reported in the different releases of the KADoNiS database.

For these reasons, new time-of-flight measurements of the capture cross sections of ^{30}Si and ^{64}Ni have been performed at the n_TOF facility, a white neutron source based on the spallation of 20 GeV/c protons on a massive lead target and located at CERN. Highly isotopically enriched samples ($> 99.5\%$ enrichment) have been employed in both measurements and for the first time in a measurement of the ^{30}Si(n,γ) cross section. The available quantity of ^{30}Si (approximately 750 mg) has made it possible to perform the measurement in the first experimental area of the facility (EAR1), located at 200 m from the spallation target and characterized by an excellent energy resolution ($10^{-4} < \Delta E/E < 10^{-2}$), particularly useful for the accurate study of resonances. On the other hand, ^{64}Ni was only available in a smaller quantity (approximately 430 mg), requiring the measurement to be performed in the second experimental area of the facility (EAR2), located at approximately 20 m from the spallation target and characterized by a higher neutron flux ($> 10^7$ neutrons/pulse). The experimental setup in both cases has consisted in arrays of deuterated benzene (C_6D_6) liquid scintillators, aimed at detecting the γ rays following neutron capture events, but minimizing the background due to the capture of scattered neutrons.

The Total Energy Detection technique coupled with the Pulse Height Weighting Technique have been employed to guarantee a constant efficiency of the detectors in detecting capture events, independent of the random de-excitation path of the compound nucleus following neutron capture reactions. The weighting functions required by this technique have been determined via accurate GEANT4 Monte Carlo simulations of the experimental setups.

The detector setup employed in this work did not allow for the discrimination between signal and background, mainly due to γ rays from the capture of neutrons scattered around the experimental areas. For this reason, the background has been evaluated with ancillary measurements (using empty sample holders, carbon and lead samples) and subtracted a posteriori. Concerning the analysis of EAR2, additional Monte Carlo simulations have been performed to estimate the background due to the neutrons scattered by the ^{64}Ni sample and immediately captured in the resonances of the aluminium making up the casings of the detectors. This background has been found indeed to significantly affect the resonances of ^{64}Ni around 30 keV, which fall within the same energy range as those of aluminium. Despite these efforts, this background component could only be characterized with a large uncertainty.

The cleaned capture yield has been normalized using gold samples of the same shape and position as the samples under study and by fitting the top of their 4.9 eV saturated resonance. This technique has allowed for the determination of the actual beam interception factor and of possible corrections to the simulated efficiency. Corrections to the normalization factors have been additionally estimated taking into account the counts lost below the deposited energy threshold, the internal conversion electrons and the variation of the beam interception factor as a function of the neutron energy, which plays a relevant role especially in the thermal and epithermal energy region.

The measured capture yield has been finally fitted with the R-Matrix code SAMMY in order to extract the resonance parameters and integrated to obtain the Maxwellian Averaged Cross Sections for astrophysical applications.

The results for the ^{30}Si(n,γ) cross section show important discrepancies with respect to evaluated nuclear data libraries and previous measurements. In particular, a huge resonance at 2.35 keV reported by JENDL-5 is not observed, while a resonance at 15.1 keV, recently adopted in ENDF/B and JEFF but not in JENDL, has been confirmed. Moreover, our kernels for the first two resonances of ^{30}Si(n,γ), fitted with an uncertainty lower than 8.5%, are respectively 35% and 50% larger than the values recommended in ENDF/B-VIII.1, JEFF-4 and reported by the latest time-of-flight measurement by Guber et al. [41]. Even if with larger uncertainty (up to 40%), resonances could be fitted up to 303 keV, excluding a resonance at 190 keV recently adopted by ENDF/B-VIII.1 and constraining the 180 keV s-wave resonance, providing an upper limit on its radiative width that is between 30% and 50% smaller than the values currently recommended in the evaluated data libraries.

Since no resonances have been observed between 15 and 180 keV, the direct capture represents the dominant reaction mechanism in this energy range and therefore plays a pivotal role in the determination of the MACS: it has been found indeed to account for up to 37% of the MACS, at 100 keV. However, since the data between the resonances are fully dominated by the background, the direct capture component could neither be measured nor constrained with our experimental setup, but it could only be estimated via theoretical calculations, which have been provided by A. Mengoni. A large systematic uncertainty (50%) has thus been associated to the results.

The MACS has been finally provided with an uncertainty within 9% up to approximately 25 keV, where it is mainly determined by the well-characterized low-energy resonances (contributing for more than 85%). In this energy range our MACS is discrepant, but intermediate between the previous measurements by Guber et al. [41] and Beer et al. [44]. Increasing the energy, the MACS gradually becomes more uncertain (up to more than 30% uncertainty at 100 keV) due to the increasing contributions of the direct capture and of the not accurately characterized high energy resonances. In this energy range, our MACS becomes compatible with the values from Guber et al. within the uncertainties, but always discrepant and intermediate between the energy extrapolations suggested by KADoNiS 0.0 and KADoNiS 0.3.

The results for the ^{64}Ni(n,γ) cross section also show important discrepancies with respect to the evaluated nuclear data libraries. In this case, resonances could be fitted up to 63 keV and three new resonances have been observed at 25.8, 39.5 and 44.7 keV, never published before, even if some of them were already mentioned in a private communication of Spencer and Macklin to Wisshak et al. [146]. On the other side, the huge p-wave resonance reported by evaluated data libraries at 9.52 keV and observed only by Hockenbury et al. [141] has not been observed, determining alone a drastic reduction of the MACS at a few keV. Moreover, an important reduction of the kernels of the s-wave resonances at 13.8 and 33.4 keV has been observed in comparison with the evaluated nuclear data libraries and the previous measurement by Beer at al. [142], that are between 60% and 140% larger. Our values are more similar to the latest measurement by Wisshak et al. [147], even if discrepant for the 13.8 keV resonance. However, the resonances around 35 keV could only be characterized with large systematic uncertainties (up to more than 40%) due to the uncertain background induced by scattered neutrons.

These large uncertainties, together with the ones due to the normalization of the capture yield, have been propagated in the calculation of the MACS, which eventually cannot be reported with an uncertainty lower than 8%. Despite this uncertainty, the MACS resulting from this work is drastically reduced with respect to the values obtained by integrating the cross sections from evaluated nuclear data libraries (up to almost 80% at 5 keV) and it is compatible within the uncertainties with the activation measurements by Heil et al. [144] and Domingo-Pardo et al. [145] at 25 keV and 52 keV, respectively. Our MACS is generally discrepant and intermediate between the energy extrapolations of KADoNiS 0.3 and KADoNiS 1.0 at low energy, while it becomes compatible with both after 25 keV, even if in general it is more similar to the former. Finally, the thermal capture cross section of ^{64}Ni has been extrapolated from the fit of the capture yield measured in the epithermal region, down to 0.04 eV. Also in this case, despite the relatively large uncertainty of 8%, the result of this work is discrepant with respect to the capture cross section recommended in the evaluated data libraries, but agrees with the latest activation measurements [148–150] that suggest a slightly higher thermal capture cross section of ^{64}Ni.

Anyway, a new time-of-flight measurement of the ^{64}Ni(n,γ) cross section is advised for the future, using aluminium-free detectors in order to reduce the large uncertainties affecting the energy region around 30 keV.

In conclusion, the results from this work concerning both ^{30}Si(n,γ) and ^{64}Ni(n,γ) cross sections call for a revision of the evaluated nuclear data libraries, given the strong discrepancies observed concerning the presence or absence of resonances and their kernels, especially for ^{64}Ni. Moreover, the new data from this work are going to be soon provided as input to the stellar nucleosynthesis and galactic chemical evolution models to assess their impact on astrophysical predictions.

Appendix A

Simulations of the effects of a cavity in second generation target

Part of the work of this thesis has been devoted to FLUKA [105, 106] Monte Carlo simulations of the previous second-generation n_TOF spallation target.

This target consisted of a 1.3 tonnes lead cylinder characterized by a radius of 40 cm and a length of 60 cm. It was surrounded by a 1-cm-thick layer of demineralized water acting as coolant and, only in the forward direction (towards EAR1), it was equipped with an additional 4-cm-thick layer of borated water acting as moderator. A thin aluminium layer separated the two water layers. Finally, the target assembly was surrounded by an aluminium container and supported by an aluminium structure. The target was in operation for ten years, from 2009 to 2018.

After a necessary period of cool-down, an autopsy of the target was performed in 2024 and a cavity of several cm was discovered in correspondence of the impact position of the proton beam (see Figure A.1). The causes of the formation of this cavity, either physical or chemical, are still under investigation. In this context, Monte Carlo simulations of the target assembly have been required to estimate the energy deposited by the proton beam in the target and to study the effects of the cavity on the neutron beams.

Energy deposition in the target

The energy deposited by the impact of the proton beam on the target represents an important input information for studying its thermo-mechanical response. This includes the study of the temperature evolution in different regions of the target, the heat transfer processes and the resulting possible stresses and mechanical deformations. A part from the beam intensity, these studies are particularly sensitive to the size of the proton beam impacting on the target. In fact, at constant beam intensity, a more focused beam results in a higher deposited energy density at the impact point, that causes a larger temperature rise. The temperature can locally exceed the melting point of lead (328°C), triggering the formation of a cavity.

Figure A.1: Pictures of the cavity discovered in the second-generation n_TOF spallation target. Pictures from O. Aberle.

In this work, Monte Carlo simulations have been performed simulating a proton beam with horizontal and vertical root mean square dimensions of 16 and 6 mm, respectively. These values have been provided by the Proton Synchrotron (PS) operators. The resulting energy deposited in a section of the target is shown in Figure A.2, together with the profile of the cavity. These results have been provided to experts for the simulation of the thermo-mechanical response of the target. Although the maximum energy deposition occurs exactly in the position where the cavity was formed, the simulated proton beam dimensions alone do not seem sufficient to justify an increase in temperature that can melt the lead (the peak temperature from preliminary simulations has been estimated to be only around 160°C).

A.1 Effects of the cavity on the neutron beams

The most consistent part of the performed Monte Carlo simulations has been aimed at studying the effects of the cavity on the neutron beams delivered to the experimental areas. A posteriori, the interest in these effects is motivated by the possibility of finding some observables particularly sensitive to the formation of a cavity in the target. The variation of these observables over time can potentially be used to determine when the cavity was formed and consequently provide a time constrain for the investigation of the causes of the cavity formation. Moreover, these observables may be exploited to monitor on-line the status of the spallation target during the future operation of the facility.

Several observables have been studied: neutron fluence, neutron beam centroids and dimensions, resolution function and γ rays production. All of them have been simulated both considering the undamaged target and implementing the cavity, in order to perform a comparison between the two situations. The cavity has been implemented according to the geometrical information provided by the autopsy, as shown in Figure A.3: it has been

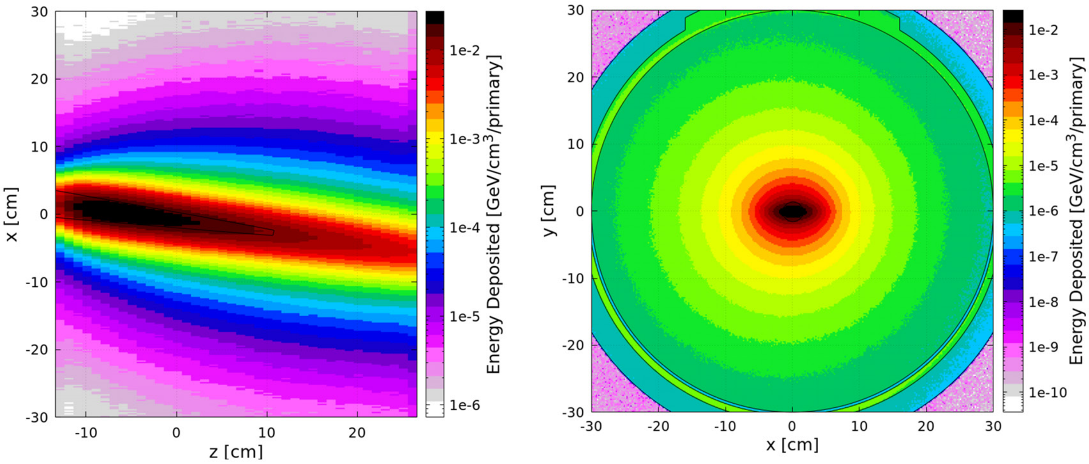

Figure A.2: FLUKA simulations of the energy deposited by the proton beam in a horizontal (left panel) and in a vertical (right panel) section of the spallation target. In the horizontal section, the profile of the cavity observed in the target is also shown.

approximated as a 24.5-cm-deep truncated cone with upstream diameter of 4 cm, downstream diameter of 1 cm, axes aligned to the direction of the proton beam that is 10° tilted with respect to the axis of the target, and filled with water. Finally, it has to be mentioned that, with or without cavity, all the analysed quantities have been scored at the beginning of the vacuum lines leading to the experimental areas (Figure A.3), imposing a cut on the direction of the particles compatible with the directions of the experimental areas. Even if this scoring choice does not allow a direct comparison between simulations and experimental data, it does anyway provide a reliable approximation of the effects of the cavity in the target, with the advantage of drastically reducing the computing time and resources. The following paragraphs will describe in detail the effects observed on each quantity that has been studied.

Neutron fluence

The cavity has been found to cause an overall reduction of approximately 7.5% of the neutron fluence at the scoring plane towards EAR1, as shown in Figure A.4. This effect is due to the shorter development of the hadronic shower triggered by the high-energy proton beam impacting the target. Due to the cavity, protons impact lead almost at the centre of the target, resulting in a reduced neutron production. On the other side, fast neutrons directly ejected by proton-induced reactions in the first step of the process have a higher chance of emerging without reinteracting in the target: this may probably explain the slight increase of the fluence of high energy neutrons when considering the cavity. The predicted decrease of the neutron fluence at lower energies is compatible with the data collected in EAR1 in 2018: at that time, the neutron flux was measured with a MicroMeGas detector during a fission measurement campaign and it was indeed found to underestimate the recommended evaluated neutron flux measured in 2014, without

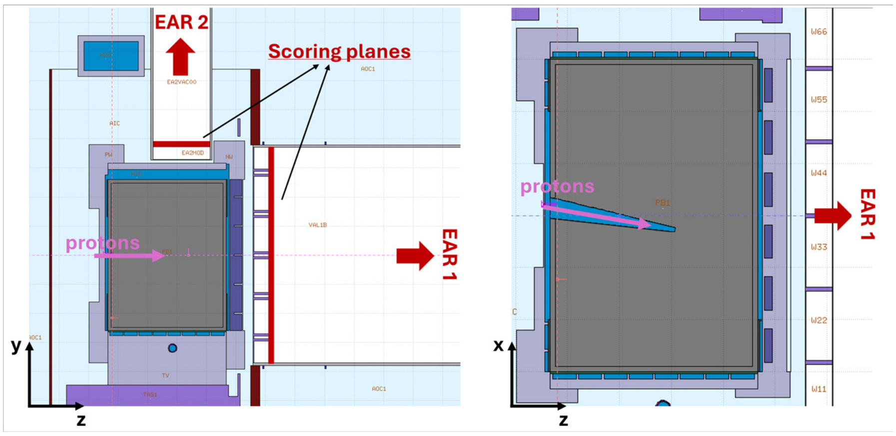

Figure A.3: Vertical (left) and horizontal (right) sections of the target-moderator assembly as simulated in FLUKA. On the right, the vacuum lines towards the experimental areas can be observed and the positions of the scoring planes are highlighted. On the left, the geometry of the cavity as provided after the autopsy of the target is visible.

any apparent reason at that time.

The neutron fluence reduction is even more significant at the scoring plane towards EAR2, where it amounts to approximately 20%. In this case, the reason for this attenuation is also geometrical and it is due to the fact that the impact position of the protons in the lead target, displaced downstream because of the cavity, is no longer optimized for EAR2.

Spatial neutron beam profile

The spatial neutron beam profile has been simulated at the scoring planes in the direction of the experimental areas in order to study possible displacements of the beam centroid or possible variations in its width due to the cavity.

Concerning EAR1, the cavity just slightly reduces the beam dimensions, probably because of the shorter development of the hadronic shower in the target that also causes a decrease of its lateral spread. Moreover, because of the higher fraction of forward-boosted high energy neutrons, the beam distribution seems slightly more peaked. However, these effects are not significant.

On the other hand, the cavity causes a significant displacement of the centroid of the neutron beam delivered to EAR2, as shown in Figure A.5. In fact, because of downstream displacement of the proton impact position in the target, a corresponding displacement of approximately 3 cm in the same direction is observed for the neutron beam centroid. Even if the beam profile is significantly altered by the collimators before reaching the experimental areas, variations in the beam profile may still be observed. However, experimental data for comparison over different years are not available.

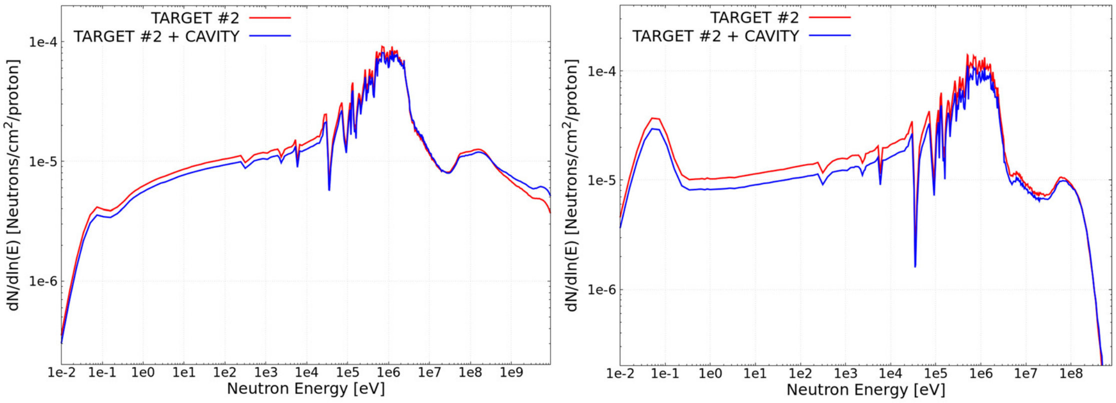

Figure A.4: FLUKA simulations of the neutron isolethargic fluences at the scoring plane towards EAR1 (left image) and EAR2 (right image) considering (blue line) or not considering (red line) the cavity in the target.

Resolution function

The resolution function, already introduced in Section 3.2, can be described as the distribution of the time spent by a neutron of a certain energy in the target-moderator assembly. The resolution function has been simulated by registering the time and the energy of neutrons crossing the scoring planes in the direction of the experimental areas. The time has been transformed into an effective moderation length λ by multiplying by the neutron velocity. The Full Width at Half Maximum of the distributions of λ at different neutron energies (related to the energy resolution of the beams) has been finally studied and compared considering or not considering the cavity in the target.

No significant differences have been observed in the energy resolution of EAR2 between the two situations.

On the other hand, after the implementation of the cavity in the target, a 20% reduction of the FWHM of the λ distributions has been observed for neutrons directed to EAR1 with energies ranging between 0.1 and 1 MeV (Figure A.5). This improvement in the energy resolution is probably due to the shorter path that neutrons have to travel in the target. At lower energies, the cavity does not produce any effect because the energy resolution is dominated by the effects of the moderator.

γ ray production

Last but not least, the fluence of the γ rays produced in the spallation target and directed towards the experimental areas has been simulated and studied at the scoring planes. As already discussed in Section 3.1, two γ rays components can be distinguished using a time threshold, as shown in Figure A.6:

- a *prompt γ ray* component that is produced by the spallation (e.g. through production and decay of neutral pions) and constitutes the γ flash that reaches EAR1

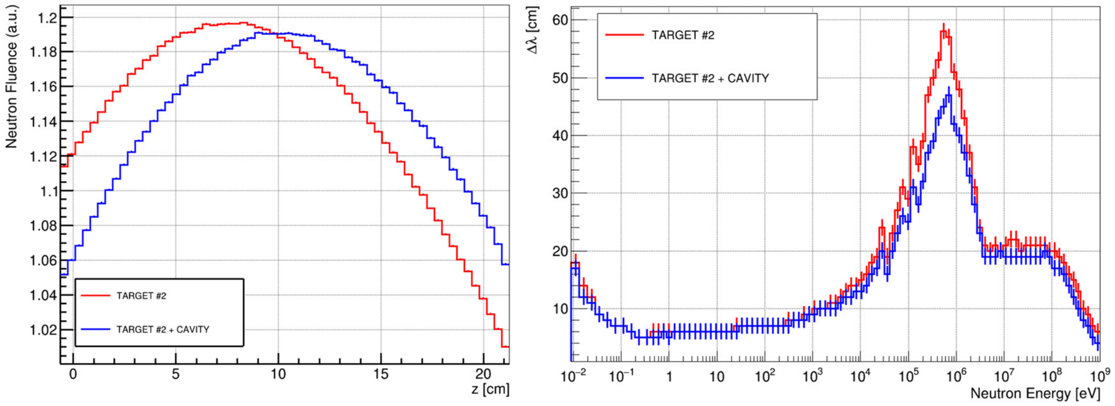

Figure A.5: FLUKA simulations of the spatial neutron beam profile at the scoring plane of EAR2 (right image) and of the FWHM of the effective moderation length λ distribution as a function of the neutron energy at the scoring plane of EAR1 (right image). Red lines refer to the simulations performed with the undamaged target, while blue lines refer to the simulations performed after implementing the cavity.

(the so-called γ flash that reaches EAR2, given its geometry, has indeed a different nature).

- a *delayed γ ray* component, due to the interaction of neutrons with the materials of the target-moderator assembly and that reaches the experimental areas together with the neutron beam (*in-beam γ rays*).

Since the delayed γ rays are due to the interactions of the neutron beams and the neutron fluence is overall reduced because of the cavity, a corresponding decrease of the in-beam γ ray fluence is observed for both experimental areas when the cavity is considered in the simulations.

In contrast, the cavity in the target has been found to cause a 60% increase in the prompt γ ray fluence towards EAR1. This is probably due to the fact that, since protons impinge more downstream in the target, the γ rays produced in the spallation process have to travel a shorter distance before exiting the target, therefore their attenuation is reduced. In conclusion, the intensity of the γ-flash of EAR1 has turned out to be the most sensitive observable to the possible presence of cavities in the target. In fact, the prompt γ ray fluence has been additionally studied by simulating cavities of different depths and, as shown in Figure A.6, a 10% increase of the EAR1 γ-flash can be already observed with a 5-cm-deep cavity.

Also as a result of this study, a diamond detector was installed in the first months of 2025 in the EAR1 beam halo, upstream of the second collimator. Besides acting as a beam monitor for the transmission measurements that only recently have been proposed in EAR1, the detector can also be used to measure and track temporal variations of the γ-flash, providing a monitor of the condition of the target during the future operations of the facility.

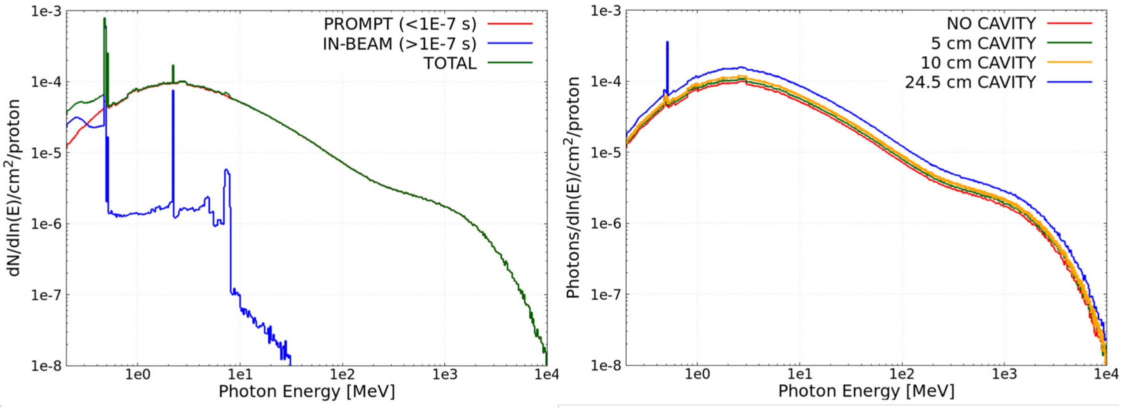

Figure A.6: Left: FLUKA simulation of the prompt (red), delayed (blue) and total (green) γ ray fluence as a function of the γ ray energy at the scoring plane in the direction of EAR1. The delayed component is characterized by peaks of fluence at the energies corresponding to photons from neutron capture reactions in hydrogen (2.2 MeV) and aluminium (7.7 MeV). The prompt γ rays component is smoother and includes γ rays of higher energy. The 511 keV peak due to electron-positron annihilation is present in both components.
Right: FLUKA simulation of the prompt γ ray fluence towards EAR1, considering cavities of different depths.

The work described in this appendix has been performed under the supervision of V. Vlachoudis (CERN, Accelerator Systems (SY) Department).

Appendix B

Parametrization of cross sections in the resonance region

A more detailed treatment of the theories used to describe and parametrize cross sections in the resonance region is presented in this appendix, complementing what introduced in Chapter 2. In particular, the R-Matrix theory and the Hauser-Feshback theory are presented.

B.1 The R-Matrix Theory

The advantages of parametrizing cross sections have already been discussed in Section 2.2.3, together with the basic ideas at the base of the R-Matrix theory.

As a reminder, it has been already discussed that the wave function of two interacting particles separated by a distance larger than the nuclear interaction radius a_c can be described by an incoming and an outgoing wave as in equation 2.1, connected by the collision matrix $U_{cc'}$ that ultimately accounts for the nuclear interaction. This wave function will be referred to as *external wave function*.

The R-Matrix theory basically provides an approximation of the so-called *internal wave function*, that is the wave function of the compound nucleus formed when the interacting particles are closer than the nuclear interaction radius. It assumes that the internal wave function can be expanded as a linear combination of its eigenstates X_λ, that correspond to the excited levels λ of the compound nucleus observed through the resonances. It can be written therefore as

$$\Psi = \sum_\lambda A_\lambda X_\lambda \tag{B.1}$$

where A_λ can be expressed as the projection of the total wave function Ψ on the corresponding eigenstate X_λ

$$A_\lambda = \int X_\lambda^* \Psi dV \tag{B.2}$$

and dV refers to the integration on the volume of the compound nucleus.

Quantum mechanics imposes that the wave functions has to be continuous and derivable, meaning the internal and external wave functions have to match in value and derivative at the surface of the compound nucleus, i.e. at the interaction radius a_c. For this reason, the values and derivatives of the radial part of the wave functions on this surface are defined explicitly for each channel c as V_c and D_c, while the non-radial part of the wave function is condensed in the so-called *surface channel functions* φ_c.

The *level width amplitudes* $\gamma_{\lambda c}$ are also defined for each combination of compound-nucleus level λ and reaction channel c, as the projection of the radial wave function of the level on the surface channel function at the nuclear surface. They are particularly important quantities, as they are related to the probability of transition between the level λ (internal wave function) and the reaction channel c (external wave function). $\delta_{\lambda,c}$ is an analogous quantity, but considering the derivative of the internal wave function instead of its value. They can be written as:

$$\gamma_{\lambda c} = \sqrt{\frac{\hbar^2}{2m_c a_c}} \int \varphi_c^* X_\lambda dS_c \tag{B.3a}$$

$$\delta_{\lambda,c} = \gamma_{\lambda c} + \sqrt{\frac{\hbar^2}{2m_c a_c}} a_c \int \varphi_c^* dS_c \tag{B.3b}$$

where m_c is the reduced mass of the particles in the channel and dS_c refers to the integration on the nuclear channel surface.

Eventually, matching values and derivatives of the internal and external wave functions at their boundary results in the following expansion for the internal wave function:

$$\Psi = \sum_c \Big[\sum_\lambda \frac{X_\lambda \, \gamma_{\lambda c}}{E_\gamma - E} \Big] (D_c - B_c V_c) \tag{B.4}$$

where E_λ is the energy of the level (resonance) and $B_c = \delta_{\gamma c}/\gamma_{\lambda c}$ is an arbitrary boundary condition.

As we are interested in the probability of transition between channels c and c', equation B.4 can be finally projected on the surface channel of the output channel c' resulting in the relation:

$$V_{c'} = \sum_c R_{cc'}(D_c - B_c V_c) \tag{B.5}$$

where

$$R_{cc'} = \sum_\lambda \frac{\gamma_{\lambda c} \gamma_{\lambda c'}}{E_\gamma - E}. \tag{B.6}$$

R is indeed the so-called *R-Matrix*, the term that ultimately accounts for what happens in the compound nucleus and expresses the probability of transition between channels as a function of the properties of its eigenstates (E_λ and $\gamma_{\lambda c}$).

Working on equation B.5, using the definitions previously given of V_c, D_c, $\gamma_{\lambda c}$ and $\delta_{\lambda c}$ (equations B.3a-B.3b) and the external wave function 2.1, the R-Matrix can be finally related to the collision matrix $\boldsymbol{U}$, that defines reaction cross sections (bold symbols refer to matrices):

$$\boldsymbol{U} = \boldsymbol{\Omega}\boldsymbol{P}^{1/2}[\boldsymbol{1} - \boldsymbol{R}(\boldsymbol{L} - \boldsymbol{B})]^{-1}[\boldsymbol{1} - \boldsymbol{R}(\boldsymbol{L}^* - \boldsymbol{B})]\boldsymbol{P}^{-1/2}\boldsymbol{\Omega} \tag{B.7}$$

Three groups of matrices can be identified in this formula:

- $\boldsymbol{R}$ is the R-Matrix and, as already mentioned, it is the only term accounting for the physics of the nuclear reaction, condensed inside the compound-nucleus
- $\boldsymbol{B}$ is a diagonal matrix of the arbitrary boundary conditions B_c
- the other matrices are diagonal matrices just related to the external wave function at the nuclear channel surface. $\boldsymbol{\Omega}$ accounts for hard-sphere phases related to the interaction of the projectile just with the nuclear potential, without formation of compound nucleus, like the *shape elastic scattering* (section 2.3) or the Coulomb interaction, in case of charged projectiles. $\boldsymbol{P}$ is the penetrability in the nuclear potential through the centrifugal barrier and therefore depends on the channel orbital angular momentum. $\boldsymbol{L} = \boldsymbol{S} + i\boldsymbol{P}$ is the logarithmic derivative of the outgoing external wave function and it is related to the penetrability and to a shift factor matrix $\boldsymbol{S}$. This last matrix in principle shifts the energy of the resonances from the energy of the levels of the compound nucleus, but this shift can be (and typically is) cancelled via proper choice of the boundary conditions B_c.

Derivation and expression for these matrices can be found in dedicated references, as [66].

Equation B.7 is exact, but it is quite difficult to handle because it implies the inversion of the complicated matrix $[\boldsymbol{1} - \boldsymbol{R}(\boldsymbol{L} - \boldsymbol{B})]^{-1}$. Instead of inverting this channel matrix, the problem is usually put in terms of the inversion of a level matrix $\boldsymbol{A}$, whose elements refer to the properties of the levels λ of the compound nucleus. The inverse of this matrix is defined as:

$$(\boldsymbol{A}^{-1})_{\lambda\nu} = (E_\lambda - E)\delta_{\lambda\nu} - \Delta_{\lambda\nu} - \frac{i}{2}\Gamma_{\lambda\nu} \tag{B.8}$$

where the subscripts λ and ν refer to the levels of the compound nucleus, Δ and Γ are the matrices of the shifts and of the level widths, respectively and can be written as:

$$\Delta_{\lambda\nu} = \sum_c \gamma_{\lambda c}\gamma_{\nu c}(S_c - B_c) \tag{B.9a}$$

$$\Gamma_{\lambda\nu} = \sum_c 2\gamma_{\lambda c}\gamma_{\nu c}P_c. \tag{B.9b}$$

As already mentioned, the shift matrix that can be cancelled with a proper choice of the boundary conditions. The diagonal elements of level width matrix represent the total widths Γ_λ of the resonances λ, that is the sum of all the partial resonance width for the different reaction channels $\Gamma_{\lambda c}$:

$$\Gamma_{\lambda c} = 2P_c\gamma_{\lambda c}^2 \tag{B.10}$$

Using this new formalism based on levels, it is easier to make approximations that simplify the general R-Matrix theory.

The Single-Level Breit-Wigner approximation has already been presented in detail in Section 2.2.3. In the following paragraph, a more detailed description of the Reich-Moore approximation will be given.

Reich-Moore Approximation

As anticipated in Section 2.2.3, the *Reich-Moore Approximation* of the R-Matrix theory [159] is significantly more complicated than the SLBW approximation, but superior and therefore employed in the R-Matrix computer code *SAMMY* [68].

The basic assumption of this approximation is that radiative capture channels behave quite differently from particle channels. In fact, there are usually a lot of possible capture channels that correspond to all the possible electromagnetic de-excitation of the compound nucleus. Since the compound nucleus is assumed to be a very complex and chaotic configuration, the width amplitudes $\gamma_{\lambda c}$ are assumed to be distributed like a Gaussian with zero mean. This implies that the products $\gamma_{\lambda c}\gamma_{\nu c}$ in equations B.9a and B.9b have random sign and, in case of a large number of contributions as for photon channels, they cancel each other and their sum can be approximated as zero. Only the diagonal terms of the product survive, and they can be summed up in the total radiative width of the resonance λ:

$$\Gamma_{\lambda\gamma} = \sum_{c\,\in\,photons} 2P_c\gamma_{\lambda c}^2. \tag{B.11}$$

The level matrix A in equation B.8, assuming proper boundary conditions that neutralize the shifts, is therefore reduced to

$$(A^{-1})_{\lambda\nu} = (E_\lambda - E - i\Gamma_{\lambda\gamma}/2)\delta_{\lambda\nu} - i \sum_{c\,\notin\,photons} \gamma_{\lambda c}\gamma_{\nu c}P_c \tag{B.12}$$

In other words, single photon channels are "eliminated" and treated in an average way in the total radiative width, enabling to reduce the A matrix to a simple number at low neutron energy, where only the neutron scattering channel is left.

B.2 The Hauser-Feshback Theory

As already discussed, resonances cannot be distinguished above a certain neutron energy. In this energy range, the *Hauser-Feshback theory* is the proper formalism to parametrize and/or predict reaction cross sections [66, 67, 160, 161]. As this energy range is not covered in this work, only an introductory treatment is presented.

This theory is based on a statistical treatment of the resonance parameters described by the R-Matrix theory. R-Matrix expressions and parameters are indeed averaged over the Gaussian Statistical Ensemble, describing the complicated configuration of the compound nucleus. For example, average cross sections $\overline{\sigma}_{cc'}$ for transitions from a channel c to c' can be written averaging the parameters in the Breit-Wigner formula 2.13 as:

$$\overline{\sigma}_{cc'} = \pi\bar{\lambda}^2 g_c(J)\frac{T_c T_{c'}}{T} W_{cc'}. \tag{B.13}$$

$W_{cc'}$ is the *width fluctuation*

$$W_{cc'} = \left(\overline{\frac{\Gamma_c\Gamma_{c'}}{\Gamma}}\right)\frac{\overline{\Gamma}}{\overline{\Gamma}_c\,\overline{\Gamma}_{c'}} \tag{B.14}$$

that corresponds to the correlation between the entrance and the outgoing channels and can be theoretically calculated [162]. T_c are the so-called *channel transmission coefficients*, that account for the penetrability of a particle in the nuclear potential region.

Transmission coefficients are really important because they bridge the optical model of nuclear interactions, used at high neutron energy, with the R-Matrix theory, used at low neutron energy. In fact, they can be either calculated solving the Schrödinger equation assuming a particular average nuclear potential given by the Optical Potential Model, or estimated using average resonance partial widths obtained from the R-Matrix analysis of experimental data. In the first case, the transmission coefficient for a channel c can be expressed as:

$$T_c = 1 - |U_{cc}|^2 \tag{B.15}$$

where U is always the collision matrix. In the second case, transmission coefficients can be written as:

$$T_c = 2\pi\frac{\overline{\Gamma}_c}{D_c} \tag{B.16}$$

where $\overline{\Gamma}_c$ are the average resonance partial widths and D_c is the average nuclear level spacing, inverse of the nuclear level density.

The distribution of the partial resonance widths can be determined with theoretical models and validated with experimental data. For example, concerning neutron widths, reduced neutron widths Γ_n^l are usually defined for each orbital angular momentum l to remove the neutron energy dependence

$$\Gamma_n^l = \frac{P_{l=0}}{P_l}\sqrt{\frac{1\ eV}{E}}\Gamma_n \tag{B.17}$$

where P are the penetrabilities for different l. These reduced neutron widths basically depend only on the square width amplitudes γ, that according the the Gaussian Orthogonal Ensemble are distributed as Gaussians with zero mean. As a consequence, the reduced neutron widths are distributed as a Porter-Thomas distribution. On the other hand, radiative widths Γ_γ, that are sums over many possible electromagnetic de-excitation channels, are distributed as a χ^2 distribution with a large number of degrees of freedom, which is basically a narrow Gaussian. For this reason, to a first approximation the radiative widths can be considered as constant for different resonances. However, while this approximation usually works well for heavy nuclei, it is not particularly precise for light nuclei, characterized by a lower number of electromagnetic de-excitation channels.

Bibliography

[1] L. Kelvin, *Macmillan's Magazine* **5**, 388 (1862).

[2] E. Rutherford, *The London, Edinburgh, and Dublin Philosophical Magazine and Journal of Science* **37**, 537 (1919).

[3] F. Aston, *Phil. Mag. and Journ. of Science* **39**, 611 (1920).

[4] A. Eddington, *Nature* **106**, 14 (1920).

[5] H. A. Bethe, *Phys. Rev.* **55**, 5 (1939).

[6] M. Burbidge, G. R. Burbidge, W. A. Fowler, and F. Hoyle, *Rev. Mod. Phys.* **29**, 4 (1957).

[7] C. Iliadis, *Nuclear Physics of Stars*, 2nd ed. (John Wiley & Sons, Ltd, 2007).

[8] M. Wiescher, *Physics* **2**, 69 (2009).

[9] S. Chandrasekhar, *Astroph. Journ.* **74**, 81 (1931).

[10] F. Matteucci, *J. Phys.: Conf. Ser.* **703**, 012004 (2016).

[11] N. Prantzos, *EAS Publications Series* **32**, 311–356 (2008).

[12] B. Pagel, *Nucleosynthesis and Chemical Evolution of Galaxies* (Cambridge University Press, 1997).

[13] C. Lederer-Woods *et al*, *Phys. Rev. C* **104**, 3 (2021).

[14] D. Dunbar, R. Pixley, W. Wenzel, and W. Whaling, *Phys. Rev.* **92**, 3 (1953).

[15] J. J. Cowan, C. Sneden, and J. L. et al., *Rev. Mod. Phys.* **93**, 1 (2021).

[16] J. J. Cowan and W. K. Rose, *ApJ* **212**, 149 (1977).

[17] M. Lugaro, A. I. Karakas, R. J. Stancliffe, and C. Rijs, *The Astrophysical Journal* **747**, 1 (2012).

[18] A. Choplin, L. Siess, and S. Goriely, *A&A* **648**, A119 (2021).

[19] F. Käppeler, *Progress in Particle and Nuclear Physics* **43**, 419 (1999).

[20] F. Käppeler, R. Gallino, S. Bisterzo, and W. Aoki, *Rev. Mod. Phys.* **83**, 157 (2011).

[21] P. A. Seeger, W. A. Fowler, and D. D. Clayton, *ApJ Suppl.* **11**, 121 (1965).

[22] D. D. Clayton, *Principles of Stellar Evolution and Nucleosynthesis* (University of Chicago Press, Chicago, 1983).

[23] M. Busso, R. Gallino, and G. J. Wasserburg, *Ann. Rev. Astron. Astrophys.* **37**, 239 (1999).

[24] S. Cristallo, The s and i processes, GIANTS XII Workshop, Catania 3-4 July 2025.

[25] E. Zinner, in *Treatise on Geochemistry*, edited by H. D. Holland and K. K. Turekian (Pergamon, Oxford, 2007) pp. 1–33.

[26] T. Stephan, R. Trappitsch, P. Hoppe, A. M. Davis, M. Bose, A. Boujibar, F. Gyngard, K. M. Hynes, N. Liu, L. R. Nittler, and R. C. Ogliore, *The Astrophysical Journal Supplement Series* **270**, 27 (2024).

[27] NIST database, `https:physics.nist.gov`.

[28] M. Lugaro, E. Zinner, R. Gallino, and S. Amari, *The Astrophysical Journal* **527**, 369 (1999).

[29] M. Pignatari, F. Herwig, R. Hirschi, M. Bennett, G. Rockefeller, C. Fryer, F. X. Timmes, C. Ritter, A. Heger, S. Jones, U. Battino, A. Dotter, R. Trappitsch, S. Diehl, U. Frischknecht, A. Hungerford, G. Magkotsios, C. Travaglio, and P. Young, *The Astrophysical Journal Supplement Series* **225**, 24 (2016).

[30] T. Rauscher, A. Heger, R. D. Hoffman, and S. E. Woosley, *The Astrophysical Journal* **576**, 323 (2002).

[31] C. Lederer-Woods and A. Mengoni, *Measurement of* ^{28,29,30}*Si*(n,γ) *capture cross sections to explain isotopic abundances in presolar grains*, Tech. Rep. (CERN-INTC-2023-009, INTC-P-653, Geneva, 2023).

[32] G. Cescutti, F. Matteucci, E. Caffau, and P. Francois, *A& A* **540**, A33 (2012).

[33] K. Bekki and T. Tsujimoto, *The Astrophysical Journal Letters* **967**, L1 (2024).

[34] E. Zinner, L. Nittler, R. Gallino, A. Karakas, M. Lugaro, O. Straniero, and J. Lattanzio, *ApJ* **650**, 350 (2006).

[35] N. Liu, T. Stephan, S. Cristallo, D. Vescovi, R. Gallino, L. R. Nittler, C. M. O. D. Alexander, and A. M. Davis, *European Physical Journal A* **58**, 10.1140/epja/s10050-022-00838-z (2022).

[36] D. Clayton, *ApJ* **484**, L67 (1997).

[37] D. Clayton, *ApJ* **598**, 313 (2003).

[38] H. K. Fok, M. Pignatari, B. Côté, and R. Trappitsch, *The Astrophysical Journal Letters* **977**, L24 (2024).

[39] C. Ritter, R. Andrassy, B. Cote, F. Herwig, P. R. Woodward, M. Pignatari, and S. Jones, *MNRAS* **474**, L1 (2018).

[40] M. Pignatari, E. Zinner, M. Bertolli, R. Trappitsch, P. Hoppe, T. Rauscher, C. Fryer, F. Herwig, R. Hirschi, F. Timmes, and F. Thielemann, *ApJ Lett* **771**, L7 (2013).

[41] K. H. Guber, P. E. Koehler, H. Derrien, T. E. Valentine, L. C. Leal, R. O. Sayer, and T. Rauscher, *Phys. Rev. C* **67**, 6 (2003).

[42] J. Boldeman, B. Allen, A. de L. Musgrove, and R. Macklin, *Nuclear Physics A* **252**, 62 (1975).

[43] Z. Bao, H. Beer, F. K appeler, F. Voss, K. Wisshak, and T. Rauscher, *Atomic Data and Nuclear Data Tables* **76**, 70 (2000).

[44] H. Beer, P. Sedyshev, W. Rochow, T. Rauscher, and P. Mohr, *Nuclear Physics A* **709**, 453 (2002).

[45] I. Dillmann, M. Heil, F. K appeler, R. Plag, T. Rauscher, and F. Thielemann, *AIP Conference Proceedings* **819**, 123 (2006).

[46] J. L. Tain *et al* (n_TOF), *The role of Fe and Ni for s-process nucleosynthesis in the early Universe and for innovative nuclear technolgies*, Tech. Rep. (CERN-INTC-2006-012, INTC-P-208, Geneva, 2006).

[47] P. Zugec *et al* (The n_TOF Collaboration), *Phys. Rev. C* **89**, 1 (2014).

[48] C. Lederer-Woods *et al* (n_TOF Collaboration), *Phys. Rev. C* **89**, 2 (2014).

[49] C. Lederer-Woods *et al* (n_TOF Collaboration), *Phys. Rev. Lett.* **110**, 2 (2013).

[50] G. Giubrone, J. L. Tain, C. Lederer, A. Pavlik, and A. Wallner, *J. Korean Phys. Soc.* **59**, 2106 (2011).

[51] G. Giubrone *et al*, *Nuclear Data Sheets* **119**, 117 (2014).

[52] T. Rauscher, N. Nishimura, R. Hirschi, G. Cescutti, A. S. J. Murphy, and A. Heger, *Monthly Notices of the Royal Astronomical Society* **463**, 4153–4166 (2016).

[53] G. Cescutti, R. Hirschi, N. Nishimura, J. W. d. Hartogh, T. Rauscher, A. S. J. Murphy, and S. Cristallo, *Monthly Notices of the Royal Astronomical Society* **478**, 4101 (2018).

[54] T. Rauscher and F.-K. Thielemann, *Atomic Data and Nuclear Data Tables* **75**, 1 (2000).

[55] R. H. Cyburt, A. M. Amthor, R. Ferguson, Z. Meisel, K. Smith, S. Warren, A. Heger, R. Hoffman, T. Rauscher, A. Sakharuk, H. Schatz, F. Thielemann, and M. Wiescher, *ApJS* **189** (2010).

[56] C. Freiburghaus and T. Rauscher, Reaction rate library in reaclib format (1999).

[57] A. Koloczek, B. Thomas, J. Glorius, R. Plag, M. Pignatari, R. Reifarth, C. Ritter, S. Schmidt, and K. Sonnabend, *Atomic Data and Nuclear Data Tables* **108**, 1–14 (2016).

[58] D. Vescovi, S. Cristallo, M. Busso, and N. Liu, *The Astrophysical Journal Letters* **897**, L25 (2020).

[59] G. Tagliente *et al*, *Measurement of the neutron capture cross section of* ^{64}*Ni*, Tech. Rep. (CERN-INTC-2022-033, INTC-P-208-ADD-1, Geneva, 2022).

[60] Kadonis 1.0 database, `https://exp-astro.de/kadonis1.0/`.

[61] E. Rutherford, *Proc. of the Royal Society London A* **97**, 374 (1920).

[62] J. Chadwick, *Nature* **129** (1932).

[63] E. Fermi, in *Nobel Lectures, Physics 1922-1941* (Elsevier Publishing Company, Amsterdam, 1965).

[64] L. Meitner and O. Frisch, *Nature* **143** (1939).

[65] A. M. Lane and R. G. Thomas, *Rev. Mod. Phys.* **30**, 2 (1958).

[66] F. Fröhner, *Evaluation and Analysis of Nuclear Resonance Data*, Tech. Rep. (JEFF Report 18 OECD/NEA, Paris, 2000).

[67] F. Gunsing, *Eur. Phys. J. Plus* **133**, 440 (2018).

[68] N. Larson, *Updated users' guide for SAMMY: multilevel R-Matrix fits to neutron data using Bayes' equations*, Tech. Rep. (ORNL/TM-9179/R8 ENDF-364/R2, Oak Ridge National Laboratory, 2008).

[69] E. Dupont, Nuclear data, Presentation at the 3^{rd} n_TOF Nuclear Physics Winter School, St. Gervais les Bains 21-26 January 2024.

[70] The ENDF/B-VIII.1 Release, www.nndc.bnl.gov/endf-releases/?version=B-VIII.1.

[71] Nuclear Energy Agency (NEA), JEFF-4.0 library (2025).

[72] O. Iwamoto, N. Iwamoto, S. Kunieda, F. Minato, S. Nakayama, Y. Abe, and *et al*, *Journal of Nuclear Science and Technology* **60**, 1 (2023).

[73] Ge, Z., Xu, R., Wu, H., Zhang, Y., Chen, G., and *et al*, *EPJ Web Conf.* **239** (2020).

[74] D. Brown, M. Chadwick, R. Capote, and *et al*, *Nuclear Data Sheets* **148**, 1 (2018).

[75] A. Plompen, O. Cabellos, C. De Saint Jean, and *et al*, *Eur. Phys. J. A* **56**, 181 (2020).

[76] A. Koning, S. Hilaire, and S. Goriely, *European Physical Journal A* **59** (2023).

[77] R. Glauber, in *Lecture on theoretical physics, vol 1*, edited by H. D. Holland and K. K. Turekian (Interscience, New York, 1959).

[78] N. Bohr, *Nature* **137** (1936).

[79] N. Bohr, *Science* **86** (1937).

[80] G. Satchler, *Introduction to nuclear reactions",*, 1st ed. (Macmillan Press LTD, 1980).

[81] H. Weidenmüller, *Annals of Physics* **158**, 120 (1984).

[82] E. Mendoza *et al*, *Nucl. Instr. Meth. A* **1047** (2023).

[83] Evaluated Nuclear Structure Data File (ENSDF), https://www.nndc.bnl.gov/ensdf/.

[84] K. S. Krane, *Introductory nuclear physics* (Wiley, New York, 1988).

[85] S. Mughabghab, *Atlas of Neutron Resonances*, 6th ed. (Elsevier, Amsterdam, 2018).

[86] R. Capote *et al*, *Nuclear Data Sheets* **110** (2009).

[87] J. M. Soto, *Study of the photon strength functions and level densities in the gamma decay following neutron capture on the isotopes* ^{234}U*,* ^{236}U *and* ^{238}U, Ph.D. thesis, Université Paris-Saclay (2020).

[88] A. Mengoni, T. Otsuka, and M. Ishihara, *Phys. Rev. C* **52**, 5 (1995).

[89] Y. Xu and S. Goriely, *Phys. Rev. C* **86**, 4 (2012).

[90] M. Moxon, T. Ware, C. Dean, O. for Economic Co-Operation, and N. E. A. O. Development, REFIT, Multilevel Resonance Parameter Least Square Fit of Neutron Transmission and Capture Data (2007).

[91] W. E. Lamb, *Phys. Rev.* **55**, 2 (1939).

[92] N. Patronis *et al*, *EPJ Techn Instrum* **10**, 13 (2023).

[93] C. Rubbia, S. A. Andriamonje, D. Bouvet-Bensimon, S. Buono, R. Cappi, P. Cennini, C. Gelès, I. Goulas, Y. Kadi, P. Pavlopoulos, J. P. C. Revol, A. Tzima, and V. Vlachoudis, *A High Resolution Spallation Driven Facility at the CERN-PS to Measure Neutron Cross Sections in the Interval from 1 eV to 250 MeV*, Tech. Rep. (CERN-LHC-98-002-EET-Add.1, Geneva, 1998).

[94] N. Colonna *et al*, *Eur. Phys. J. A* **56**, 48 (2020).

[95] R. Esposito and M. Calviani, *J. Neutron Res.* **22**, 221 (2020).

[96] R. Esposito, M. Calviani, O. Aberle, M. Barbagallo, D. Cano-Ott, T. Coiffet, N. Colonna, C. Domingo-Pardo, F. Dragoni, R. Franqueira Ximenes, L. Giordanino, D. Grenier, F. Gunsing, K. Kershaw, R. Logé, V. Maire, P. Moyret, A. Perez Fontenla, A. Perillo-Marcone, F. Pozzi, S. Sgobba, M. Timmins, and V. Vlachoudis, *Phys. Rev. Accel. Beams* **24**, 9 (2021).

[97] U. Abbondanno, S. A. Andriamonje, P. Cennini, E. Chiaveri, M. Dario, A. Mengoni, P. Pavlopoulos, F. Saldaña, V. Vlachoudis, and H. Wendler (n_TOF), *CERN n_TOF facility*, Tech. Rep. (CERN-n_TOF-PUB-2010-001, CERN-INTC-O-011, INTC-2002-037, CERN-SL-2002-053-ECT, Geneva, 2002).

[98] C. Guerrero *et al*, *Eur. Phys. J. A* **49**, 27 (2013).

[99] C. Weiß, E. Chiaveri, S. Girod, V. Vlachoudis, and the n_TOF collaboration, *Nucl. Inst. and Meth. in Phys. Res. A* **799**, 90 (2015).

[100] A. Mengoni and the n_TOF Collaboration, *The new n_TOF NEAR Station*, Tech. Rep. (CERN-INTC-2020-073, INTC-I-222, Geneva, 2020).

[101] G. Gervino, O. Aberle, A.-P. Bernardes, N. Colonna, S. Cristallo, M. Diakaki, S. Fiore, A. Manna, C. Massimi, P. Mastinu, A. Mengoni, R. Mucciola, E. Musacchio González, N. Patronis, E. Stamati, P. Vaz, and R. Vlastou, *Universe* **8**, 5 (2022).

[102] E. Stamati, A. Manna, G. Gervino, A.-P. Bernardes, N. Colonna, M. Diakaki, C. Massimi, A. Mengoni, R. Mucciola, N. Patronis, P. Vaz, R. Vlastou, and the n_TOF collaboration, *Neutron capture cross section measurements by the activation method at the n_TOF NEAR Station*, Tech. Rep. (CERN-INTC-2022-008, INTC-P-623, Geneva, 2022).

[103] J. Praena, M. Calviani, and the n_TOF Collaboration, *Commissioning of the third-generation spallation target and neutron beam characteristics of the n_TOF facility*, Tech. Rep. (CERN-INTC-2020-072, INTC-P-587, Geneva, 2020).

[104] J. Pavón-Rodríguez, J. Lerendegui-Marco, A. Manna, S. Amaducci, M. Sabaté-Gilarte, E. Musacchio-Gonzalez, M. Bacak, V. Alcayne, M. Cortés-Giraldo, V. Vlachoudis, R. Zarrella, F. García-Infantes, M. Stamati, A. Casanovas, N. Patronis, L. Tassan-Got, J. Quesada, and the n_TOF Collaboration, *submitted to Europ. Phys. Journal A* (2025).

[105] G. Battistoni, T. Boehlen, F. Cerutti, P. Chin, L. Esposito, A. Fassò, A. Ferrari, A. Lechner, A. Empl, A. Mairani, A. Mereghetti, P. G. Ortega, J. Ranft, S. Roesler, P. Sala, V. Vlachoudis, and G. Smirnov, *Annals of Nuclear Energy* **82**, 10 (2015).

[106] FLUKA website, https://fluka.cern.

[107] Stamati, M. E., Torres-Sánchez, P., Pérez-Maroto, P., Cecchetto, M., Goula, S., Mastromarco, M., Chasapoglou, S., Beltrami, C., Chiesa, D., Manna, A., Mucciola, R., Patronis, N., Praena, J., Guerrero, C., Colonna, N., Mengoni, A., Massimi, C., and the n_TOF Collaboration, *EPJ Web of Conf.* **284**, 06009 (2023).

[108] M. Diakaki, M. Bacak, C. Weiss, E. Griesmayer, C. Guerrero, E. Jericha, K. Kaperoni, M. Kokkoris, A. Manna, N. Patronis, E. Stamati, R. Vlastou, and the n_TOF Collaboration, *Direct measurement of the n_TOF NEAR neutron fluence with diamond detectors*, Tech. Rep. (CERN-INTC-2022-022, INTC-P-631, Geneva, 2022).

[109] A. Masi *et al*, in *Proceedings of theInternational Conference on Accelerator and Large Experimental Control Systems (16th)* (2018).

[110] P. Schillebeeckx, B. Becker, Y. Danon, K. Guber, H. Harada, J. Heyse, A. Junghans, S. Kopecky, C. Massimi, M. Moxon, N. Otuka, I. Sirakov, and K. Volev, *Nuclear Data Sheets* **113** (2012).

[111] V. Vlachoudis, M. Sabate-Gilarte, V. Alcayne, F. Gunsing, E. Mendoza, F. Ogallar, I. Rejwan, M. Bacak, C. Guerrero, C. Massimi, and A. Stamatopoulos, *On the resolution function of the n_TOF facility: a comprehensive study and user guide*, Tech. Rep. (CERN, 2021).

[112] C. Guerrero and the n_TOF collaboration, *Nucl. Instr. and Meth. in Phys. Res. A* **608**, 424 (2009).

[113] M. Moxon and E. Rae, *Nuclear Instruments and Methods* **24**, 445 (1963).

[114] A. Borella, G. Aerts, F. Gunsing, M. Moxon, P. Schillebeeckx, and R. Wynants, *Nucl. Instr. and Meth. in Phys. Res. A* **577**, 626 (2007).

[115] R. L. Macklin and J. H. Gibbons, *Phys. Rev.* **159**, 4 (1967).

[116] P. Mastinu, R. Baccomi, E. Berthoumieux, D. Cano-Ott, F. Gramegna, C. Guerrero, C. Massimi, P. M. Milazzo, F. Mingrone, J. Praena, G. Prete, and A. R. García, *New C_6D_6 detectors: reduced neutron sensitivity and improved safety*, Tech. Rep. (CERN n_TOF-PUB-2013-002, 2013).

[117] P. Zugec, N. Colonna, D. Bosnar, and the n_TOF collaboration, *Nucl. Instr. and Meth. in Phys. Res. A* **760**, 57–67 (2014).

[118] V. Alcayne, D. Cano-Ott, J. Garcia, E. González-Romero, T. Martínez, A. P. de Rada, J. Plaza, A. Sánchez-Caballero, J. Balibrea-Correa, C. Domingo-Pardo, J. Lerendegui-Marco, A. Casanovas, F. Calviño, and the n_TOF collaboration, *Radiation Physics and Chemistry* **217**, 111525 (2024).

[119] V. Alcayne, D. Cano-Ott, J. Garcia, E. González-Romero, T. Martínez, E. Mendoza, A. Sánchez, J. Plaza, J. Balibrea-Correa, A. Casanovas, C. Domingo-Pardo, J. Lerendegui-Marco, and the n_TOF Collaboration, *EPJ Web of Conf.* **284**, 01043 (2023).

[120] J. Lerendegui-Marco and M. Bacak, *Towards an optimized experimental setup for future neutron capture measurements at n_TOF-EAR2*, Tech. Rep. (CERN-INTC-2023-036, INTC-P-587-ADD-1, Geneva, 2023).

[121] V. Alcayne Aicua, *Measurement of the ^{244}Cm, ^{246}Cm and ^{248}Cm neutron-induced capture cross sections at the CERN n_TOF facility*, Ph.D. thesis, Universidad Complutense Madrid (2022).

[122] S. Marrone, P. Mastinu, U. Abbondanno, R. Baccomi, E. Marchi, N. Bustreo, N. Colonna, F. Gramegna, M. Loriggiola, S. Marigo, P. Milazzo, C. Moreau, M. Sacchetti, G. Tagliente, R. Terlizzi, G. Vannini, G. Aerts, E. Berthomieux, D. Cano-Ott, P. Cennini, C. Domingo-Pardo, L. Ferrant, E. Gonzalez-Romero, F. Gunsing, M. Heil, F. Kaeppeler, T. Papaevangelou, C. Paradela, P. Pavlopoulos, L. Perrot, R. Plag, J. Tain, and H. Wendler, *Nucl. Instr. and Meth. in Phys. Res. A* **517**, 389 (2004).

[123] L. Cosentino, A. Musumarra, M. Barbagallo, N. Colonna, L. Damone, A. Pappalardo, M. Piscopo, and P. Finocchiaro, Silicon detectors for the n-tof neutron beams monitoring (2015).

[124] A. Carlson, V. Pronyaev, R. Capote, G. Hale, Z.-P. Chen, I. Duran, F.-J. Hambsch, S. Kunieda, W. Mannhart, B. Marcinkevicius, R. Nelson, D. Neudecker, G. Noguere, M. Paris, S. Simakov, P. Schillebeeckx, D. Smith, X. Tao, A. Trkov, A. Wallner, and W. Wang, *Nuclear Data Sheets* **148**, 143 (2018).

[125] Isoflex usa, https://www.isoflex.com.

[126] Cortecnet, https://www.cortecnet.com/.

[127] P. Zugec, C. Weiß, C. Guerrero, F. Gunsing, V. Vlachoudis, M. Sabate-Gilarte, A. Stamatopoulos, T. Wright, J. Lerendegui-Marco, F. Mingrone, J. Ryan, S. Warren, A. Tsinganis, and M. Barbagallo, *Nucl. Inst. and Meth. in Phys. Res. A* **812**, 134 (2016).

[128] P. Zugec, Users' guide through Pulse Shape Analysis routines (2017).

[129] S. Agostinelli *et al*, *Nucl. Instr. and Meth. in Phys. Res. A* **506**, 250 (2003).

[130] P. Zugec, D. Bosnar, N. Colonna, F. Gunsing, and the n_TOF collaboration, *Nucl. Instr. and Meth. in Phys. Res. A* **826**, 80 (2016).

[131] V. Babiano Suarez, *High resolution* ^{80}*Se(n,*γ*) cross section measurement at CERN n_TOF and development of the novel i-TED detection system*, Ph.D. thesis, Universitat de Valencia (2022).

[132] G. A. Morton, H. M. Smith, and R. Wasserman, *IEEE Transactions on Nuclear Science* **14**, 443 (1967).

[133] F. Garcia Infantes, *The* ^{176}*Yb(n,*γ*) reaction cross-section measurement at n_TOF - CERN and its application for studying the production of* ^{177}*Lu in accelerator-based neutron source facilities as IFMIF-DONES*, Ph.D. thesis, Universidad de Granada (2024).

[134] W. R. Leo, *Techniques for Nuclear and Particle Physics Experiments*, 2nd ed. (Springer Berlin, Heidelberg, 1994).

[135] R. Macklin, J. Halperin, and R. Winters, *Nuclear Instruments and Methods* **164**, 213 (1979).

[136] A. Casanovas Hoste, *Neutron capture cross section measurement of the heaviest s-process branching* ^{204}*Tl and of* ^{203}*Tl at CERN n_TOF*, Ph.D. thesis, Universitat Politecnica de Catalunya (2020).

[137] J. Balibrea-Correa, J. Lerendegui-Marco, V. Babiano-Suarez, C. Domingo-Pardo, I. Ladarescu, A. Tarifeño-Saldivia, G. de la Fuente-Rosales, V. Alcayne, D. Cano-Ott, E. González-Romero, T. Martínez, E. Mendoza, A. P. de Rada, J. P. del Olmo, A. Sánchez-Caballero, A. Casanovas, F. Calviño, S. Valenta, and the n_TOF collaboration, *Nucl. Instr. and Meth. in Phys. Res. A* **1064**, 169385 (2024).

[138] A. Manna and R. Zarrella, Study of the BIF in EAR2 with PPACMon, Presentation at the n_TOF Collaboration General Meeting 2024, Padova 27-29 November 2024.

[139] R. Mucciola, Neutron capture and total cross section measurements on Mo isotopes at n_TOF and GELINA, Presentation at the n_TOF Collaboration General Meeting 2024, Padova 27-29 November 2024.

[140] J. A. Harvey, W. M. Good, R. F. Carlton, B. Castel, J. B. McCrrory, and S. F. Mughabghab, *Phys. Rev. C* **28**, 1 (1984).

[141] R. Hockenbury *et al.*, *Phys. Rev.* **178**, 4 (1969).

[142] H. Beer and R. Spencer, *Nucl. Phys.* **A240**, 29 (1975).

[143] J. Farrell, E. Bilpuch, and H. Newson, *Annals of Physics* **37**, 367 (1966).

[144] M. Heil, F. Kappeler, E. Uberseder, R. Gallino, and M. Pignatari, *Phys. Rev. C* **77**, 015808 (2008).

[145] C. Domingo-Pardo *et al*, *AIP Conference Proceedings* **1090**, 230 (2009).

[146] K. Wisshak *et al*, "Neutron Capture in s-Wave Resonances of 64Ni", Report Kernforschungszentrum Karlsruhe KfK, nr. 3582 (1983).

[147] K. Wisshak *et al*, *Nucl. Sci. Eng.* **87**, 48 (1984).

[148] F. Farina Arboccò, P. Vermaercke, K. Smits, and *et al*, *J. Radioanalytical and Nucl. Chem.* **296**, 931 (2013).

[149] B. Shivashankar, H. Naik, S. Suryanarayana, and *et al*, *J Radioanal Nucl Chem* **292** (2012).

[150] L. Venturini and B. Pecequilo, *Applied Radiation and Isotopes* **48** (1997).

[151] F. D. Corte and A. Simonits, "A compilation of accurately measured 2200 m/s cross-sections for 101 n,γ reactions of interest in activation analysis; a critical comparison with literature", Conf. on Nucl. Data For Sci. and Technol., Mito 1988, p.583 (1988).

[152] E. Gryntakis and J. Kim, *J. Radioanal. Chem.* **46**, 159 (1978).

[153] R. Heft, "A Consistent Set of Nuclear-Parameter Values for Absolute INAA", Conf. on Computers in Activ. Analysis, Mayaguez 1978, p. 495 (1978).

[154] G. Gleason *et al*, *J. Radiochem. Radioan. Lett.* **23**, 317 (1975).

[155] T. Ryves, *Journal of Nuclear Energy* **24** (1970).

[156] J. Emery, "nuclear properties of radionuclides. thermal-neutron cross sections", Oak Ridge National Lab. Reports, No.4343, p.71 (1968).

[157] W. S. Lyon, *Nuclear Science and Engineering* **8**, 378 (1960).

[158] L. Seren, H. N. Friedlander, and S. H. Turkel, *Phys. Rev.* **72**, 10 (1947).

[159] C. W. Reich and M. S. Moore, *Phys. Rev.* **111**, 3 (1958).

[160] W. Hauser and H. Feshbach, *Phys. Rev.* **87**, 2 (1952).

[161] F. H. Fröhner, *Nuclear Science and Engineering* **103** (1989).

[162] P. A. Moldauer, *Phys. Rev. C* **14**, 2 (1976).

This project has received funding from the European Union's Horizon Europe Research and Innovation programme under grant agreement No 101057511